Numerical Methods for Nonlinear Bending: From Multiscale Models to Neural Approximations

Dissertation
zur
Erlangung des Doktorgrades (Dr. rer. nat.)
der
Mathematisch-Naturwissenschaftlichen Fakultät
der
Rheinischen Friedrich-Wilhelms-Universität Bonn

vorgelegt von
Christoph Jannick Norden-Smoch
aus Troisdorf

Bonn, Dezember 2025

Angefertigt mit Genehmigung der Mathematisch-Naturwissenschaftlichen Fakultät
der Rheinischen Friedrich-Wilhelms-Universität Bonn

Gutachter/Betreuer: Prof. Dr. Martin Rumpf
Gutachter: Prof. Dr. Sergio Conti

Tag der Promotion: 20.02.2026
Erscheinungsjahr: 2026

Summary

This thesis examines numerical methods for approximating various nonlinear bending models for elastic plates and shells. The numerical treatment of these models is challenging because they involve fourth-order partial differential equation problems that cannot be solved using standard methods and are often formulated with nonlinear constraints. This thesis contributes to the development of reliable and efficient numerical schemes tailored to several nonlinear bending problems.

Specifically, four different models are considered. The first contribution concerns the numerical approximation of bending deformations in elastic shells described by parametrized surfaces. Here, a finite element method based on the discrete Kirchhoff triangle is developed that enables the computation of bending deformations under an isometry constraint.

Moreover, this thesis addresses the numerical approximation of a nonlinear homogenized bending model for elastic plates featuring microstructures in the material. To this end, a multiscale finite element method is proposed, coupling a linear three-dimensional microscopic problem with a nonlinear two-dimensional macroscopic problem.

Furthermore, a model is introduced to represent the nonlinear bending of elastic plates with prescribed folds. These folds are described by a phase field function. The model is discretized via finite elements and applied to compute elastic deformations of folded plates. Furthermore, this model serves as the foundation for a fold-optimization framework based on the same phase field formulation.

Finally, a novel numerical method is presented for simulating phase field-based Willmore flow, a time-dependent problem governed by bending energies of shells. Here, a minimizing movement formulation is combined with a neural network approach for approximating the mean curvature flow. This method demonstrates potential applications in geometry processing and computer graphics.

Acknowledgements

I would like to thank *Martin Rumpf* for his invaluable support, for introducing me to the topics explored in this thesis, and for continually encouraging me to take on new challenges. I am also grateful to *Sergio Conti* for co-reviewing this thesis and for the exceptional lectures I attended during my PhD studies. Moreover, I would like to thank *Christian Brennecke* and *Zorah Lähner* for kindly agreeing to serve on my doctoral committee.

My special thanks go to my co-author *Stefan Simon*, who supported me with great patience during my Master's thesis and at the beginning of my PhD studies, and in particular for introducing me to his finite element implementation. I am also grateful to my co-author *Josua Sassen* for our shared adventures in the world of phase fields.

I would like to express my appreciation to *Florine Hartwig*, *Konstantinos Zemas*, and *Samuel Weidemaier* for proofreading parts of this thesis.

I am thankful to *Denis Zorin* and *Daniele Panozzo* for hosting me from September to November 2023 at the Geometric Computing Lab in New York.

Special thanks go to *Carole Rossignol* and *Martin Lenz* for their support with administrative and technical matters, and for many enjoyable lunch breaks.

I would also like to thank *Lorena Pohl*, *Max Mihailescu*, *Jens Scholten*, and *Pascal Steinke* for fun coffee breaks and vivid (mostly cycling-related) discussions, and *Florine Hartwig*, *Josua Sassen*, and *Samuel Weidemaier* for their wonderful companionship in the office at the end of the hallway.

I thank my parents, *Bettina Riße-Smoch* and *Martin Smoch*, for everything they have done for me.

Last but not least, I would like to thank *Kristina Norden* for her love and laughter.

Funding The work presented in this thesis was partly funded by the *Collaborative Research Centre* 1060 of the *German Research Foundation* (DFG). I gratefully acknowledge the support of the *Hausdorff School for Mathematics*, part of the Cluster of Excellence *Hausdorff Center for Mathematics*, especially for funding my stay at New York University via the *Global Math Exchange Program* and for providing an outstanding research environment.

Contents

Chapter 1

Introduction

This thesis examines numerical methods for dimension-reduced nonlinear bending models of thin elastic plates and shells, with a particular focus on *isometric* deformations that do not involve stretching, compression, or shearing. Plates are flat elastic structures whose thickness is small compared to their planar dimensions, with shells being their curved counterpart. Nonlinear bending is an everyday phenomenon. In fact, if this thesis is read in printed form, the simple act of turning a page most probably provides an example of nonlinear bending of a thin elastic plate, namely the sheet of paper itself. Bending describes the deformation of a thin object in the direction perpendicular to its surface. When this deformation is large, linear approximations are insufficient for accurately describing the bending behavior. In this case, nonlinear bending models are required. In order to use these models to predict the bending behavior of thin elastic plates and shells, numerical methods are needed that accurately represent the nonlinearity while being efficient at the same time.

Although thin elastic plates are, of course, three-dimensional objects in the three-dimensional world, they are often described by two-dimensional models. For large elastic deformations of thin plates, the deformation of the *midsurface* (the imaginary two-dimensional surface that lies exactly halfway between the top and bottom surfaces of the plate) essentially captures most of the overall deformation of the three-dimensional thin plate. Hence, a *dimension-reduced* model describing the deformation of the midsurface accurately is desirable, because it eliminates one spatial dimension, since the midsurface does not have thickness, unlike the full three-dimensional plate.

The derivation and study of dimension-reduced models of thin elastic plates have a long history, with a first formal derivation from three-dimensional elasticity by Kirchhoff [Kir50] and Love [Lov88] in the 19th century. It is remarkable that despite the long history of this topic, a rigorous derivation of a dimension-reduced plate model from three-dimensional elasticity was only achieved in the early 2000s by Friesecke, James, and Müller [FJM02], using Γ-convergence theory developed in 1975 by De Giorgi [DGF75].

Mathematically, the methods used to derive the dimension-reduced models, as well as the general elasticity theory, can be attributed to the calculus of variations, a branch of mathematical analysis that deals with finding functions (in our case, the deformation of the midsurface of a thin plate or shell) that make a certain functional (typically an integral), called energy, minimal. Since the bending of a thin object naturally involves the *curvature* of the two-dimensional midsurface, the resulting model formulation necessarily involves geometric quantities such as curvature. Hence, studying these problems requires both analytical and differential geometry tools.

These dimension-reduced nonlinear bending models for thin elastic plates and shells can be used to compute the deformation of a thin structure when a force is applied. In general, a solution to this problem cannot be written down explicitly because it involves solving a partial differential equation (PDE). Instead, numerical methods are used to find approximate deformations. Suitable discretizations reduce the continuous nonlinear bending model to a finite-dimensional minimization problem, which can be solved algorithmically. Classically, these discretizations are derived with *finite element* (FE) methods, relying on a grid on the midsurface, subdividing it into small polygons. On every polygon, the solution is approximated by a polynomial of finite degree. Analytically, the quantitative approximation quality of the discretization can be studied by investigating the limit of the discrete model for vanishing grid size.

More recently, discretizations based on *neural networks* (NN) emerged. There, the study of the quantitative approximation quality is often not feasible analytically. Hence, numerical experiments, evaluating the method on meaningful examples, are an important tool to study the accuracy of the discretization.

This thesis investigates how numerical methods can be employed to approximate solutions to various nonlinear bending problems. It is structured to first introduce the theoretical foundations of nonlinear bending models, followed by a detailed exploration of how different nonlinear bending problems can be approximated numerically. To this end, the thesis is organized into the following chapters.

Mathematical Preliminaries. Chapter 2 begins with an overview of three-dimensional elasticity theory, followed by the derivation of the dimension-reduced nonlinear bending models for isometric deformations of plates and shells that are discussed in this thesis. In these models, isometric deformations play an important role. These are deformations that do not stretch, compress, or shear the plate or shell, and hence preserve length. Some important results about isometric embeddings are presented in the third part of this chapter. The fourth part focuses on the numerical methods used to approximate solutions to these nonlinear bending problems, specifically the discrete Kirchhoff triangle (DKT), a FE method specifically designed for bending problems. In the fifth part of this chapter, we will take a look at a time-dependent bending problem, the Willmore flow. The last part of this chapter provides an overview of phase field methods as a variational representation of geometric objects, like surfaces, which can themselves be representations of thin elastic shells.

Finite Element Approximation of Large-Scale Isometric Deformations of Parametrized Surfaces. In Chapter 3, a numerical method is described that approximately computes isometric deformations of thin elastic shells, which are given as parametrized surfaces. We consider the nonlinear bending energy for thin shells

$$\mathcal{W}^A[\psi_B] := \begin{cases} \frac{\alpha}{2} \int_\omega \sqrt{\det g_A}\ \mathrm{tr}\left(S^{\mathrm{rel}}_{\psi_B} S^{\mathrm{rel}}_{\psi_B}\right) \mathrm{d}x & \text{if } g_B = g_A \text{ a.e. in } \omega\,, \\ \infty & \text{otherwise}\,, \end{cases}$$

derived from three-dimensional nonlinear elasticity in [FJMM03], where the thin shell is given as a surface parametrized by a single chart $\psi_A \colon \omega \to \mathbb{R}^3$, with chart domain $\omega \subset \mathbb{R}^2$. This energy is defined on $W^{2,2}$-functions ψ_B that describe the parametrization of the deformed surface in three dimensions. It involves the *relative shape operator* $S^{\mathrm{rel}}_{\psi_B}$, a quantity depending on the first and second fundamental form of the undeformed surface, and the second fundamental

form of the deformed surface. We denote by g_B and g_A the first fundamental forms of the surfaces parametrized by ψ_B and ψ_A, respectively, evaluated on the chart domain ω. The minimization of this energy results in solving a fourth-order partial differential equation. Additionally, a first-order nonlinear metric constraint, namely

$$\nabla\psi_B^\top\nabla\psi_B = g_B = g_A = \nabla\psi_A^\top\nabla\psi_A \quad \text{almost everywhere,}$$

is enforced, implying that deformations of the thin shell have to be isometric. We use this metric constraint to reformulate the nonlinear energy, such that it is quadratic in the Hessian $D^2\psi_B$ of the parametrization of the deformed surface. Moreover, we consider clamped boundary conditions for the deformation, which are compatible with the metric constraint, and body forces that act on the undeformed thin shell. The reformulation of the nonlinear bending energy allows us to prove the existence of minimizers of this energy for compatible boundary conditions and body forces. We derive a discretization of the energy, based on the DKT element, with grid-size $H > 0$, where the metric constraint is only enforced on the nodes of the underlying mesh. This non-conforming FE method is based on a discrete gradient operator $\theta_H\colon \mathbf{W}_H \to \mathbf{\Theta}_H$ between two FE spaces $\mathbf{W}_H$ and $\mathbf{\Theta}_H$ that approximates the gradient. The gradient of the discrete gradient operator $\nabla\theta_H[\psi_H]$, evaluated on a discrete parametrization ψ_H, serves as an approximation of the Hessian of the continuous parametrization of the deformed surface $D^2\psi$. DKT allows for enforcing the metric constraint on the nodes of the triangulation. The main result of this chapter is the convergence of minimizers of the discrete energy to a minimizer of the continuous nonlinear bending energy, as the grid-size of the discretization tends to zero, i.e., $H \to 0$. The proof of this convergence is built upon the assumption that twice weakly differentiable deformations, satisfying the metric constraint, can be approximated in the strong $W^{2,2}$-topology by smooth functions that also satisfy this metric constraint. In the case when the shell can be deformed to a flat plate isometrically, Hornung established such a density property, cf. [Hor11]. The general case of curved shells is unclear. The convergence proof was first carried out for the flat case by Bartels, cf. [Bar13]. We mainly follow this proof strategy, using Γ-convergence techniques, and extend it to the case of curved surfaces. Our result therefore generalizes [Bar13]. The theoretical convergence result is accompanied by numerical experiments. To this end, a Lagrangian formulation of the metric constraint is taken into account. A critical point of this Lagrangian is determined by employing Newton's method, involving first and second derivatives of the nonlinear bending energy and the metric constraint with respect to the deformation and the Lagrange multipliers. Parametrizations of several curved surfaces over different parameter domains are examined for various clamped boundary conditions and volumetric forces. The numerical experiments establish the convergence under spatial refinement quantitatively. The convergence of the discrete Gauss curvature is also investigated experimentally.

Chapter 3 is based on work that began in the author's master's thesis [Smo21] supervised by Martin Rumpf. This work was extended and fundamentally revised in collaboration with Martin Rumpf and Stefan Simon, and published in [RSS22]. This chapter largely matches this article, with minor changes in notation for the sake of consistency throughout this thesis. In particular, the reformulation of the bending energy based on the metric constraint and the proof of convergence of discrete minimizers to a continuous minimizer were contributed by the author. Furthermore, the author implemented the discrete bending energy and its derivatives based on the implementation of the DKT element by Stefan Simon, and conducted the numerical experiments.

Two-Scale Finite Element Approximation of a Homogenized Plate Model. Chapter 4 is devoted to the numerical approximation of a two-dimensional thin plate model for isometric bending deformations that involves a periodic microstructure in the material, which is of the same size as the thickness of the plate. In [HNV14], this model was derived from nonlinear three-dimensional elasticity by simultaneous homogenization and dimension reduction. The resulting elastic energy has the form

$$\mathcal{W}^{\gamma}_{\mathrm{hom}}[\psi] = \begin{cases} \int_{\omega} Q^{2,\gamma}(I\!I)\,\mathrm{d}x & , \nabla\psi^{\top}\nabla\psi = I_2 \text{ a.e. in } \omega\,, \\ +\infty & , \text{ else} \end{cases}$$

for deformations $\psi \in W^{2,2}(\omega;\mathbb{R}^3)$. Here, $\omega \subset \mathbb{R}^2$ describes the rest state of a flat plate, and ψ is a deformation with second fundamental form $I\!I(x) \in \mathbb{R}^{2\times 2}$. The energy density $Q^{2,\gamma}(\cdot)$ is a quadratic form resulting from a three-dimensional linear corrector problem on the unit cube, depending on the microstructure of the material, with periodic boundary conditions in the in-plane directions for the correctors. Here, $\gamma \in (0,\infty)$ describes the ratio of the thickness $\delta > 0$ of the plate and the size of the microstructure $\varepsilon > 0$ in the limit $\delta, \varepsilon \to 0$. As in Chapter 3, now for the flat case, the isometry constraint

$$\nabla\psi^{\top}\nabla\psi = I_2 \quad \text{almost everywhere}$$

is enforced. We use the isometry constraint in order to reformulate the elastic energy, such that it is quadratic in the Hessian $D^2\psi(x) \in \mathbb{R}^{3\times 2\times 2}$. Additionally, we extend the model by also introducing the dependence of $Q^{2,\gamma}$ on the macroscopic variable $x \in \omega$, and hence allowing for macroscopically varying microstructures. To accurately approximate isometric bending deformations for this model, two levels of discretizations are required: A FE discretization of the three-dimensional linear corrector problem on the unit cube, describing the microscopic behavior of the material, and a FE discretization of the effective (macroscopic) bending deformation of the thin plate. We develop a two-scale discretization, based on the heterogeneous multiscale method (HMM), cf. [EEH03]. It involves a tri-affine FE discretization on a three-dimensional mesh with grid-size $h > 0$ to compute an approximate quadratic form $Q_h^{2,\gamma}$ by solving the linear corrector problem on the unit cube. Furthermore, for the macroscopic, isometric bending deformation, the DKT element is employed on a two-dimensional triangular mesh with grid-size $H > 0$. As in Chapter 3, the gradient of the discrete gradient operator is used to approximate the Hessian, and the isometry constraint is enforced on the nodes of the triangulation. The resulting discrete two-scale problem hence depends on the discretization parameters h and H. In addition, for both the micro- and macroscopic discretization, we introduce quadrature rules for an accurate approximation of the involved integrals on the micro- and macroscale. We show that minimizers $(\psi_H^h)_{H,h}$ of the discrete energy converge to a minimizer of the continuous homogenized bending energy, as the discretization parameters H and h simultaneously tend to zero, provided the material coefficients are at least Lipschitz-continuous in the micro- and macroscopic variables. This proof again relies on the result of Hornung, cf. [Hor11], for approximating $W^{2,2}$ isometries by smooth ones. Numerical experiments investigate the convergence quantitatively, for $h \to 0$, and the simultaneous limit $(H,h) \to 0$. Here, the linear microscopic corrector problem is solved with a direct linear solver, whereas the macroscopic nonlinear problem is solved with Newton's method, applied on the Lagrangian, which involves the isometry constraint, as in Chapter 3. Also, the influence of the parameter γ is studied experimentally. Furthermore, various numerical experiments are compared qualitatively to physical experiments with deformations of microstructured sheets of paper.

The results presented in Chapter 4 are the outcome of the recurrent collaboration with Martin Rumpf and Stefan Simon, which was published in [RSS24]. This chapter largely matches this article, with minor changes in notation for the sake of consistency throughout this thesis. A paragraph for the quadrature error estimate of the DKT was added. The author's main contributions are the proof of the convergence theorem, the implementation of the two-scale finite element scheme based on the DKT element implementation by Stefan Simon, and conducting the numerical and physical experiments.

Phase Field Approximation of a Nonlinear Folding Model. Chapter 5 examines a nonlinear bending model for isometric deformations of thin plates with folds, where the set of folds $\Sigma \subset \omega$ is approximated by a phase field function defined on the plate domain $\omega \subset \mathbb{R}^2$. In [BBH22], Bartels, Bonito, and Hornung derived a two-dimensional bending model with a single fold from three-dimensional elasticity by considering a weakening of the plate material in a small tubular neighborhood of the fold curve. It is assumed here that the fold curve divides the domain ω into two Lipschitz domains ω_1 and ω_2. The resulting bending energy reads

$$\mathcal{W}^{\Sigma}[\psi] := \begin{cases} \frac{1}{2}\int_{\omega\setminus\Sigma} |D^2\psi|^2 \,\mathrm{d}x & , \text{ if } \nabla\psi^\top\nabla\psi = I_2 \text{ a.e. in } \omega\,, \\ \infty & , \text{ else,} \end{cases}$$

and is defined on deformations $\psi \in W^{2,2}(\omega\setminus\Sigma;\mathbb{R}^3) \cap W^{1,2}(\omega;\mathbb{R}^3)$, whose gradient is allowed to jump along the fold curve Σ. As before, this bending energy inherits the nonlinear isometry constraint $\nabla\psi^\top\nabla\psi = I_2$. The existing FE discretization of this energy, also presented in [BBH22], relies on an alignment of the underlying mesh with the fold curve Σ, based on isoperimetric elements, together with a discontinuous Galerkin method, which allows for jumping of the discrete gradient along the fold curve. In Chapter 5, we introduce a nonlinear bending energy based on a phase field $v_\varepsilon\colon \omega \to \mathbb{R}_+$ that approximates a set of fold curves $\Sigma \subset \omega$ diffusively. In particular, the phase field function v_ε takes values close to one on a large part of ω, and only takes values close to zero in a small neighborhood around Σ. This neighborhood is determined by a small parameter $\varepsilon > 0$. The exact construction is inspired by the recovery sequence proposed by Ambrosio and Tortorelli in [AT92], which was used in the context of a phase field approximation of the Mumford-Shah functional, cf. [MS89]. The phase field-based bending energy with folds we introduce here reads

$$\mathcal{W}^{\varepsilon}[\psi] := \frac{1}{2}\int_\omega (v_\varepsilon^2 + \eta_\varepsilon)|D^2\psi|^2 \,\mathrm{d}x + \frac{\alpha}{\varepsilon}\int_\omega \left|\nabla\psi^\top\nabla\psi - I_2\right|^2 \,\mathrm{d}x\,,$$

and is defined on deformations $\psi \in W^{2,2}(\omega;\mathbb{R}^3)$. Instead of enforcing the isometry constraint pointwise almost everywhere, here we introduce a penalty term weighted with a factor $\frac{1}{\varepsilon}$, allowing for small deviations of isometric deformations, and hence enabling non-isometric bending deformations in a neighborhood of the fold set Σ. The fact that the fold-describing phase field v_ε is almost vanishing around Σ allows for large bending in this area while keeping the value of the energy $\mathcal{W}^{\varepsilon}[\cdot]$ low. We show that this energy Γ-converges in the strong $W^{1,2}(\omega;\mathbb{R}^3)$-topology to the above nonlinear, sharp interface bending energy with a fixed fold curve set Σ, as $\varepsilon \to 0$, provided that the finite one-dimensional *Haussdorff measure* of Σ coincides with the one-dimensional *Minkowski content* of Σ. Furthermore, we introduce a discretization of the energy $\mathcal{W}^{\varepsilon}[\cdot]$ based on the DKT element for the deformation ψ, with a piece-wise affine interpolation of the phase field v_ε for the given fold curve Σ, on a mesh with grid-size $H > 0$. With this, an approximation of the sharp interface bending energy with folds,

without aligning the mesh to the fold curve, is possible. Here, we choose the parameter $\varepsilon > 0$ to be proportional to the grid-size, i.e., $\varepsilon = CH$. We present various numerical experiments with different fold structures and boundary conditions. For the qualitative evaluation, we compare the results to physical experiments of sheets of paper with curved folds. The second part of Chapter 5 deals with the problem of optimizing the set of fold curves Σ with respect to a cost functional that depends on a deformation ψ, subject to the constraint that ψ minimizes $\mathcal{W}^\varepsilon[\cdot]$. This PDE-constraint optimization problem is defined on phase field functions $v \in W^{1,2}(\omega)$ approximating Σ. To this end, an Ambrosio-Tortorelli-type energy, cf. [AT92], is considered as a regularization term. We propose a nested optimization algorithm, where the inner problem of finding a minimizer ψ is implemented using Newton's method, and the outer problem is a gradient descent for the phase field function v. Two experiments with different forces and boundary conditions, and a simple cost functional, show the applicability of the optimization algorithm for finding the optimal fold structure.

In Chapter 5, ongoing work in collaboration with Sergio Conti and Martin Rumpf is presented. The results displayed here were part of the successful proposal for research area B2 of the collaborative research center 1720 "Analysis of Criticality", funded by the German Research Foundation (DFG). The author's main contributions are the proof of the sharp interface limit as $\varepsilon \to 0$ of the bending energy with folds approximated by phase field functions v_ε, the numerical experiments for the forward simulation, and the optimization of phase field fold curves.

A Hybrid Minimizing Movement and Neural Network Approximation of Willmore Flow. In Chapter 6, a numerical method for the approximation of Willmore flow is presented. The Willmore flow is the L^2-gradient flow of the Willmore energy, a quantity closely related to the dimension-reduced bending energy of a thin shell, represented by a closed hypersurface embedded in two or three dimensions. It reads

$$\frac{1}{2}\int_{\mathcal{M}} \mathbf{h}^2 \,\mathrm{d}\mathcal{H}^{d-1}\,.$$

Here, $\mathcal{M} \subset \mathbb{R}^d$ is a $(d-1)$-dimensional hypersurface, and $\mathbf{h}(x) \in \mathbb{R}$ is the mean curvature of $\mathcal{M}$ at $x \in \mathcal{M}$. We study the Willmore flow in the phase field setting, where the closed, orientable surfaces are represented by a diffuse transition zone of size $\varepsilon > 0$ of a phase field function, which arises as a minimizer of the Modica-Mortola energy, cf. [MM77]. We pick up the approach from [FRW11] for a nested formulation of phase field Willmore flow, based on a minimizing movement variational time discretization scheme. There, the mean curvature is approximated by an implicit time discretization of the Allen-Cahn equation, the phase field version of mean curvature flow. This results in a nested time discretization of Willmore flow, with a nonlinear *inner* problem for the Allen-Cahn equation, and an *outer* problem of computing the next time step for Willmore flow, and hence leads to a PDE-constraint optimization problem. In the method presented in Chapter 6, we follow this approach, but replace the inner problem with an operator $v_{\tilde{\tau}}[\cdot]$ approximating one time step of phase field mean curvature flow, with time step size $\tilde{\tau} > 0$. This operator consists of a linear convolution operator, concatenated with a nonlinear continuous function. This explicit architecture resembles the thresholding scheme for the approximation of mean curvature flow from [MBO92], and has been proposed by Bretin et al., cf. [BDMT22], in the context of phase field mean curvature flow. We prove that there exists a minimizer of the minimizing movement time discretization energy of the nested phase field Willmore flow incorporating an operator of this form for the inner problem.

The numerical approximation is based on a discretization of the phase fields on a regular grid in two or three dimensions. The nonlinear operator $v_{\tilde{\tau}}[\cdot]$ approximating mean curvature flow is discretized using a neural network, with a discrete convolution layer, and a multi-layer perceptron for the pointwise evaluation of the nonlinear function. Following [BDMT22], this neural operator is trained on the evolutions of phase field representations of hyperspheres, for which the analytic solution to mean curvature flow is known. Numerical experiments on several examples in two dimensions show that, quantitatively, the neural operator and the hybrid minimizing movement and neural network approach for Willmore flow, incorporating this neural operator, accurately approximate mean curvature and Willmore flow, respectively. Furthermore, the hybrid approach significantly decreases the computing time, compared to the nested scheme from [FRW11], discretized by a piece-wise multi-affine FE method. Also in three dimensions, our hybrid scheme performs well qualitatively, at a much lower computing time, compared to FE methods. We show, on various examples in three dimensions, that our scheme captures typical phenomena of Willmore flow. Typical applications for Willmore flow are in image and geometry processing. There, Willmore flow can be used for *surface fairing* and *surface inpainting*, where the preservation of C^1 boundary conditions is advantageous, compared to second-order methods like mean curvature flow. Numerical experiments in two and three dimensions display the applicability of our hybrid scheme for these tasks.

The work on the Willmore flow presented in Chapter 6 is the result of the collaboration with Martin Rumpf and Josua Sassen, which is currently under review. A preprint is available, see [RSS25]. This chapter largely matches the current state of the article, with minor changes in notation for the sake of consistency. An experiment of the Willmore flow of two neighboring spheres is added. Among the author's key contributions are parts of the implementation of the learning algorithm of the neural network, based on [BDMT22], and the nested Willmore scheme, both for the hybrid approach and the classic FE scheme from [FRW11]. Furthermore, the numerical experiments were conducted by the author. Also, the proof of the existence of minimizers for the minimizing movement formulation with neural operator was contributed by the author.

In Chapter 7, we provide a brief conclusion on the topics covered in this thesis, and provide an outlook on possible future research directions based on the results presented in this thesis.

Chapter 2

Mathematical Preliminaries

In this background chapter, the foundational theory for the following chapters is laid out. In Section 2.1, a brief summary of the theory of nonlinear elasticity in three dimensions is presented. In Section 2.2, the derivation of nonlinear bending models for plates and shells from three-dimensional elasticity via dimension reduction is explored. These models typically involve an *isometry* constraint. Some properties of functions satisfying this constraint are discussed in Section 2.3. The numerical discretization of nonlinear bending models requires special finite element methods. In Section 2.4, such a method, the discrete Kirchhoff triangle, is introduced. Section 2.5 is devoted to the Willmore flow, a time-dependent problem related to nonlinear bending. Section 2.6 deals with phase fields, scalar-valued functions that can be used to describe geometric objects like hypersurfaces via a *diffuse* transition zone. These functions naturally arise in a variational setting as minimizers of certain functionals.

2.1 Hyperelasticity

This section gives a brief overview of the theory of hyperelastic bodies in three dimensions. Here, we will mainly follow the book by Ciarlet [Cia88]; the reader is also referred to [Gur81].

Let $\Omega \subset \mathbb{R}^3$ be a bounded domain with Lipschitz boundary. The domain Ω denotes the *reference configuration* of an elastic body. This means that if no forces are applied, and the elastic body is at rest, it takes the form of Ω. Assume that there is some part on the boundary $\Gamma_D \subset \partial\Omega$, with $\mathcal{H}^2(\Gamma_D) > 0$, where the elastic body is fixed. Let $f : \Omega \to \mathbb{R}^3$ be a conservative force field. A typical example is the gravity field $f(x) = -g\rho(x)e_3$, where g is the gravitational constant, $\rho : \Omega \to \mathbb{R}_+$ is the mass density, and e_3 is the unit vector pointing "upwards" (in the third coordinate direction). Although other types of forces, like boundary forces, could be applied, we will restrict ourselves to body forces. Given an *energy density* $W \colon \mathbb{R}^{3\times 3} \to \mathbb{R}_+ ;\ \xi \mapsto W(\xi)$, assuming a homogeneous material, the elastic deformation $\phi : \Omega \to \mathbb{R}^3$ of Ω, under the force f, is given as the minimizer of the energy

$$E[\phi] := \int_\Omega W(\nabla\phi(x))\,\mathrm{d}x - \int_\Omega f(x)\cdot\phi(x)\,\mathrm{d}x\,. \tag{2.1}$$

Since Ω is not allowed to be deformed on Γ_D, ϕ has to fulfill the property $\phi(x) = x$ for all $x \in \Gamma_D$.

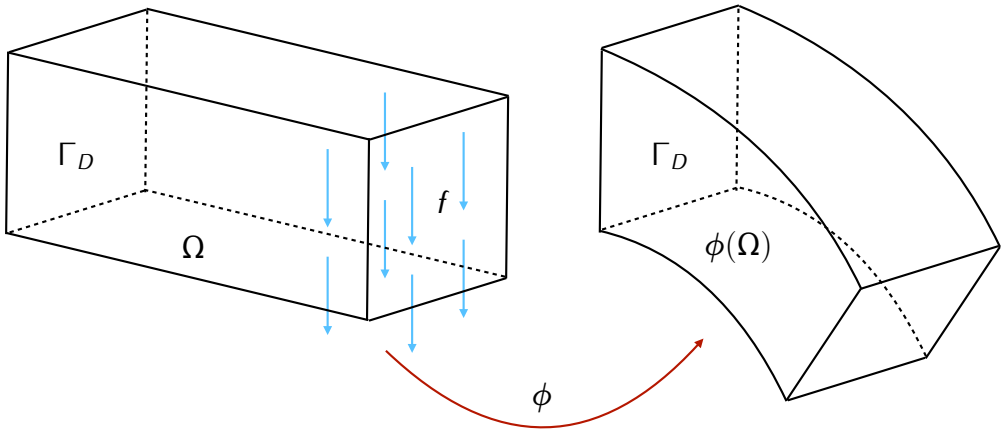

Figure 2.1: Sketch of an elastic cuboid deformed under a body force f (blue arrows), fixed on the left side Γ_D.

If ϕ is a minimizer of the elastic energy (2.1), it satisfies the *Euler-Lagrange equation*

$$\left(\frac{\mathrm{d}}{\mathrm{d}t} E[\phi + t\vartheta]\right)_{\big|t=0} = 0 \qquad \text{for all } \vartheta \in C_c^\infty(\Omega;\mathbb{R}^3)\,. \tag{2.2}$$

The energy density $W(\cdot)$ describes the *material properties* of the elastic body Ω. The strong formulation of (2.2) can be derived using integration by parts. It reads

$$\begin{aligned} -\mathrm{div}(\partial_\xi W(\nabla\phi)) &= f \quad \text{in } \Omega \\ \phi(x) &= x \quad \text{on } \Gamma_D\,. \end{aligned}$$

Physically, $\partial_\xi W(\nabla\phi(x))$ is the *stress* the elastic object is subjected to, when being deformed by ϕ. We assume that $W(\xi) \geqslant 0$ for all $\xi \in \mathbb{R}^{3\times 3}$. Furthermore, some additional properties are imposed on $W(\cdot)$ from a physical modeling perspective. If no force is acting, and the elastic body is not deformed at all, so $\phi(x) = x$ for all $x \in \Omega$, the total elastic energy should be zero: $\int_\Omega W(\nabla\phi(x))\,\mathrm{d}x = 0$. If this is the case, then the gradient of ϕ is the identity matrix $\nabla\phi = I_3$. Hence, it must hold

$$W(I_3) = 0\,. \tag{2.3}$$

If an elastic body (deformed or undeformed) is rotated in space, the internal elastic energy should not change. This imposes the additional assumption on $W(\cdot)$ that it is *frame indifferent*

$$W(Q\xi) = W(\xi) \qquad \text{for all } \xi \in \mathbb{R}^{3\times 3} \text{ and all } Q \in \mathrm{SO}(3)\,, \tag{2.4}$$

with $\mathrm{SO}(3) = \left\{Q \in \mathbb{R}^{3\times 3} \,:\, Q^\top Q = I_3\,,\ \det(Q) = 1\right\}$. Equations (2.3) and (2.4) together imply

$$W(Q) = 0 \qquad \text{for all } Q \in \mathrm{SO}(3)\,.$$

Hence, rotations $\phi = Qx$, with $Q \in \mathrm{SO}(3)$, are minimizers of $\int_\Omega W(\nabla\phi)\,\mathrm{d}x$, if no boundary conditions are imposed.

Of course, the choice of $W(\cdot)$ heavily depends on the kind of material one wants to model. If the response of the material is the same in all directions (think of rubber), the material is called *isotropic*. In this case $W(\cdot)$ satisfies

$$W(\xi Q) = W(\xi) \qquad \text{for all } \xi \in \mathbb{R}^{3\times 3} \text{ and all } Q \in \mathrm{SO}(3)\,.$$

A concrete example is the St. Venant-Kirchhoff model for isotropic materials, cf. [Ogd97]. It reads

$$W(\xi) = \begin{cases} \mu|\sqrt{\xi^\top \xi} - I_3|^2 + \frac{\lambda}{2}(\operatorname{tr}(\sqrt{\xi^\top \xi} - I_3))^2 & , \text{ if } \det(\xi) > 0 \\ +\infty & , \text{ else,} \end{cases} \tag{2.5}$$

with the *Lamé constants* $\mu > 0$ and $\lambda \geqslant 0$. The constraint $\det(\xi) > 0$ models the non-interpenetration of matter. A typical example of an *anisotropic* material is wood, which has a different elastic response along its fibers than perpendicular to them.

Remark 2.1. *The term* $|\sqrt{\xi^\top \xi} - I_3|$ *in* (2.5) *is equal to the distance of* ξ *to* $SO(3)$*, if* ξ *is positive definite, i.e.*

$$\operatorname{dist}(\xi, \mathrm{SO}(3)) := \inf_{R \in \mathrm{SO}(3)} |\xi - R| = |\sqrt{\xi^\top \xi} - I_3| \,,$$

which was first proven in [MPG79].

2.2 Derivation of nonlinear bending models via dimension reduction

In this section, we state the most important results that rigorously derive nonlinear bending models from three-dimensional elasticity. In Section 2.1 we saw that minimizing the functional (2.1) gives the deformation of a hyperelastic object for a given force. Now consider a thin elastic object $\Omega_\delta = \omega \times (-\frac{\delta}{2}, \frac{\delta}{2})$, with thickness $\delta > 0$, and a Lipschitz domain $\omega \subset \mathbb{R}^2$ as midsurface. We look at the *rescaled* elastic energy

$$\mathcal{W}_\delta[\phi] := \frac{1}{\delta} \int_{\Omega_\delta} W(\nabla \phi) \, \mathrm{d}x \,. \tag{2.6}$$

A mathematically natural question is to ask what happens if the thickness tends to zero: $\delta \to 0$. This is not only interesting from the analytical perspective, but also highly relevant in practical applications: For very thin objects, the deformation of the midsurface ω includes most of the information of the overall deformation of the object. Hence, a dimension-reduced model formulated on $\omega \subset \mathbb{R}^2$ might be more efficient to compute elastic deformations. To this end, mathematical tools to derive a limit model as $\delta \to 0$ are necessary. The most important tool to analyze sequences of minimization problems is the concept of Γ-convergence, first introduced by De Giorgi [DGF75]. We refer to [DM93] and [Bra02] for an extensive introduction to the theory.

Definition 2.2 (Γ-convergence, [Bra02])**.** *Let* (X, d) *be a metric space. Let* $(\mathcal{W}_\delta[\cdot])_{\delta>0}$ *be a sequence of functionals* $\mathcal{W}_\delta \colon X \to (-\infty, +\infty]$*. We say* $(\mathcal{W}_\delta[\cdot])_{\delta>0}$ Γ*-converges to a functional* $\mathcal{W}_0 \colon X \to (-\infty, +\infty]$*, if the following two conditions hold*

(i) For every sequence $(x_\delta)_{\delta>0} \subset X$ *with* $x_\delta \xrightarrow{d} x$ *as* $\delta \to 0$ *we have*

$$\liminf_{\delta \to 0} \mathcal{W}_\delta[x_\delta] \geqslant \mathcal{W}_0[x] \,.$$

(ii) For every $x \in X$ there exists a sequence $(x_\delta)_{\delta>0} \subset X$ with $x_\delta \xrightarrow{d} x$ as $\delta \to 0$, such that

$$\limsup_{\delta\to 0} \mathcal{W}_\delta[x_\delta] \leqslant \mathcal{W}_0[x]\,.$$

Remark 2.3. *If $(\mathcal{W}_\delta[\cdot])_{\delta>0}$ Γ-converges to $\mathcal{W}_0[\cdot]$ and $(x_\delta)_{\delta>0} \subset X$ is a sequence of minimizers of $(\mathcal{W}_\delta[\cdot])_{\delta>0}$, which converges to $x \in X$, then x is a minimizer of $\mathcal{W}_0[\cdot]$, cf. [Bra02].*

Typically, the metric space X is replaced by some function space (often a Sobolev space) that is defined on a fixed domain. The functional (2.6) instead takes functions as input, which are defined on domains Ω_δ for different $\delta > 0$. To circumvent this issue, we rewrite (2.6) by a coordinate transformation as

$$\mathcal{W}_\delta[\phi] = \int_{\Omega_1} W(\nabla_\delta \phi)\,\mathrm{d}x\,. \tag{2.7}$$

Here, we write $\nabla_\delta \phi := (\partial_1\phi, \partial_2\phi, \frac{1}{\delta}\partial_3\phi)$. In [LDR95], the Γ-limit of (2.7) was derived. The resulting functional is the so-called *membrane energy*, which models in-plane deformations of the thin plate, like stretching and shearing. In the following, we will see how the *bending energy* for different models was derived, by studying Γ-convergence of $\frac{1}{\delta^2}\mathcal{W}_\delta[\cdot]$.

Nonlinear plate theory. We start with the celebrated work by Friesecke, James, and Müller [FJM02]. They studied the Γ-limit of the rescaled elastic energy

$$\frac{1}{\delta^2}\mathcal{W}_\delta[\phi] = \frac{1}{\delta^2}\int_\Omega W(\nabla_\delta \phi)\,\mathrm{d}x \tag{2.8}$$

under the following assumptions on the stored energy function $W(\cdot)$.

Assumption 2.4. *Assume that $W(\xi) \geqslant 0$ and $W(\xi) = 0$ for $\xi \in SO(3)$. Furthermore we assume*

(i) frame indifference, i.e. (2.4),

(ii) $W \in C^0(\mathbb{R}^{3\times 3})$, and $W \in C^2(\mathbb{R}^{3\times 3})$ in a neighborhood of $\mathrm{SO}(3)$,

(iii) quadratic growth conditions at $\mathrm{SO}(3)$*: $W(\xi) \geqslant C\mathrm{dist}(\xi, \mathrm{SO}(3))^2$.*

Since we assume $W \in C^2(\mathbb{R}^{3\times 3})$ in a neighborhood of $\mathrm{SO}(3)$, we can define the *linearized* stored energy function $Q^3(F) := \partial^2_{\xi\xi} W(I_3)(F, F)$ for a matrix $F \in \mathbb{R}^{3\times 3}$. In [FJM02], the following Γ-convergence result was shown.

Theorem 2.5 (Friesecke, James, and Müller, cf. [FJM02])**.** *Under Assumption 2.4 the energies $(\frac{1}{\delta^2}\mathcal{W}_\delta[\cdot])_{\delta>0}$ defined in* (2.8) *Γ-converge in the strong $W^{1,2}(\Omega_1;\mathbb{R}^3)$ topology to*

$$\mathcal{W}_0[\psi] := \begin{cases} \frac{1}{24}\int_\omega Q^2(II)\,\mathrm{d}x & , \quad \text{if } \nabla\psi^\top\nabla\psi = I_2 \text{ a.e. in } \omega\,, \\ +\infty & , \quad \text{else.} \end{cases} \tag{2.9}$$

$\mathcal{W}_0[\cdot]$ is defined on functions $\psi \in W^{2,2}(\omega;\mathbb{R}^3)$, with normal $n[\psi] := \frac{\partial_1\psi\times\partial_2\psi}{|\partial_1\psi\times\partial_2\psi|} \in \mathbb{R}^3$ and second fundamental form

$$II := -D^2\psi \cdot n[\psi] = -(\partial_i\partial_j\psi \cdot n[\psi])_{i,j=1,2} \in \mathbb{R}^{2\times 2}\,.$$

Here, ψ is constantly extended in the thickness direction e_3 to define it on Ω_1. Furthermore we define $Q^2(A) := \inf_{d\in\mathbb{R}^3} Q^3(\sum_{i,j=1}^2 A_{ij} e_i \otimes e_j + d \otimes e_3)$ for matrices $A \in \mathbb{R}^{2\times 2}$.

Remark 2.6. *The constraint $\nabla\psi^\top\nabla\psi = I_2 \Leftrightarrow \partial_i\psi\cdot\partial_j\psi = \delta_{ij}$ for all $i,j\in\{1,2\}$ allows only isometric deformations of the midsurface ω, i.e., no stretching, compression, or shearing is allowed in the limit model. In Section 2.3, properties of isometric immersions will be discussed further.*

Example 2.7. *In the case of an isotropic material law, when $W(\cdot)$ is given by* (2.5)*, the linearized stored energy function $Q^3(\cdot) = \partial_\xi^2 W(I_3)(\cdot,\cdot)$ is of the form*

$$Q^3(F) = 2\mu\left|\frac{F+F^\top}{2}\right|^2 + \lambda(\operatorname{tr}(F))^2\,,\quad F\in\mathbb{R}^{3\times 3}\,,$$

cf. [FJM02]. Then we have

$$Q^2(A) = \inf_{d\in R^3} Q^3\Big(\sum_{i,j=1}^{2} A_{ij}e_i\otimes e_j + d\otimes e_3\Big) = 2\mu\left|\frac{A+A^\top}{2}\right|^2 + \frac{2\mu\lambda}{2\mu+\lambda}(\operatorname{tr}(A))^2\,,\quad A\in\mathbb{R}^{2\times 2}\,.$$

Proof. For a vector $d\in\mathbb{R}^3$ and $A\in\mathbb{R}^{2\times 2}$ we have

$$Q^3\Big(\sum_{i,j=1}^{2} A_{ij}e_i\otimes e_j + d\otimes e_3\Big) = 2\mu\left(\left|\frac{A+A^\top}{2}\right|^2 + d_1^2+d_2^2+d_3^2\right) + \lambda(A_{11}+A_{22}+d_3)^2\,.$$

Minimizing this polynomial expression in $d=(d_1,d_2,d_3)$, we get

$$d_1 = d_2 = 0\,,\quad d_3 = -\frac{\lambda}{2\mu+\lambda}(A_{11}+A_{22})$$

for $d = \arg\min_{d\in\mathbb{R}^3} Q^3(\sum_{i,j=1}^2 A_{ij}e_i\otimes e_j + d\otimes e_3)$. So,

$$\begin{aligned} Q^2(A) =& 2\mu\left(\left|\frac{A+A^\top}{2}\right|^2 + \left(\frac{\lambda}{2\mu+\lambda}\right)^2(\operatorname{tr}(A))^2\right) + \lambda\left(\frac{2\mu}{2\mu+\lambda}\right)^2(\operatorname{tr}(A))^2\\ =& 2\mu\left|\frac{A+A^\top}{2}\right|^2 + \frac{2\mu\lambda}{2\mu+\lambda}(\operatorname{tr}(A))^2\,. \end{aligned}$$

□

The key ingredient for proving Theorem 2.5 is the theorem on geometric rigidity, also proven in [FJM02], which we will state here for the sake of completeness.

Theorem 2.8 (Geometric Rigidity, [FJM02])**.** *Let U be a bounded Lipschitz domain in $\mathbb{R}^d$, with $d\geqslant 2$. Then, there exists a constant $C(U)>0$ with the following property: For each $v\in W^{1,2}(U;\mathbb{R}^d)$ there exists a rotation $R\in SO(d)$ such that*

$$\big\|\nabla v - R\big\|_{L^2(U;\mathbb{R}^{d\times d})} \leqslant C(U)\,\big\|\operatorname{dist}(\nabla v, SO(d))\big\|_{L^2(U)}\,.$$

This theorem is a fundamental result in analysis, with applications not only in the theory of dimension reduction but also, for example, in the rigorous derivation of models for linearized elasticity from finite nonlinear elasticity, cf. [MNP02]

Nonlinear shell theory. In [FJMM03], the theory of dimension reduction for flat plates from [FJM02] is extended to thin, *curved* objects, so-called *shells*. A bounded Lipschitz domain of the form

$$\mathcal{M}_A^\delta := \left\{ x + s\nu_A(x) \,:\, x \in \mathcal{M}_A\,,\ s \in (-\frac{\delta}{2}, \frac{\delta}{2}) \right\}\,,$$

with curved midsurface $\mathcal{M}_A \subset \mathbb{R}^3$ is considered. Here, $\nu_A(x)$ is the unit normal of $\mathcal{M}_A$ at $x \in \mathcal{M}_A$, and $\mathcal{M}_A$ is assumed to be parametrized by a single C^2 chart $\psi_A\colon \omega \to \mathcal{M}_A$, with $\omega \subset \mathbb{R}^2$. The three-dimensional elastic energy, with a stored energy function $W(\cdot)$ satisfying Assumption 2.4, considered here is

$$\mathcal{W}_\delta^A[\phi] = \frac{1}{\delta} \int_{\mathcal{M}_A^\delta} W(\nabla \phi)\, \mathrm{d}x\,. \tag{2.10}$$

In [FJMM03], the following Γ-convergence result was shown

Theorem 2.9 (Friesecke, James, Mora, and Müller, cf. [FJMM03])**.** *Under Assumption 2.4 the rescaled energies* $(\frac{1}{\delta^2}\mathcal{W}_\delta^A[\cdot])_{\delta>0}$ *defined in* (2.10) *Γ-converge to*

$$\mathcal{W}^A[\phi] := \begin{cases} \frac{1}{24}\int_{\mathcal{M}_A} Q^2(x, S_{\mathcal{M}_A,\phi})\, \mathrm{d}\mathcal{H}^2 & , \quad \text{if } \nabla_{tan}\phi^\top \nabla_{tan}\phi = I_2 \text{ a.e. in } \mathcal{M}_A \\ +\infty & , \quad \text{else.} \end{cases} \tag{2.11}$$

Here, $\phi \in W^{2,2}(\mathcal{M}_A; \mathbb{R}^3)$, and $S_{\mathcal{M}_A,\phi} \in \mathbb{R}^{3\times 3}$ is the relative shape operator, also called Weingarten map, cf. [FJMM03], and $Q^2(x,F) = \inf_{d\in\mathbb{R}^3} Q^3(F + d\otimes \nu_A(x))$, with the linearized stored energy function Q^3 defined above. We denote by $\nabla_{tan}\phi$ the tangential derivative of ϕ on the manifold $\mathcal{M}_A$.

Remark 2.10. *The limit energy is formulated as an integral over the manifold $\mathcal{M}_A$. Let $\psi_B\colon \omega \to \mathbb{R}^3$, with $\psi_B(x) = \phi(\psi_A(x))$, be the parametrization of the deformed mid-surface $\phi(\mathcal{M}_A)$, cf. Figure 2.2. With this,* (2.11) *can be reformulated as an integral over the chart domain $\omega \subset \mathbb{R}^2$, assuming for instance $W(\cdot)$ is of the form* (2.5)*, with $\mu = 8\alpha > 0$ and $\lambda = 0$, as*

$$\mathcal{W}^A[\psi_B] := \begin{cases} \frac{\alpha}{2}\int_\omega \sqrt{\det g_A}\ \mathrm{tr}\left(S_{\psi_B}^{rel} S_{\psi_B}^{rel}\right) \mathrm{d}x & \text{if } g_B = g_A \text{ a.e. in } \omega\,, \\ \infty & \text{otherwise}\,. \end{cases} \tag{2.12}$$

Here, we use the matrix representation of the relative shape operator, i.e.

$$S_{\psi_B}^{rel} := g_A^{-1}(II_A - II_B) = g_A^{-1}\left(D^2\psi_B \cdot n_B - D^2\psi_A \cdot n_A\right) \in \mathbb{R}^{2\times 2}\,. \tag{2.13}$$

The normal of $\mathcal{M}_B = \psi_B(\omega) = \phi(\mathcal{M}_A)$ pulled back on the chart domain ω is

$$n_B(x) = n[\psi_B](x) = \frac{\partial_1\psi_B(x) \times \partial_2\psi_B(x)}{|\partial_1\psi_B(x) \times \partial_2\psi_B(x)|}\,,$$

and the corresponding first fundamental form g_B and second fundamental form II_B at $x \in \omega$ are given by

$$\begin{aligned} g_B(x) &= (\nabla\psi_B(x))^\top \nabla\psi_B(x) \in \mathbb{R}^{2\times 2}\,, \\ II_B(x) &= \nabla n_B(x) \cdot \nabla\psi_B(x) = -D^2\psi_B(x) \cdot n_B(x) \in \mathbb{R}^{2\times 2}\,. \end{aligned}$$

Normal, metric and second fundamental form are analogously defined for $\mathcal{M}_A$ and the given parametrization ψ_A.

The reader is referred to [Hee16] for the exact derivation of (2.12) *from* (2.11)*.*

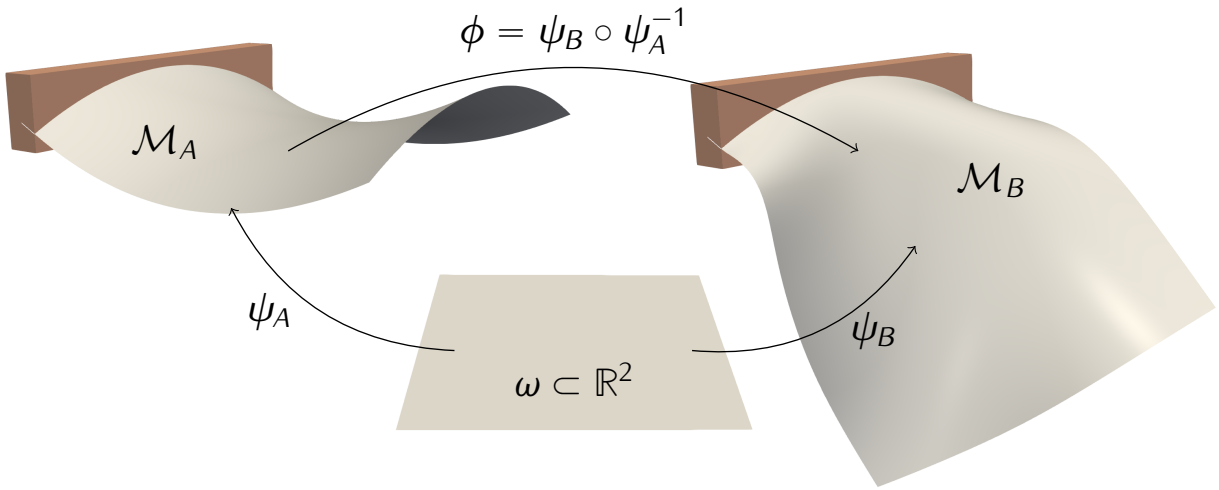

Figure 2.2: A deformation ϕ of a parametrized surface $\mathcal{M}_A$ onto an image surface $\mathcal{M}_B$ with clamped boundary is described by parametrizations ψ_A, ψ_B over the chart domain ω.

Homogenized nonlinear plate theory. In [HNV14], Hornung, Neukamm, and Velčić studied the simultaneous homogenization of a microstructured thin plate and a dimension reduction from 3D volume elasticity to a 2D elastic bending model. More precisely, they studied a plate with thickness $\delta > 0$, whose material oscillates on a scale $\varepsilon > 0$ in the in-plane directions. The limit model in the bending regime is studied for $\delta \to 0$ and $\varepsilon \to 0$ simultaneously. Let $\Omega_\delta := \omega \times \delta I$ be the reference configuration of a thin elastic plate, with a Lipschitz domain with piecewise C^1 boundary $\omega \subset \mathbb{R}^2$ as midsurface, $I = (-\frac{1}{2}, \frac{1}{2})$ and thickness $\delta > 0$. Let $W : \mathbb{R}^2 \times \mathbb{R}^{3\times 3} \to \mathbb{R}$ be a nonlinear energy density which is periodic with period 1 in the first component. We consider a nonlinear elastic energy

$$\frac{1}{\delta^3} \int_{\Omega_\delta} W(\frac{x'}{\varepsilon}, \nabla \phi_\delta(x)) \, \mathrm{d}x \tag{2.14}$$

for the thin plate, composed of a microstructure of width $\varepsilon > 0$, which is homogeneous in vertical direction (cf. Figure 2.3). The scaling δ^{-3} corresponds to the bending regime. Here, $x' = (x_1, x_2)$ represents the in-plane coordinates. A rescaling of (2.14) onto the fixed 3D domain $\Omega := \omega \times I$ reads as

$$\mathcal{W}^{\delta,\varepsilon}[\psi_\delta] := \frac{1}{\delta^2} \int_\Omega W(\frac{z'}{\varepsilon}, \nabla_\delta \psi_\delta(z)) \, \mathrm{d}z \,, \tag{2.15}$$

for the rescaled deformation $\psi_\delta(z', z_3) := \phi_\delta(z', \delta z_3)$ and the rescaled gradient

$$\nabla_\delta \psi_\delta := (\nabla' \psi_\delta, \frac{1}{\delta} \partial_3 \psi_\delta) \,, \qquad \text{with } \nabla' \psi_\delta = (\partial_1 \psi_\delta, \partial_2 \psi_\delta) \,.$$

In [HNV14], Hornung et al. studied the Γ-limit of (2.15) for δ and ε converging to zero, under the following assumptions. Given $\varepsilon = \varepsilon(\delta)$ as a monotone function from $(0, \infty)$ to $(0, \infty)$ we assume that $\frac{\delta}{\varepsilon(\delta)} \to \gamma$ as $\delta \to 0$ with $\gamma \in (0, \infty)$. The energy density $W : \mathbb{R}^2 \times \mathbb{R}^{3\times 3} \to [0, \infty]$ is Borel measurable and $W(\cdot, F)$ is periodic for all $F \in \mathbb{R}^{3\times 3}$ with $W(y', \cdot) \in C^0(\mathbb{R}^{3\times 3}, [0, \infty])$ for

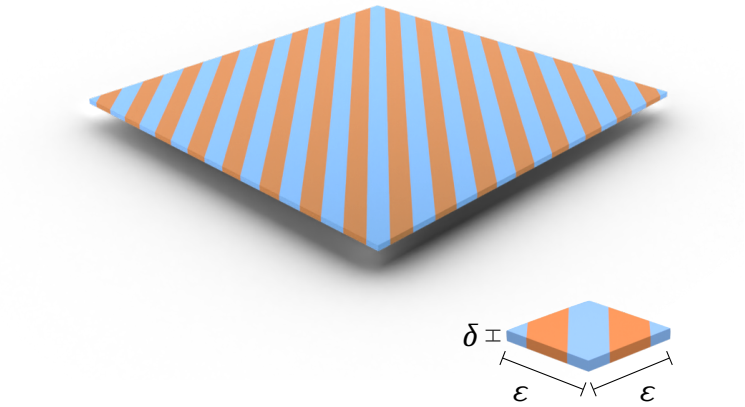

Figure 2.3: Thin plate with thickness δ and periodic in-plane microstructure with size ε.

almost every $y' \in \mathbb{R}^2$. Furthermore, $W(y', RF) = W(y', F)$ for all $F \in \mathbb{R}^{3\times 3}$ and all $R \in SO(3)$ and there exist positive constants c_1, c_2, ρ such that

$$\begin{aligned} &W(y', F) \geqslant c_1 \mathrm{dist}^2(F, SO(3)) \quad \text{for all } F \in \mathbb{R}^{3\times 3}, \\ &W(y', F) \leqslant c_2 \mathrm{dist}^2(F, SO(3)) \quad \text{for all } F \in \mathbb{R}^{3\times 3} \text{ with } \mathrm{dist}^2(F, SO(3)) \leqslant \rho. \end{aligned}$$

Finally, we assume that there exists a quadratic form $Q^3(y, \cdot)$, defined as the quadratic expansion of $W(y, \cdot)$ at the identity, i.e. there exists a monotone function $r : [0, \infty) \to [0, \infty]$ with $r(t) \to 0$ as $t \to 0$, such that, for almost every $y' \in \mathbb{R}^2$

$$|W(y', I_3 + G) - Q^3(y', G)| \leqslant r(|G|)|G|^2 \quad \text{for all } G \in \mathbb{R}^{3\times 3} \tag{2.16}$$

with $|G|$ for $G \in \mathbb{R}^{3\times 3}$ denoting the Frobenius norm.

Example 2.11. *Consider a thin elastic plate as displayed in Figure 2.3, consisting of two materials (blue and orange), oscillating at the scale ε. In the case of an isotropic material law, Q^3 is given by*

$$Q^3(y', G) = \mu(y') \left| \tfrac{G+G^\top}{2} \right|^2 + \frac{\lambda(y')}{2} |tr(G)|^2$$

where the Lamé-Navier parameters $\mu(y')$ and $\lambda(y')$ are periodic functions with period cell being the unit square $Y' := (0,1)^2$ with different values on the orange and blue phases, respectively.

Based on Q^3 now define

$$Q^{2,\gamma} : \mathbb{R}^{2\times 2}_{\mathrm{sym}} \to \mathbb{R}; \quad Q^{2,\gamma}(A) := \inf_{\vartheta \in \mathcal{V}} \int_Y Q^3(y', \iota(y_3 A) + \nabla_\gamma \vartheta(y))\, \mathrm{d}y \tag{2.17}$$

with $Y := Y' \times Y_3$ denoting the fundamental cell in 3D for $Y_3 := (-\frac{1}{2}, \frac{1}{2})$,

$$\iota(A) := \begin{pmatrix} & A & & 0 \\ & & & 0 \\ 0 & & 0 & 0 \end{pmatrix} \in \mathbb{R}^{3\times 3},$$

for $A \in \mathbb{R}^{2\times 2}$, and $\nabla_\gamma \vartheta(y) := \left(\nabla_{y'}\vartheta(y), \frac{1}{\gamma}\partial_3\vartheta(y)\right)$. Here, the infimum in (2.17) is taken over all $\vartheta \in \mathcal{V}$, with

$$\mathcal{V} := \big\{ \vartheta \in W^{1,2}(Y;\mathbb{R}^3) \,:\, \vartheta(y) = (By', 0)^\top + \varphi(y)\,, \\ B \in \mathbb{R}^{2\times 2}_{\mathrm{sym}}\,,\ \varphi \in W^{1,2}(Y;\mathbb{R}^3)\,,\ \varphi(y) \text{ periodic in } y'\,,\ \int_Y \varphi \,\mathrm{d}y = 0 \big\}\,.$$

Hornung, Neukamm, and Velčić proved the following Γ-convergence result.

Theorem 2.12 (Hornung, Neukamm, and Velčić, cf. [HNV14]). *Under the above assumptions the energies $(\mathcal{W}^{\delta,\varepsilon(\delta)}[\cdot])_{\delta>0}$, defined in* (2.15)*, Γ-convergence in the strong L^2-topology to the homogenized elastic plate energy*

$$\mathcal{W}^\gamma_{hom}[\psi] = \begin{cases} \int_\omega Q^{2,\gamma}(II(x))\,\mathrm{d}x & ,\ \nabla\psi^\top\nabla\psi = I_2 \text{ a.e. in } \omega\,, \\ +\infty & ,\ \text{else} \end{cases} \tag{2.18}$$

for $\psi \in W^{2,2}(\omega;\mathbb{R}^3)$.

Note that this is a generalization of [FJM02], where the plate model with homogeneous material was derived. In [HNV14], the case $\gamma = \infty$ was also discussed, resulting in a different quadratic form $Q^{2,\infty}$. Here, we confine ourselves to the case $\gamma \in (0,\infty)$.

Nonlinear plate theory with a fold. In [BBH22] Bartels, Bonito, and Hornung derived a dimension-reduced model for the bending of a plate with a prescribed fold. As above, they considered a thin three-dimensional domain $\Omega_\delta = \omega \times (-\frac{\delta}{2}, \frac{\delta}{2})$, with thickness $\delta > 0$ and bounded Lipschitz mid-surface $\omega \subset \mathbb{R}^2$. Additionally, a folding curve $\Sigma \subset \omega$ is given, around which the material of the elastic body is assumed to be weakened. In explicit, a three-dimensional elastic energy of the form

$$\mathcal{W}^\Sigma_\delta[\phi] := \int_{\Omega_1} f_\delta(x')\, W(\nabla_\delta \phi)\,\mathrm{d}x \tag{2.19}$$

is considered, where $f_\delta \colon \omega \to \mathbb{R}_+$ is of the form $f_\delta = s_\delta \chi_{\Sigma_{r_\delta}} + 1 - \chi_{\Sigma_{r_\delta}}$. Here, $\chi_{\Sigma_{r_\delta}}$ is the characteristic function of the set $\Sigma_{r_\delta} := \{x \in \omega \,:\, \mathrm{dist}(x,\Sigma) < r_\delta\}$. Hence, r_δ determines the area around the fold Σ that is weakened, and s_δ defines how much the material is weakened in this area. The parameters $s_\delta > 0$ and $r_\delta > 0$ depend on the thickness $\delta > 0$, satisfying

$$\limsup_{\delta\to 0} \frac{\delta^2}{s_\delta} < \infty\,, \quad \limsup_{\delta\to 0} \frac{\delta}{r_\delta} < \infty\,, \quad \lim_{\delta\to 0} \frac{s_\delta r_\delta}{\delta^2} = 0\,.$$

Additionally, the following regularity of the fold curve Σ is assumed.

Assumption 2.13. *The fold curve Σ is parametrized by a continuous and injective map $\sigma : [0,1] \to \omega$, with $\Sigma = \sigma(0,1)$, and $\partial\Sigma = \{\sigma(0),\sigma(1)\}$ is contained in one single connected component of $\partial\omega$. This implies that Σ divides ω in exactly two connected components ω_1 and ω_2. Additionally, we assume Σ is such that both connected components are Lipschitz domains.*

See Figure 2.4 for a small sketch of the described quantities. In [BBH22], the following rigorous dimension reduction limit for this nonlinear bending model with a fold was shown.

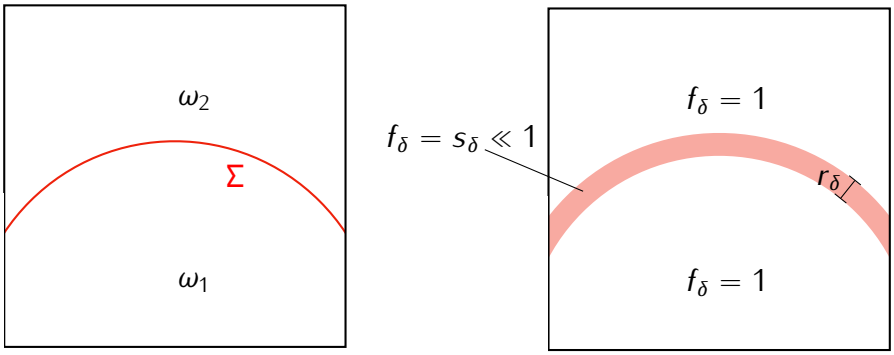

Figure 2.4: Left: Mid-surface ω with regular fold curve Σ, dividing ω into two connected components ω_1 and ω_2. Right: Representation of the function f_δ describing the material weakening near the fold.

Theorem 2.14 (Bartels, Bonito, and Hornung, cf. [BBH22]). *Let Σ fulfill Assumption 2.13, and the stored energy function $W(\cdot)$ fulfill Assumption 2.4. Then the rescaled energies $(\frac{1}{\delta^2}\mathcal{W}_\delta^\Sigma[\cdot])_{\delta>0}$, defined in (2.19), Γ-converge in the weak $W^{1,2}$-topology to the two-dimensional functional*

$$\mathcal{W}^\Sigma[\psi] := \begin{cases} \int_{\omega\setminus\Sigma} Q^2(II)\,\mathrm{d}x \quad , & \text{if } \nabla\psi^\top\nabla\psi = I_2 \text{ a.e. in } \omega\,, \\ +\infty \quad , & \text{else.} \end{cases} \tag{2.20}$$

Here, $\mathcal{W}^\Sigma[\cdot]$ is defined on $W^{2,2}(\omega\setminus\Sigma;\mathbb{R}^3)\cap W^{1,2}(\omega;\mathbb{R}^3)$, with $Q^2(\cdot)$ and II as previously defined.

The proof of Theorem 2.14 relies on the theory of geometric rigidity developed in [FJM02], applying Theorem 2.5 separately on the two domains ω_1 and ω_2, and a careful study of the continuity along the fold Σ.

Remark 2.15. *In this section, we have provided the results of rigorous two-dimensional nonlinear bending models from three-dimensional elasticity, which we discuss in this thesis. Of course, there are many more results for other models, for instance for multilayered plates [Sch07], incompressible plates [CD08], prestrained plates [LL20], and plates with voids [FKZ25].*

2.3 Isometric immersions

As we have seen, the two-dimensional nonlinear bending models presented in Section 2.2 involve the nonlinear first-order pointwise constraint

$$\nabla\psi^\top\nabla\psi = I_2\,, \text{ i.e. } \partial_i\psi\cdot\partial_j\psi = \delta_{ij} \text{ for all } i,j\in\{1,2\}$$

for a map $\psi\colon \omega\subset\mathbb{R}^2\to\mathbb{R}^3$. Such maps are called *isometric immersions* (or simply *isometries*), and they have the property to preserve length. This can be illustrated by a simple experiment: Take a sheet of paper, and draw a line on it. If you then deform the sheet, the line is deformed as well, but still has the same length (if an ant were to crawl along the line, it would take the same amount of time as in the flat case). This is because it is very hard to stretch, compress, or shear a sheet of paper in comparison to its soft response to bending deformations. Hence, for small forces, the sheet (almost) deforms isometrically.

The quantity $g = \nabla\psi^\top \nabla\psi$ is the *first fundamental form*, also called *metric*, of the curved surface $\psi(\omega) \subset \mathbb{R}^3$. It contains the information regarding lengths and angles *inside* the curved surface, i.e., the *inner* geometry of the surface, whereas the *shape operator* $S_\psi = g^{-1}II$, with the *second fundamental form* $II = -D^2\psi \cdot n[\psi]$, quantifies the *outer* geometry, i.e., the curvature of the surface. The intrinsic and extrinsic geometry of a curved surface however, is not independent of each other. Gauss's *theorema egregium* of 1827, cf. [Gau27] says that the *Gauss curvature* $K_\psi = \det(S_\psi)$, that is the product of the principal curvatures, is determined by derivatives of the first fundamental form g. In the case of an isometric immersion ($g = I_2$), this implies that the Gauss curvature is zero everywhere: $K_\psi = 0$. Hence, one of the two principal curvatures always has to be zero, which means locally the curved surface $\psi(\omega)$ is only curved in at most one direction (like a cylinder, a cone, or a flat surface). Surfaces satisfying this property are called *developable* surfaces. In 1959, Hartman and Nirenberg proved that this is indeed the case for isometric immersions that are C^2-regular.

Theorem 2.16 (Hartman-Nirenberg, [HN59]). *Let $\psi \in C^2(\omega;\mathbb{R}^3)$ be an isometric immersion, i.e. $\nabla\psi(x)^\top\nabla\psi(x) = I_2$ for all $x \in \omega$, with $\omega \subset \mathbb{R}^2$ open and bounded. Then ψ is developable, i.e. for every $x \in \omega$ it holds*

(i) There exists an open neighborhood $U \subset \omega$ of x such that ψ is affine on U,

or

(ii) There exist $a, b \in \partial\omega$ with $x \in (a,b) := \{y \in \omega : \ y = (1-t)a + tb, \ t \in (0,1)\}$, such that ψ is affine on (a,b).

This theorem implies that any C^2 isometric deformation of the unit square has a line segment of length one that is straight. In other words, you cannot smoothly (in the sense of C^2) isometrically push a square sheet of paper inside a sphere that has a diameter that is smaller than the side length of the sheet. However, if one omits the C^2-regularity and only C^1-regularity is demanded, the situation is completely different, as the following theorem, attributed to Nash and Kuiper, shows.

Theorem 2.17 (Nash-Kuiper, [Nas54, Kui55]). *Let $\psi\colon \omega \to \mathbb{R}^3$ be a short map, i.e. $Lip(\psi) \leqslant 1$. Then there exists a sequence $(\psi_k)_{k\in\mathbb{N}} \subset C^1(\omega;\mathbb{R}^3)$ of isometric immersions ($\nabla\psi_k^\top\nabla\psi_k = I_2$), with $\psi_k \to \psi$ uniformly.*

This means that for any short map $\psi\colon (0,1)^2 \to \mathbb{R}^3$ whose image lies in the ball of radius $\frac{1}{2}$, i.e $\psi((0,1)^2) \subset B_{\frac{1}{2}}(0)$, there exists an isometric immersion $\psi_\varepsilon \in C^1((0,1)^2;\mathbb{R}^3)$ with $\psi_\varepsilon((0,1)^2) \subset B_{\frac{1}{2}+\varepsilon}(0)$, for any $\varepsilon > 0$. This is in high contrast to the previous example of not being able to smoothly push a square sheet of paper into a small ball.

In Section 2.2 we saw that the two-dimensional nonlinear bending models derived from three-dimensional elasticity are formulated for deformations $\psi \in W^{2,2}(\omega;\mathbb{R}^3)$, which are isometric immersions. This regularity assumption is of course weaker than C^2-isometries. On the other hand, $W^{2,2}(\omega;\mathbb{R}^3)$ is exactly the borderline case for the embedding into $C^1(\omega;\mathbb{R}^3)$, because in two dimensions, only $W^{2,p}(\omega;\mathbb{R}^3)$, with $p > 2$, can be embedded compactly into $C^1(\omega;\mathbb{R}^3)$. In the case of isometric embeddings, the following theorems imply that $W^{2,2}$-regularity is a stronger assumption than C^1. Hence, regularity properties of $W^{2,2}$-isometric immersions are an interesting field that is extensively studied. In 2005, Müller and Pakzad proved the following result of improved regularity, if the boundary of the domain $\omega \subset \mathbb{R}^2$ is sufficiently regular.

Theorem 2.18 (Müller-Pakzad, [MP05]). *Let $\omega \subset \mathbb{R}^2$ be a bounded domain with $C^{1,\alpha}$-boundary. Let $\psi \in W^{2,2}(\omega;\mathbb{R}^3)$ be an isometric immersion, i.e. $\nabla\psi^\top\nabla\psi = I_2$ almost everywhere in ω. Then $\psi \in C^1(\overline{\omega};\mathbb{R}^3)$.*

In [MP05], they also showed that a piecewise Lipschitz boundary, or even C^1-boundary, is not enough to get the C^1-regularity of ψ up to the boundary.

For the numerical treatment of the nonlinear bending models derived in Section 2.2, finite element methods that require pointwise evaluations of the gradient are often used, for example, the discrete Kirchhoff triangle presented in Section 2.4. Hence, $C^1(\overline{\omega};\mathbb{R}^3)$-regularity of $W^{2,2}$-isometries is desirable. Unfortunately, as stated in Theorem 2.18, this is only guaranteed for domains with $C^{1,\alpha}$-boundary, which are not compatible with polygonal domains that are normally considered in the application of finite elements. A workaround is provided by the following approximation result, first proved in 2004 by Pakzad for convex domains, and extended to more general domains in 2011 by Hornung.

Theorem 2.19 (Pakzad, Hornung, [Pak04, Hor11]). *Let $\omega \subset \mathbb{R}^2$ be a bounded domain with piecewise C^1-boundary. Let $\psi \in W^{2,2}(\omega;\mathbb{R}^3)$ be an isometric immersion, i.e. $\nabla\psi^\top\nabla\psi = I_2$ almost everywhere in ω. Then there exists a sequence $(\psi_k)_{k\in\mathbb{N}} \subset W^{2,2}(\omega;\mathbb{R}^3) \cap C^\infty(\omega;\mathbb{R}^3)$ of isometries, i.e. $\nabla\psi_k^\top\nabla\psi_k = I_2$, with $\psi_k \to \psi$ strongly in $W^{2,2}(\omega;\mathbb{R}^3)$ as $k \to \infty$.*

Remark 2.20. *In this section, some properties of isometric immersions of a two-dimensional domain ω into $\mathbb{R}^3$ were presented. In* (2.11) *we have seen that in the nonlinear bending model for shells, an isometry constraint of the form $\nabla_{tan}\phi^\top\nabla_{tan}\phi = I_2$ for a map $\phi \in W^{2,2}(\mathcal{M}_A;\mathbb{R}^3)$, defined on a curved surface $\mathcal{M}_A \subset \mathbb{R}^3$, appears. Hilbert showed that C^2 isometric immersions of the unit sphere S^2 into $\mathbb{R}^3$ are rigid, that means rigid body motions are the only possible isometric immersions. For a general smooth hypersurface $\mathcal{M}_A \subset \mathbb{R}^3$ much less is known. The regularity results presented above heavily rely on the two-dimensionality of the domain $\omega \subset \mathbb{R}^2$.*

2.4 Discrete Kirchhoff triangle

As we have seen in Section 2.2, nonlinear bending models for elastic plates and shells have the advantage of being formulated on a two-dimensional, instead of a three-dimensional domain. In the finite element context, this is beneficial, since we now only have to discretize our domain in two-dimensional directions. However, this comes at a price, since the elastic energies derived via dimension-reduction now contain second derivatives. This is a challenge for designing finite element spaces: There it is desirable that the FE space is *conforming*, which means that functions in the FE space are also elements of the function space of the continuous problem. For variational problems involving only first derivatives, this is easier in most cases, since every globally continuous, piecewise polynomial finite element space is $W^{1,2}$-conforming, cf. [Cia78, Theorem 2.1.1.]. For the bending problems discussed here, where the underlying space is $W^{2,2}(\omega,\mathbb{R}^3)$, a conforming finite element space requires that the piecewise gradient is not allowed to jump along edges of the elements, i.e., that functions in this FE space are globally continuously differentiable, cf. [Cia78, Theorem 2.1.2.]. Examples of finite element spaces fulfilling this requirement are the Argyris element, the Bell element, and the Hsieh-Clough-Tocher element [Bra13]. The first two rely on 5-th order polynomials, whereas the third is a so-called *macro-element* because it relies on a division of the element into smaller

elements. Other approaches to discretize bending problems are *non-conforming* methods, i.e., FE spaces where the functions are not in $W^{2,2}$ globally. The reason for considering such kinds of discretizations is that typically, they require fewer degrees of freedom than conforming methods, while preserving the property of converging to the right $W^{2,2}$ function in the limit as the grid size approaches zero. A classical example is the *mixed method*, where the FE space is conforming to $W^{1,2} \times (W^{1,2})^2$, with the additional constraint that the gradient of the first function is equal to the second function in a certain metric, cf. [Bra13]. Another non-conforming method is the discontinuous Galerkin (DG) method. There, one considers functions which are piecewise at least quadratic polynomials, but may jump from element to element. The jump of the function and the jump of the gradient of the function on every edge are then penalized with carefully chosen parameters, depending on the grid size, leading to convergence to $W^{2,2}$ functions in the limit of vanishing grid size, cf. [BNN21].

In this work, we will focus on another non-conforming finite element approximation, the Discrete Kirchhoff Triangle (DKT), originally introduced in [BBH80], which will be introduced in the following.

For simplicity, we directly assume that ω is a polygonal domain and Γ_D is a union of edges of its boundary. Let $\mathcal{T}_H$ be a regular triangulation of ω with maximal triangle diameter $H > 0$. We denote by $\mathcal{N}_H$ the set of vertices and by $\mathcal{E}_H$ the set of edges. For $k \in \mathbb{N}$, we denote by $\mathcal{P}_k$ the set of polynomials of degree at most k. For vertices $z_1, z_2, z_3 \in \mathcal{N}_H$ of a triangle $\mathbf{t}$ we define $z_\mathbf{t} = (z_1 + z_2 + z_3)/3$ as the center of mass of $\mathbf{t}$ and introduce the reduced space of cubic polynomials

$$\mathcal{P}_{3,\mathrm{red}}(\mathbf{t}) := \left\{ p \in \mathcal{P}_3(\mathbf{t}) \;\middle|\; 6p(z_\mathbf{t}) = \sum_{i=1,2,3} (2p(z_i) - \nabla p(z_i) \cdot (z_i - z_\mathbf{t})) \right\} .$$

This space of polynomials has dimension 9, by excluding the bubble function $p_{\mathrm{bubble}}(z) = \lambda_1\lambda_2\lambda_3$ from the 10-dimensional space $\mathcal{P}_3$. Here, $\lambda_1, \lambda_2, \lambda_3$ are the barycentric coordinates of $\mathbf{t}$, i.e. $p_{\mathrm{bubble}}(x, y) = xy(1 - x - y)$ in the reference triangle, cf. [Bra13]. Hence, if a polynomial $p \in \mathcal{P}_{3,\mathrm{red}}(\mathbf{t})$ is zero on the entire boundary of $\mathbf{t}$, it must be $p \equiv 0$. The space $\mathcal{P}_{3,\mathrm{red}}(\mathbf{t})$ still has $\mathcal{P}_2(\mathbf{t})$ as a subspace. We define the finite element spaces

$$\begin{aligned} \mathbf{W}_H &:= \{ w_H \in C(\bar{\omega}) \mid w_H|_\mathbf{t} \in \mathcal{P}_{3,\mathrm{red}}(\mathbf{t}) \text{ for all } \mathbf{t} \in \mathcal{T}_H \text{ and } \nabla w_H \text{ is continuous at } \mathcal{N}_H \} , \\ \mathbf{\Theta}_H &:= \left\{ \theta_H \in C(\bar{\omega}; \mathbb{R}^2) \mid \theta_H|_\mathbf{t} \in \mathcal{P}_2(\mathbf{t})^2 \text{ and } \theta_H \cdot n_E|_E \text{ is affine for all } E \in \mathcal{E}_h \right\} . \end{aligned}$$

In Figure 2.5, the interpolation for these finite element spaces is displayed, showing where the degrees of freedom are defined.

For a function $w \in W^{3,2}(\omega)$, the interpolation $w_H = \mathcal{I}^{\mathrm{DKT}} w \in \mathbf{W}_H$ is defined on every triangle $\mathbf{t} \in \mathcal{T}_H$ by $w_H(z) = w(z)$ and $\nabla w_H(z) = \nabla w(z)$ for all vertices $z \in \mathcal{N}_H \cap \mathbf{t}$, which is well-defined due to the continuous embedding of $W^{3,2}(\omega)$ into $C^1(\bar{\omega})$. The discrete gradient operator $\theta_H \colon \mathbf{W}_H \to \mathbf{\Theta}_H$ is defined via

$$\theta_H[w_H](z) = \nabla w_H(z) , \quad \theta_H[w_H](z_E) \cdot \tau_E = \nabla w_H(z_E) \cdot \tau_E$$

for all vertices $z \in \mathcal{N}_H$, all edges $E \in \mathcal{E}_H$ with τ_E denoting a unit tangent vector on E, and z_E the midpoint of E. We use superscripts $(\theta_H^j[w_H])_{j=1,2}$ to indicate the components of $\theta_H[w_H]$. The operator θ_H can analogously be defined on $W^{3,2}(\omega)$. This operator has the following properties, cf. [Bar13, Bra13]:

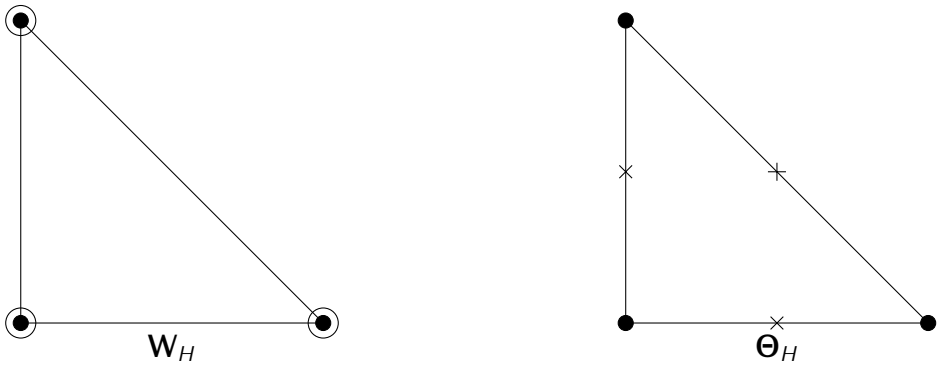

Figure 2.5: The DKT element introduced in [BBH80]. At the black dots • the function value is prescribed, at the circles ○, the gradient is prescribed, and at the crosses ×, the tangential component of the function is prescribed.

There exists constants c_0, c_1, c_2, $c_3 > 0$ such that for $\mathbf{t} \in \mathcal{T}_H$ with $H = \operatorname{diam}(\mathbf{t})$, $w \in W^{3,2}(\mathbf{t})$ and $w_H \in \mathbf{W}_H$

$$\|w - \mathcal{I}^{\mathrm{DKT}} w\|_{W^{m,2}(\mathbf{t})} \leqslant c_0 H^{3-m} \|w\|_{W^{3,2}(\mathbf{t})} \quad \text{for } m = 0, 1, 2, 3\,, \tag{2.21}$$

$$c_1^{-1} \left\|D^{k+1} w_H\right\|_{L^2(\mathbf{t})} \leqslant \left\|D^k \theta_H[w_H]\right\|_{L^2(\mathbf{t})} \leqslant c_1 \left\|D^{k+1} w_H\right\|_{L^2(\mathbf{t})} \quad \text{for } k = 0, 1\,, \tag{2.22}$$

$$\left\|\theta_H[w_H] - \nabla w_H\right\|_{L^2(\mathbf{t})} \leqslant c_2 H \left\|D^2 w_H\right\|_{L^2(\mathbf{t})}\,, \tag{2.23}$$

$$\left\|\theta_H[w] - \nabla w\right\|_{L^2(\mathbf{t})} + H \left\|\nabla \theta_H[w] - D^2 w\right\|_{L^2(\mathbf{t})} \leqslant c_3 H^2 \, |w|_{W^{3,2}(\mathbf{t})}\,. \tag{2.24}$$

Furthermore, as shown in [Bra13], the mapping $w_H \mapsto \left\|\nabla \theta_H[w_H]\right\|_{L^2(\omega)}$ defines a norm on

$$\{w_H \in \mathbf{W}_H \mid \ w_H(z) = 0,\ \nabla w_H(z) = 0 \text{ for all } z \in \mathcal{N}_H \cap \Gamma_D\}\,.$$

As the reader might have guessed, the idea of this non-conforming finite element discretization is to take $\nabla \theta_H[\cdot]$ as an approximation of the Hessian. With this, one can formulate a discrete version of the nonlinear bending energies introduced in Section 2.1. For the case of the nonlinear homogeneous plate model, Bartels [Bar13] was able to show Γ-convergence of a discrete bending energy based on this DKT element. In this work, the ideas of this result are extended to shells in Chapter 3, and to a nonlinear homogenized plate model in Chapter 4. In Chapter 5 the DKT element is also used to approximate nonlinear bending deformations with folds. There, only numerical experiments are displayed, without a convergence analysis of the numerical approximation.

2.5 Willmore flow

This section is dedicated to the Willmore energy of a $(d-1)$-dimensional hypersurface $\mathcal{M} \subset \mathbb{R}^d$, with $d = 2$ or $d = 3$, and its L^2-gradient flow, the Willmore flow. The Willmore energy is a quantity similar to the bending energy of a curved shell, and the Willmore flow is a time-dependent evolution of a surface that decreases the Willmore energy.

Willmore energy. The Willmore energy is, up to a prefactor, defined as the integral of the squared mean curvature over the surface, i.e.

$$\frac{1}{2} \int_{\mathcal{M}} \mathbf{h}^2 \, \mathrm{d}\mathcal{H}^{d-1}\,.$$

We define the mean curvature $\mathbf{h}(y)$ as the sum of the principal curvatures at $y \in \mathcal{M}$. Another choice is defining it as the mean of the principal curvatures. If $\mathcal{M}$ is the image of a chart $\psi\colon \omega \subset \mathbb{R}^2 \to \mathbb{R}^3$, i.e., $\mathcal{M} = \psi(\omega)$, the mean curvature is the trace of the shape operator:

$$\mathbf{h}(\psi(x)) = \operatorname{tr}\,(S_\psi(x)) = \operatorname{tr}\,\left(g^{-1}(x)I\!I(x)\right)\,, \quad x \in \omega\,.$$

If the isometry constraint is omitted, the Willmore energy looks very similar to (2.9), since

$$\frac{1}{2}\int_{\mathcal{M}} \mathbf{h}^2\,\mathrm{d}\mathcal{H}^{d-1} = \frac{1}{2}\int_\omega \sqrt{\det g}\,Q^2(g^{-1}I\!I)\,\mathrm{d}x\,,$$

with $Q^2(A) = (\operatorname{tr}(A))^2$ for $A \in \mathbb{R}^{2\times 2}$. Hence, it can also be interpreted as the stored bending energy of a thin shell, whose mid-surface is represented by $\mathcal{M}$. In fact, if $\mathcal{M}$ is the image of an isometric immersion, i.e. $g = I_2$, then

$$\mathbf{h}(\psi)^2 = |I\!I|^2 = |D^2\psi|^2 = |\Delta\psi|^2\,,$$

cf. [Bar15, proposition 8.2], so the Willmore energy *is*, up to a possible factor, the stored bending energy. In the following, we will focus on closed two-dimensional hypersurfaces $\mathcal{M}$, which are in general not given by a single chart ψ. Hence, all quantities in this section, and in Chapter 6 are formulated directly on $\mathcal{M}$, and not on a chart domain ω. For hyperspheres, the Willmore energy is easy to compute: In two dimensions, for a circle S^1_r with radius $r > 0$, the mean curvature is just the curvature of the circle, i.e. $\mathbf{h} \equiv \frac{1}{r}$. Hence, it holds

$$\frac{1}{2}\int_{S^1_r} \mathbf{h}^2\,\mathrm{d}\mathcal{H}^1 = \frac{1}{2r^2}\mathcal{H}^1(S^1_r) = \frac{1}{2r^2}2\pi r = \frac{\pi}{r}\,, \qquad S^1_r := \{x \in \mathbb{R}^2 \,:\, |x| = r\}\,. \tag{2.25}$$

This implies that the larger the radius of the circle, the smaller the Willmore energy is. For a sphere S^2_r with radius $r > 0$ embedded in three dimensions, the mean curvature is $\mathbf{h} \equiv \frac{2}{r}$, since both principal curvatures are $\frac{1}{r}$. This implies

$$\frac{1}{2}\int_{S^2_r} \mathbf{h}^2\,\mathrm{d}\mathcal{H}^2 = \frac{2}{r^2}\mathcal{H}^2(S^2_r) = \frac{2}{r^2}4\pi r^2 = 8\pi\,, \qquad S^2_r := \{x \in \mathbb{R}^3 \,:\, |x| = r\}\,. \tag{2.26}$$

Hence, the Willmore energy of a two-dimensional sphere is *scale-invariant*, it does not depend on the radius of the sphere.

Gradient flows in Hilbert spaces. In the following, we introduce the notion of gradient flows in Hilbert spaces. For an extensive overview, the reader is referred to [San17]. Let us start with gradient flows in the Euclidean space $\mathbb{R}^d$. Let $F\colon \mathbb{R}^d \to \mathbb{R}$ be a differentiable function. The gradient flow of F starting at $x_0 \in \mathbb{R}^d$ is the system of ordinary differential equations

$$\begin{cases} \dot{x}(t) &= -\nabla F(x(t)) \\ x(0) &= x_0\,. \end{cases} \tag{2.27}$$

The gradient ∇F points in the direction of the *steepest ascent*. Hence (2.27) can be interpreted in the following way: $x(t)$ is the position at time t when one is starting at x_0 and walking through a landscape that is the graph of the function F, by always going in the direction

of the *steepest descent*. This implies that $F(x(t))$ can only decrease in time, by the simple calculation

$$\frac{\mathrm{d}}{\mathrm{d}t}\left(F(x(t))\right) = \nabla F(x(t)) \cdot \dot{x}(t) = -|\nabla F(x(t))|^2 \leqslant 0\,.$$

An implicit time discretization of (2.27) with time step size τ reads

$$\frac{x_{k+1} - x_k}{\tau} = -\nabla F(x_{k+1})\,, \tag{2.28}$$

with time steps $(x_k)_{k\in\mathbb{N}}$. A more general formulation of (2.28) that requires less regularity of the function F is the *minimizing movement scheme*, cf. [DG93],

$$x_{k+1} = \operatorname*{arg\,min}_{x\in\mathbb{R}^d} \left(|x - x_k|^2 + 2\tau F(x)\right)\,. \tag{2.29}$$

Indeed, if F is differentiable, by differentiating the expression to be minimized on the right-hand side of (2.29) and plugging in the minimizer x_{k+1}, one gets

$$2(x_{k+1} - x_k) + 2\tau\nabla F(x_{k+1}) = 0 \quad \Leftrightarrow \quad \frac{x_{k+1} - x_k}{\tau} = -\nabla F(x_{k+1})\,.$$

If F is defined on a Hilbert space $(X, (\cdot,\cdot)_X)$, we define the gradient flow of F in $(X, (\cdot,\cdot)_X)$ as

$$\begin{cases} (\dot{x}(t), \hat{x})_X &= -\frac{\mathrm{d}}{\mathrm{d}s}\left(F(x(t) + s\hat{x})\right)\big|_{s=0} \qquad \text{for all } \hat{x} \in X\,, \\ x(0) &= x_0\,. \end{cases}$$

Similar to (2.29), a time discretization of the gradient flow of F in $(X, (\cdot,\cdot)_X)$ can be derived as

$$x_{k+1} = \operatorname*{arg\,min}_{x\in X} \left(\|x - x_k\|_X^2 + 2\tau F(x)\right)\,. \tag{2.30}$$

Mean curvature flow. This paragraph mainly follows [BDGP23]. For a smooth, compact, orientable hypersurface $\mathcal{M} \subset \mathbb{R}^d$ without boundary we define the area functional

$$F[\mathcal{M}] := \mathcal{H}^{d-1}(\mathcal{M}) = \int_{\mathcal{M}} 1 \,\mathrm{d}\mathcal{H}^{d-1}\,.$$

Let $\zeta\colon \mathbb{R}^d \to \mathbb{R}^d$ be a smooth vector field. For a small parameter $s > 0$ we define a perturbation of $\mathcal{M}$ as

$$\mathcal{M}(s) := \{x + s\zeta(x) \,:\, x \in \mathcal{M}\}\,.$$

Then, the first variation of the area functional, using a transport theorem, cf. [BDGP23], gives

$$\frac{d}{ds} F(\mathcal{M}(s))\big|_{s=0} = -\int_{\mathcal{M}} \mathbf{h}\nu \cdot \zeta \,\mathrm{d}\mathcal{H}^{d-1}\,,$$

with ν being the outer unit normal to $\mathcal{M}$. Since ζ was an arbitrary test vector field, this implies that formally, the L^2-gradient $\nabla_{\mathcal{M}}^{(\cdot,\cdot)_{L^2}} F[\cdot]$ of the area functional in the space of all closed, orientable hypersurfaces is the negative mean curvature vector $\mathbf{h}\nu$:

$$\nabla_{\mathcal{M}}^{(\cdot,\cdot)_{L^2}} F[\mathcal{M}] = -\mathbf{h}\nu\,.$$

The L^2-gradient flow of the area functional is therefore called *mean curvature flow*. In the parametric setting, with parametrization $x\colon \mathcal{M} \to \mathbb{R}^d$ it reads

$$\partial_t x = \mathbf{h}\nu\,.$$

For a given hypersurface $\mathcal{M}_k \subset \mathbb{R}^d$ let $x_k\colon \mathcal{M}_k \to \mathbb{R}^d$ denote the identity map. Following the previous paragraph, the minimizing movement time discretization of mean curvature flow hence reads

$$x_{k+1} = \operatorname*{arg\,min}_{x\colon \mathcal{M}_k \to \mathbb{R}^d} \left(\left\| x - x_k \right\|^2_{L^2(\mathcal{M}_k;\mathbb{R}^d)} + 2\tau \mathcal{H}^{d-1}(x(\mathcal{M}_k)) \right)\,.$$

Willmore flow. We now come to the *Willmore flow*, the L^2-gradient flow of the Willmore energy $w[x(t)] = \int_{\mathcal{M}(t)} \mathbf{h}^2 \,\mathrm{d}\mathcal{H}^{d-1}$, with time parameter t. In the parametric setting, with parametrization $x\colon \mathcal{M} \to \mathbb{R}^d$ it has the form

$$\partial_t x = \Delta_{\mathcal{M}} \mathbf{h}\nu + \mathbf{h}\left(|S|^2 - \frac{1}{2}\mathbf{h}^2 \right)\nu\,.$$

For a detailed calculation, see [Sim01, OR09]. The time-discrete minimizing movement scheme for Willmore flow hence, is

$$x_{k+1} = \operatorname*{arg\,min}_{x\colon \mathcal{M}_k \to \mathbb{R}^d} \left(\left\| x - x_k \right\|^2_{L^2(\mathcal{M}_k;\mathbb{R}^d)} + 2\tau w[x] \right)\,.$$

In Chapter 6 we will see how this minimizing movement scheme can be approximated by a nested scheme that involves solving one step of mean curvature flow as an inner problem, to approximate the mean curvature $\mathbf{h}$, and a classic outer minimization problem. This is then handled not in the parametric setting, but in the phase field setting, where the surface $\mathcal{M}$ is implicitly given by the diffuse phase transition of a two-phase function. These phase field functions are introduced in the next section.

2.6 Phase fields

In the previous section, the (hyper-) surfaces were described in the *parametric* setting. In this section, the notion of *phase fields* is introduced. A phase field is a scalar-valued function that describes a geometric object, like a curve, a surface, or the boundary of a set, in an implicit, *diffuse* way. Before we come to the most important functionals describing phase fields, the Modica-Mortola and the Ambrosio-Tortorelli functional, we first introduce the notion of functions of *bounded variation* (in short: BV functions). Here, we follow the book by Rindler [Rin18].

Functions of bounded variation. Here, we provide a brief overview of the space of functions of bounded variation. For an extensive study, the reader is referred to [AFP00]. Let $\Omega \subset \mathbb{R}^d$ be a bounded Lipschitz domain. We denote by $\mathrm{BV}(\Omega)$ the space of all functions $u \in L^1(\Omega)$ such that there exists a vector-valued Radon measure Du with

$$\int_\Omega u \operatorname{div}(\phi)\,\mathrm{d}x = -\int_\Omega \phi \cdot \,\mathrm{d}Du\,, \qquad \text{for all } \phi \in C_c^1(\Omega;\mathbb{R}^d)\,.$$

Note that this definition clearly implies that $W^{1,1}(\Omega)$ functions are also in $\mathrm{BV}(\Omega)$, with $\mathrm{d}Du = \nabla u(x)\,\mathrm{d}x$. For an $\mathbb{R}^d$-valued Radon measure μ, we call

$$|\mu|(\Omega) := \sup\left\{ \int_\Omega \phi \cdot \,\mathrm{d}\mu \;:\; \phi \in C_c^1(\Omega;\mathbb{R}^d)\,,\ \|\phi\|_\infty \leqslant 1 \right\}$$

the *total variation* of μ in Ω. For a set $E \subset \Omega$ with smooth boundary, the characteristic function $\chi_E \colon \Omega \to \{0,1\}$ is in $\mathrm{BV}(\Omega)$, and

$$|D\chi_E|(\Omega) = \mathrm{Per}(E;\Omega) := \mathcal{H}^{d-1}(\partial E \cap \Omega)$$

is the perimeter of E in Ω. This notion allows us to talk about geometric properties of closed, orientable hypersurfaces (boundaries of sufficiently regular sets) in the language of functions of bounded variation. Actually, the BV-theory allows to also deal with less regular objects, opening up the field for *geometric measure theory*. Unfortunately, analytically and computationally, it is much harder to deal with Radon measures in comparison to (weak) derivatives. In the next paragraph, we will hence introduce phase fields as a diffuse approximation of the perimeter of a set.

Modica-Mortola phase fields. We now come to the Modica-Mortola energy, also known as Cahn-Hilliard or Ginzburg-Landau functional. It reads

$$\mathcal{P}^\varepsilon[v] := \frac{1}{2}\int_\Omega \varepsilon|\nabla v|^2 + \frac{1}{\varepsilon}\Psi(v)\,\mathrm{d}x\,, \tag{2.31}$$

and is defined for functions $v \in W^{1,2}(\Omega)$. Here, $\varepsilon > 0$ is small. The function $\Psi : \mathbb{R} \to \mathbb{R}$ satisfies $\Psi(z) \geqslant 0$ for all $z \in \mathbb{R}$ and $\Psi(z) = 0$ if and only if $z \in \{a,b\}$, with $a < b$. Hence $\Psi(\cdot)$ is called a *double-well potential* with wells $a, b \in \mathbb{R}$. If the parameter ε is small, and this functional is to be minimized, together with a possible mass constraint for u, or other continuous pertubations, the term $\frac{1}{\varepsilon}\Psi(v)$ enforces the function v to stay close to the two *phases* $v = a$ or $v = b$, while $\varepsilon|\nabla v|^2$ ensures regularity in the *transition* between the two phases. The parameter ε hence controls the width of this transition zone. In 1977, Modica and Mortola were able to show the following *sharp interface limit* of (2.31) as $\varepsilon \to 0$.

Theorem 2.21 (Modica-Mortola, [MM77]). *The functionals $(\mathcal{P}^\varepsilon[\cdot])_{\varepsilon>0}$, defined in* (2.31)*, Γ-converge as $\varepsilon \to 0$ in the strong L^1-topology to the functional*

$$\mathcal{P}^0[v] := \begin{cases} c_0 \mathrm{Per}(\{x \in \Omega \;:\; v(x) = a\},\Omega) & , \quad \text{if } v \in BV(\Omega;\{a,b\}) \\ +\infty & , \quad \text{else,} \end{cases}$$

with $c_0 = \int_a^b \sqrt{\Psi(z)}\,\mathrm{d}z$.

If $\varepsilon > 0$ is small, (2.31) hence gives a diffuse approximation of the perimeter functional of a set E, or more specifically, of the area of the boundary between the two sets $E \cap \Omega$ and $E^c \cap \Omega$.

The construction of the recovery sequence in the proof of the lim sup-inequality of Theorem 2.21 gives us an idea of how minimizers of (2.31) look like. By Young's inequality, the following inequality holds

$$\frac{1}{2}\int_\Omega \varepsilon|\nabla v|^2 + \frac{1}{\varepsilon}\Psi(v)\,\mathrm{d}x \geqslant \int_\Omega |\nabla v|\sqrt{\Psi(v)}\,\mathrm{d}x\,,$$

with equality if and only if $|\nabla v| = \sqrt{\Psi(v)}$ almost everywhere. In one dimension, this leads to the ordinary differential equation

$$\hat{v}'(s) = \sqrt{\Psi(\hat{v}(s))}\,. \tag{2.32}$$

Using a *slicing* argument, cf. [MM77], the one-dimensional *optimal* profile determined by (2.32) is then used to construct the recovery sequence for the lim sup-inequality of Theorem 2.21, by defining

$$v_\varepsilon(x) := \hat{v}(-\frac{\operatorname{sdist}(x, E)}{\varepsilon})$$

for a given set E. Here,

$$\operatorname{sdist}(x, E) := \operatorname{dist}(x, E) - \operatorname{dist}(x, E^c)$$

is the signed distance function of $E \subset \Omega$.

Example 2.22. *Here, we will give two examples of possible choices for the double-well potential* $\Psi(\cdot)$.

1. *Let* $\Psi(z) = \frac{9}{16}(1-z^2)^2$. *Hence, the two wells are* $a = -1$ *and* $b = 1$. *The choice of the factor* $\frac{9}{16}$ *comes from the computation*

$$c_0 = \int_{-1}^{1} \sqrt{\Psi(z)}\,\mathrm{d}z = \frac{3}{4}\int_{-1}^{1}(1-z^2)\,\mathrm{d}z = \frac{3}{4}\left(2 - \frac{2}{3}\right) = 1\,.$$

The optimal profile determined by the ordinary differential equation (2.32)*, together with the initial condition*

$$\hat{v}(\frac{a+b}{2}) = \hat{v}(0) = 0$$

then is

$$\hat{v}(s) = \tanh(\frac{3s}{4})\,.$$

Sketches of this double-well potential and the corresponding optimal profile are displayed in Figure 2.6 on the left. Note that this construction can easily be adapted for double-well potentials of the form $\Psi(z) = c(a-z)^2(b-z)^2$ *with other wells* $a < b$, *and constant* $c > 0$.

2. *Now consider a double-well potential of the form*

$$\Psi(z) = \begin{cases} 1 - z^2 & , \quad \text{if } |z| \leqslant 1 \\ +\infty & , \quad \text{else.} \end{cases}$$

This enforces the phase field to always stay between -1 *and* 1*, which are also the two wells of the function. Then we have*

$$c_0 = \int_{-1}^{1} \sqrt{\Psi(z)}\, \mathrm{d}z = \int_{-1}^{1} \sqrt{1 - z^2}\, \mathrm{d}z = \frac{\pi}{2}\,.$$

The optimal profile given by $\hat{v}' = \sqrt{1 - \hat{v}^2}$ *with initial condition* $\hat{v}(0) = 0$ *is hence given as*

$$\hat{v}(s) = \begin{cases} \sin(s) & , \quad \text{if } |s| \leqslant \frac{\pi}{2} \\ -1 & , \quad \text{if } s < -\frac{\pi}{2} \\ 1 & , \quad \text{if } s > \frac{\pi}{2}\,. \end{cases}$$

Sketches of this double-well potential and the corresponding optimal profile are displayed in Figure 2.6 on the right.

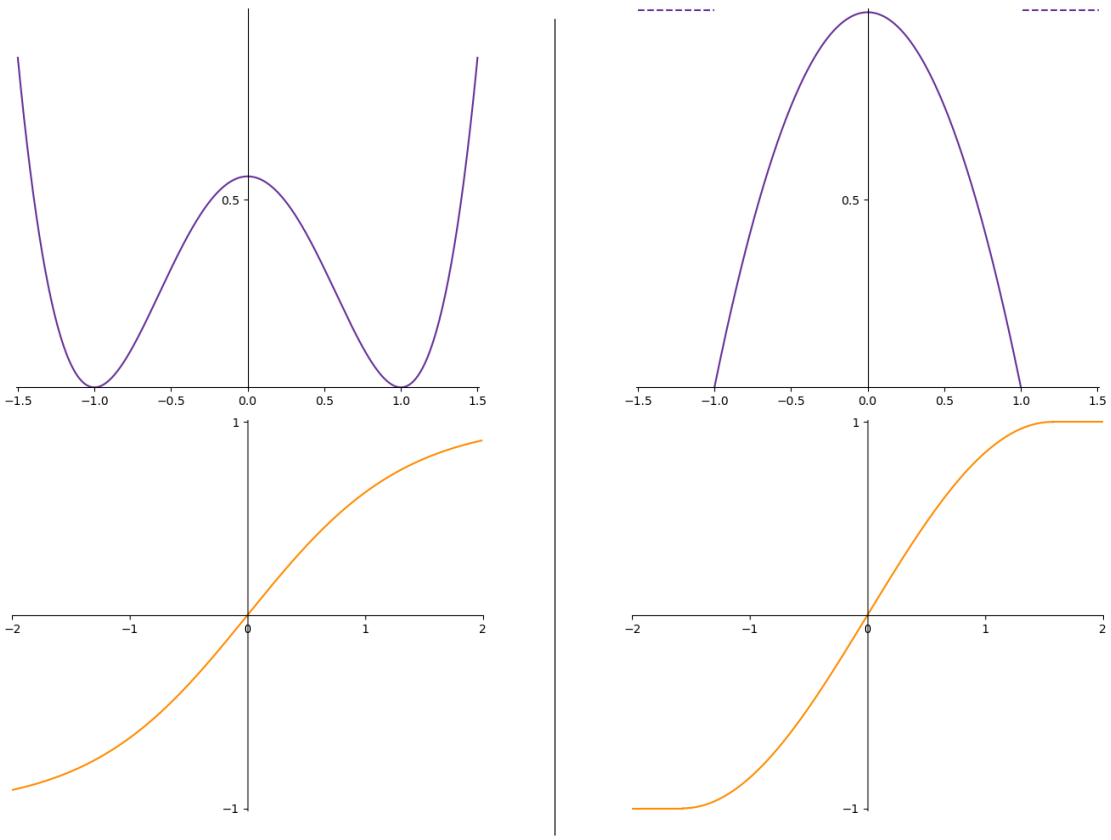

Figure 2.6: Left: Sketches of the double-well potential $\Psi(z) = \frac{9}{16}(1 - z^2)^2$ (purple, top), and the optimal profile $\hat{v}(s) = \tanh(\frac{3s}{4})$ (orange, bottom). Right: Sketches of the double-well potential : $\Psi(z) = 1 - z^2$, if $|z| \leqslant 1$; $\Psi(z) = +\infty$, else (purple, top), and the optimal profile $\hat{v}(s) = \sin(s)$, if $|s| \leqslant \frac{\pi}{2}$; $\hat{v}(s) = -1$, if $s < -\frac{\pi}{2}$; $\hat{v}(s) = 1$, if $s > \frac{\pi}{2}$ (orange, bottom).

Summarizing this paragraph, we saw how the perimeter of a set E can be approximated by a diffuse phase field function in the variational sense of Γ-convergence. This phase field formulation is suitable to compute an approximation of the mean curvature flow of the hypersurface that is given by the boundary of this set. This will be leveraged to compute the Willmore flow, as we will explore in Chapter 6. However, if one is interested in approximating non-orientable surfaces, or for example a network of curves in two dimensions that have crossings, another phase field formulation is needed. This is what the following paragraph is about.

Ambrosio-Tortorelli phase fields. In the previous paragraph, phase field functions with two phases were explored. Now we consider phase field functions that only have one phase $v = 1$, and are only allowed to drop down to zero in a diffuse region around a set of zero Lebesgue measure. We consider the following *Ambrosio-Tortorelli energy*

$$\mathcal{AT}^\varepsilon[v] := \int_\Omega \varepsilon|\nabla v|^2 + \frac{(1-v)^2}{4\varepsilon}\,\mathrm{d}x\,.$$

As in (2.31), $\varepsilon|\nabla v|^2$ ensures regularity, while $\frac{(1-v)^2}{4\varepsilon}$ is a penalty term that pushes the phase field in the single well $v = 1$. This functional was introduced in [AT92] in order to formulate a phase field approximation of the Mumford-Shah functional [MS89]

$$\mathcal{F}^0[\phi, \Sigma] := \int_{\Omega\setminus\Sigma} \alpha|\nabla\phi|^2 + \beta(\phi - g)^2\,\mathrm{d}x + \mathcal{H}^{d-1}(\Sigma)\,, \tag{2.33}$$

a variational approach to image segmentation. Here, $\Sigma \subset \Omega$ is a closed subset, $\phi \in C^1(\Omega\setminus\Sigma)$, and $\alpha, \beta \geqslant 0$. In $d = 2$ $g \in L^\infty(\Omega)$ has the role of a pixel-valued image that is to be approximated by a piecewise smooth function ϕ with jump set Σ. The complete phase field functional approximating (2.33) reads as

$$\mathcal{F}^\varepsilon[\phi, v] := \int_\Omega \alpha(v^2 + \eta_\varepsilon)|\nabla\phi|^2 + \beta(\phi - g)^2\,\mathrm{d}x + \mathcal{AT}^\varepsilon[v]\,. \tag{2.34}$$

Here, $(\eta_\varepsilon)_{\varepsilon>}$ is an infinitesimal sequence with $\frac{\eta_\varepsilon}{\varepsilon} \to 0$ as $\varepsilon \to 0$. The idea is that the phase field v is approximately equal to 1, but drops down to zero around the area where the gradient of ϕ explodes. In the sharp interface limit as $\varepsilon \to 0$ this area shrinks down to the lower-dimensional jump part of ϕ. The variational phase field approximation (2.34) of (2.33) was proven in 1992 by Ambrosio and Tortorelli:

Theorem 2.23 (Ambrosio-Tortorelli, [AT92])**.** *As $\varepsilon \to 0$, the functionals $(\mathcal{F}^\varepsilon[\cdot])_{\varepsilon>0}$, defined in* (2.34)*, Γ-converge in the strong $L^2(\Omega)$ topology to the Mumford-Shah functional* (2.33)*.*

In Chapter 5, a phase field model similar to (2.34) is proposed to approximate folds in a thin plate. There, the gradient of the deformation jumps along the folds in the sharp interface limit.

Chapter 3

Finite Element Approximation of Large-Scale Isometric Deformations of Parametrized Surfaces

In this chapter, the numerical approximation of isometric deformations of thin elastic shells is discussed. To this end, for a thin shell represented by a parametrized surface, it is shown how to transform the stored elastic energy for an isometric deformation such that the highest order term is quadratic. For this reformulated model, the existence of optimal isometric deformations is shown. A finite element approximation is obtained using the Discrete Kirchhoff Triangle (DKT) approach and the convergence of discrete minimizers to a continuous minimizer is demonstrated. In that respect, the work in this chapter generalizes the results by Bartels for the approximation of bending isometries of plates. A Newton scheme is derived to numerically simulate large bending isometries of shells. The proven convergence properties are experimentally verified and characteristics of isometric deformations are discussed.

Collaboration. This chapter is a continuation and extension of the work from the author's Master's thesis [Smo21]. As such, it is the result of joint work with Stefan Simon and Martin Rumpf that has been published in [RSS22]. In particular, Stefan Simon implemented the finite element library that is used for the numerical experiments in this chapter.

We investigate deformations of thin elastic objects and their numerical approximation. These objects are frequently characterized by a small thickness $\delta > 0$ and a regular and orientable two-dimensional midsurface $\mathcal{M}_A$. Given an external force $f_A \colon \mathcal{M}_A \to \mathbb{R}^3$ acting on the thin object, equilibrium deformations have been extensively studied in the literature. In particular, considering the limit of vanishing thickness, Γ-convergence allows to express the 3D deformation of the thin object by a 2D deformation of its midsurface.

Throughout this chapter, we will restrict ourselves to parametrized surfaces, i.e. $\mathcal{M}_A = \psi_A(\omega)$ for a bounded and connected Lipschitz domain $\omega \subset \mathbb{R}^2$ and an injective parametrization $\psi_A \in W^{3,2}(\omega;\mathbb{R}^3)$. An external force $f_A \in L^2(\mathcal{M}_A;\mathbb{R}^3)$ acting on the midsurface is given via some $f \in L^2(\omega;\mathbb{R}^3)$ on the parameter domain with $f = f_A \circ \psi_A$. The deformed midsurface $\mathcal{M}_B = \psi_B(\omega)$ is described by a parametrization $\psi_B \in W^{2,2}(\omega;\mathbb{R}^3)$. The resulting actual deformation $\phi \colon \psi_A(\omega) \to \mathbb{R}^3$ of the thin shell midsurface $\psi_A(\omega)$ is then given by $\phi = \psi_B \circ \psi_A^{-1}$, cf. Figure 2.2 and Section 2.2.

Following Friesecke et al. [FJMM03], the bending energy $\mathcal{W}^A \colon W^{2,2}(\omega;\mathbb{R}^3) \to [0,\infty]$ of

the deformed object is given by

$$\mathcal{W}^A[\psi_B] := \begin{cases} \frac{\alpha}{2} \int_\omega \sqrt{\det g_A}\ \mathrm{tr}\ \left(S^{\mathrm{rel}}_{\psi_B} S^{\mathrm{rel}}_{\psi_B} \right) \mathrm{d}x & \text{if } g_B = g_A\,, \\ \infty & \text{otherwise}\,, \end{cases}$$

see (2.12). Note that for the relative shape operator (2.13) it holds

$$\mathrm{tr}\ \left(S^{\mathrm{rel}}_{\psi_B} S^{\mathrm{rel}}_{\psi_B} \right) = \left| g_A^{-\frac{1}{2}} (II_B - II_A) g_A^{-\frac{1}{2}} \right|^2 ,$$

as it was derived for a prestrained plate model in [BLS16]. A bending energy on prestrained plates involving the same integrand was also applied in [BGNY23]. Here, $\alpha > 0$ denotes an elastic constant and the condition $g_B = g_A$ encodes the metric constraint on the map $\phi = \psi_B \circ \psi_A^{-1}$, i.e.

$$\nabla \psi_B(x)^\top \nabla \psi_B(x) = g_B(x) = g_A(x) = \nabla \psi_A(x)^\top \nabla \psi_A(x) \quad \text{for a.e. } x \in \omega\,. \tag{3.1}$$

Moreover, we define the potential energy by

$$E_{\mathrm{pot}}[\psi_B] := -\int_\omega \sqrt{\det g_A}\ f \cdot \psi_B \,\mathrm{d}x$$

and consider clamped boundary conditions on $\Gamma_D \subset \partial\omega$ with $\mathcal{H}^1(\Gamma_D) > 0$, i.e.

$$\psi_B = \psi_A\,, \quad \nabla \psi_B = \nabla \psi_A \quad \text{ on } \Gamma_D. \tag{3.2}$$

Finally, we ask for a minimizer ψ_B of the total free energy

$$E[\psi] := \mathcal{W}^A[\psi] + E_{\mathrm{pot}}[\psi] = \frac{\alpha}{2} \int_\omega \sqrt{\det g_A}\, \mathrm{tr}\ \left(S^{\mathrm{rel}}_{\psi} S^{\mathrm{rel}}_{\psi} \right) \mathrm{d}x - \int_\omega \sqrt{\det g_A}\ f \cdot \psi \,\mathrm{d}x \tag{3.3}$$

over all $\psi \in W^{2,2}(\omega; \mathbb{R}^3)$ satisfying the metric constraint (3.1) and the clamped boundary conditions (3.2). In a more general setting, other Dirichlet boundary conditions could be considered, such as $\psi_B = \varphi$, $\nabla \psi_B = \Phi$ on Γ_D. In general, it is not clear if such a deformation ψ_B satisfying the metric constraint (3.1) exists, even if $\Phi^\top \Phi = \nabla \psi_A^\top \nabla \psi_A$ on Γ_D is satisfied. However, with the assumption that admissible deformations exist, the analysis presented in this chapter could be extended to more general Dirichlet boundary conditions, as in [Bar13].

In this work, we are primarily interested in a numerical approximation scheme for the above variational problem.

Our goal is to extend the approximation result of Bartels [Bar13] to the case of curved surfaces $\mathcal{M}_A$ under the assumption that $\mathcal{M}_A$ is a parametrized surface as described above. For isometric deformations in the flat case, the relative shape operator is symmetric and the Frobenius norm of the relative shape operator is equal to the Frobenius norm of the second derivative of the deformation, i.e.

$$\mathrm{tr}\ \left(S^{\mathrm{rel}}_{\psi_B} S^{\mathrm{rel}}_{\psi_B} \right) = \mathrm{tr}\ \left((S^{\mathrm{rel}}_{\psi_B})^\top S^{\mathrm{rel}}_{\psi_B} \right) = |S^{\mathrm{rel}}_{\psi_B}|^2 = |D^2 \psi_B|^2\,, \tag{3.4}$$

which drastically simplifies the computational effort, since the second variation of the corresponding bending energy becomes independent of ψ_B. In that respect, the central insight is a simplification of the relative shape operator similar to (3.4).

Related work. In [LDR95, LDR96], Le Dret and Raoult obtained a membrane theory describing tangential distortion on the surface. In this chapter, we focus on a bending theory taking into account isometric deformations. For such bending isometries, a first Γ-convergence result was provided by Friesecke et al. in [FJM02] by rigorously deriving Kirchhoff's plate theory from nonlinear three-dimensional elasticity. In this special case of the two-dimensional midsurface being a flat object, smooth isometric deformations are characterized by the global property that they are developable surfaces. This has been shown for smooth isometries by Hartman and Nirenberg in [HN59]. Moreover, Hornung [Hor11] has proven that this result holds true for $W^{2,2}$-isometries. A geometrically natural generalization of isometry-constrained bending functionals and their stationary solutions has been investigated in [Hor17]. In [FJMM03], Friesecke et al. extended the Γ-convergence result to the case of thin elastic shells, where the corresponding midsurface $\mathcal{M}_A$ is in general allowed to be curved. More precisely, it was shown that the bending energy depends on the so-called relative shape operator, which we will detail in this chapter.

A conforming finite element approximation of the bending energy for thin elastic shells would require globally C^1-elements, which are computationally demanding and require a proper notion of discrete isometric deformations. As an alternative, Bonito et al. [BNN21] proposed a discontinuous Galerkin approach for isometric deformations of thin elastic plates, and in [BGNY23] Bonito et al. established a Γ-convergence theory of a local discontinuous Galerkin approach for prestrained plates. In this chapter, we follow Bartels [Bar13], who made use of the DKT element to approximate bending isometries in the case of deformations of thin elastic plates. This approach has also been applied in [Bar17] to approximate deformations of plates for a Föppl–von Kármán model, which has been used to verify a break of symmetry for deformations of smooth, circular cones. Furthermore, the DKT element was also used in [BBN17] to approximate bending isometries of bilayer plates. The key ingredient of the DKT element is a non-conforming second derivative with suitable approximation properties. Nodal-wise degrees of freedom for the Jacobian of the deformation enable enforcing the isometry constraint on the nodes of the underlying triangular mesh. Furthermore, Bartels considered a linearization of the isometry constraint and a discrete gradient flow approach to minimize the energy. In [HRS20], Hornung et al. applied the DKT element for a material optimization problem on thin elastic plates, where the isometry constraint was strictly enforced in a second-order scheme.

A different approach for computing bending deformations of elastic shells is the *discrete shell* paradigm introduced in [GHDS03]. Within this framework, the elastic shell is directly conceptualized as a discretized geometry composed of triangular elements. A discrete bending energy is formulated, measuring the change of dihedral angles between two neighboring triangles, whereas the discrete counterpart of a membrane energy involves changes of the lengths of edges. Especially in computer graphics, discrete shells are widely used in practice. Recently, Olbermann and Gladbach showed Γ-convergence of a discrete geometry model to the Willmore energy in [GO23]. In [WBH+07], a family of discrete isometric bending models for triangulated surfaces was derived, which are quadratic in surface positions, under the assumption of isometric surface deformations. Discrete bending and membrane energies can also be used to study the geometry of the space of discrete surfaces, cf. [HRWW12, HRS+14, HRS+16, HZRS18, SSRC24].

Outline. The outline of this chapter is as follows. In Section 3.1, we will rewrite the total elastic energy via a simplification of the relative shape operator and prove the existence of

a minimizing deformation. In Section 3.2, the non-conforming finite element approximation via the Discrete Kirchhoff Triangle will be revisited and used to discretize the total elastic energy. Instead of a linearization, we incorporate an exact metric constraint at nodal positions. To solve the resulting constraint optimization problem numerically, we take into account a Newton method for an associated Lagrangian in Section 3.3. Finally, in Section 3.4, we discuss several selected examples and study the convergence behaviour experimentally.

3.1 Reformulation of the bending energy

In this section, we will show an identity for the Frobenius norm of the relative shape operator $S^{\mathrm{rel}}_{\psi_B}$ under the metric constraint. This reformulation will ensure that the dependence of the elastic energy on second-order derivatives of the parametrization ψ_B is quadratic and the remaining nonlinearity is a quadratic term involving the normal n_B in the deformed configuration.

Proposition 3.1 (transformed bending energy density). *Let $\psi_B = (\psi_B^m)_{m=1,2,3} \in W^{2,2}(\omega;\mathbb{R}^3)$ with $\nabla\psi_B^\top\nabla\psi_B = \nabla\psi_A^\top\nabla\psi_A$ almost everywhere in ω. Then, we have the identity* $\operatorname{tr}\left(S^{rel}_{\psi_B}S^{rel}_{\psi_B}\right) = |g_A^{-\frac{1}{2}}(II_B - II_A)g_A^{-\frac{1}{2}}|^2 = B[\psi_B]$, *where*

$$B[\psi_B] := \sum_{m=1}^{3} |g_A^{-\frac{1}{2}} D^2\psi_B^m g_A^{-\frac{1}{2}}|^2 - 2II_B : (g_A^{-1}II_A g_A^{-1}) + C_A \tag{3.5}$$

where the constant C_A depends only on derivatives of ψ_A.

Proof. Differentiation of $\partial_i\psi_B\cdot\partial_i\psi_B = \partial_i\psi_A\cdot\partial_i\psi_A$ for $i\in\{1,2\}$ in direction $j\in\{1,2\}$ yields $\partial_j\partial_i\psi_B\cdot\partial_i\psi_B = \partial_j\partial_i\psi_A\cdot\partial_i\psi_A$. Similarly, differentiation of $\partial_i\psi_B\cdot\partial_j\psi_B = \partial_i\psi_A\cdot\partial_j\psi_A$ in direction $i\in\{1,2\}$ gives

$$\partial_i^2\psi_B\cdot\partial_j\psi_B + \partial_j\partial_i\psi_B\cdot\partial_i\psi_B = \partial_i^2\psi_A\cdot\partial_j\psi_A + \partial_j\partial_i\psi_A\cdot\partial_i\psi_A$$

and taking into account the first identity we obtain $\partial_i^2\psi_B\cdot\partial_j\psi_B = \partial_i^2\psi_A\cdot\partial_j\psi_A$. Altogether, using the fact that the parameter domain is two dimensional, we obtain

$$\partial_i\partial_j\psi_B\cdot\partial_k\psi_B = \partial_i\partial_j\psi_A\cdot\partial_k\psi_A \quad \forall i,j,k\in\{1,2\}. \tag{3.6}$$

Next, we consider the Gram-Schmidt orthonormalization of the columns of the Jacobian $\nabla\psi_B$

$$y_B^1 := \frac{1}{|\partial_1\psi_B|}\partial_1\psi_B\,, \quad y_B^2 := \frac{1}{|\hat{y}_B^2|}\hat{y}_B^2 \quad \text{with} \quad \hat{y}_B^2 := \partial_2\psi_B - (\partial_2\psi_B\cdot y_B^1)y_B^1$$

and define $y_A^1, y_A^2, \hat{y}_A^2$ analogously for the parametrization ψ_A.
Then, both $\{y_B^1, y_B^2, n_B\}$ and $\{y_A^1, y_A^2, n_A\}$ form an orthonormal basis of $\mathbb{R}^3$. In particular, we get the orthogonal decomposition

$$\partial_k\partial_j\psi_B = (\partial_k\partial_j\psi_B\cdot n_B)n_B + (\partial_k\partial_j\psi_B\cdot y_B^1)y_B^1 + (\partial_k\partial_j\psi_B\cdot y_B^2)y_B^2\,. \tag{3.7}$$

By the metric constraint $|\partial_1\psi_A| = |\partial_1\psi_B|$ and $\partial_2\psi_A\cdot\partial_1\psi_A = \partial_2\psi_B\cdot\partial_1\psi_B$ and consequently

$$y_B^1 = \frac{1}{|\partial_1\psi_A|}\partial_1\psi_B\,, \quad \hat{y}_B^2 = \partial_2\psi_B - (\partial_2\psi_A\cdot y_A^1)\frac{1}{|\partial_1\psi_A|}\partial_1\psi_B.$$

Furthermore, we obtain

$$\begin{aligned}|\hat{y}_B^2|^2 =&|\partial_2\psi_B|^2 - 2(\partial_2\psi_A \cdot y_A^1)\frac{1}{|\partial_1\psi_A|}\partial_1\psi_B \cdot \partial_2\psi_B + \left|(\partial_2\psi_A \cdot y_A^1)\frac{1}{|\partial_1\psi_A|}\right|^2 |\partial_1\psi_B|^2\\ =&|\partial_2\psi_A|^2 - 2(\partial_2\psi_A \cdot y_A^1)\frac{1}{|\partial_1\psi_A|}\partial_1\psi_A \cdot \partial_2\psi_A + \left|(\partial_2\psi_A \cdot y_A^1)\frac{1}{|\partial_1\psi_A|}\right|^2 |\partial_1\psi_A|^2\\ =&|\hat{y}_A^2|^2.\end{aligned}$$

Taking into account (3.6), it follows that

$$\begin{aligned}\partial_k\partial_j\psi_B \cdot y_B^1 &= \frac{1}{|\partial_1\psi_A|}\partial_k\partial_j\psi_B \cdot \partial_1\psi_B = \frac{1}{|\partial_1\psi_A|}\partial_k\partial_j\psi_A \cdot \partial_1\psi_A = \partial_k\partial_j\psi_A \cdot y_A^1,\\ \partial_k\partial_j\psi_B \cdot y_B^2 &= \frac{1}{|\hat{y}_B^2|}\partial_k\partial_j\psi_B \cdot \hat{y}_B^2 = \frac{1}{|\hat{y}_A^2|}\partial_k\partial_j\psi_B \cdot (\partial_2\psi_B - (\partial_2\psi_B \cdot y_B^1)y_B^1)\\ &= \frac{1}{|\hat{y}_A^2|}\partial_k\partial_j\psi_A \cdot (\partial_2\psi_A - (\partial_2\psi_A \cdot y_A^1)y_A^1) = \partial_k\partial_j\psi_A \cdot y_A^2.\end{aligned}$$

Thus, we obtain

$$\partial_k\partial_j\psi_B = (\partial_k\partial_j\psi_B \cdot n_B)n_B + (\partial_k\partial_j\psi_A \cdot y_A^1)y_B^1 + (\partial_k\partial_j\psi_A \cdot y_A^2)y_B^2.$$

Next, we consider the integrand of the bending energy. Similar to the calculations in [BBN17] in the context of prestrained plates, we can write

$$\left|g_A^{-\frac{1}{2}}(II_B - II_A)g_A^{-\frac{1}{2}}\right|^2 = \left|g_A^{-\frac{1}{2}}II_B g_A^{-\frac{1}{2}}\right|^2 - 2(g_A^{-\frac{1}{2}}II_B g_A^{-\frac{1}{2}}) : (g_A^{-\frac{1}{2}}II_A g_A^{-\frac{1}{2}}) + \left|g_A^{-\frac{1}{2}}II_A g_A^{-\frac{1}{2}}\right|^2.$$

The last term only depends on the initial configuration ψ_A and can hence be neglected. Let $g_A^{-\frac{1}{2}} = \left(g_{A,ij}^{-\frac{1}{2}}\right)_{i,j=1,2}$. Using $|n_B|^2 = 1$ and the decomposition (3.7), $\left|g_A^{-\frac{1}{2}}II_B g_A^{-\frac{1}{2}}\right|^2$ can be written as

$$\begin{aligned}&\sum_{i,j=1}^{2}\left|\sum_{k,l=1}^{2} g_{A,ik}^{-\frac{1}{2}}g_{A,lj}^{-\frac{1}{2}}(\partial_k\partial_l\psi_B \cdot n_B)\right|^2 = \sum_{i,j=1}^{2}\left|\sum_{k,l=1}^{2} g_{A,ik}^{-\frac{1}{2}}g_{A,lj}^{-\frac{1}{2}}(\partial_k\partial_l\psi_B \cdot n_B)\, n_B\right|^2\\ =&\sum_{i,j=1}^{2}\left|\sum_{k,l=1}^{2} g_{A,ik}^{-\frac{1}{2}}g_{A,lj}^{-\frac{1}{2}}\left(\partial_k\partial_l\psi_B - \left[\left(\partial_k\partial_l\psi_A \cdot y_A^1\right)y_B^1 + \left(\partial_k\partial_l\psi_A \cdot y_A^2\right)y_B^2\right]\right)\right|^2\\ =&\sum_{i,j=1}^{2}\left|\sum_{k,l=1}^{2} g_{A,ik}^{-\frac{1}{2}}g_{A,lj}^{-\frac{1}{2}}\partial_k\partial_l\psi_B\right|^2 + \sum_{i,j=1}^{2}\left|\sum_{k,l=1}^{2} g_{A,ik}^{-\frac{1}{2}}g_{A,lj}^{-\frac{1}{2}}\left[\left(\partial_k\partial_l\psi_A \cdot y_A^1\right)y_B^1 + \left(\partial_k\partial_l\psi_A \cdot y_A^2\right)y_B^2\right]\right|^2\\ &- 2\sum_{i,j=1}^{2}\left(\sum_{k,l=1}^{2} g_{A,ik}^{-\frac{1}{2}}g_{A,lj}^{-\frac{1}{2}}\partial_k\partial_l\psi_B\right)\cdot\left(\sum_{k,l=1}^{2} g_{A,ik}^{-\frac{1}{2}}g_{A,lj}^{-\frac{1}{2}}\left[\left(\partial_k\partial_l\psi_A \cdot y_A^1\right)y_B^1 + \left(\partial_k\partial_l\psi_A \cdot y_A^2\right)y_B^2\right]\right).\end{aligned}$$

Since $|y_B^1|^2 = |y_B^2|^2 = 1$ and $y_B^1 \cdot y_B^2 = 0$, the second term on the right-hand side only depends on ψ_A and can hence be regarded as constant. The same applies to the third term, considering the metric constraint and the calculations made above. Furthermore, we can rewrite, using the

symmetry of $g_A^{-\frac{1}{2}}$

$$(g_A^{-\frac{1}{2}} I\!I_B g_A^{-\frac{1}{2}}) : (g_A^{-\frac{1}{2}} I\!I_A g_A^{-\frac{1}{2}}) = \sum_{i,j=1}^{2} \left(\sum_{k,l=1}^{2} g_{A,ik}^{-\frac{1}{2}} I\!I_B^{kl} g_{A,lj}^{-\frac{1}{2}} \right) \left(\sum_{m,n=1}^{2} g_{A,im}^{-\frac{1}{2}} I\!I_A^{mn} g_{A,nj}^{-\frac{1}{2}} \right)$$
$$= \sum_{k,l=1}^{2} I\!I_B^{kl} \left(\sum_{m,n=1}^{2} \left(\sum_{i=1}^{2} g_{A,ki}^{-\frac{1}{2}} g_{A,im}^{-\frac{1}{2}} \right) I\!I_A^{mn} \left(\sum_{j=1}^{2} g_{A,lj}^{-\frac{1}{2}} g_{A,jn}^{-\frac{1}{2}} \right) \right) = I\!I_B : (g_A^{-1} I\!I_A g_A^{-1})$$

which proves the claim. □

As an immediate consequence, we obtain the following transformed total free energy.

Corollary 3.2 (transformation of the total free energy). *Let $\psi_B \in W^{2,2}(\omega;\mathbb{R}^3)$ with $\nabla\psi_B^\top \nabla\psi_B = \nabla\psi_A^\top \nabla\psi_A$ almost everywhere in ω. Then, the total free energy* (3.3) *can, up to a constant, be rewritten as*

$$E[\psi_B] = \frac{\alpha}{2} \int_\omega \sqrt{\det g_A} \left(\sum_{m=1}^{3} |g_A^{-\frac{1}{2}} D^2 \psi_B^m g_A^{-\frac{1}{2}}|^2 - 2 I\!I_B : (g_A^{-1} I\!I_A g_A^{-1}) \right) \mathrm{d}x \qquad (3.8)$$
$$- \int_\omega \sqrt{\det g_A}\, f \cdot \psi_B \, \mathrm{d}x$$

Using this reformulation, we obtain the following existence result.

Theorem 3.3 (Existence). *For the set*

$$\mathcal{A} = \{\psi \in W^{2,2}(\omega;\mathbb{R}^3) \mid \nabla\psi^\top \nabla\psi = \nabla\psi_A^\top \nabla\psi_A \text{ a.e. in } \omega;\ \psi = \psi_A, \nabla\psi = \nabla\psi_A \text{ on } \Gamma_D\}$$

of admissible parametrizations subject to the metric constraint and clamped boundary conditions, and for $f \in L^2(\omega,\mathbb{R}^3)$ there exists a parametrization $\psi_B \in \mathcal{A}$ which minimizes the total free energy $E[\psi]$ given in (3.8) *over all $\psi \in \mathcal{A}$.*

Proof. We begin remarking that $\mathcal{A}$ is nonempty, because $\psi_A \in \mathcal{A}$. To apply the direct method in the calculus of variations, we at first show the uniform boundedness of a minimizing sequence in $W^{2,2}(\omega,\mathbb{R}^3)$. To this end, we first estimate for $\psi \in \mathcal{A}$

$$E[\psi] \geqslant \frac{\alpha}{2} \int_\omega \sqrt{\det g_A} \sum_{m=1}^{3} \left| g_A^{-\frac{1}{2}} D^2 \psi^m g_A^{-\frac{1}{2}} \right|^2 \mathrm{d}x$$
$$- \alpha \int_\omega \sqrt{\det g_A} \left| D^2\psi \cdot n[\psi] \right| \left| g_A^{-1} I\!I_A g_A^{-1} \right| \mathrm{d}x - \int_\omega \sqrt{\det g_A}\, |f||\psi| \, \mathrm{d}x\,.$$

using Cauchy-Schwarz' inequality. Note that $\left|D^2\psi \cdot n[\psi]\right| \leqslant \left|D^2\psi\right|$ again by Cauchy-Schwarz with $|n[\psi]| = 1$. Thus, since g_A and $g_A^{-\frac{1}{2}}$ are uniformly bounded, we obtain

$$E[\psi] \geqslant c \left\|D^2\psi\right\|_{L^2(\omega)}^2 - C \left(\int_\omega \left|D^2\psi\right| \left| g_A^{-1} I\!I_A g_A^{-1} \right| \mathrm{d}x + \int_\omega |f||\psi| \, \mathrm{d}x \right)$$

for generic constants c, $C > 0$ depending only on ψ_A and α. Making use of Poincaré's inequality and Young's inequality, we obtain $E[\psi] \geqslant c \left\|D^2\psi\right\|_{L^2(\omega)}^2 - C$. Next, let $(\psi_l)_l \subset \mathcal{A}$

be a minimizing sequence with $\inf_{\psi\in\mathcal{A}} E[\psi] = \lim_{l\to\infty} E[\psi_l]$. Then, the last estimate ensures that $\|\psi_l\|_{W^{2,2}(\omega,\mathbb{R}^3)} \leqslant C$. By the reflexivity of $W^{2,2}$, there exists a subsequence and a function $\psi_B \in W^{2,2}(\omega,\mathbb{R}^3)$ s.t. after a reindexing ψ_l converges weakly to some ψ_B in $W^{2,2}(\omega,\mathbb{R}^3)$. By the Rellich–Kondrachov compactness theorem, we can extract another subsequence ensuring that $\nabla\psi_l(x) \to \nabla\psi_B(x)$ point-wise almost everywhere. Thus, the limit ψ_B also fulfills the metric constraint, and by the trace theorem, the clamped boundary conditions. Hence, $\psi_B \in \mathcal{A}$.

Furthermore, the sequence of normal fields $n[\psi_l]$ is uniformly bounded in $L^\infty(\omega,\mathbb{R}^3)$ and $n[\psi_l]$ converges point-wise almost everywhere to $n[\psi_B]$. Altogether, $D^2\psi_l \cdot n[\psi_l]$ converges weakly in $L^2(\omega,\mathbb{R}^{2\times 2})$ to $D^2\psi_B \cdot n[\psi_B] = I\!I_B$. Finally, the convexity of $|\cdot|^2$ implies that the total free energy $E[\cdot]$ is weakly lower semi-continuous and thereby

$$E[\psi_B] \leqslant \liminf_{l\to\infty} E[\psi_l] = \inf_{\psi\in\mathcal{A}} E[\psi]\,.$$

□

3.2 Discretization based on the Discrete Kirchhoff Triangle

In this section, we will derive a non-conforming finite element discretization of the total free energy and the corresponding discrete metric constraint. This derivation follows the general approach proposed by Bartels for discrete deformations of plates in [Bar13]. In addition, we refer to the monograph [Bar15].

Based on the DKT element, cf. Section 2.4, we discretize the total free energy (3.8). More precisely, we consider $\psi_H \in \mathbf{W}^3_H$ to approximate a parametrization $\psi \in W^{2,2}(\omega;\mathbb{R}^3)$. Then, a discrete unit normal field $n[\psi_H]$ is defined as $n[\psi_H] := \frac{1}{|\partial_1\psi_H\times\partial_2\psi_H|}\partial_1\psi_H \times \partial_2\psi_H$, and we apply $\nabla\theta_H[\psi_H]$ as a discrete (non-conforming) approximation of the Hessian $D^2\psi_H$ in $L^2(\omega;\mathbb{R}^{3,2,2})$. Furthermore, for the given fixed parametrization $\psi_A \in W^{3,2}(\omega;\mathbb{R}^3)$ define $\psi_{A,H} = \mathcal{I}^{\mathrm{DKT}}\psi_A \in \mathbf{W}^3_H$. Then, we define $g_H = \nabla\psi_{A,H}^\top\nabla\psi_{A,H}$, $I\!I_H = \nabla\theta_H[\psi_{A,H}]\cdot n[\psi_{A,H}]$. Let us assume that $\psi_A \in W^{3,2}(\omega;\mathbb{R}^3)$ and $f_H \in L^2(\omega;\mathbb{R}^3)$. In particular, the above coefficients, depending on ψ_A, are well approximated by their discrete counterparts obtained by the interpolation in $\mathbf{W}^3_H$ taking into account the estimates on the discrete gradient operator. Note that instead of a DKT interpolation $\psi_{A,H}$, we could directly consider ψ_A evaluated at quadrature points. However, if one applies the presented approach to shape optimization (cf. [BCC+21]), one usually wants to optimize ψ_A. Then, a DKT discretization $\psi_{A,H}$ would enable to actually perform such an optimization. Now, the discrete transformed bending energy density is given by

$$B_H[\psi_H] := \sum_{m=1}^{3} |g_H^{-\frac{1}{2}}\nabla\theta_H[\psi_H^m]g_H^{-\frac{1}{2}}|^2 - 2(\nabla\theta_H[\psi_H]\cdot n[\psi_H]) : (g_H^{-1}I\!I_H g_H^{-1}) \tag{3.9}$$

Correspondingly, the discrete total free energy is defined as

$$E_H[\psi_H] = \frac{\alpha}{2}\int_\omega \sqrt{\det g_H} B_H[\psi_H]\,\mathrm{d}x - \int_\omega \sqrt{\det g_H}\; f_H\cdot\psi_H\,\mathrm{d}x\,. \tag{3.10}$$

We aim at minimizing this discrete energy over the following constraint set of discrete

deformations

$$\mathcal{A}_H = \Big\{ \psi_H \in \mathbf{W}_H^3 \,\Big|\, \nabla\psi_H(z)^\top \nabla\psi_H(z) = \nabla\psi_A(z)^\top \nabla\psi_A(z) \quad \forall z \in \mathcal{N}_H; \\ \psi(z) = \psi_A(z), \nabla\psi(z) = \nabla\psi_A(z) \quad \forall z \in \mathcal{N}_H \cap \Gamma_D \Big\}.$$

Since $\psi_{A,H} \in \mathcal{A}_H$, this set is not empty. In explicit, we require the metric constraint only on the nodes of the triangulation, and the clamped boundary condition is applied solely on boundary nodes.

Now, we are in the position to formulate our main theorem on the approximation of large-scale isometric deformations of parametrized surfaces, minimizing the total free energy in the case of clamped boundary conditions.

Theorem 3.4 (Convergence of discrete solutions). *Let $(\mathcal{T}_H)_H$ be a sequence of uniformly regular triangulations of ω with maximal triangle diameter $H > 0$. Furthermore, let $\psi_A \in W^{3,2}(\omega;\mathbb{R}^3)$ and $f \in L^2(\omega;\mathbb{R}^3)$ and $(f_H)_H$ be a sequence of force fields in $L^2(\omega,\mathbb{R}^3)$ weakly converging to f in $L^2(\omega,\mathbb{R}^3)$. Assume that there exists a minimizer ψ_B of the continuous total free energy $E[\cdot]$ (3.8) on $\mathcal{A}$ which can be approximated in $W^{2,2}(\omega;\mathbb{R}^3)$ by functions $\psi_\rho \in W^{3,2}(\omega;\mathbb{R}^3) \cap \mathcal{A}$. Then, for every $H \leqslant \bar{H}$, for $\bar{H}$ sufficiently small, there exists a minimizer $\psi_H \in \mathbf{W}_H^3$ of the discrete total free energy $E_H[\cdot]$ (3.10) on $\mathcal{A}_H$. Furthermore, for $(E_H[\cdot])_H$ with $H \to 0$, let $(\psi_H)_H$ be a sequence of minimizers. Then*

$$\big\|\theta_H[\psi_H]\big\|_{W^{1,2}(\omega;\mathbb{R}^{3\times 2})} + \big\|\psi_H\big\|_{W^{1,2}(\omega;\mathbb{R}^3)} \leqslant C$$

and there exists a subsequence that converges strongly in $W^{1,2}(\omega;\mathbb{R}^3)$ to some $\psi^* \in W^{2,2}(\omega;\mathbb{R}^3) \cap \mathcal{A}$. Furthermore, ψ^* is a minimizer of the energy $E[\cdot]$ defined in (3.8) *on $\mathcal{A}$.*

Finally, let us remark that in the flat case $g_A = I_2$ with $\psi_B \in W^{2,2}(\omega;\mathbb{R}^3)$ and $g_B = I_2$ the mapping ψ_B can be approximated in the strong $W^{2,2}$-topology by smooth isometries as shown by Hornung in [Hor11], see also Section 2.3 for more about regularity of isometric immersions. We also refer to the monograph by Bartels [Bar15] for further properties of isometries in the flat case. In the curved case, to the best of our knowledge, such a density result is unclear, since the proof in the flat case is based on the developability by Hartman and Nirenberg in [HN59].

Proof. The general procedure of this proof follows the basic procedure of the convergence proof given in [Bar13] for the case of plates, in [BBN17] for the case of bilayer plates, and in [BGNY23] for prestrained plates, and uses Γ-convergence arguments. With a slight misuse of notation, we do not perform a reindexing when subsequences are selected. Let $\mathcal{I}_H[\cdot]$ be the nodal interpolation operator mapping into the space of piecewise affine, globally continuous functions in $\mathcal{T}_H$.

At first, using similar arguments as in the proof of Theorem 3.3 we can bound the discrete energy $E_H[\psi_H]$ for $\psi_H \in \mathbf{W}_H^3$ from below

$$E_H[\psi_H] \geqslant c\,\big\|\nabla\theta_H[\psi_H]\big\|_{L^2(\omega)}^2 - C\Big(\big\|\nabla\theta_H[\psi_H]\big\|_{L^2(\omega)}\,\big\|n[\psi_H]\big\|_{L^2(\omega)} + \big\|f\big\|_{L^2(\omega)}\,\big\|\psi_H\big\|_{L^2(\omega)}\Big), \tag{3.11}$$

where $\left\|n[\psi_H]\right\|^2_{L^2(\omega)}$ equals the area of ω. Based on the nodal metric constraint, which implies $|\nabla\psi_H(z)|^2 = |\nabla\psi_A(z)|^2$ for all $z \in \mathcal{N}_H$, and applying an inverse inequality, see [Bra13], we obtain for all $\mathbf{t} \in \mathcal{T}_H$:

$$\begin{aligned}&\left\||\nabla\psi_H|^2 - \mathcal{I}_H[|\nabla\psi_A|^2]\right\|_{L^1(\mathbf{t})} \leqslant CH_{\mathbf{t}}^2 \left\|D^2(|\nabla\psi_H|^2)\right\|_{L^1(\mathbf{t})} \qquad (3.12)\\ &\leqslant CH_{\mathbf{t}}^2 \left(\left\|D^3\psi_H\right\|_{L^2(\mathbf{t})} \left\|\nabla\psi_H\right\|_{L^2(\mathbf{t})} + \left\|D^2\psi_H\right\|^2_{L^2(\mathbf{t})}\right) \leqslant CH_{\mathbf{t}} \left\|D^2\psi_H\right\|_{L^2(T)} \left\|\nabla\psi_H\right\|_{L^2(\mathbf{t})}.\end{aligned}$$

Now, using the triangle inequality, Young's inequality, the nodal metric constraint, and the norm equivalence estimates (2.22), we obtain

$$\left\|\nabla\psi_H\right\|^2_{L^2(\mathbf{t})} \leqslant CH_{\mathbf{t}} \left(\left\|\nabla\theta_H[\psi_H]\right\|^2_{L^2(\mathbf{t})} + \left\|\theta_H[\psi_H]\right\|^2_{L^2(\mathbf{t})}\right) + \left\|\mathcal{I}_H[|\nabla\psi_A|^2]\right\|_{L^1(\mathbf{t})},$$

and with summation over all $\mathbf{t} \in \mathcal{T}_H$ we get

$$\left\|\nabla\psi_H\right\|^2_{L^2(\omega)} \leqslant CH \left(\left\|\nabla\theta_H[\psi_H]\right\|^2_{L^2(\omega)} + \left\|\theta_H[\psi_H]\right\|^2_{L^2(\omega)}\right) + \left\|\mathcal{I}_H[|\nabla\psi_A|^2]\right\|_{L^1(\omega)}.$$

Taking into account the clamped boundary conditions and applying Poincaré's inequality for $\theta_H[\psi_H]$ we achieve $\left\|\nabla\psi_H\right\|^2_{L^2(\omega)} \leqslant CH \left\|\nabla\theta_H[\psi_H]\right\|^2_{L^2(\omega)} + C$. Now, applying Poincaré's inequality for ψ_H and Young's inequality, we obtain $\left\|\psi_H\right\|_{L^2(\omega)} \leqslant C(1 + H\left\|\nabla\theta_H[\psi_H]\right\|_{L^2(\omega)})$. Thus, using that $\left\|f_H\right\|_{L^2(\omega)}$ is uniformly bounded, and using again Young's inequality for the term $C\left\|\nabla\theta_H[\psi_H]\right\|_{L^2(\omega)}\left\|n[\psi_H]\right\|_{L^2(\omega)}$ we obtain

$$E_H[\psi_H] \geqslant c\left\|\nabla\theta_H[\psi_H]\right\|^2_{L^2(\omega)} - C \qquad (3.13)$$

for H small enough. From this, the continuity of $E_H[\cdot]$ on $\mathbf{W}^3_H$, and the norm property of $\psi_H \mapsto \left\|\nabla\theta_H[\psi_H]\right\|_{L^2(\omega)}$ the existence of a minimizer ψ_H of $E_H[\cdot]$ follows for h sufficiently small and $\left\|\nabla\theta_H[\psi_H]\right\|_{L^2(\omega)} \leqslant C$. Then, Poincaré's inequality yields $\left\|\theta_H[\psi_H]\right\|_{L^2(\omega)} \leqslant C$. Applying once more the norm equivalence estimates (2.22) we obtain $\left\|\nabla\psi_H\right\|_{L^2(\omega)} \leqslant C$.

Now, we consider the lim inf inequality. By reflexivity of $W^{1,2}$, there exist functions $\psi^* \in W^{1,2}(\omega;\mathbb{R}^3)$ and $\theta^* \in W^{1,2}(\omega;\mathbb{R}^{3\times2})$, such that (up to subsequences) ψ_H converges weakly to ψ^* in $W^{1,2}(\omega;\mathbb{R}^3)$ and $\theta_H[\psi_H]$ converges weakly to θ^* in $W^{1,2}(\omega;\mathbb{R}^{3\times2})$. Furthermore, one observes by (2.23)

$$\left\|\nabla\psi_H - \theta_H[\psi_H]\right\|_{L^2(\omega)} \leqslant cH\left\|\nabla\theta_H[\psi_H]\right\|_{L^2(\omega)} \leqslant CH.$$

By the Rellich–Kondrachov theorem, $\theta_H[\psi_H]$ converges strongly to θ^* in $L^2(\omega;\mathbb{R}^3)$ for another subsequence. Thus, the strong convergence $\nabla\psi_H$ to θ^* and the weak convergence of $\nabla\psi_H$ to $\nabla\psi^*$ yields $\nabla\psi^* = \theta^*$ and in particular $\psi^* \in W^{2,2}(\omega;\mathbb{R}^3)$. The continuity of the trace operator $W^{2,2}(\omega;\mathbb{R}^3) \to W^{1,2}(\Gamma_D;\mathbb{R}^3)$ and interpolation estimates imply that ψ^* fulfills the clamped boundary conditions. To verify that ψ^* fulfills the metric constraint, we estimate

$$\begin{aligned}&\left\|\nabla\psi_H^\top\nabla\psi_H - \nabla\psi_A^\top\nabla\psi_A\right\|_{L^1(\mathbf{t})}\\ &\leqslant \left\|\nabla\psi_H^\top\nabla\psi_H - \mathcal{I}_H[\nabla\psi_A^\top\nabla\psi_A]\right\|_{L^1(\mathbf{t})} + \left\|\mathcal{I}_H[\nabla\psi_A^\top\nabla\psi_A] - \nabla\psi_A^\top\nabla\psi_A\right\|_{L^1(\mathbf{t})}\\ &\leqslant CH_{\mathbf{t}}\left\|D^2\psi_H\right\|_{L^2(\mathbf{t})}\left\|\nabla\psi_H\right\|_{L^2(\mathbf{t})} + CH_{\mathbf{t}}^2\left(\left\|D^3\psi_A\right\|_{L^2(\mathbf{t})}\left\|\nabla\psi_A\right\|_{L^2(\mathbf{t})} + \left\|D^2\psi_A\right\|^2_{L^2(\mathbf{t})}\right).\end{aligned}$$

Here, we applied similar interpolation error estimates as in (3.12). Summation over $\mathbf{t} \in \mathcal{T}_H$ and the fact that $\nabla\psi_H \to \nabla\psi^*$ strongly in L^2 finally imply that $\nabla\psi^{*\top}\nabla\psi^* = \nabla\psi_A^\top\nabla\psi_A$ a.e. in ω. Since $(n[\psi_H])_H$ is a bounded sequence in $L^2(\omega,\mathbb{R}^3)$ and $\nabla\psi_H$ converges point-wise to $\nabla\psi^*$ a.e., we have $n[\psi_H] \to n[\psi^*]$ in $L^2(\omega,\mathbb{R}^3)$. Furthermore, due to interpolation estimates, $g_H^{-\frac{1}{2}}$, g_H^{-1} and $I\!I_H$ converge strongly to $g_A^{-\frac{1}{2}}$, g_A^{-1} and $I\!I_A$, respectively. Altogether, recalling the definitions (3.5) and (3.9), we finally achieve the lim inf-inequality

$$E[\psi^*] \leqslant \liminf_{H\to 0} E_H[\psi_H].$$

With respect to the definition of a recovery sequence, we consider a function $\psi \in W^{3,2}(\omega;\mathbb{R}^3) \cap \mathcal{A}$. For $H > 0$, let $\psi_H = \mathcal{I}^{\mathrm{DKT}}\psi \in \mathbf{W}_H^3$ be the interpolation of ψ defined on every triangle $\mathbf{t} \in \mathcal{T}_H$ by $\psi_H(z) = \psi(z)$ and $\nabla\psi_H(z) = \nabla\psi(z)$ for all vertices $z \in \mathcal{N}_H \cap T$. Taking into account (2.21), (2.22), and (2.24) we have for every $\mathbf{t} \in \mathcal{T}_H$

$$\begin{aligned}
&\left\|\theta_H[\psi_H] - \nabla\psi\right\|_{L^2(\mathbf{t})} + H_\mathbf{t}\left\|\nabla\theta_H[\psi_H] - D^2\psi\right\|_{L^2(\mathbf{t})}\\
\leqslant{}& \left\|\theta_H[\psi_H - \psi]\right\|_{L^2(\mathbf{t})} + \left\|\theta_H[\psi] - \nabla\psi\right\|_{L^2(\mathbf{t})}\\
&+ H_\mathbf{t}\left(\left\|\nabla\theta_H[\psi_H - \psi]\right\|_{L^2(\mathbf{t})} + \left\|\nabla\theta_H[\psi] - D^2\psi\right\|_{L^2(\mathbf{t})}\right) \leqslant c_3 H_\mathbf{t}^2\left\|\psi\right\|_{W^{3,2}(\mathbf{t})}. \qquad (3.14)
\end{aligned}$$

Using the estimate

$$\left|\frac{a}{|a|} - \frac{b}{|b|}\right|^2 = 2\left(1 - \frac{|b|}{|a|} + \frac{(b-a)\cdot b}{|a|\,|b|}\right) \leqslant 2\left(\frac{|a|-|b|}{|a|} + \frac{|b-a|}{|a|}\right) \leqslant 4\frac{|b-a|}{|a|}$$

for $a = \partial_1\psi \times \partial_2\psi$, $b = \partial_1\psi_H \times \partial_2\psi_H$, and the identity $|\partial_1\psi \times \partial_2\psi| = \sqrt{\det(\nabla\psi^\top\nabla\psi)} = \sqrt{\det g_A}$ which follows from the metric constraint, we get

$$\int_\omega \sqrt{\det g_A}\,|n[\psi] - n[\psi_H]|^2\,\mathrm{d}x \leqslant 4\int_\omega |(\partial_1\psi_H \times \partial_2\psi_H) - (\partial_1\psi \times \partial_2\psi)|\,\mathrm{d}x.$$

Furthermore, by the interpolation estimate (2.21) we obtain

$$\begin{aligned}
&\left\|\partial_1\psi_m\partial_2\psi_l - \partial_1\psi_{H,m}\partial_2\psi_{H,l}\right\|_{L^1(\omega)}\\
\leqslant{}& \left\|\partial_1\psi_m - \partial_1\psi_{H,m}\right\|_{L^2(\omega)}\left\|\partial_2\psi_l\right\|_{L^2(\omega)} + \left\|\partial_1\psi_{H,m}\right\|_{L^2(\omega)}\left\|\partial_2\psi_l - \partial_2\psi_{H,l}\right\|_{L^2(\omega)} \leqslant CH^2\left\|\psi\right\|_{W^{3,2}(\omega)}^2
\end{aligned}$$

and hence

$$\left(\int_\omega \sqrt{\det g_A}\,\left|n[\psi] - n[\psi_H]\right|^2\mathrm{d}x\right)^{\frac{1}{2}} \leqslant CH\left\|\psi\right\|_{W^{3,2}(\omega)}.$$

Now, let $\psi_B \in \mathcal{A}$ be a minimizing isometry for $E[\cdot]$. In Theorem 3.3, it is shown that such a minimizer exists. By our assumption, we have

$$\forall\rho > 0\ \exists\psi_\rho \in W^{3,2}(\omega;\mathbb{R}^3)\cap\mathcal{A}:\ \left\|\psi_B - \psi_\rho\right\|_{W^{2,2}(\omega;\mathbb{R}^3)} < \rho.$$

Applying the above estimates to ψ_ρ and its interpolation $\psi_{\rho,H} = \mathcal{I}^{\mathrm{DKT}}\psi_\rho$ in $\mathbf{W}_H^3$ and using the estimates (2.21), (2.24) and (3.14) we achieve

$$\begin{aligned}
&\int_\omega \sqrt{\det g_H}\;B_H[\psi_{\rho,H}]\,\mathrm{d}x \leqslant \int_\omega \sqrt{\det g_A}\;B[\psi_\rho]\,\mathrm{d}x + CH\left\|\psi_\rho\right\|_{W^{3,2}} \qquad (3.15)\\
\leqslant{}& \int_\omega \sqrt{\det g_A}\;B[\psi_B]\,\mathrm{d}x + C\left(\rho + H\left\|\psi_\rho\right\|_{W^{3,2}}\right)
\end{aligned}$$

Now, we choose $H = H(\rho)$ small enough such that

$$H(\rho) \left\| \psi_\rho \right\|_{W^{3,2}(\omega)} < \rho \,. \tag{3.16}$$

and use for the estimation of the potential energy that $\psi_{\rho,H(\rho)}$ converges strongly to ψ_B in L^2 to obtain

$$\limsup_{\rho \to 0} E_{H(\rho)}[\psi_{\rho,H(\rho)}] \leqslant E[\psi_B].$$

Finally, we get

$$E[\psi^*] \leqslant \liminf_{\rho \to 0} E_{H(\rho)}[\psi_{H(\rho)}] \leqslant \limsup_{\rho \to 0} E_{H(\rho)}[\psi_{\rho,H(\rho)}] \leqslant E[\psi_B] = \min_{\tilde{\psi} \in \mathcal{A}} E[\tilde{\psi}] \leqslant E[\psi^*].$$

Hence, ψ^* is a minimizer of $E[\cdot]$. □

In fact, the coupling of H and the $W^{3,2}$-norm of the approximations determines the rate of convergence. This rate cannot be predicted under the assumption of this theorem.

3.3 Implementation via Newton's method

Now, we will describe the numerical implementation to minimize the discrete total energy E_H as defined in (3.10) over all discrete isometries $\phi_H \in \mathcal{A}_H$. First, we observe that a function $\psi_H \in \mathcal{A}_H = \{\phi_H \in \mathbf{W}_H^3 \mid \phi_H(z) = \psi_A(z), \nabla \phi_H(z) = \nabla \psi_A(z) \text{ on } \Gamma_D\}$ is determined by its values at the nodes and the values of the gradient at the nodes. So, for the discrete constraint minimization problem, there are $9 \times |\mathcal{N}_H \backslash \Gamma_D|$ degrees of freedom. To implement the nodal-wise metric constraint, we define the Lagrangian

$$L_H[\psi_H, p_H] := E_H[\psi_H] - G_H[\psi_H](p_H) \,.$$

Here, $E_H[\psi_H]$ is the discrete total free energy and

$$G_H[\psi_H](p_H) := \int_\omega \mathcal{I}_H \left(\left[\nabla \psi_H(z)^\top \nabla \psi_H(z) - \nabla \psi_A(z)^\top \nabla \psi_A(z) \right] : p_H \right) \mathrm{d}x$$

with Lagrange multiplier $p_H \in \mathbf{S}_H^{2\times 2}$, where $\mathbf{S}_H^{2\times 2}$ denotes the space of continuous piecewise affine, symmetric matrices in $\mathbb{R}^{2\times 2}$. In particular, $G_H[\psi_H](p_H) = 0$ for all $p_H \in \mathbf{S}_H^{2\times 2}$ is equivalent to an enforcement of the metric constraint on all nodes of the triangulation. The saddle point conditions are

$$\partial_{\psi_H} L_H[\psi_H, p_H](v_H) = 0 \,, \quad \partial_{p_H} L_H[\psi_H, p_H](q_H) = 0$$

for all $v_H \in \{\phi_H \in \mathbf{W}_H^3 \mid \phi_H(z) = 0, \nabla \phi_H(z) = 0 \text{ on } \Gamma_D\}$ and for all $q_H \in \mathbf{S}_H^{2\times 2}$.

To compute a saddle point, we use the Interior Point Optimizer (IPOPT) software library introduced in [WB06]. This library provides a primal-dual barrier method to solve nonlinear optimization problems of the form

$$\min_{x \in \mathbb{R}^n} f(x) \,, \quad \text{s.t. } c(x) = 0 \text{ and } x_i^L \leqslant x_i \leqslant x_i^U \,,\ i = 1, \ldots, n \,,$$

with objective function $f\colon \mathbb{R}^n \to \mathbb{R}$, equality constraint function $c\colon \mathbb{R}^n \to \mathbb{R}^m$, and vectors $x^L \in [-\infty, \infty)^n$ and $x^L \in (-\infty, \infty]^n$. In our case, the unknown x is the vector representing a deformation ψ_H, f is the elastic energy, and the isometry constraint is incorporated in the constraint function c. The boundary conditions are incorporated in the vectors x^L and x^U, by setting $x_i^L = x_i^U = (\psi_{A,H})_i$ for all degrees of freedom i that correspond to nodes on the boundary $z \in \mathcal{N}_H \cap \Gamma_D$.

We apply a Newton scheme for the Lagrangian, which requires the computation of the first and second variations of the discrete energy $E_H[\cdot]$ and of $G_H[\cdot](\cdot)$, respectively. In IPOPT this corresponds to setting `hessian_approximation` to `exact`. Here, we take into account the default backtracking strategy by setting `line_search_method` to `filter`. As stopping criterion we set `tol` to 10^{-12}. For the required integral evaluations, we implemented a Gauss quadrature of degree 6 with 12 quadrature points. For the ease of presentation, we consider the continuous Lagrangian

$$L[\psi, p] = E[\psi] - G[\psi](p)$$

with $G[\psi](p) = \int_\omega \left(\nabla\psi^\top \nabla\psi - \nabla\psi_A^\top \nabla\psi_A\right) : p \,\mathrm{d}x$ and provide first and second variations of $E[\cdot]$ and of $G[\cdot](\cdot)$, respectively. Here, $X : Y$ denotes the canonical scalar product for tensors X and Y. The transfer to the discrete counterparts is straightforward. The energy is given by $E[\psi] = \frac{\alpha}{2}\int_\omega \sqrt{\det g_A} B[\psi] \,\mathrm{d}x - \int_\omega \sqrt{\det g_A} f \cdot \psi \,\mathrm{d}x$, where we can write $B[\psi] = \sum_{m=1}^3 \left(g_A^{-1} D^2\psi^m g_A^{-1}\right) : D^2\psi^m - 2\left(D^2\psi \cdot n[\psi]\right) : \left(g_A^{-1} I\!I_A g_A^{-1}\right)$. For the first and second variation, we obtain

$$\begin{aligned}
\partial_\psi E[\psi](v) &= \frac{\alpha}{2}\int_\omega \sqrt{\det g_A}\, \partial_\psi B[\psi](v) \,\mathrm{d}x - \int_\omega \sqrt{\det g_A} f \cdot v \,\mathrm{d}x\,,\\
\partial_\psi^2 E[\psi](v,w) &= \frac{\alpha}{2}\int_\omega \sqrt{\det g_A}\, \partial_\psi^2 B[\psi](v,w) \,\mathrm{d}x
\end{aligned}$$

where

$$\begin{aligned}
\partial_\psi B[\psi](v) =& 2\sum_{m=1}^3 \left(g_A^{-1} D^2\psi^m g_A^{-1}\right) : D^2 v^m \\
&- 2\left(D^2 v \cdot n[\psi] + D^2\psi \cdot \partial_\psi n[\psi](v)\right) : \left(g_A^{-1} I\!I_A g_A^{-1}\right)\,,\\
\partial_\psi^2 B[\psi](v,w) =& 2\sum_{m=1}^3 \left(g_A^{-1} D^2 w^m g_A^{-1}\right) : D^2 v^m \\
&- 2\left(D^2 v \cdot \partial_\psi n[\psi](w) + D^2 w \cdot \partial_\psi n[\psi](v)\right) : \left(g_A^{-1} I\!I_A g_A^{-1}\right)\\
&- 2\left(D^2\psi \cdot \partial_\psi^2 n[\psi](v,w)\right) : \left(g_A^{-1} I\!I_A g_A^{-1}\right)\,.
\end{aligned}$$

To compute the first and second variation of the normal field $n[\psi]$, we recall the definition of the metric $g[\psi] = \nabla\psi^\top\nabla\psi$ in the deformed configuration and observe that $|n[\psi]|^2 = 1$ implies

$$0 = \partial_\psi(|n[\psi]|^2)(v) = 2n[\psi] \cdot \partial_\psi n[\psi](v)\,.$$

Hence, there exist $\alpha_1,\ \alpha_2 \in \mathbb{R}$ s.t. $\partial_\psi n[\psi](v) = \alpha_1\partial_1\psi + \alpha_2\partial_2\psi$ and therefore

$$\partial_\psi n[\psi](v) \cdot \partial_k\psi = \alpha_1 g[\psi]_{k1} + \alpha_2 g[\psi]_{k2}\,.$$

Furthermore,

$$0 = \partial_\psi(n[\psi]\cdot\partial_k\psi)(v) = \partial_\psi n[\psi](v)\cdot\partial_k\psi + n[\psi]\cdot\partial_k v$$

implies

$$g[\psi](\alpha_1, \alpha_2)^\top = \nabla\psi^\top \partial_\psi n[\psi](v) = -\nabla v^\top n[\psi]$$

and thus

$$(\alpha_1, \alpha_2)^\top = -g[\psi]^{-1}\nabla v^\top n[\psi]\,.$$

Finally, for the first variation of $n[\phi]$, we obtain

$$\partial_\psi n[\psi](v) = -\nabla\psi g[\psi]^{-1}\nabla v^\top n[\psi].$$

For the second variation, we obtain

$$\begin{aligned}\partial^2_\psi n[\psi](v, w) = &- \nabla w g[\psi]^{-1}\nabla v^\top n[\psi] - \nabla\psi\partial_\psi\left(g[\psi]^{-1}\right)(w)\nabla v^\top n[\psi] \\ &- \nabla\psi g[\psi]^{-1}\nabla v^\top \partial_\psi n[\psi](w).\end{aligned}$$

where $\partial_\psi\left(g[\psi]^{-1}\right)(w)$ can be evaluated taking into account

$$0 = \partial_\psi\left(g[\psi]^{-1}g[\psi]\right)(w) = \partial_\psi\left(g[\psi]^{-1}\right)(w)g[\psi] + g[\psi]^{-1}\partial_\psi\left(g[\psi]\right)(w)$$

and $\partial_\psi\left(g[\psi]\right)(w) = \nabla w^\top\nabla\psi + \nabla\psi^\top\nabla w$, which implies

$$\begin{aligned}\partial_\psi\left(g[\psi]^{-1}\right)(w) = &- g[\psi]^{-1}\partial_\psi\left(g[\psi]\right)(w)g[\psi]^{-1} \\ = &- g[\psi]^{-1}\left(\nabla w^\top\nabla\psi + \nabla\psi^\top\nabla w\right)g[\psi]^{-1}\,.\end{aligned}$$

Based on this, we straightforwardly obtain

$$\begin{aligned}\partial_\psi G[\psi](p)(v) &= \int_\omega \left(\nabla v^\top\nabla\psi + \nabla\psi^\top\nabla v\right) : p\,\mathrm{d}x\,, \\ \partial^2_\psi G[\psi](p)(v, w) &= \int_\omega \left(\nabla v^\top\nabla w + \nabla w^\top\nabla v\right) : p\,\mathrm{d}x\,.\end{aligned}$$

We remark that a proof of convergence of the second-order method would require invertibility of the Hessian D^2L, which we have always obtained in our numerical computations. However, note that the Hessian D^2E is, in general, not invertible.

Finally, note that an algorithmic generalization on multiple charts would be straightforward. E.g. for two DKT charts ψ^1_B, ψ^2_B of the deformed configuration corresponding to given DKT charts ϕ^1_A, ϕ^1_A, which share degrees of freedom on the common boundary $\mathcal{S} = \partial\mathcal{M}^1_A \cap \partial\mathcal{M}^2_A$, we require consistency of the DKT degrees of freedom, i.e. $\psi^1_B(z) = \psi^2_B(z)$ and $\nabla\psi^1_B(z) = \nabla\psi^2_B(z)$ for all $z \in \mathcal{S}_H$.

3.4 Numerical results

In this section, the presented method is applied for specific choices of ψ_A, f, and ω, and for $\alpha = \frac{1}{12}$. In all our examples, we consider a sequence of triangulations on ω, generated by uniform, regular (so-called red) refinement starting from a coarse rectangular mesh with each rectangular cell subdivided into two triangles. We use ψ_A as initialization for ψ_B on the coarsest mesh. On a refined mesh, we use a prolongation of the result on the previous coarser mesh as an initialization. In the first three examples, the surfaces are parametrized over the unit square $\omega = (0, 1) \times (0, 1)$ and the part of the boundary for the clamped boundary

condition is set to $\Gamma_D = \{0\} \times [0,1]$. Furthermore, we will also consider an L-shaped parameter domain. Finally, an example with modified boundary conditions is shown.

(1) Square-shaped plate. In the first experiment, the undeformed surface is a flat unit square in $\mathbb{R}^3$ with $\psi_A(x_1,x_2) = (x_1,x_2,0)^\top$ and $f(x_1,x_2) = (0,0,-0.1)^\top$. Thus, $a_i^{kj} = 0$ for all $i \in \{0,1,2\}$ and $k,j \in \{1,2\}$. Note that this flat case is already covered by Bartels [Bar13]. However, as mentioned above, our numerical method differs in the enforcement of a nodal-wise metric constraint as in [HRS20] instead of the linearization of the constraint in a gradient descent. In Table 3.1, for decreasing grid size H, the minimal discrete energy, the isometry error in L^1, the L^1-norm of the discrete Gauss-curvature $K_H[\psi_H] = \det(g[\psi_H]^{-1}\nabla\theta_H[\psi_H]\cdot n[\psi_H])$ with $\nabla\theta_H[\psi_H]\cdot n[\psi_H] = \left(\sum_{l=1}^3 n_l[\psi_H]\partial_k\theta_H^j[\psi_H^l]\right)_{k,j=1,2}$ and the L^2 approximate error in the Hessian of the energy are shown. Since we do not know the minimizer of this problem explicitly, we compare the discrete Hessian of the discrete minimizer for grid size H to the discrete Hessian of the finest solution with grid size $H^* = 0.0014$. For a numerical quadrature, we prolongate functions onto the finest mesh. We obtain an approximate linear convergence rate for $\nabla\theta[\psi_H]$. This rate coincides with the rate for the DKT interpolation on $W^{3,2}(\omega,\mathbb{R}^3)$ as stated in Section 3.2. Note that this is the same convergence rate as obtained for the linearized gradient flow scheme in [Bar13]. Furthermore, the convergence of the isometry error is of second order, whereas theoretically we can only guarantee a linear convergence rate. Compare here the results in Table 3.4. By Gauss's theorema egregium, a smooth surface isometric to the plate has a vanishing Gaussian curvature. Here, we observe that K_H indeed approaches zero, with approximately linear order of convergence.

H	$E_H[\psi_H]$	$\|g[\psi_H]-g_A\|_{L^1}$	$\|K_H[\psi_H]\|_{L^1}$	$\|\nabla\theta_H[\psi_H]-\nabla\theta_{H^*}[\psi_{H^*}]\|_{L^2}$
0.0442	0.00595312	5.332e-05	0.0009403	0.00899
0.0221	0.00595271	1.329e-05	0.0002892	0.003455
0.0111	0.00595210	3.324e-06	0.000140	0.001711
0.0055	0.00595195	8.310e-07	6.928e-05	0.000847
0.0028	0.00595191	2.078e-07	3.438e-05	0.0004139
0.0014	0.00595190	5.194e-08	1.712e-05	-

Table 3.1: Experimental convergence evaluation for example (1): grid size, discrete energy, isometry error in L^1, L^1 norm of the discrete Gaussian curvature, and approximate L^2 error for the Hessian.

(2) Half Cylinder. In the second experiment, we consider

$$\psi_A : [0,1]^2 \to \mathbb{R}^3;\ \psi_A(x_1,x_2) = \left(\pi^{-1}\sin(\pi x_1), x_2, \pi^{-1}\cos(\pi x_1)\right)^\top,$$

which isometrically parametrizes a half-cylinder as the undeformed configuration and apply the loads

$$f_1(x_1,x_2) = (0,1,0)^\top, \quad f_2(x_1,x_2) = \begin{cases} (-8,1,0)^\top & \text{if } (x_1,x_2)^\top \in [0,\frac{1}{2}]\times[\frac{1}{2},1], \\ (0,1,0)^\top & \text{else}. \end{cases}$$

In Table 3.2, we list the same quantities as for example (1), now for both loads f_1 and f_2. Since the half cylinder is isometric to the plate, an isometric deformation of it should also

have vanishing Gaussian curvature. Here, we observe a less-than-linear experimental rate of convergence of the discrete Gaussian curvature, whereas the convergence of the discrete Hessian again appears to be linear. In Figure 3.1, the undeformed cylinder parametrized by ψ_A, and the different discrete deformations of the half cylinder due to the two different loads are displayed from different perspectives for the numerical results on the finest grid size. Here, the elongated box attached to the surfaces illustrates the clamped boundary condition.

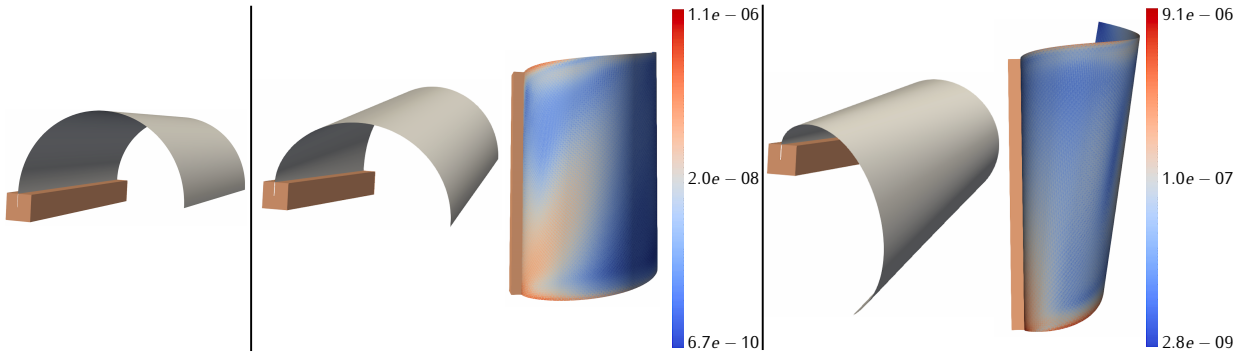

Figure 3.1: Left: Undeformed configuration for example (2). Middle: Deformed configuration for load f_1 and color-coded corresponding to an element-wise evaluation of $\left\|\nabla\theta_H[\psi_H] - \nabla\theta_{H^*}[\psi_{H^*}]\right\|_{L^2(T)}$ for $H = 0.0028, H^* = 0.0014$ with associated deformation ψ_{H^*} using logarithmic scaling. Right: the same for load f_2.

H	$E_H[\psi_H]$		$\left\|K_H[\psi_H]\right\|_{L^1}$		$\left\|\nabla\theta_H[\psi_H] - \nabla\theta_{H^*}[\psi_{H^*}]\right\|_{L^2}$	
	f_1	f_2	f_1	f_2	f_1	f_2
0.0442	0.0416	1.0628	0.1164	0.4478	0.2927	0.7181
0.0221	0.0386	1.0427	0.0703	0.2545	0.1497	0.3590
0.0111	0.0377	1.0367	0.0413	0.1537	0.0854	0.2064
0.0055	0.0376	1.0346	0.0249	0.0906	0.0489	0.1205
0.0028	0.0373	1.0338	0.0150	0.0523	0.0255	0.0625
0.0014	0.0372	1.0335	0.0093	0.0309	-	-

Table 3.2: Experimental convergence evaluation for example (2): grid size, discrete energy, L^1 norm of the discrete Gaussian curvature and approximate L^2 error in the Hessian for loads f_1 and f_2.

(3) Saddle-shaped surface. We consider a saddle-shaped surface as reference configuration parametrized via

$$\psi_A(x_1, x_2) = \left(x_1, x_2, \tfrac{1}{2}\left((x_1 - \tfrac{1}{2})^2 - (x_2 - \tfrac{1}{2})^2\right)\right)^\top . \tag{3.17}$$

over the unit square. Obviously, ψ_A is no isometric deformation of ω. Figure 3.2 shows the undeformed saddle and two different deformed configurations for $f_1(x_1, x_2) = (0, 0, -1)^\top$ and $f_2(x_1, x_2) = (0, 0, -2.5)^\top$, respectively. In Table 3.3, the discrete energies, and the experimental convergence of the discrete Gaussian curvature and the discrete Hessian for decreasing grid size h are shown for both forces. As approximate ground truth, we consider

again the evaluation on the finest grid. Different from the first two examples, where the reference configurations are isometric to a planar domain (the plate and the half cylinder), we observe a less than linear experimental order of convergence, both for the Gaussian curvature, and for the discrete Hessian. Here, let us recall that Theorem 3.4 only applies to functions that can be approximated by smooth isometries. In fact, we can only guarantee $W^{2,2}$ regularity for a minimizer ψ_B due to the lower bound for the continuous energy. However, for the estimate (3.15), we require an approximation of ψ_B in $W^{3,2}$ which is isometric to ψ_A. This approximation result was proven by Hornung [Hor11] in the flat case, where he essentially made use of the property that smooth isometries are developable. On this background, a generalization of Hornung's result remains unclear in the general case of curved surfaces. Here, we actually need the smooth approximation property as an additional assumption. Furthermore, the dependence of H on ρ and the $W^{3,2}$ norm of the approximation in (3.16) impacts the resulting convergence rate.

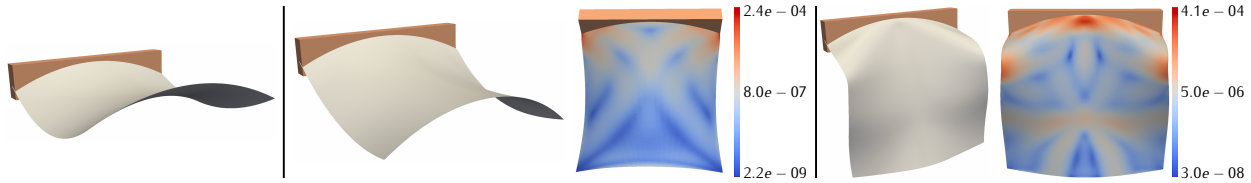

Figure 3.2: Left: Undeformed configuration for example (3). Middle: Deformed configuration for load f_1 and colorcoded corresponding to an element-wise evaluation of $\left\|\nabla\theta_H[\psi_H] - \nabla\theta_{H^*}[\psi_{H^*}]\right\|_{L^2(T)}$ for $H = 0.0028$, $H^* = 0.0014$ using logarithmic scaling. Right: the same for load f_2.

H	$E_H[\psi_H]$		$\left\|K_H[\psi_H] - K_{H^*}[\psi_{H^*}]\right\|_{L^1(\omega)}$		$\left\|\nabla\theta_H[\psi_H] - \nabla\theta_{H^*}[\psi_{H^*}]\right\|_{L^2(\omega)}$	
	f_1	f_2	f_1	f_2	f_1	f_2
0.0442	0.3236	1.2792	0.4212	0.9486	1.5903	3.5378
0.0221	0.2442	1.1052	0.2666	0.9135	1.0699	2.5771
0.0111	0.2136	1.0062	0.1989	0.7499	0.8182	2.3427
0.0055	0.1975	0.9190	0.1212	0.5657	0.6336	2.0894
0.0028	0.1843	0.8203	0.0520	0.3510	0.4046	1.5613
0.0014	0.1745	0.7077	-	-	-	-

Table 3.3: Experimental convergence evaluation for example (3): grid size, discrete energy, approximate L^1 error of the discrete Gaussian curvature, and approximate L^2 error in the Hessian for loads f_1 and f_2.

(4) L-shaped saddle-shaped surface. In this example, the parameter domain is given by an L-shape $\omega = (0, \frac{1}{2}) \times (0, \frac{1}{2}) \cup (0, 1) \times (\frac{1}{2}, 1)$. We consider the initial configuration parametrized by ψ_A as defined in (3.17). The clamped boundary conditions are enforced on $\Gamma_D = \{1\} \times [\frac{1}{2}, 1]$ and two different loads

$$f_1(x_1, x_2) = (0, 0, -1)^\top, \quad f_2(x_1, x_2) = \begin{cases} (-5, 0, -2)^\top & \text{if } (x_1, x_2) \in [0, \frac{1}{2}] \times [0, \frac{1}{2}], \\ (0, 0, -2)^\top & \text{else}. \end{cases}$$

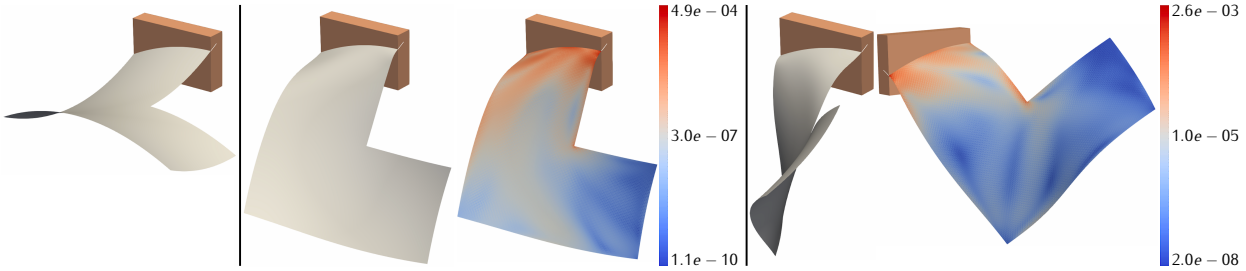

Figure 3.3: Left: Undeformed configuration for example (4). Middle: Deformed configuration for load f_1 and color-coded corresponding to an element-wise evaluation of $\left\|\nabla\theta_H[\psi_H] - \nabla\theta_{H^*}[\psi_{H^*}]\right\|_{L^2(T)}$ for $H = 0.0028$, $H^* = 0.0014$ using logarithmic scaling. Right: the same for load f_2.

are applied. In Figure 3.3, the undeformed and the deformed configurations are shown.

(5) Saddle-shaped surface with different boundary conditions. In this last example, we consider as in (3.17) an initial configuration parametrized by ψ_A over the unit square $\omega = (0,1)^2$. Instead of applying a force, we now enforce a deformation by imposing a modified clamped boundary conditions, namely $\psi_B(x) = \psi_A(x) + \frac{3}{16}$ for $x \in \{0\} \times [0,1]$, $\psi_B(x) = \psi_A(x) - \frac{3}{16}$ for $x \in \{1\} \times [0,1]$ and $\nabla\psi_B(x) = \nabla\psi_A(x)$ on $\{0\} \times [0,1] \cup \{1\} \times [0,1]$. In Figure 3.4, the undeformed and the resulting deformed configuration are shown.

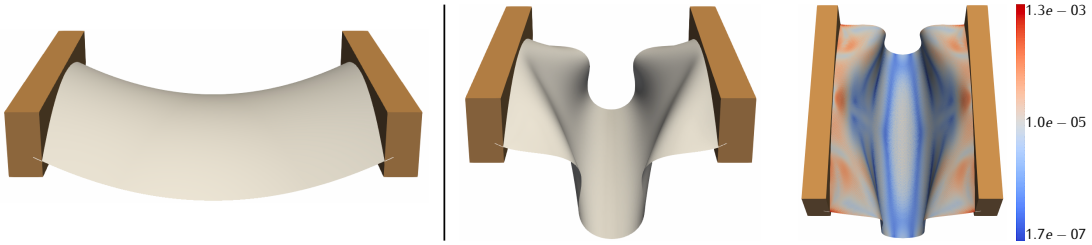

Figure 3.4: Left: undeformed configuration of example (5). Right: different views of the deformed configuration with prescribed boundary conditions, one image color-coded corresponding to an element-wise evaluation of $\left\|\nabla\theta_H[\psi_H] - \nabla\theta_{H^*}[\psi_{H^*}]\right\|_{L^2(T)}$ for $H = 0.0028$, $H^* = 0.0014$ using logarithmic scaling.

In Table 3.4, for decreasing grid size h, we depict the isometry error in L^1, the L^1-norm of the discrete Gauss-curvature, and the L^2 approximate error in the Hessian of the energy. As proven in Theorem 3.4, we obtain a linear convergence rate of the isometry error in L^1. Note that in this case, an approximation result of the admissible deformations by $W^{3,2}$ functions is unknown. In accordance, we only obtain a sublinear convergence rate for the approximate second derivative.

H	$\left\|g[\psi_H] - g_A\right\|_{L^1(\omega)}$	$\left\|K_H[\psi_H] - K_{H*}[\psi_{H*}]\right\|_{L^1(\omega)}$	$\left\|\nabla\theta_H[\psi_H] - \nabla\theta_{H*}[\psi_{H*}]\right\|_{L^2(\omega)}$
0.0442	0.1025	2.3768	6.4416
0.0221	0.0441	2.2603	5.0329
0.0111	0.0168	1.8826	4.1574
0.0055	0.0078	1.2785	3.4613
0.0028	0.0041	0.7431	2.5670
0.0014	0.0025	-	-

Table 3.4: Experimental convergence evaluation for example (5): grid size, isometry error in L^1, L^1 norm of the discrete Gaussian curvature, and approximate L^2 error for the Hessian.

Chapter 4

Two-Scale Finite Element Approximation of a Homogenized Plate Model

This chapter studies the discretization of a homogenization and dimension reduction model for the elastic deformation of microstructured thin plates proposed by Hornung, Neukamm, and Velčić [HNV14]. There, the derived nonlinear bending energy is based on a homogenized quadratic form, which acts on the second fundamental form associated with the elastic deformation. Convergence is proved for a multi-affine finite element discretization of the involved three-dimensional microscopic cell problems and a discrete Kirchhoff triangle discretization of the two-dimensional isometry-constrained macroscopic problem. Finally, the convergence properties are numerically verified in selected test cases and qualitatively compared with deformation experiments for microstructured sheets of paper.

Collaboration. This chapter is the result of joint work with Stefan Simon and Martin Rumpf that has been published in [RSS24]. In particular, Stefan Simon implemented the finite element library that is used for the numerical experiments in this chapter.

In this chapter, the numerical approximation of a homogenized model of a thin plate is investigated. We will pick up the model derived in [HNV14], and derive a discretization and approximation of this model, using the heterogeneous multiscale method (HMM) [EMZ05]. To this end, we consider the straightforward generalization to macroscopically varying microstructures. Hornung et al. in [HNV14] combined methods from [FJM02] with homogenization to derive a homogenized nonlinear plate model from three-dimensional nonlinear elasticity via simultaneous homogenization and dimension reduction. They considered a plate with thickness $\delta > 0$ with a three-dimensional periodic microstructure of size $\varepsilon > 0$, composed of elastic material, which is homogeneous in the vertical direction. The derived limit energy is the integral over a quadratic form acting on the second fundamental form of the elastic deformation and describing the effective deformation of the plate. This quadratic form describes the effective behavior in the simultaneous limit for vanishing plate thickness δ and microstructure size ε with fixed ratio $\gamma = \frac{\delta}{\varepsilon}$ It results from a minimization problem on the unit cell similar to the usual corrector problem in two-scale models [EEH03, AB05]. In [HNV14], as revisited in Section 2.2, solely a macroscopically homogeneous microstructure was taken into account. In [BNPGS23], Böhnlein et al. extended this theory to the case of piecewise constant macroscopic dependence on grain domains. Here, we consider the more general case of a macroscopically varying microstructure. Introducing the macroscopic variable $x \in \omega$ we

consider the linearized elasticity density

$$Q^3 : \omega \times Y' \times \mathbb{R}^{3\times 3} \to \mathbb{R};\ (x, y', G) \to Q^3(x, y', G) \tag{4.1}$$

on the fundamental cell Y, which is assumed to be quadratic in the third argument. In particular, for fixed macroscopic position x, the material properties are constant in the y_3 direction and depend solely on y'.

In fact, we consider the homogenized elastic energy

$$\mathcal{W}^\gamma[\psi] = \begin{cases} \int_\omega Q^{2,\gamma}(x, D^2\psi(x) \cdot n[\psi](x))\,\mathrm{d}x & , \psi \in \mathcal{A}, \\ +\infty & , \text{ else}, \end{cases} \tag{4.2}$$

where $x \in \omega$ denotes the macroscopic variable, and

$$\mathcal{A} = \{\psi \in W^{2,2}(\omega; \mathbb{R}^3) \ :\ \nabla\psi^\top \nabla\psi = I_2 \text{ a.e. in } \omega\}\,.$$

We assume that $Q^{2,\gamma} \colon \omega \times \mathbb{R}^{2\times 2}_{\mathrm{sym}} \to \mathbb{R}$ results from a microscopic optimization problem rescaled to the fundamental cell Y similar to (2.17) and reads as

$$Q^{2,\gamma}(x, A) = \inf_{\vartheta \in \mathcal{V}} \int_Y Q^3(x, y', \iota(y_3 A) + \nabla_\gamma \vartheta(y))\,\mathrm{d}y\,, \tag{4.3}$$

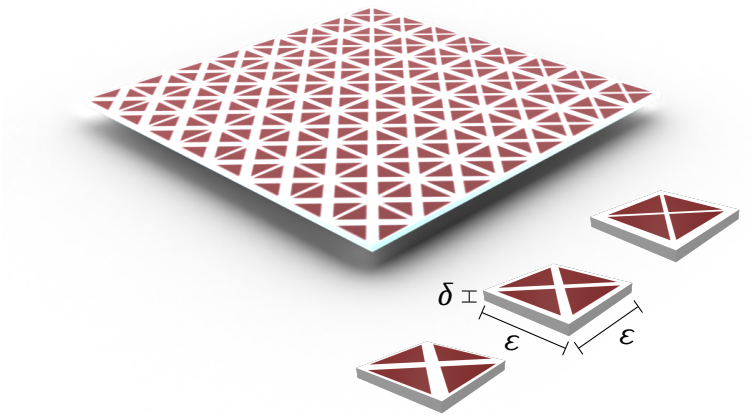

Figure 4.1: Thin plate with thickness δ and macroscopically varying in-plane microstructure with size ε.

This is illustrated in Figure 4.1 for a material with macroscopically varying energy density reflecting two phases (red and white). Here,

$$Q^3(x, y', G) = \mu(x, y') \left|\tfrac{G+G^\top}{2}\right|^2 + \frac{\lambda(x, y')}{2} \left|\mathrm{tr}\,(G)\right|^2$$

is defined on $\omega \times Y' \times R^{3\times 3}$ with Lamé-Navier parameters $\mu(x, y')$ and $\lambda(x, y')$ defined as functions on $\omega \times Y'$.

Finally, given a force $f \in L^2(\omega; \mathbb{R}^3)$ and clamped boundary conditions on a set $\Gamma_D \subset \partial\omega$, with $\mathcal{H}^1(\Gamma_D) > 0$, we ask for a minimizer of the homogenized and dimension reduced total free energy

$$E[\psi] = \begin{cases} \mathcal{W}^\nu[\psi] - \int_\omega f(x) \cdot \psi(x)\,\mathrm{d}x & , \psi \in \mathcal{A}^{\mathrm{BC}} \\ +\infty & , \text{else} \end{cases} \tag{4.4}$$

with constraint set $\mathcal{A}^{\mathrm{BC}} := \{\psi \in \mathcal{A} : \psi = \phi\,,\ \nabla\psi = \nabla\phi \text{ on } \Gamma_D\}$, for some fixed $\phi \in \mathcal{A}$ representing the clamped boundary conditions. In particular ϕ itself is in $\mathcal{A}^{\mathrm{BC}}$.

Related work. The case where $\varepsilon^2 \leqslant \delta \leqslant \varepsilon$ was discussed by Velčić in [Vel15]. A homogenized von Kármán plate theory was derived in [NV13]. Böhnlein et al. extended theory from [HNV14] to homogenized prestrained plates in [BNPGS23], which was applied to model self-shaping wooden composite bilayers in [BNRS25]. A two-scale discretization of a homogenized prestrained plate model, based on the DKT-element, was recently developed in [BNS25]. In [NO15], Neukamm and Olbermann considered the spatial periodic homogenization in the context of nonlinear bending functionals for plates. In this case, the limit functional is not simply a quadratic function of the second fundamental of the deformed plate. In [dBDS21], de Benito Delgado and Schmidt investigated the plate theory limit for heterogeneous multilayers with material parameters varying strongly in vertical direction. The derivation of a homogenized bending-torsion theory for inextensible rods was established in [Neu12]. Recently, Böhnlein et al. [BBN$^+$25] discussed the (non-)commutativity of homogenization and dimension reduction limits for the derivation of prestrained microheterogeneous plate models.

HMM was introduced in [EE03] to compute solutions to problems, where separation of (multiple) scales occurs. If the data of the problem is oscillating on a small scale (as in the problem described in this chapter), it is often out of reach to fully resolve the data. Instead, one is interested in the effective macroscopic behavior of the problem. In most cases, apart from toy problems in one dimension, the effective macroscopic problem cannot explicitly be written down, but has to be computed as the solution of a problem on the unit cell. In [EMZ05], error estimates for HMM were given under the assumption that the solutions to the microscopic problems were given. In [Abd05] and [Abd06], the fully discrete HMM for linear elliptic and elastic problems was analyzed.

The minimization of the homogenized nonlinear bending energy leads to a fourth-order system of Euler-Lagrange equations. We will again make use of the nonconforming DKT element, which only requires fulfilling the isometry constraint at the nodes of the triangulation.

Outline. This chapter is organized as follows: In Section 4.1, the model we consider is formulated, the associated corrector problem is derived and the isometry constraint is used to rewrite the bending energy such that it is quadratic in the Hessian of the deformation. Then, Section 4.2 presents the numerical approximation of the microscopic problem, and in Section 4.3, as the main result of this chapter, the convergence of the fully discrete two-scale problem to the continuous two-scale problem is stated. The proof relies on Γ-convergence and uses the paradigm of the heterogeneous multiscale method. Finally, in Section 4.4, details on the implementation of the numerical method are presented, the results of several numerical experiments are shown and the convergence behavior is quantitatively analyzed. Furthermore, we compare the simulation results with mechanical experiments for microstructured sheets of paper.

4.1 A quadratic homogenized plate bending energy

In what follows, we rewrite the bending energy (4.4). As it was proved in [BNPGS23], by Poincare's and Korn's inequality using the L^2-orthogonality of $\iota(y_3 A)$ and $\nabla_\gamma \vartheta$ for $\vartheta \in \mathcal{V}$, for every $A \in \mathbb{R}^{2\times 2}_{\mathrm{sym}}$, and $x \in \omega$, there exists a unique $\vartheta(x, A, \cdot) \in \mathcal{V}$ such that

$$Q^{2,\gamma}(x, A) = \int_Y Q^3(x, y', \iota(y_3 A) + \nabla_\gamma \vartheta(x, A, y))\, \mathrm{d}y\,. \tag{4.5}$$

This solution $\vartheta(x, A, \cdot)$ solves the Euler-Lagrange equation

$$\int_Y \left(\mathcal{C}^3(x, y')\nabla_\gamma \vartheta(y)\right) : \nabla_\gamma v(y)\, \mathrm{d}y = -\int_Y \left(\mathcal{C}^3(x, y')\iota(y_3 A)\right) : \nabla_\gamma v(y)\, \mathrm{d}y \tag{4.6}$$

for all $v \in \mathcal{V}$, where $\mathcal{C}^3(x, y') \in \mathbb{R}^{3\times 3\times 3\times 3}$ denotes the linearized elasticity tensor associated with the quadratic form $Q^3(x, y', \cdot)$ for $(x, y') \in \omega \times Y$, i.e.

$$\left(\mathcal{C}^3(x, y')(\iota(y_3 A) + \nabla_\gamma \vartheta)\right) : (\iota(y_3 A) + \nabla_\gamma \vartheta) \coloneqq Q^3(x, y', \iota(y_3 A) + \nabla_\gamma \vartheta) \tag{4.7}$$

for all $A \in \mathbb{R}^{2\times 2}_{\mathrm{sym}}$, $\vartheta \in \mathcal{V}$. From its definition, the symmetries $\mathcal{C}^3_{ijkl} = \mathcal{C}^3_{jikl} = \mathcal{C}^3_{ijlk} = \mathcal{C}^3_{klij}$ for all $i, j, k, l \in \{1, 2, 3\}$ are deduced.

Since $Q^3(x, y', \cdot)$ is quadratic, the solution $\vartheta(x, A, \cdot)$ of the Euler-Lagrange is linear in A for every $x \in \omega$. Hence, $Q^{2,\gamma}(x, \cdot)$ is a quadratic form on $\mathbb{R}^{2\times 2}_{\mathrm{sym}}$ for every $x \in \omega$. Furthermore, there are constants $0 < \alpha < \beta$ such that

$$\frac{\alpha}{12}|A|^2 \leqslant Q^{2,\gamma}(x, A) \leqslant \frac{\beta}{12}|A|^2 \tag{4.8}$$

for all $A \in \mathbb{R}^{2\times 2}_{\mathrm{sym}}$, see [HNV14].

Using the isometry constraint $\nabla\psi^\top \nabla\psi = I_2$ one can simplify the nonlinear term $D^2\psi \cdot n[\psi]$ in (4.4). A similar argument was presented in [Bar15], and adapted in [RSS22] for the case of isometric deformations of shells. In [BGNY22, Proposition 1], an analogous result for a specific energy density in the prestrained case was derived using Christoffel symbol calculus.

Proposition 4.1. *Let $\psi \in \mathcal{A}$. Then we have the identity*

$$Q^{2,\gamma}(x, D^2\psi(x) \cdot n[\psi](x)) = \sum_{m=1}^{3} Q^{2,\gamma}(x, D^2\psi_m(x))\,.$$

Proof. In the following, we write $n = n[\psi]$ for the sake of simplicity. Differentiation of $\partial_i\psi \cdot \partial_i\psi = 1$ for $i \in \{1, 2\}$ in direction $j \in \{1, 2\}$ yields $\partial_j\partial_i\psi \cdot \partial_i\psi = 0$. Similarly, differentiation of $\partial_i\psi \cdot \partial_j\psi = 0$ for $j \neq i$ in direction $i \in \{1, 2\}$ gives $\partial_i^2\psi \cdot \partial_j\psi + \partial_j\partial_i\psi \cdot \partial_i\psi = 0$. Altogether, using the fact that the parameter domain is two-dimensional, we obtain $\partial_i\partial_j\psi \cdot \partial_k\psi = 0 \quad \forall i, j, k \in \{1, 2\}$. Now, writing $\partial_i\partial_j\psi$ in terms of the orthonormal basis $\{\partial_1\psi, \partial_2\psi, n\}$, the identity $\partial_i\partial_j\psi = (\partial_i\partial_j\psi \cdot n)n + (\partial_i\partial_j\psi \cdot \partial_1\psi)\partial_1\psi + (\partial_i\partial_j\psi \cdot \partial_2\psi)\partial_2\psi = (\partial_i\partial_j\psi \cdot n)n$ holds.

For $x \in \omega$, since $Q^{2,\gamma}(x, \cdot)$ is quadratic, there exists a tensor $\mathcal{C}^{2,\gamma}(x) \in \mathbb{R}^{2\times 2\times 2\times 2}$, such that for all $A \in \mathbb{R}^{2\times 2}$

$$Q^{2,\gamma}(x, A) = \sum_{i,j,k,l=1}^{2} \mathcal{C}^{2,\gamma}_{ijkl}(x) A_{ij} A_{kl}\,.$$

Since $|n| = 1$ we can write

$$\begin{aligned} Q^{2,\gamma}(x, D^2\psi \cdot n) &= \sum_{i,j,k,l=1}^{2} \mathcal{C}^{2,\gamma}_{ijkl}(x)(\partial_i\partial_j\psi \cdot n)(\partial_k\partial_l\psi \cdot n)|n|^2 \\ &= \sum_{i,j,k,l=1}^{2} \mathcal{C}^{2,\gamma}_{ijkl}(x) \sum_{m=1}^{3} (\partial_i\partial_j\psi \cdot n)n_m(\partial_k\partial_l\psi \cdot n)n_m \\ &= \sum_{m=1}^{3} \sum_{i,j,k,l=1}^{2} \mathcal{C}^{2,\gamma}_{ijkl}(x)\partial_i\partial_j\psi_m\partial_k\partial_l\psi_m = \sum_{m=1}^{3} Q^{2,\gamma}(x, D^2\psi_m)\,. \end{aligned}$$

□

In the following, with a slight misuse of notation, we write $Q^{2,\gamma}(x, D^2\psi)$ instead of $\sum_{m=1}^{3} Q^{2,\gamma}(x, D^2\psi_m)$. Hence, the total free energy (4.4) reads as

$$E[\psi] = \begin{cases} \int_\omega Q^{2,\gamma}(x, D^2\psi(x))\,\mathrm{d}x - \int_\omega f(x)\cdot\psi(x)\,\mathrm{d}x & , \psi \in \mathcal{A}^{\mathrm{BC}}, \\ +\infty & , \text{else.} \end{cases} \tag{4.9}$$

Since $Q^{2,\gamma}(x,\cdot)$ is convex, by the lower order isometry constraint, the existence of minimizers for clamped boundary conditions induced by $\phi \in \mathcal{A}$ and force $f \in L^2(\omega;\mathbb{R}^3)$ follows by the direct method.

4.2 Discretization of the microscopic problem

In this section, we investigate the finite element approximation of the microscopic minimization problem (4.3). In what follows, we will use generic constants in the estimates. Let $\mathcal{M}_h$ be a regular hexahedral mesh partition of Y, with cells $\mathbf{c} \in \mathcal{M}_h$ and define the finite element space

$$\begin{aligned} \mathcal{V}_h := \big\{ &\vartheta_h \in C^0(Y;\mathbb{R}^3) \,:\, \vartheta_h(y) = (By', 0)^\top + \varphi_h(y)\,, \\ &B \in \mathbb{R}^{2\times 2}_{\mathrm{sym}}\,,\ \varphi_h|_{\mathbf{c}} \text{ multi-affine } \forall \mathbf{c} \in \mathcal{M}_h\,,\ \varphi_h(y)\ Y\text{-periodic in } y'\,, \int_Y \varphi_h = 0\,\mathrm{d}y\big\}. \end{aligned}$$

On every $\mathbf{c} \in \mathcal{M}_h$ we consider a numerical quadrature scheme with quadrature points $r_{\mathbf{c},i} = (r'_{\mathbf{c},i}, r_{\mathbf{c},3,i}) \in \mathbf{c}$, $i = 1 \dots k$, and weights $\nu_i > 0$, which is exact on tri-affine functions. Furthermore, we assume that the set of quadrature points $\{r_{\mathbf{c},i}\}_{i=1,\dots,k}$ is unisolvent with respect to the set of tri-affine functions in the sense of [Cia78, Section 2.3]. Actually, we consider a quadrature scheme defined on a reference cell and transferred by the tri-affine reference map to the actual cell. Then, for $A \in \mathbb{R}^{2\times 2}_{\mathrm{sym}}$, and for a macroscopic position $x \in \omega$ we make use of this quadrature and define the discrete quadratic form

$$Q^{2,\gamma}_h(x, A) := \inf_{\theta_h \in \mathcal{V}_h} \Big(\sum_{\mathbf{c}\in\mathcal{M}_h} |\mathbf{c}| \sum_{i=1}^{k} \nu_i Q^3(x, r'_{\mathbf{c},i}, \iota(r_{\mathbf{c},3,i}A) + \nabla_\gamma\theta_h(r_{\mathbf{c},i})) \Big) \tag{4.10}$$

as the discrete counterpart of (4.3). Let us remark that microscopic approximation error $Q^{2,\gamma}_h(x, A) - Q^{2,\gamma}(x, A)$ is numerically evaluated and referenced in the numerical estimates (4.24) solely at macroscopic quadrature points (cf. Section 4.3).

The above assumptions on the exactness of the quadrature scheme and the unisolvent property of the set of quadrature nodes imply that

$$\frac{\tilde{\alpha}}{12}|A|^2 \leqslant Q_h^{2,\gamma}(x,A) \leqslant \frac{\tilde{\beta}}{12}|A|^2 \tag{4.11}$$

for all $A \in \mathbb{R}^{2\times 2}_{\mathrm{sym}}$, using the strong coercivity of $Q^3(x,y',\cdot)$, with $0 < \tilde{\alpha} < \tilde{\beta}$ that depend on the reference quadrature rule, as pointed out in [BNS25].

This ensures that there exists a unique $\vartheta_h(x,A,\cdot) \in \mathcal{V}_h$ with

$$Q_h^{2,\gamma}(x,A) = \sum_{\mathbf{c}\in\mathcal{M}_h} |\mathbf{c}| \sum_{i=1}^{k} \nu_i Q^3(x, r'_{\mathbf{c},i}, \iota(r_{\mathbf{c},3,i}A) + \nabla_\gamma \vartheta_h(x, r_{\mathbf{c},i}, A))\,, \tag{4.12}$$

which solves the linear system

$$\begin{aligned}
&\sum_{\mathbf{c}\in\mathcal{M}_h} |\mathbf{c}| \sum_{i=1}^{k} \nu_i \left(\mathcal{C}^3(x, r'_{\mathbf{c},i})\nabla_\gamma \vartheta_h(x, r_{\mathbf{c},i}, A)\right) : \nabla_\gamma v_h(r_{\mathbf{c},i}) \\
&= -\sum_{\mathbf{c}\in\mathcal{M}_h} |\mathbf{c}| \sum_{i=1}^{k} \nu_i \left(\mathcal{C}^3(x, r'_{\mathbf{c},i})\iota(r_{\mathbf{c},3,i}A)\right) : \nabla_\gamma v_h(r_{\mathbf{c},i})
\end{aligned} \tag{4.13}$$

with $r_{\mathbf{c},i} = (r'_{\mathbf{c},i}, r_{\mathbf{c},3,i})$ and for all $v_h \in \mathcal{V}_h$.

The following proposition gives estimates for the finite element approximation of the microscopic problem:

Proposition 4.2. *Let $A \in \mathbb{R}^{2\times 2}_{sym}$ and $x \in \omega$ and suppose that the elasticity tensor $\mathcal{C}^3$ is bounded in $W^{1,\infty}(\omega \times Y', \mathbb{R}^{3\times 3\times 3\times 3}))$. Furthermore, we assume that the quadrature scheme is exact on the set of tri-affine functions and unisolvent with respect to this set. Then for $\vartheta(x,A,\cdot) \in \mathcal{V}$ and $\vartheta_h(x,A,\cdot) \in \mathcal{V}_h$ denoting the solutions to* (4.6) *and* (4.13)*, respectively, there exists a constant $C > 0$ depending on γ and on $\mathcal{C}^3$, such that*

$$\left\|\vartheta_h(x,A,\cdot) - \vartheta(x,A,\cdot)\right\|_{W^{1,2}(Y;\mathbb{R}^3)} \leqslant Ch|A|\,, \quad \left|Q_h^{2,\gamma}(x,A) - Q^{2,\gamma}(x,A)\right| \leqslant Ch|A|^2\,. \tag{4.14}$$

If the quadrature in the definition of $Q_h^{2,\gamma}(x,A)$ (cf. (4.10)*) is exact, i.e.*

$$\int_{\mathbf{c}} \left(\mathcal{C}^3(x,y')\nabla u_h(y)\right) : \nabla v_h(y)\,\mathrm{d}y = |\mathbf{c}| \sum_{i=1}^{k} \nu_i \left(\mathcal{C}^3(x, r'_{\mathbf{c},i})\nabla u_h(r_{\mathbf{c},i})\right) : \nabla v_h(r_{\mathbf{c},i})\,, \tag{4.15}$$

for all $u_h, v_h \in \mathcal{V}_h$ and all $x \in \omega$, then $\left|Q_h^{2,\gamma}(x,A) - Q^{2,\gamma}(x,A)\right| \leqslant Ch^2|A|^2$.

Proof. Let $A \in \mathbb{R}^{2\times 2}_{\mathrm{sym}}$ and $x \in \omega$ be arbitrary. We define the bilinear forms for the left-hand side of (4.6), (4.13), respectively,

$$\begin{aligned}
a(x,\vartheta,v) &:= \int_Y \left(\mathcal{C}^3(x,y')\nabla_\gamma \vartheta(y)\right) : \nabla_\gamma v(y)\,\mathrm{d}y\,, \\
a_h(x,\vartheta_h,v_h) &:= \sum_{\mathbf{c}\in\mathcal{M}_h} |\mathbf{c}| \sum_{i=1}^{k} \nu_i \left(\mathcal{C}^3(x, r'_{\mathbf{c},i})\nabla_\gamma \vartheta_h(r_{\mathbf{c},i})\right) : \nabla_\gamma v_h(r_{\mathbf{c},i})\,,
\end{aligned}$$

and, the linear forms for the right-hand side of (4.6), (4.13), respectively,

$$l(x,v) := \int_Y \left(\mathcal{C}^3(x,y')\iota(y_3 A)\right) : \nabla_y v(y)\,\mathrm{d}y\,,$$
$$l_h(x,v_h) := \sum_{\mathbf{c}\in\mathcal{M}_h} |\mathbf{c}| \sum_{i=1}^{k} v_i \left(\mathcal{C}^3(x,r'_{\mathbf{c},i})\iota(r_{\mathbf{c},3,i}A)\right) : \nabla_y v_h(r_{\mathbf{c},i})\,.$$

By Strang's first lemma [Cia78, Theorem 4.1.1], using the ellipticity property of $Q^3(x,\cdot)$, there exists a constant $C>0$, such that

$$\begin{aligned}
&\left\|\vartheta_h(x,A,\cdot)-\vartheta(x,A,\cdot)\right\|_{W^{1,2}(Y;\mathbb{R}^3)}\\
&\leqslant C\inf_{v_h\in\mathcal{V}_h}\left\{\left\|v_h-\vartheta(x,A,\cdot)\right\|_{W^{1,2}(Y;\mathbb{R}^3)}+\sup_{u_h\in\mathcal{V}_h}\frac{|a(x,v_h,u_h)-a_h(x,v_h,u_h)|}{\left\|u_h\right\|_{W^{1,2}(Y;\mathbb{R}^3)}}\right\}\\
&\quad + C\sup_{u_h\in\mathcal{V}_h}\frac{|l(x,u_h)-l_h(x,u_h)|}{\left\|u_h\right\|_{W^{1,2}(Y;\mathbb{R}^3)}}\,.
\end{aligned}$$

Classical elliptic regularity theory [GT83, Theorem 8.12], adapted to linearized elasticity on the domain $Y=Y'\times Y_3$ with periodic boundary conditions on $\partial Y'\times Y_3$ and Neumann boundary conditions on $Y'\times\{-\frac{1}{2},\frac{1}{2}\}$ implies $\vartheta(x,A,\cdot)\in W^{2,2}(Y;\mathbb{R}^3)$. Furthermore, by the linearity of l, one gets

$$\left\|\vartheta\right\|_{W^{2,2}(Y;\mathbb{R}^3)}\leqslant C|A|\,. \tag{4.16}$$

By the Sobolev embedding theorem the Lagrangian interpolation $\mathcal{I}_h : W^{2,2}(Y;\mathbb{R}^3)\to\mathcal{V}_h$, based on nodal interpolation, is well-defined. Making use of the regularity of $\mathcal{M}_h$ the Bramble-Hilbert-Lemma [Bra13], and (4.16) imply

$$\left\|\mathcal{I}_h[\vartheta(x,A,\cdot)]-\vartheta(x,A,\cdot)\right\|_{W^{1,2}(Y)}\leqslant Ch\left\|\vartheta(x,A,\cdot)\right\|_{W^{2,2}(Y;\mathbb{R}^3)}\leqslant Ch|A|\,. \tag{4.17}$$

Furthermore, applying the consistency error estimate in [Cia78, Theorem 4.1.4 and Theorem 4.1.5′] involving the assumption on the numerical quadrature, and (4.16) one obtains

$$\sup_{u_h\in\mathcal{V}_h}\frac{|(a-a_h)(x,\mathcal{I}_h[\vartheta(x,A,\cdot)],u_h)|}{\left\|u_h\right\|_{W^{1,2}(Y;\mathbb{R}^3)}}\leqslant Ch\left\|\vartheta(x,A,\cdot)\right\|_{W^{2,2}(Y;\mathbb{R}^3)}\leqslant Ch|A|\,, \tag{4.18}$$
$$\sup_{u_h\in\mathcal{V}_h}\frac{|(l-l_h)(x,u_h)|}{\left\|u_h\right\|_{W^{1,2}(Y;\mathbb{R}^3)}}\leqslant Ch|A|\,, \tag{4.19}$$

Using the regularity (4.16) of the microscopic solution combined with the approximation error (4.17) and the consistency errors (4.18), (4.19), the first Strang Lemma ensures the first estimate in (4.14).

With respect to the second estimate in (4.14), we get with the notation $\vartheta=\vartheta(x,A,\cdot)$ and

$\vartheta_h = \vartheta_h(x, A, \cdot)$

$$
\begin{aligned}
&\left| Q^{2,\gamma}(x,A) - Q_h^{2,\gamma}(x,A) \right| \\
&\leqslant \left| \int_Y Q^3(x, y', \iota(y_3 A) + \nabla_\gamma \vartheta(y)) - Q^3(x, y', \iota(y_3 A) + \nabla_\gamma \vartheta_h(y)) \, \mathrm{d}y \right| \\
&\quad + \left| \int_Y Q^3(x, y', \iota(y_3 A) + \nabla_\gamma \vartheta_h(y)) \, \mathrm{d}y - \sum_{\mathbf{c} \in \mathcal{M}_h} |\mathbf{c}| \sum_{i=1}^{k} \nu_i Q^3(x, r'_{\mathbf{c},i}, \iota(r_{\mathbf{c},3,i} A) + \nabla_\gamma \vartheta_h(r_{\mathbf{c},i})) \right|
\end{aligned}
$$

The first term on the right-hand side can be estimated as follows

$$
\begin{aligned}
&\left| \int_Y Q^3(x, y', \iota(y_3 A) + \nabla_\gamma \vartheta + (\nabla_\gamma \vartheta_h - \nabla_\gamma \vartheta)) - Q^3(x, y', \iota(y_3 A) + \nabla_\gamma \vartheta) \, \mathrm{d}y \right| \\
&= \left| \int_Y 2\mathcal{C}^3(x, y')(\iota(y_3 A) + \nabla_\gamma \vartheta) : (\nabla_\gamma \vartheta_h - \nabla_\gamma \vartheta) + \mathcal{C}^3(x, y')(\nabla_\gamma \vartheta_h - \nabla_\gamma \vartheta) : (\nabla_\gamma \vartheta_h - \nabla_\gamma \vartheta) \, \mathrm{d}y \right| \\
&= 0 + \left| \int_Y \mathcal{C}^3(x, y')(\nabla_\gamma \vartheta_h - \nabla \vartheta) : (\nabla_\gamma \vartheta_h - \nabla_\gamma \vartheta) \, \mathrm{d}y \right| \\
&\leqslant C \left\| \vartheta_h(x, A, \cdot) - \vartheta(x, A, \cdot) \right\|^2_{W^{1,2}(Y;\mathbb{R}^3)} \leqslant C h^2 |A|^2 .
\end{aligned}
$$

Here, the second equality follows from the Euler-Lagrange equation (4.6). Applying the general theory for quadrature errors in [Cia78] and taking into account the regularity of $\mathcal{C}^3$, the second term can be estimated by $Ch\|\mathcal{C}^3\|_{L^\infty(\omega, W^{1,\infty}(Y, \mathbb{R}^{2\times 2\times 2\times 2}))}|A|^2$, which is bounded by $Ch|A|^2$, and vanishes under the consistency assumption (4.15). This implies the claim. □

The assumption $\mathcal{C}^3 \in W^{1,\infty}(\omega \times Y'; \mathbb{R}^{2\times 2\times 2\times 2})$ is crucial for this estimate: the Lipschitz continuity in the microscopic variable y' ensures a first order error estimate with respect to the microscopic grid size h given the microscopic discretization for a given macroscopic $x \in \omega$. The Lipschitz continuity in the macroscopic variable x then implies a uniform error bound of the macroscopic approximation error, later used in the actual two-scale error estimation. These regularity assumptions match the assumptions in the literature on numerical homogenization for elliptic problems on volumetric domains, cf. [Abd05], [Abd06].

In typical engineering applications, the material parameters are frequently piecewise constant on the microscale. In this less regular case, one would lose the first order error estimate for the microscopic approximation error. This would prevent us from controlling the microscopic finite element error needed in the lim inf- estimate and in the recovery sequence estimate of our main result on Γ-convergence in Theorem 4.4.

4.3 Discretization of the macroscopic problem

In this section, we numerically approximate the energy (4.9). To this end, we will derive a non-conforming finite element discretization for the two-scale problem and the corresponding discrete isometry constraint for the macroscopic deformation.

In our case of macroscopically varying microstructures, we have to take into account the associated macroscopic quadrature error. In fact, on every $\mathbf{t} \in \mathcal{T}_H$ we use a numerical quadrature scheme with quadrature points $q_{\mathbf{t},i} \in T$, $i = 1 \dots l$ and weights $\mu_i > 0$, which

is exact on quadratic polynomials. The quadrature scheme is supposed to be defined on a reference triangle and transferred by the affine reference map to the actual triangle. Then, the associated discrete homogenized total free energy is given by

$$E_H^h[\psi_H] = \begin{cases} \sum_{\mathbf{t}\in\mathcal{T}_H} |\mathbf{t}| \sum_{i=1}^{l} \mu_i \left(Q_h^{2,\gamma}(q_{\mathbf{t},i}, \nabla\theta_H[\psi_H](q_{\mathbf{t},i})) - f(q_{\mathbf{t},i}) \cdot \psi_H(q_{\mathbf{t},i}) \right) , & \text{if } \psi_H \in \mathcal{A}_H^{\mathrm{BC}} \\ +\infty , & \text{else,} \end{cases} \tag{4.20}$$

with

$$\begin{aligned} \mathcal{A}_H^{\mathrm{BC}} = \Big\{ \psi_H \in \mathbf{W}_H^3 \,\Big|\, & \nabla\psi_H(z)^\top \nabla\psi_H(z) = I_2 \ \forall z \in \mathcal{N}_H; \\ & \psi_H(z) = \phi(z), \nabla\psi_H(z) = \nabla\phi(z) \ \forall z \in \mathcal{N}_H \cap \Gamma_D \Big\} . \end{aligned} \tag{4.21}$$

Hence, the isometry property is only enforced on the nodes of the triangulation.

To estimate the quadrature error of the macroscopic discretization, we write $Q^{2,\gamma}(x, A) = \left(\mathcal{C}^{2,\gamma}(x)A\right) : A$. Note that $\left\|\mathcal{C}^{2,\gamma}\right\|_{W^{1,\infty}} \leqslant C \left\|\mathcal{C}^3\right\|_{W^{1,\infty}}$. The following result is later used in the proof of Theorem 4.4. A similar result is also stated in [BNS25, Appendix A].

Lemma 4.3. *Let $\mathbf{t} \in \mathcal{T}_H$ and $\psi_H^h \in \mathbf{W}_H^3$. Assume that the quadrature is exact on quadratic polynomials, and $Q^{2,\gamma}(\cdot, A) \in W^{1,\infty}$ for all A. Then it holds*

$$\begin{aligned} & \left| |\mathbf{t}| \sum_{i=1}^{l} \mu_i Q^{2,\gamma}(q_{\mathbf{t},i}, \nabla\theta_H[\psi_H^h](q_{\mathbf{t},i})) - \int_{\mathbf{t}} Q^{2,\gamma}(x, \nabla\theta_H[\psi_H^h](x)) \,\mathrm{d}x \right| \\ \leqslant & C H \left\|\mathcal{C}^{2,\gamma}\right\|_{W^{1,\infty}(\mathbf{t})} \left\|\nabla\theta_H[\psi_H^h]\right\|_{L^2(\mathbf{t})}^2 . \end{aligned}$$

Proof. For simplicity we write $\mathbf{p} := \nabla\theta_H[\psi_H^h] \in \mathcal{P}_1(\mathbf{t})$. For an element $\mathbf{t} \in \mathcal{T}_H$ and a function $\vartheta : \mathbf{t} \to \mathbb{R}$ we write

$$E_{\mathbf{t}}[\vartheta] := |\mathbf{t}| \sum_{i=1}^{l} \mu_i \vartheta(q_{\mathbf{t},i}) - \int_{\mathbf{t}} \vartheta(x) \,\mathrm{d}x$$

for the quadrature error. We pull back everything onto the reference element $\hat{\mathbf{t}}$, and infer

$$E_{\mathbf{t}}[\vartheta] = \det(B_{\mathbf{t}}) \hat{E}[\hat{\vartheta}] ,$$

where $\hat{E}[\cdot]$ is the quadrature error on the reference element, and $\mathbf{t} = B_{\mathbf{t}}\hat{\mathbf{t}} + b_{\mathbf{t}}$. From now on, every quantity with a hat denotes the pullback of the quantity onto the reference element. Here, we follow Ciarlet's book [Cia78, Chapter 4]. Hence, $\vartheta(x) = \hat{\vartheta}(\hat{x})$. Note that $\hat{\mathbf{p}} = \widehat{(\nabla\theta_H[\psi_H^h])} \neq \nabla\widehat{(\theta_H[\psi_H^h])}$.

We want to estimate

$$E_{\mathbf{t}}\left[\left(\mathcal{C}^{2,\gamma}\mathbf{p}\right) : \mathbf{p}\right] = |\mathbf{t}| \sum_{i=1}^{l} \mu_i \left(\mathcal{C}^{2,\gamma}(q_{\mathbf{t},i})\mathbf{p}(q_{\mathbf{t},i})\right) : \mathbf{p}(q_{\mathbf{t},i}) - \int_{\mathbf{t}} \left(\mathcal{C}^{2,\gamma}(x)\mathbf{p}(x)\right) : \mathbf{p}(x) \,\mathrm{d}x .$$

First note that

$$\hat{\mathcal{C}}^{2,\gamma} \mapsto \hat{E}\left[\left(\hat{\mathcal{C}}^{2,\gamma}\hat{\mathbf{p}}\right) : \hat{\mathbf{p}}\right] = |\hat{\mathbf{t}}| \sum_{i=1}^{l} \mu_i \left(\hat{\mathcal{C}}^{2,\gamma}(\hat{q}_{\hat{\mathbf{t}},i})\hat{\mathbf{p}}(\hat{q}_{\hat{\mathbf{t}},i})\right) : \hat{\mathbf{p}}(\hat{q}_{\hat{\mathbf{t}},i}) - \int_{\hat{\mathbf{t}}} \left(\hat{\mathcal{C}}^{2,\gamma}(\hat{x})\hat{\mathbf{p}}(\hat{x})\right) : \hat{\mathbf{p}}(\hat{x}) \,\mathrm{d}\hat{x}$$

is a linear map $W^{1,\infty}(\hat{\mathbf{t}}) \to \mathbb{R}$.

Now we estimate

$$\begin{aligned}\left|\hat{E}\left[\left(\hat{\mathcal{C}}^{2,\gamma}\hat{\mathbf{p}}\right):\hat{\mathbf{p}}\right]\right| &\leqslant \left\|\hat{\mathcal{C}}^{2,\gamma}\right\|_{L^\infty(\hat{\mathbf{t}})}\left(|\hat{\mathbf{t}}|\sum_{i=1}^{l}|\mu_i||\hat{\mathbf{p}}(\hat{q}_{\hat{\mathbf{t}},i})|^2+\int_{\hat{\mathbf{t}}}|\hat{\mathbf{p}}(\hat{x})|^2\,\mathrm{d}\hat{x}\right)\\ &\leqslant C\left\|\hat{\mathcal{C}}^{2,\gamma}\right\|_{L^\infty(\hat{\mathbf{t}})}\left\|\hat{\mathbf{p}}\right\|^2_{L^2(\hat{\mathbf{t}})}\leqslant C\left\|\hat{\mathcal{C}}^{2,\gamma}\right\|_{W^{1,\infty}(\hat{\mathbf{t}})}\left\|\hat{\mathbf{p}}\right\|^2_{L^2(\hat{\mathbf{t}})},\end{aligned}$$

where $C>0$ is a generic constant. Here, in the first inequality we applied the triangle inequality, and in the second inequality we used that $\hat{\mathbf{p}}\mapsto\sqrt{|\hat{\mathbf{t}}|\sum_{i=1}^{l}|\mu_i||\hat{\mathbf{p}}(\hat{q}_{\hat{\mathbf{t}},i})|^2}$ defines a norm on the finite dimensional space $\mathcal{P}_1(\hat{\mathbf{t}})$, which is equivalent to the norm $\hat{\mathbf{p}}\mapsto\left\|\hat{\mathbf{p}}\right\|_{L^2(\hat{\mathbf{t}})}$. Hence, the map $\hat{\mathcal{C}}^{2,\gamma}\mapsto\hat{E}\left[\left(\hat{\mathcal{C}}^{2,\gamma}\hat{\mathbf{p}}\right):\hat{\mathbf{p}}\right]$ has an operator norm $\leqslant C\left\|\hat{\mathbf{p}}\right\|^2_{L^2(\hat{\mathbf{t}})}$ on the space $W^{1,\infty}(\mathbf{t})$.

By assumption, $\hat{E}\left[\left(\hat{\mathcal{C}}^{2,\gamma}\hat{\mathbf{p}}\right):\hat{\mathbf{p}}\right]$ vanishes for $\hat{\mathcal{C}}^{2,\gamma}\in\mathcal{P}_0(\hat{\mathbf{t}})$, since the quadrature is exact for quadratic polynomials, and $\hat{\mathbf{p}}\in\mathcal{P}_1(\hat{\mathbf{t}})$.

Using the Bramble-Hilbert Lemma with $k=0$ and $p=\infty$, it holds

$$\hat{E}\left[\left(\hat{\mathcal{C}}^{2,\gamma}\hat{\mathbf{p}}\right):\hat{\mathbf{p}}\right]\leqslant C\left|\hat{\mathcal{C}}^{2,\gamma}\right|_{1,\infty,\hat{\mathbf{t}}}\left\|\hat{\mathbf{p}}\right\|^2_{L^2(\hat{\mathbf{t}})}.$$

Transforming back to the element $\mathbf{t}$, from [Cia78] we get the estimates

$$\left\|\hat{\mathbf{p}}\right\|_{L^2(\hat{\mathbf{t}})}\leqslant C(\det(B_{\mathbf{t}}))^{-\frac{1}{2}}\left\|\mathbf{p}\right\|_{L^2(\mathbf{t})},\qquad \left|\hat{\mathcal{C}}^{2,\gamma}\right|_{1,\infty,\hat{\mathbf{t}}}\leqslant CH\left|\mathcal{C}^{2,\gamma}\right|_{1,\infty,\mathbf{t}}\leqslant CH\left\|\mathcal{C}^{2,\gamma}\right\|_{W^{1,\infty}(\mathbf{t})}.$$

Putting everything together yields

$$\begin{aligned}&\left||\mathbf{t}|\sum_{i=1}^{l}\mu_i Q^{2,\gamma}(q_{\mathbf{t},i},\nabla\theta_H[\psi_H^h](q_{\mathbf{t},i}))-\int_{\mathbf{t}}Q^{2,\gamma}(x,\nabla\theta_H[\psi_H^h](x))\,\mathrm{d}x\right|\\ =&E_{\mathbf{t}}\left[\left(\mathcal{C}^{2,\gamma}\mathbf{p}\right):\mathbf{p}\right]=\det(B_{\mathbf{t}})\hat{E}\left[\left(\hat{\mathcal{C}}^{2,\gamma}\hat{\mathbf{p}}\right):\hat{\mathbf{p}}\right]\\ \leqslant&C\det(B_{\mathbf{t}})\left|\hat{\mathcal{C}}^{2,\gamma}\right|_{1,\infty,\hat{\mathbf{t}}}\left\|\hat{\mathbf{p}}\right\|^2_{L^2(\hat{\mathbf{t}})}\\ \leqslant&CH\det(B_{\mathbf{t}})\left\|\mathcal{C}^{2,\gamma}\right\|_{W^{1,\infty}(\mathbf{t})}(\det(B_{\mathbf{t}}))^{-1}\left\|\mathbf{p}\right\|^2_{L^2(\mathbf{t})}=CH\left\|\mathcal{C}^{2,\gamma}\right\|_{W^{1,\infty}(\mathbf{t})}\left\|\nabla\theta_H[\psi_H^h]\right\|^2_{L^2(\mathbf{t})}\end{aligned}$$

□

We now state the main convergence result.

Theorem 4.4. *Assume $(\mathcal{T}_H)_H$ is a family of regular triangulation of ω with grid size $H\to 0$, the microscopic quadrature rule is exact on the set of tri-affine functions and unisolvent with respect to this set, the macroscopic quadrature rule is exact on quadratic polynomials, $f\in W^{1,p}(\omega,\mathbb{R}^3)$, with $p>2$, and $\mathcal{C}^3\in W^{1,\infty}(\omega\times Y,\mathbb{R}^{3\times3\times3\times3})$. Then, for every macroscopic grid size H and every microscopic grid size $h>0$, there exists a minimizer ψ_H^h of the discrete homogenized total free energy $E_H^h[\cdot]$ (cf. (4.20)) in $\mathcal{A}_H^{BC}$. For any sequence $(\psi_H^h)_{H,h}$ of such minimizers with $H,\ h\to 0$ there is a subsequence, such that with out reindexing $\psi_H^h\to\psi$ strongly in $W^{1,2}(\omega;\mathbb{R}^3)$. Furthermore, $\psi\in\mathcal{A}^{BC}$ is a minimizer of the continuous total free genergy $E[\cdot]$ as defined in (4.9).*

Proof. The proof combines Γ-convergence arguments related to those used in [Bar13] and the paradigm of the heterogeneous multiscale method as it is discussed in [EMZ05].

From the boundedness of $Q_h^{2,\gamma}$ stated in (4.11), the clamped boundary conditions, the Poincaré inequality, and the assumption on the macroscopic quadrature scheme, we deduce that there exist constants $C,\ c>0$ such that $E_H^h[\psi_H^h] \geqslant c \left\|\nabla \theta_H[\psi_H^h]\right\|_{L^2(\omega)}^2 - C$.

Since $\left\|\nabla \theta_H[\cdot]\right\|_{L^2(\omega)}$ is a norm on $\{w_H \in \mathbf{W}_H |\ w_H(z)=0,\ \nabla w_H(z)=0\ \forall z \in \mathcal{N}_H \cap \Gamma_D\}$, for every $H, h>0$ there exists a minimizer ψ_H^h for the discrete minimization problem and using (2.22) we have that $\left\|\nabla \theta_H[\psi_H^h]\right\|_{L^2(\omega)} + \left\|\nabla \psi_H^h\right\|_{L^2(\omega)} \leqslant C$. Thus, there exists a subsequence (not relabeled), and $\psi \in W^{1,2}(\omega;\mathbb{R}^3)$, $z \in W^{1,2}(\omega;\mathbb{R}^{3\times 2})$, such that $\psi_H^h \rightharpoonup \psi$ in $W^{1,2}(\omega;\mathbb{R}^3)$ and $\theta_H[\psi_H^h] \rightharpoonup z$ in $W^{1,2}(\omega;\mathbb{R}^{3\times 2})$. Using the estimate (2.23) and summing over all $T \in \mathcal{T}_H$, we get $\left\|\nabla \psi_H^h - \theta_H[\psi_H^h]\right\|_{L^2(\omega)} \leqslant cH \left\|\nabla \theta_H[\psi_H^h]\right\|_{L^2(\omega)}$, hence $\nabla \psi_H^h \to \nabla \psi = z$ strongly in L^2. This yields $\psi \in W^{2,2}(\omega;\mathbb{R}^3)$. As in [Bar13], the attainment of the boundary conditions and the isometry constraint is straightforward. Hence, ψ is admissible. Next, we investigate the convergence of the discrete force term.

$$\left| \sum_{\mathrm{t}\in\mathcal{T}_H} |\mathrm{t}| \sum_{i=1}^{l} \mu_i f(q_{\mathrm{t},i}) \cdot \psi_H^h(q_{\mathrm{t},i}) - \int_\omega f \cdot \psi_H^h \,\mathrm{d}x \right| \leqslant CH \left\|f\right\|_{W^{1,p}(\omega)} \left\|\psi_H^h\right\|_{W^{1,2}(\omega)} \tag{4.22}$$

follows from the approximation properties of the quadrature rule, the regularity of f, and the estimate for the corresponding force term quadrature error in [Cia78, Theorem 4.1.5, Theorem 4.1.6 and the corresponding estimate in its proof]. By the boundedness of ψ_H^h in $W^{1,2}(\omega;\mathbb{R}^3)$ the right hand side vanishes for $H \to 0$. Furthermore, by Lemma 4.3, we obtain

$$\left| |\mathrm{t}| \sum_{i=1}^{l} \mu_i Q^{2,\gamma}(q_{\mathrm{t},i}, \nabla \theta_H[\psi_H^h](q_{\mathrm{t},i})) - \int_{\mathrm{t}} Q^{2,\gamma}(x, \nabla \theta_H[\psi_H^h]) \,\mathrm{d}x \right| \leqslant CH \left\|\nabla \theta_H[\psi_H^h]\right\|_{L^2(\mathrm{t})}^2 , \tag{4.23}$$

since $Q^{2,\gamma}(\cdot, A)$ arising from the microscopic problem is in $W^{1,\infty}(\omega)$ and quadratic in $A \in \mathbb{R}^{2\times 2}_{\mathrm{sym}}$, and $\nabla \theta[\psi_H^h]$ is affine on every $\mathrm{t} \in \mathcal{T}_H$. In particular, the constant on the right-hand side depends on the $W^{1,\infty}(\omega \times Y)$-norm of the microscopic elasticity tensor $\mathcal{C}^3$.

Next, we estimate

$$\begin{aligned}
&\sum_{\mathrm{t}\in\mathcal{T}_H} |\mathrm{t}| \sum_{i=1}^{l} \mu_i Q_h^{2,\gamma}(q_{\mathrm{t},i}, \nabla \theta_H[\psi_H^h](q_{\mathrm{t},i})) = \sum_{\mathrm{t}\in\mathcal{T}_H} |\mathrm{t}| \sum_{i=1}^{l} \mu_i Q^{2,\gamma}(q_{\mathrm{t},i}, \nabla \theta_H[\psi_H^h](q_{\mathrm{t},i})) \\
&\qquad + \sum_{\mathrm{t}\in\mathcal{T}_H} |\mathrm{t}| \sum_{i=1}^{l} \mu_i \left(Q_h^{2,\gamma}(q_{\mathrm{t},i}, \nabla \theta_H[\psi_H^h](q_{\mathrm{t},i})) - Q^{2,\gamma}(q_{\mathrm{t},i}, \nabla \theta_H[\psi_H^h](q_{\mathrm{t},i})) \right) \\
&\geqslant \sum_{\mathrm{t}\in\mathcal{T}_H} |\mathrm{t}| \sum_{i=1}^{l} \mu_i Q^{2,\gamma}(q_{\mathrm{t},i}, \nabla \theta_H[\psi_H^h](q_{\mathrm{t},i})) - Ch \sum_{\mathrm{t}\in\mathcal{T}_H} |\mathrm{t}| \sum_{i=1}^{l} \mu_i |\nabla \theta_H[\psi_H^h](q_{\mathrm{t},i})|^2 \\
&= \int_\omega Q^{2,\gamma}(x, \nabla \theta_H[\psi_H^h]) \,\mathrm{d}x - Ch \left\|\nabla \theta_H[\psi_H^h]\right\|_{L^2(\omega)}^2 \\
&\quad - \sum_{\mathrm{t}\in\mathcal{T}_H} \left(|\mathrm{t}| \sum_{i=1}^{l} \mu_i Q^{2,\gamma}(q_{\mathrm{t},i}, \nabla \theta_H[\psi_H^h](q_{\mathrm{t},i})) - \int_{\mathrm{t}} Q^{2,\gamma}(x, \nabla \theta_H[\psi_H^h]) \,\mathrm{d}x \right) \\
&\geqslant \int_\omega Q^{2,\gamma}(x, \nabla \theta_H[\psi_H^h]) \,\mathrm{d}x - C(h+H) \left\|\nabla \theta_H[\psi_H^h]\right\|_{L^2(\omega)}^2 .
\end{aligned} \tag{4.24}$$

Here, in the first inequality, we used the error estimate (4.14). Furthermore, we used the fact that $|\nabla\theta_H[\psi_H^h]|^2$ is a quadratic polynomial and thus can be integrated exactly by the macroscopic quadrature scheme. The second inequality is an application of (4.23). Since $\nabla\theta_H[\psi_H^h]$ converges weakly to $D^2\psi$ in $L^2(\omega,\mathbb{R}^{3\times2\times2})$ and $(x,A)\mapsto Q^{2,\gamma}(x,A)$ is Lipschitz continuous in x, and convex and quadratic in A, we deduce by weak lower semicontinuity that $E[\psi]\leqslant\liminf_{H,h\to0}E_H^h[\psi_H^h]$.

Regarding a recovery sequence, let $\psi^*\in\mathcal{A}$ be a minimizer of $E[\cdot]$, in particular $\psi^*\in W^{2,2}(\omega;\mathbb{R}^3)$. To make use of the estimate (2.24), $W^{3,2}$-regularity is required. On sets with smooth boundary, isometric immersions satisfy this regularity, cf. [MP05], but for polygonal boundary this is no longer the case. Hence, a density result together with a diagonal sequence argument would suffice to get convergence. Standard mollification of ψ^* is not suitable, since it violates the isometry constraint. However, Hornung showed in [Hor11, Theorem 1] that for $\rho>0$ there exists $\psi^\rho\in W^{3,2}(\omega;\mathbb{R}^3)\cap\mathcal{A}$ such that $\left\|\psi^*-\psi^\rho\right\|_{W^{2,2}}<\rho$. A version of this density result was first proved by Pakzad for isometric immersions $\psi\colon\omega\to\mathbb{R}^3$ of convex sets $\omega\subset\mathbb{R}^2$ in [Pak04, Theorem I]. See Section 2.3 for more information on isometric immersions.

Let $\psi_H^\rho\in\mathbf{W}_H^3$ be the DKT-interpolant of ψ^ρ. The same construction of a recovery sequence for DKT was already used in [Bar13, BBN17, RSS22]. Then we can estimate

$$
\begin{aligned}
&\sum_{\mathbf{t}\in\mathcal{T}_H}|\mathbf{t}|\sum_{i=1}^{l}\mu_i Q_h^{2,\gamma}(q_{\mathbf{t},i},\nabla\theta_H[\psi_H^\rho](q_{\mathbf{t},i}))\\
&=\sum_{\mathbf{t}\in\mathcal{T}_H}|\mathbf{t}|\sum_{i=1}^{l}\mu_i Q^{2,\gamma}(q_{\mathbf{t},i},\nabla\theta_H[\psi_H^\rho](q_{\mathbf{t},i}))\\
&\quad+\sum_{\mathbf{t}\in\mathcal{T}_H}|\mathbf{t}|\sum_{i=1}^{l}\mu_i\left(Q_h^{2,\gamma}(q_{\mathbf{t},i},\nabla\theta_H[\psi_H^\rho](q_{\mathbf{t},i}))-Q^{2,\gamma}(q_{\mathbf{t},i},\nabla\theta_H[\psi_H^\rho](q_{\mathbf{t},i}))\right)\\
&\leqslant\sum_{\mathbf{t}\in\mathcal{T}_H}|\mathbf{t}|\sum_{i=1}^{l}\mu_i Q^{2,\gamma}(q_{\mathbf{t},i},\nabla\theta_H[\psi_H^\rho](q_{\mathbf{t},i}))+Ch\sum_{\mathbf{t}\in\mathcal{T}_H}|\mathbf{t}|\sum_{i=1}^{l}\mu_i|\nabla\theta_H[\psi_H^h](q_{\mathbf{t},i})|^2\\
&=\int_\omega Q^{2,\gamma}(x,\nabla\theta_H[\psi_H^\rho])\,\mathrm{d}x+Ch\left\|\nabla\theta_H[\psi_H^\rho]\right\|_{L^2(\omega)}^2\\
&\quad+\sum_{\mathbf{t}\in\mathcal{T}_H}\left(|\mathbf{t}|\sum_{i=1}^{l}\mu_i Q^{2,\gamma}(q_{\mathbf{t},i},\nabla\theta_H[\psi_H^\rho](q_{\mathbf{t},i}))-\int_{\mathbf{t}}Q^{2,\gamma}(x,\nabla\theta_H[\psi_H^\rho])\,\mathrm{d}x\right)\\
&\leqslant\int_\omega Q^{2,\gamma}(x,\nabla\theta_H[\psi_H^\rho])\,\mathrm{d}x+C(H+h)\left\|\nabla\theta_H[\psi_H^\rho]\right\|_{L^2(\omega)}^2,
\end{aligned}
$$

where we again used the microscopic error estimate (4.14), and the quadrature error estimate (4.23) for the DKT element. With this, we can further estimate

$$
\begin{aligned}
&\int_\omega Q^{2,\gamma}(x,\nabla\theta_H[\psi_H^\rho])\,\mathrm{d}x+C(H+h)\left\|\nabla\theta_H[\psi_H^\rho]\right\|_{L^2(\omega)}^2\\
&\leqslant\int_\omega Q^{2,\gamma}(x,D^2\psi^\rho)+\mathcal{C}^{2,\gamma}\left(D^2\psi^\rho+\nabla\theta_H[\psi_H^\rho]\right):\left(D^2\psi^\rho-\nabla\theta_H[\psi_H^\rho]\right)\mathrm{d}x\\
&\quad+C(H+h)\left\|\nabla\theta_H[\psi_H^\rho]\right\|_{L^2(\omega)}^2
\end{aligned}
$$

$$
\begin{aligned}
&\leqslant \int_\omega Q^{2,\gamma}(x, D^2\psi^\rho)\,\mathrm{d}x + C\left\|D^2\psi^\rho + \nabla\theta_H[\psi_H^\rho]\right\|_{L^2(\omega)}\left\|D^2\psi^\rho - \nabla\theta_H[\psi_H^\rho]\right\|_{L^2(\omega)} \\
&\quad + C(H+h)\left(\left\|\psi^\rho\right\|_{W^{2,2}(\omega)}^2 + H^2\left\|\psi^\rho\right\|_{W^{3,2}(\omega)}^2\right) \\
&\leqslant \int_\omega Q^{2,\gamma}(x, D^2\psi^*)\,\mathrm{d}x + C\left\|D^2\psi^* + D^2\psi^\rho\right\|_{L^2(\omega)}\left\|D^2\psi^* - D^2\psi^\rho\right\|_{L^2(\omega)} \\
&\quad + CH\left\|\psi^\rho\right\|_{W^{3,2}(\omega)}\left(\left\|\psi^\rho\right\|_{W^{2,2}(\omega)} + H\left\|\psi^\rho\right\|_{W^{3,2}(\omega)}\right) \\
&\quad + C(H+h)\left(\left\|\psi^\rho\right\|_{W^{2,2}(\omega)}^2 + H^2\left\|\psi^\rho\right\|_{W^{3,2}(\omega)}^2\right) \\
&\leqslant \int_\omega Q^{2,\gamma}(x, D^2\psi^*)\,\mathrm{d}x + C(1+\rho)\rho + CH\left\|\psi^\rho\right\|_{W^{3,2}(\omega)}\left(1 + \rho + H\left\|\psi^\rho\right\|_{W^{3,2}(\omega)}\right) \\
&\quad + C(H+h)\left((1+\rho)^2 + H^2\left\|\psi^\rho\right\|_{W^{3,2}(\omega)}^2\right).
\end{aligned}
$$

Here, we used the estimate

$$
\left\|\nabla\theta_H[\psi_H^\rho]\right\|_{L^2(\omega)} \leqslant \left\|D^2\psi^\rho\right\|_{L^2(\omega)} + \left\|\nabla\theta_H[\psi_H^\rho] - D^2\psi^\rho\right\|_{L^2(\omega)} \leqslant \left\|\psi^\rho\right\|_{W^{2,2}(\omega)} + H\left\|\psi^\rho\right\|_{W^{3,2}(\omega)}
$$

as a consequence of (2.24), and the estimate $\left\|\psi^* - \psi^\rho\right\|_{W^{2,2}} < \rho$. For the force term, we get, using the estimate for the linear form quadrature error in [Cia78, Theorem 4.1.5],

$$
\begin{aligned}
\sum_{\mathrm{t}\in\mathcal{T}_H}|\mathrm{t}|\sum_{i=1}^{l}\mu_i f(q_{\mathrm{t},i})\cdot\psi_H^\rho(q_{\mathrm{t},i}) &\leqslant \int_\omega f\cdot\psi^*\,\mathrm{d}x + \int_\omega f\cdot(\psi_H^\rho - \psi^*)\,\mathrm{d}x \\
&\quad + \left(\sum_{\mathrm{t}\in\mathcal{T}_H}|\mathrm{t}|\sum_{i=1}^{l}\mu_i f(q_{\mathrm{t},i})\cdot\psi_H^\rho(q_{\mathrm{t},i}) - \int_\omega f\cdot\psi_H^\rho\,\mathrm{d}x\right) \\
&\leqslant \int_\omega f\cdot\psi^*\,\mathrm{d}x + \left\|f\right\|_{L^2(\omega)}\left(\left\|\psi_H^\rho - \psi^\rho\right\|_{L^2(\omega)} + \left\|\psi^\rho - \psi^*\right\|_{L^2(\omega)}\right) \\
&\quad + CH\left\|f\right\|_{W^{1,p}(\omega)}\left\|\psi_H^\rho\right\|_{W^{1,2}(\omega)} \\
&\leqslant \int_\omega f\cdot\psi^*\,\mathrm{d}x + C\left(H^3\left\|\psi^\rho\right\|_{W^{3,2}(\omega)} + \rho\right) + CH(H^2+1)\left\|\psi^\rho\right\|_{W^{3,2}(\omega)}
\end{aligned}
$$

Finally, we choose $h = h(\rho)$ and $H = H(\rho)$ such that

$$
h(\rho) + H(\rho) + (h(\rho)+1)\left(H(\rho) + H(\rho)^3\right)\left(\left\|\psi^\rho\right\|_{W^{3,2}(\omega)} + \left\|\psi^\rho\right\|_{W^{3,2}(\omega)}^2\right) < \rho \tag{4.25}
$$

and obtain

$$
E[\psi^*] \geqslant \limsup_{\rho\to 0} E_{H(\rho)}^{h(\rho)}[\psi_{H(\rho)}^\rho] \geqslant \liminf_{\rho\to 0} E_{H(\rho)}^{h(\rho)}[\psi_{H(\rho)}^{h(\rho)}] \geqslant E[\psi]\,.
$$

Hence, ψ is a minimizer of $E[\cdot]$. □

Remark 4.5. *The convergence of the recovery sequence is crucially controlled by the approximation parameter ρ via the appearance of the norm $\left\|\psi^\rho\right\|_{W^{3,2}(\omega)}$. The choice of $h = h(\rho)$ and $H = H(\rho)$ in* (4.25) *is implicit and thus does not provide a rate of convergence. This disadvantage is shared with similar results in [Bar13] and [BBN17] and is caused by the nonlinearity of the problem, more precisely, the nonlinear isometry constraint.*

Remark 4.6. *Note that the regularity assumption on the force $f \in W^{1,p}(\omega;\mathbb{R}^3)$ with $p > 2$ is necessary to control the force term integration error. To this end, as outlined in the proof, one uses [Cia78, Theorem 4.1.5 and Theorem 4.1.6]. This assumption is not a peculiarity of the homogenized plate model. In fact, it would also be necessary for the numerical analysis of a finite element approximation of a homogeneous plate model as in [Bar13] with a general right-hand side.*

4.4 Numerical experiments

Following the paradigm of the heterogeneous multiscale method (HMM), the actual macroscopic plate deformation is computed using the DKT discretization described in Section 4.3 and minimizing the discrete energy E_H^h defined in (4.20). To this end, for each macroscopic quadrature the function $Q_h^{2,\gamma}(A)$ has to be computed for a basis of the space of symmetric 2×2 matrices A, which requires the solution of the micrscopic optimization problem (4.10).

In explicit terms, the microscopic problem results in solving the linear system (4.12) for x in the set of all macroscopic quadrature points $q_{\mathrm{t},i}$ and for

$$A \in \left\{ \begin{pmatrix} 1 & 0 \\ 0 & 0 \end{pmatrix}, \begin{pmatrix} 0 & 0 \\ 0 & 1 \end{pmatrix}, \begin{pmatrix} 0 & 1 \\ 1 & 0 \end{pmatrix} \right\}, \tag{4.26}$$

which represents a three-dimensional, linearized elasticity corrector problem rescaled to the unit cube $Y = [0,1]^2 \times [-\frac{1}{2},\frac{1}{2}] \subset \mathbb{R}^3$. As described in Section 4.2, continuous, piecewise 3-affine finite elements are considered on the unit cube discretized by a uniform hexahedral mesh $\mathcal{M}_h$ with h denoting the maximal edge length. For the assembly of the stiffness matrix and the right-hand side, we apply a tensor product Gauss quadrature rule, with 27 quadrature points per cell. Hence, the quadrature is exact on tensor products of quintic functions, and thus fulfills the consistency condition to be exact on and unisolvent with respect to tri-affine functions. This is sufficient to ensure a first-order convergence under the assumption that the solution of the linearized elasticity problem is in $W^{2,2}$ on Y [Cia78, Chapter 4.1.] . In fact, the strong consistency condition (4.15) holds if the entries of the elasticity tensor $\mathcal{C}^3_{jikl}$ are assumed to be tensor products of cubic functions.

On the macroscale, we consider a uniform triangulation of ω with grid size H and ask for a minimizing deformation ψ^H of $E_H^h[\cdot]$ under the nonlinear, discrete isometry constraint $\nabla\psi_H(z)^\top \nabla\psi_H(z) = I_2$ for all $z \in \mathcal{N}_H$ (cf. (4.21)). To compute the discrete energy $E_H^h[\psi_H]$ for $\psi_H \in \mathbf{W}^3_H$ a simplicial Gauss quadrature with 12 quadrature points on each triangle is used, which is exact on polynomials of order 6. Hence, if the components of the tensor representing the quadratic form $Q^{2,\gamma}(x,\cdot)$ as a function of x are quartic polynomials the integration of the energy $\mathcal{W}^\gamma$ defined in (4.2) is exact.

The macroscopic problem consists of minimizing the energy $E_H^h[\cdot]$ over all discrete isometries $\phi_H \in \mathcal{A}_H^{\mathrm{BC}}$. To deal with the isometry constraint, we take into account the Lagrangian

$$L_H^h[\psi_H, p_H] := E_H^h[\psi_H] - \int_\omega \mathcal{I}_H \left[\left(\nabla\psi_H^\top \nabla\psi_H - I_2 \right) : p_H \right] \mathrm{d}x \,. \tag{4.27}$$

with a Lagrangian multiplier $p_H \in \mathcal{S}_H^{2\times 2}$, where $\mathcal{S}_H^{2\times 2}$ is the space of continuous piecewise affine, symmetric 2×2-matrices. Let us remark that the quadrature scheme applied to the stored elastic energy is exact on the second term of the Lagrangian multiplying the constraint and

the multiplier. As in [RSS22], cf. Chapter 3, we use the IPOPT software library presented in [WB06] to compute a saddle point of this Lagrangian using a Newton scheme with backtracking. This requires evaluating first and second variations of the discrete energy and the constraint. In IPOPT, we used the default backtracking strategy by setting "filter" for "line_search_method". The (relative) stopping tolerance "tol" was set to 10^{-12}. We always used a small perturbation of the identity with L^∞ norm 0.001 as the initial deformation in the Newton scheme. Note that an application of Newton's scheme requires the invertibility of the Hessian of the Lagrangian. Although there is no theoretical guarantee, in our experiments, the solvability of the associated linear system was always observed.

In this section, we numerically verify the established convergence results, discuss the qualitative properties of the homogenized plate model, and compare it with bending experiments for paper with different fine-scale structures. We always consider a square-shaped plate, described by $\omega = (0,1)^2$.

We take into account a material distribution function v on a rescaled microscopic cell $Y \times I$ with Lamé constants $\lambda(y)$ and $\mu(y)$ given by

$$\lambda(y) = (r + (1-r)v(y))\lambda\,, \quad \mu(y) = (r + (1-r)v(y))\mu\,.$$

where $\lambda = \frac{5}{3}, \mu = \frac{5}{2}$, and $r = \frac{1}{50}$ is the ratio between soft and hard material. This corresponds to Young's modulus $E = 6$ and Poisson ratio $\nu = 0.2$ on the hard phase.

The triangulations on ω are generated by uniform, regular (so-called red) refinement, starting from a single, coarse rectangular mesh subdivided into two triangles. The plate deformations are caused by a constant force f and/or prescribed boundary conditions.

Experimentally observed convergence behaviour. To examine the convergence rates, we consider a homogenized bending energy with a constant microstructure given by the continuous, piecewise affine material distribution function

$$v(y) = \begin{cases} 2y_1\,, & \text{if } y_1 \leqslant \frac{1}{2} \\ -2y_1 + 2\,, & \text{if } y_1 > \frac{1}{2} \end{cases} \tag{4.28}$$

on the unit cell and a size-of-microstructure-to-thickness ratio of $\gamma = 1$. We take into account two different load scenarios: (a) clamped boundary conditions

$$\psi(x) = (x_1 \pm \tfrac{3}{16}, x_2, 0)^\top, \quad \nabla\psi(x) = \begin{pmatrix} I_2 \\ 0\ 0 \end{pmatrix} \tag{4.29}$$

on $(0,1) \times \{\frac{1}{2} \mp \frac{1}{2}\}$ and zero load, (b) a uniform vertical load $f = (0,0,5)^\top$, and clamped boundary conditions

$$\psi(x) = \begin{pmatrix} x \\ \pm 0 \end{pmatrix}, \quad \nabla\psi(x) = \begin{pmatrix} I_2 \\ 0\ 0 \end{pmatrix}$$

on $(0,1) \times \{0\}$. For experiments (a) and (b), the resulting deformations are shown in Table 4.1 on the right. Note that in experiment (a), for different random initial data, either a buckled-up, or a buckled-down deformation can be observed, as displayed. In the same table, we evaluate the impact of the microscopic grid size h on the approximation of the effective tensor $\mathcal{C}^{2,\gamma}$. Since the minimizer of the continuous problem is unknown, we compare it with the discrete

solution on the finest mesh ($h^* = \frac{1}{128}$) and list $|\mathcal{C}_h^{2,\gamma} - \mathcal{C}_{h^*}^{2,\gamma}|_\infty$ for decreasing h. In addition, the L^2-norm of the difference of the discrete Hessians $\left\|\nabla\theta_{H^*}[\psi_{H^*}^h] - \nabla\theta_{H^*}[\psi_{H^*}^{h^*}]\right\|_{L^2}$ is given for a macroscopic grid size $H^* = \frac{\sqrt{2}}{256}$. In both cases, we experimentally observe a quadratic convergence rate.

h	$\lvert\mathcal{C}_h^{2,\gamma} - \mathcal{C}_{h^*}^{2,\gamma}\rvert_\infty$	$\left\|\nabla\theta_{H^*}[\psi_{H^*}^h] - \nabla\theta_{H^*}[\psi_{H^*}^{h^*}]\right\|_{L^2}$		Deformations	
		(a)	(b)	(a)	(b)
2^{-3}	0.004265	0.005098	0.0947412	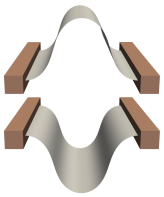	
2^{-4}	0.001021	0.001259	0.0235653		
2^{-5}	0.000243	0.000311	0.00566203		
2^{-6}	4.8e-05	6.4e-05	0.00112114		
2^{-7}	-	-	-		

Table 4.1: Evaluation of the experimental convergence of the homogenized tensor $\mathcal{C}_h^{2,\gamma}$ and the discrete Hessian for fixed macroscopic grid size $H^* = \frac{\sqrt{2}}{256}$ and decreasing microscopic grid size h.

Next, in Table 4.2 we investigate the convergence behavior for the load configurations (a) and (b) in the case of a simultaneous decrease of the microscopic and macroscopic grid size h and H, respectively. The minimal discrete energy $E_H^h[\psi_H^h(H)]$ and the L^2-norm of the difference of the discrete Hessians $\left\|\nabla\theta_H[\psi_H^h] - \nabla\theta_{H^*}[\psi_{H^*}^{h^*}]\right\|_{L^2}$ are shown for $H^* = \frac{\sqrt{2}}{256}$ and $h^* = 2H^*$. Here, one observes a linear convergence rate.

$\frac{1}{\sqrt{2}}H$	h	$E_H^h[\psi_H^h]$		$\left\|\nabla\theta_H[\psi_H^h] - \nabla\theta_{H^*}[\psi_{H^*}^{h^*}]\right\|_{L^2}$	
		(a)	(b)	(a)	(b)
2^{-4}	2^{-3}	1.7228944	-1.6769788	1.17653	0.428218
2^{-5}	2^{-4}	1.676654	-1.6963124	0.586753	0.208557
2^{-6}	2^{-5}	1.6688657	-1.7005727	0.284853	0.10684
2^{-7}	2^{-6}	1.6666743	-1.7015843	0.138362	0.0528297
2^{-8}	2^{-7}	1.6664753	-1.7017899	-	-

Table 4.2: Evaluation of the experimental convergence of the energy and the Hessian of the macroscopic deformation for simultaneous decreasing macroscopic and microscopic grid size H and h, respectively.

Furthermore, we investigate the dependence of $Q^{2,\gamma}$ on the ratio $\gamma = \frac{\delta}{\varepsilon}$ of the thickness δ and the size of the microstructure ε for the same microscopic material distribution (4.28) as before. Using the known symmetries of $\mathcal{C}^{2,\gamma}$ one can consider with a slight misuse of notation $\mathcal{C}^{2,\gamma,\nu} \in \mathbb{R}^{3\times 3}$ following the Voigt notation for elasticity tensors with

$$Q^{2,\gamma}(A) = \left(\mathcal{C}^{2,\gamma,\nu}\begin{pmatrix} A_{11} \\ A_{22} \\ A_{12}+A_{21} \end{pmatrix}\right) \cdot \begin{pmatrix} A_{11} \\ A_{22} \\ A_{12}+A_{21} \end{pmatrix}.$$

Due to the symmetry of the material distribution, we get that $\mathcal{C}^{2,\gamma,\nu}_{13} = \mathcal{C}^{2,\gamma,\nu}_{23} = 0$. For $\gamma_i = 10^{(-1+\frac{2i}{31})}$, $i = 0, \dots, 31$, we computed $\mathcal{C}^{2,\gamma_i,\nu}$ on the unit cube with gridsize $h^* = \frac{1}{128}$. The values of the different components of $\mathcal{C}^{2,\gamma,\nu}$ are plotted in Figure 4.2 with γ on the x-axis plotted with logarithmic scaling.

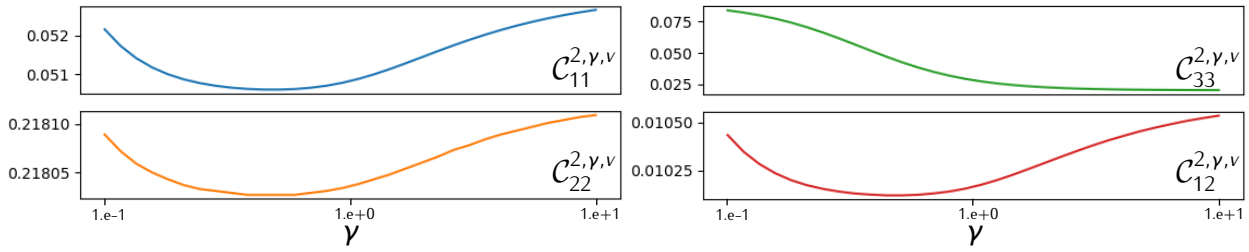

Figure 4.2: Plots of the different components of the homogenized tensor $\mathcal{C}^{2,\gamma}$ for varying γ.

From now on, we consider microstructures that only consist of a hard and a soft phase with piecewise constant $v : Y \to [0,1] \to \{0,1\}$. Such microstructures do not fulfill the assumptions of our convergence theory. Still, they are closer to real applications, and we indeed compare our numerical findings with physical experiments for the bending of fine-scale structured paper. Paper and paperboard are known to deform only isometrically. Note that paper behaves, in contrast to the model we are simulating here, in a non-isotropic way, depending on the direction of manufacturing. In [YN07], in-plane orthotropic constants for paper and paperboard were experimentally derived. Nevertheless, for simplicity, we assume in our experiments an isotropic model with Lamé constants $\mu = \frac{5}{3}$, $\lambda = \frac{5}{2}$ inspired by the constants derived in [YN07]. Note that the theory provided in this work is not limited to isotropic material laws, since Proposition 4.2 is formulated for a more general elastic tensor $\mathcal{C}^3$.

As proof of concept, we carried out experiments with glued layers of paper. In explicit, a thick paperboard (300g/m^2) with cut out fine-scale structures was glued on a sheet of paper (120g/m^2). The cutting of the 300g/m^2 layer of thick paper was performed with a Cricut©Maker. Regions with glued paper layers are considered the hard phase, whereas the complement is considered the soft phase. Given the fact that the thickness of the paper layers is much smaller than the scale on which the pattern is approximately periodic a model approximation with a homogeneous thick thin plate with vertically constant hard and soft material properties appears to be feasible.

Calibration of the layered, glued paper model. Given the thickness of two paper types, one is at first led to a material property ratio of $r = \frac{120}{420} \approx 0.286$. But, due to the layer of glue in between the glued paper layers of the hard phase, one observes a proportionally much higher stiffness as examined in Figure 4.3. To compensate for this, we quantitatively compared the bending in the experiment (b) of a single 120g/m^2 sheet and the homogeneous compound of glued 300g/m^2 and 120g/m^2 paper, which gave rise to the effective material ratio of $r = \frac{1}{50}$. We used this ratio in the following experiments.

Microstructure with axes aligned stripes. We consider a material distribution with $\gamma = 0.1$ that corresponds to a periodic pattern of stripes of alternating hard and soft material aligned with the coordinate directions. On the rescaled microscopic cell $Y \times I$ this corresponds to hard material in the volumes $[\frac{1}{4}, \frac{3}{4}] \times [0,1] \times [-\frac{1}{2}, \frac{1}{2}]$, and soft material elsewhere. We also take into account the same configuration rotated by 90 degrees in the Y plane. The constant

Figure 4.3: Top row: numerically computed deformed configurations of a plate, clamped on the left side, under a uniform vertical load, with homogeneous material, with Lamé constants scaled with 1.0 (left), 0.286 (middle), and 0.02 (right). Bottom row: photos of physical deformations of paper. Left: thick paper (300g/m^2) glued on thinner paper (120g/m^2). Middle: only thin paper (120g/m^2).

homogenized tensors $\mathcal{C}^{2,\nu}$ were computed for a uniformly hexagonal mesh on the unit cube with grid size $h = \frac{1}{128}$. The resulting tensors $\mathcal{C}^{2,\nu}_{||}$ and $\mathcal{C}^{2,\nu}_{=}$, respectively, written as matrices in Voigt type notation, corresponding to the basis (4.26) are

$$\mathcal{C}^{2,\nu,\nu}_{||} = \begin{pmatrix} 0.04265 & 0.00853 & 0 \\ 0.00853 & 0.5149 & 0 \\ 0 & 0 & 0.05099 \end{pmatrix}, \quad \mathcal{C}^{2,\nu,\nu}_{=} = \begin{pmatrix} 0.5149 & 0.00853 & 0 \\ 0.00853 & 0.04265 & 0 \\ 0 & 0 & 0.05099 \end{pmatrix}.$$

The plate is clamped on $[0, \frac{1}{5}] \times [\frac{2}{5}, \frac{3}{5}]$ and a uniform force $f = (0, 0, -5)^\top$ is taken into account. The resulting deformations are shown in Figure 4.4. One observes that the microscopic pattern leads to very stiff behavior of the plate in the direction of the stripes and a very flexible behavior in the perpendicular direction. We compare it with a corresponding paper experiment. To this end, a sheet of paper (green, 120g/m^2) of size $28cm \times 28$cm is used, with stripes of thick paper (red, 300g/m^2) of width 4mm glued on top, with a stripe distance of 4mm. The resulting layered paper is clamped between two pieces of wood (cf. Figure 4.4).

Microstructure reflecting radially arranged stripes. Under the force and boundary conditions of the above experiment, we next consider a microstructure that mimics radially arranged rays of hard material centered at the midpoint $(0, 0.5)$ of the left-hand side of the plate. The width of the stripes is proportional to the distance from the center.

First, we consider a stripe pattern similar to the one considered above, with hard material on $(0, 1) \times (\frac{1}{3}, \frac{2}{3}) \times (-\frac{1}{2}, \frac{1}{2})$ and soft material elsewhere, where the ratio of the hard material $\frac{1}{3}$ equals the ratio of the angle of a single hard material stripe and the angle of a single soft material stripe in the radially arranged strip pattern in the corresponding experiment. For a point $x \in \omega$ with $x - (0, 0.5) = (r \cos \alpha, r \sin \alpha)$ for $\alpha \in (0, \pi)$ and $r \in \mathbb{R}_+$, we consider

$\gamma = ar + b$, for $a, b \in \mathbb{R}$, such that $1 = \frac{1}{5}a + b$ and $\frac{1}{10} = \frac{\sqrt{5}}{2}a + b$. This models the widening of the strips while maintaining the thickness of the plate. Let us denote the resulting homogenized tensor by $\widehat{\mathcal{C}}^{2,\gamma}$.

Then, applying the coordinate transformation formula [AGDP19, Section 3.4] the resulting homogenized tensor $\mathcal{C}^{2,\gamma}(x)$ reflecting the radially arranged stripe pattern at $x \in \omega$ is given by

$$\mathcal{C}^{2,\gamma}(x)A : A := \widehat{\mathcal{C}}^{2,\gamma}A_\alpha : A_\alpha \text{ with } A_\alpha := \begin{pmatrix} \cos\alpha & \sin\alpha \\ -\sin\alpha & \cos\alpha \end{pmatrix} A \begin{pmatrix} \cos\alpha & -\sin\alpha \\ \sin\alpha & \cos\alpha \end{pmatrix}$$

for all $A \in \mathbb{R}^{2\times 2}_{\mathrm{sym}}$.

In Figure 4.4 in the top right, the resulting deformation is shown. Below, on a $28cm \times 28$cm sheet of paper (purple, 120g/m^2), we take into account 16 glued-on stripes of thicker paper (yellow, 300g/m^2), radially symmetric, broadening with the distance from the clamped center part of the paper. The opening angle of the hard material (yellow) is 3.75°, and the opening angle of the soft material (purple) is 7.5° with the width of the hard material stripes ranging from 1mm to 1.2cm.

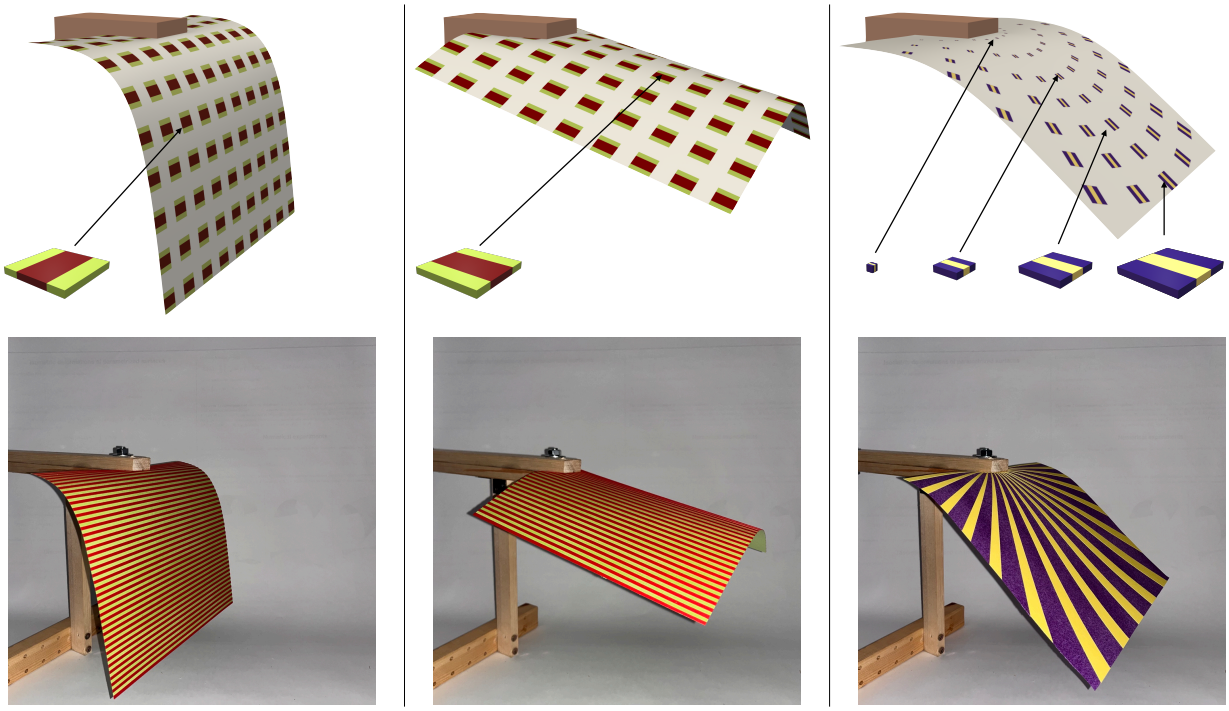

Figure 4.4: Top row: deformed configurations under a uniform vertical load for stripe-type microstructures (left and middle) and a microstructure with radial rays (right). Bottom row: photos of physical experiments with stripes of thicker paper (300g/m^2, left and middle: red, right: yellow) glued on thinner paper (120g/m^2, left and middle: green, right: purple).

Microstructure with periodic diagonal aligned stripe pattern. Now, we consider a constantly distributed microstructure consisting of layers of hard and soft material oriented diagonally in the first two coordinates. The hard material phase is given by all $y = (y', y_3)$ with

$$\left| y' - \begin{pmatrix} 1 \\ 0 \end{pmatrix} \right|_1 \in (\tfrac{1}{4}, \tfrac{3}{4}) \cap (\tfrac{5}{4}, \tfrac{7}{4})$$

where $|\cdot|_1$ is the 1-norm in $\mathbb{R}^2$. The resulting homogenized tensor in Voigt-type notation is

$$\mathcal{C}^{2,\gamma,\nu} = \begin{pmatrix} 0.17883 & 0.10699 & 0.11725 \\ 0.10699 & 0.17883 & 0.11725 \\ 0.11725 & 0.11725 & 0.13436 \end{pmatrix}.$$

The deformation was enforced by the boundary conditions (4.29) reflecting a compression in the x_1 direction by a factor $\frac{3}{8}$. No surface load applies. Again, a small random initial deformation is considered. The computed deformation is shown in Figure 4.5 on the top left. The qualitative behavior is compared with a sheet of paper (blue, 120g/m^2) of size $28cm \times 28$cm, where stripes of thick paper (orange, 300g/m^2) of width 5mm were glued on, with a distance of 5mm, in the direction of one diagonal of the sheet of paper. A photo of this experiment is shown in Figure 4.5 on the left of the bottom row. Due to the anisotropic microscopic material distribution, the macroscopic elastic energy is also anisotropic, leading both in the simulation and the experiment to a firm twist of the resulting valley formed by the bent plate.

Microstructure with axes aligned and diagonal trusses of hard material. In this experiment, we take into account a macroscopically varying microstructure with trusses of hard material on a soft material background. In the rescaled model with vertically homogeneous material on $(0,1)^2 \times (-\frac{1}{2}, \frac{1}{2})$ the hard material phase is given by

$$\begin{aligned}\big\{y \ : 1 - \tfrac{b}{\sqrt{2}}|y' - (1,0)^\top|_1 < 1 + \tfrac{b}{\sqrt{2}} \vee 1 - \tfrac{b}{\sqrt{2}}|y'|_1 < 1 + \tfrac{b}{\sqrt{2}} \vee \\ y_1 < \tfrac{a}{2} \vee y_1 > 1 - \tfrac{a}{2} \vee y_2 < \tfrac{a}{2} \vee y_2 > 1 - \tfrac{a}{2}\big\}\end{aligned}$$

with thicknesses $a(x_1) = (1 - x_1)\frac{2-\sqrt{3}}{2}$, $b(x_1) = x_1\frac{2-\sqrt{3}}{2}$ of the axes aligned and diagonal trusses, respectively. The prototype of the fundamental cell and the resulting fine-scale pattern with cell size $\varepsilon = \frac{1}{16}$ in y' coordinates is depicted in Figure 4.5 on the right. On the macroscale, the boundary conditions (4.29) and load are applied. Furthermore, for the paper experiment counterpart, the truss structure with 14^2 $2cm \times 2$cm cells of thick paper (300g/m^2) is glued on a $28cm \times 28$cm sheet of thin paper (120g/m^2). A comparison of the simulated deformation for the homogenized model and the experiment is shown as well in Figure 4.5. It is clearly visible that the bent plate is no longer symmetric in the x_1 direction and the bending is much stronger on the right.

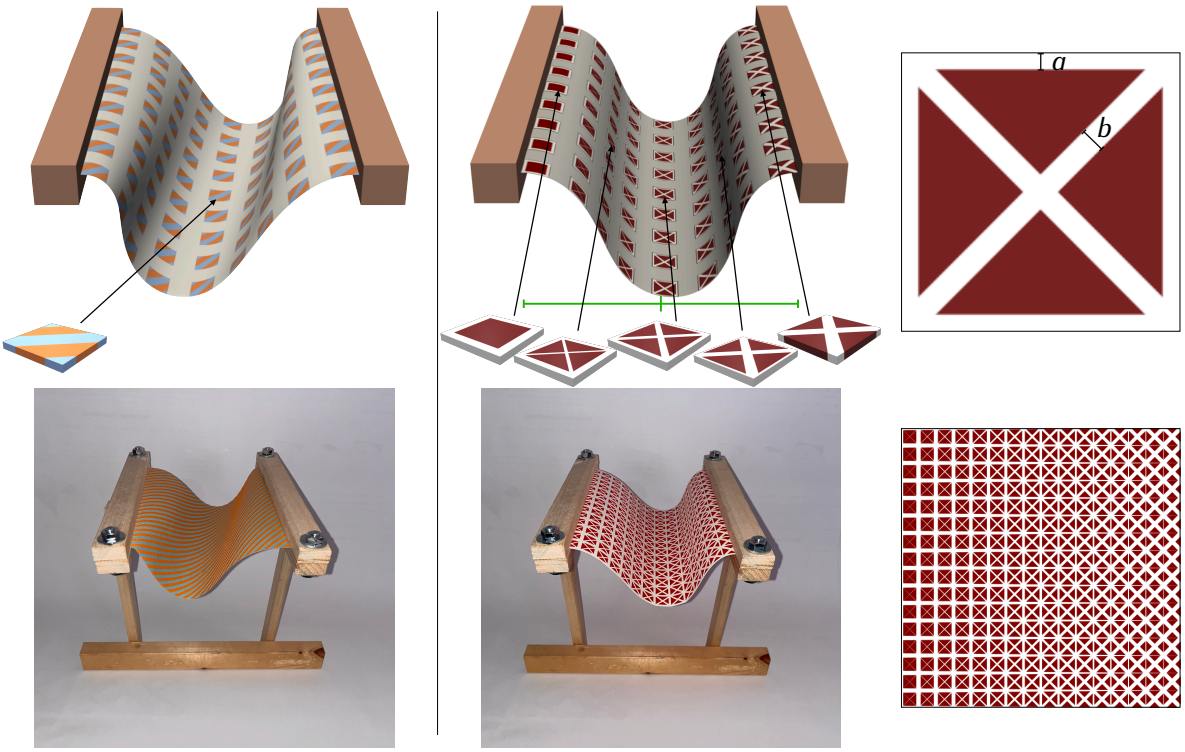

Figure 4.5: Top left: deformed configuration under compression enforced by the boundary conditions (4.29) with soft material in blue and hard material in orange, bottom left: corresponding experiment with stripes of thicker paper (300g/m^2, orange) glued on thin paper (120g/m^{2}blue); top middle: deformed configuration for a truss type microstructure under the same boundary conditions, with soft material in red and hard material in white, top right material distribution on the rescaled microscopic cell, bottom middle: a correspondingly deformed sheet of paper (red) with glued layer structure of the thicker paper (white), bottom right: undeformed experimental plate configuration viewed from above.

Chapter 5

Phase Field Approximation of a Nonlinear Folding Model

This chapter studies a phase field model for the elastic bending deformation of thin plates with folds. A nonlinear elastic energy is introduced, based on the diffuse phase field approximation of given fold curves. A Γ-convergence result as the phase field parameter $\varepsilon \to 0$ is presented, resulting in a sharp interface limit of a bending energy with folds introduced in [BBH22]. A finite element discretization of the phase field elastic energy with folds is proposed, and numerical experiments are provided, showing deformations similar to physical experiments with folded sheets of paper. Additionally, a framework for the optimization of folds for cost functionals is introduced. Numerical experiments show the practicability of this optimization framework.

Collaboration. This chapter is the result of joint work with Sergio Conti and Martin Rumpf that was incorporated into the successful proposal for research area B2 of the collaborative research center 1720 "Analysis of Criticality".

The work presented in this chapter deals with the analytical and numerical approximation of the nonlinear bending of thin elastic plates that additionally inherit fold structures. Additionally, the optimization of such folds for a given target cost functional is taken into account. As we saw in Section 2.3, $W^{2,2}$-regular isometric deformations of two-dimensional objects (the mid-surface of a thin plate) embedded into $\mathbb{R}^3$ behave very rigidly, cf. Theorem 2.19. This changes drastically if the thin plate is allowed to be folded: A flat sheet of paper can be folded into the shape of a swan, but deforming the sheet into this shape by only bending it smoothly is not possible.

From a mechanical point of view, folds can be characterized as thin regions, where the thin plate is damaged, and hence the cost for bending is reduced significantly. In Section 2.2, the derivation of a dimension-reduced nonlinear bending model for thin plates with a single fold by Bartels et al. [BBH22] was presented. There, in addition to certain regularity assumptions on the fold curve, they assumed that the material of the thin plate with thickness $\delta > 0$ is weakened significantly (of the order δ^2, for example) in an area of size δ around the fold Σ. The nonlinear bending model derived there reads

$$\mathcal{W}^{\Sigma}[\psi] := \begin{cases} \frac{1}{2}\int_{\omega\setminus\Sigma} |D^2\psi|^2 \,\mathrm{d}x & , \text{ if } \nabla\psi^\top\nabla\psi = I_2 \text{ a.e.} \\ \infty & , \text{ else.} \end{cases} \tag{5.1}$$

In this chapter, we study a diffuse approximation of the nonlinear bending energy (5.1), where the fold curve $\Sigma \subset \omega$ is represented by a phase field function $v_\varepsilon \in W^{1,2}(\omega)$ with a small parameter $\varepsilon > 0$, which is converging to the constant function $v_0 \equiv 1$ strongly in $L^2(\omega)$ as $\varepsilon \to 0$, but is close to zero in a small neighborhood around Σ. The nonlinear energy we consider is

$$\mathcal{W}^\varepsilon[\psi] := \frac{1}{2}\int_\omega (v_\varepsilon(x)^2 + \eta_\varepsilon)|D^2\psi(x)|^2 \,\mathrm{d}x + \frac{\alpha}{\varepsilon}\int_\omega \left|\nabla\psi(x)^\top\nabla\psi(x) - I_2\right|^2 \,\mathrm{d}x\,. \tag{5.2}$$

This functional takes as input functions $\psi \in W^{2,2}(\omega;\mathbb{R}^3)$, in contrast to the functional (5.1) that is defined on functions $\psi \in W^{2,2}(\omega\backslash\Sigma;\mathbb{R}^3) \cap W^{1,2}(\omega;\mathbb{R}^3)$, and hence can be interpreted as a smooth approximation. Here, $\eta_\varepsilon > 0$ is a small parameter that makes minimization of (5.2) well-posed, and $\alpha > 0$ is a positive constant. The isometry constraint in (5.1) is replaced in (5.2) by the penalty term $\frac{\alpha}{\varepsilon}\int_\omega \left|\nabla\psi^\top\nabla\psi - I_2\right|^2 \,\mathrm{d}x$ to allow more flexibility of the deformation around the fold curve.

Related work. In [CM08] it was shown that *origami-maps*, i.e., piecewise flat isometric deformations with folds, can approximate any given shape. This means that an enthusiastic paper plane builder could, in theory, build any tiny airplane there is from a single sheet of paper. Of course, in practice, this is too optimistic, since every sheet of paper has a certain thickness, and hence is not a two-dimensional object. The interested reader may try to fold a sheet of paper more than seven times to see that thickness indeed plays a significant role.

The flexibility of isometric deformations with folds allows for using them as a design tool, especially when folds along curved creases are considered. In [KFC+08], two-dimensional surfaces with curved folds have been explored using a discretization based on quad meshes, where the folds are given as grid line segments. Spline representations of developable surfaces are used in [TBWP16] to design curved-creased origami structures. Pleated structures generated by folding paper along curved creases are investigated in [JMR+19]. Since origami structures possess interesting mechanical properties, such as reconfigurability, the simulation of curved origami with deformable panels from a structural engineering point of view is presented in [LP17], based on discrete membrane and bending energies.

Interesting phenomena occur when microscopic folding patterns influence the geometry of the effective macroscopic deformation. In [CZ18], the deformation of flat sheets with microstructure origami patterns into curved three-dimensional surfaces is presented, together with physical experiments. A method for the inverse design of periodic origami structures to approximate a given curved surface is proposed in [DFP+22]. In [LJ24], microscopic curved folding patterns and the overall stored elastic energy are investigated.

In [BBH22], a discretization of (5.1) based on the discontinuous Galerkin (dG) method was introduced. This discretization involves penalty terms for the jump of the function and the gradient along edges of the triangulation. The fold curve is given as a piecewise polynomial chain of edges and thus is encoded in the grid of the discretization. Along all edges that are part of the fold curve, the jump of the gradient of the discrete deformation is not penalized. Bonito et al. [BGM23] studied a dG approximation of a nonlinear fold model with a bending and a stretching energy. In [BBT23], error estimates of a dG method with an isoparametric approach for a linear fold model were established. Here, the isoparametric approach is used to more accurately approximate a curved crease line. In [BST25], the numerical approximation of a Föppl–von Kármán model with folds was studied. The approximation of bending and stretching deformations of thin structures with folding was examined in [BGM24]. The problems

of piecewise affine approximations of a curved crease line involving Babuska's paradox were recently investigated in [BBHN25], and a possible solution was proposed by only enforcing continuity of the deformation at the nodes that belong to the fold curve.

Outline. The rest of this chapter is structured as follows: in Section 5.1, Γ-convergence of (5.2) to (5.1) is established for the case where v_ε is a diffuse representation of a given set of fold curves Σ that satisfies certain regularity properties. The main result is stated in Theorem 5.4. In Section 5.2, a discretization of (5.2) based on the discrete Kirchhoff triangle (DKT), cf. Section 2.4, is presented, and numerical experiments minimizing this discrete energy are displayed. Finally, in Section 5.3, the optimization of fold curves is addressed. Phase field methods have proven to be a powerful tool in elastic shape optimization, cf. [PRW12, MRS21]. Applying this framework to the optimization of fold curves, the minimization of the elastic energy (5.2) serves as a PDE constraint, and the diffuse approximation function v_ε representing the fold curves is the variable for minimizing a certain cost functional together with a regularizer of Ambrosio-Tortorelli type, cf. [AT92].

5.1 Sharp interface limit of the diffuse fold energy

In the following, let $\omega \subset \mathbb{R}^2$ be a bounded Lipschitz domain, representing the mid-surface of a thin elastic plate. Let $\Sigma \subset \omega$ be the set of given fold curves on ω, which is assumed to satisfy $\mathcal{H}^1(\Sigma) < \infty$. Let $\eta_\varepsilon > 0$ be a sequence satisfying $\frac{\eta_\varepsilon}{\varepsilon} \to 0$ as $\varepsilon \to 0$.

Definition 5.1. *Let $\Sigma \subset \mathbb{R}^2$. For $\delta > 0$ we define*

$$\Sigma_\delta := \left\{ x \in \mathbb{R}^d \,:\, \operatorname{dist}(x,\Sigma) := \inf_{y\in\Sigma} |x-y| < \delta \right\}.$$

We denote by $|\Sigma_\delta|$ the d-dimensional Lebesgue measure of Σ_δ.

The phase field function $v_\varepsilon \in L^\infty(\omega)$ representing Σ should satisfy the following assumptions.

Assumption 5.2. *Let $(b_\varepsilon)_{\varepsilon>0}$ be a sequence with $\frac{b_\varepsilon}{\varepsilon} \to 0$ and $\frac{\eta_\varepsilon}{b_\varepsilon} \to 0$ as $\varepsilon \to 0$. We assume that $v_\varepsilon \colon \omega \to \mathbb{R}$ is a function satisfying*

$$0 \leqslant v_\varepsilon \leqslant \sqrt{1-\eta_\varepsilon}\,, \tag{5.3}$$

$$\exists c > 0 \text{ such that } v_\varepsilon \leqslant c\sqrt{\eta_\varepsilon} \text{ in } \Sigma_{b_\varepsilon}\,, \tag{5.4}$$

$$\exists (d_\varepsilon)_{\varepsilon>0} \text{ with } d_\varepsilon > b_\varepsilon,\ d_\varepsilon \to 0 \text{ such that } v_\varepsilon = \sqrt{1-\eta_\varepsilon} \text{ on } \omega\backslash\Sigma_{d_\varepsilon}\,. \tag{5.5}$$

Remark 5.3. *The recovery sequence for the phase field in the construction of the* lim sup*-inequality in the Γ-convergence proof in [AT92] satisfies the above assumptions, with*

$$v_\varepsilon(x) = \begin{cases} 0 \quad , & \text{in } \Sigma_{b_\varepsilon} \\ 1-\exp\left(\frac{b_\varepsilon - \operatorname{dist}(x,\Sigma)}{2\varepsilon}\right) \quad , & \text{in } \Sigma_{a_\varepsilon+b_\varepsilon}\backslash\Sigma_{b_\varepsilon} \\ \sqrt{1-\eta_\varepsilon} \quad , & \text{in } \omega\backslash\Sigma_{a_\varepsilon+b_\varepsilon}\,, \end{cases} \tag{5.6}$$

with $a_\varepsilon = -2\varepsilon\log(1-\sqrt{1-\eta_\varepsilon})$, and $d_\varepsilon = a_\varepsilon + b_\varepsilon$. In Figure 5.1, for a given fold curve Σ, such a phase field is displayed.

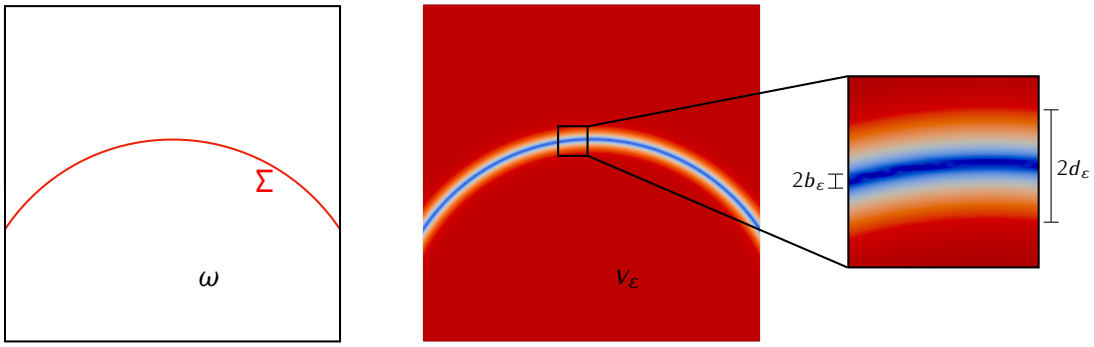

Figure 5.1: Left: Domain ω with fold curve Σ. Right: Phase field representation v_ε of Σ. The red color corresponds to values close to 1, whereas blue is for values close to 0.

We now state the main theorem of this chapter, showing that the diffuse fold energy (5.2) Γ-converges to the sharp fold energy (5.1) in the strong $W^{1,2}$-topology, under some regularity assumptions on the fold curves Σ.

Theorem 5.4. *Let $\Sigma \subset \omega$ with $\frac{|\Sigma_\delta|}{2\delta} \to \mathcal{H}^1(\Sigma) < \infty$ as $\delta \to 0$. Let $v_\varepsilon : \omega \to \mathbb{R}$ fulfill Assumption 5.2. Then, the functionals $(\mathcal{W}^\varepsilon[\cdot])_{\varepsilon>0}$, defined in* (5.2)*, Γ-converges in the strong $W^{1,2}$-topology to $\mathcal{W}^\Sigma[\cdot]$, defined in* (5.1)*, that is*

(i) For every sequence $(\psi_\varepsilon)_{\varepsilon>0} \subset W^{2,2}(\omega;\mathbb{R}^3)$ with $\sup_{\varepsilon>0}\mathcal{W}^\varepsilon[\psi_\varepsilon] < \infty$, there exists $\psi \in W^{1,\infty}(\omega;\mathbb{R}^3) \cap W^{2,2}(\omega\backslash\Sigma;\mathbb{R}^3)$ such that $\psi_\varepsilon - \frac{1}{|\omega|}\int_\omega \psi_\varepsilon \,\mathrm{d}x \to \psi$ strongly in $W^{1,2}(\omega;\mathbb{R}^3)$ for a subsequence, and

$$\liminf_{\varepsilon\to 0} \mathcal{W}^\varepsilon[\psi_\varepsilon] \geqslant \mathcal{W}^\Sigma[\psi]\,. \tag{5.7}$$

(ii) For every $\psi \in W^{1,\infty}(\omega;\mathbb{R}^3)\cap W^{2,2}(\omega\backslash\Sigma;\mathbb{R}^3)$ there exists a sequence $(\psi_\varepsilon)_{\varepsilon>0} \subset W^{2,2}(\omega;\mathbb{R}^3)$ with $\psi_\varepsilon \to \psi$ strongly in $W^{1,2}(\omega;\mathbb{R}^3)$, and

$$\limsup_{\varepsilon\to 0} \mathcal{W}^\varepsilon[\psi_\varepsilon] \leqslant \mathcal{W}^\Sigma[\psi]\,. \tag{5.8}$$

Proof. $\liminf$**-inequality** *(i).* Let $(\psi_\varepsilon)_{\varepsilon>0} \subset W^{2,2}(\omega;\mathbb{R}^3)$. Without loss of generality, we assume

$$\int_\omega \psi_\varepsilon \,\mathrm{d}x = 0 \qquad \text{for all } \varepsilon > 0\,, \tag{5.9}$$

and $\sup_{\varepsilon>0}\mathcal{W}^\varepsilon[\psi_\varepsilon] \leqslant C < \infty$, for a generic constant C. In particular,

$$\int_\omega \left|\nabla\psi_\varepsilon^\top\nabla\psi_\varepsilon - I_2\right|^2 \,\mathrm{d}x \leqslant C\varepsilon\,, \tag{5.10}$$

hence $\nabla\psi_\varepsilon^\top\nabla\psi_\varepsilon \to I_2$ strongly in $L^2(\omega;\mathbb{R}^{2\times 2})$, and thus also in $L^1(\omega;\mathbb{R}^{2\times 2})$, since ω is bounded. From this it also follows that $\nabla\psi_\varepsilon$ is bounded in $L^2(\omega;\mathbb{R}^3)$, hence, by Poincaré's inequality, using (5.9), and the reflexivity of $W^{1,2}(\omega;\mathbb{R}^3)$, there exists $\psi \in W^{1,2}(\omega;\mathbb{R}^3)$ with $\psi_\varepsilon \rightharpoonup \psi$ weakly in $W^{1,2}(\omega;\mathbb{R}^3)$ for a subsequence (not relabeled).

Let now $R > 0$, and Σ_R as in Definition 5.1. Since $\mathcal{W}^\varepsilon[\psi_\varepsilon]$ is uniformly bounded, and because of the assumption (5.5) on v_ε, there exists $\varepsilon_0 = \varepsilon_0(R)$ such that for all $\varepsilon < \varepsilon_0$ we have

$$\mathcal{W}^\varepsilon[\psi_\varepsilon] \geqslant \int_{\omega\setminus\Sigma_{d_\varepsilon}} |D^2\psi_\varepsilon|^2 \,\mathrm{d}x \geqslant \int_{\omega\setminus\Sigma_R} |D^2\psi_\varepsilon|^2 \,\mathrm{d}x\,. \tag{5.11}$$

Poincaré's inequality, together with the estimate

$$\left\|\nabla\psi_\varepsilon\right\|^2_{L^2(\omega;\mathbb{R}^{3\times 2})} + \left\|D^2\psi_\varepsilon\right\|^2_{L^2(\omega\setminus\Sigma_R;\mathbb{R}^{3\times 2\times 2})} \leqslant C\,,$$

derived by (5.11), leads to the boundedness of $(\psi_\varepsilon)_{\varepsilon>0}$ in $W^{2,2}(\omega\setminus\Sigma_R;\mathbb{R}^3)$. By reflexivity, there hence exists $\psi_R \in W^{2,2}(\omega\setminus\Sigma_R;\mathbb{R}^3)$, such that, up to another subsequence, $\psi_\varepsilon \rightharpoonup \psi_R$ weakly in $W^{2,2}(\omega\setminus\Sigma_R;\mathbb{R}^3)$, and $\psi_\varepsilon \to \psi_R$ strongly in $W^{1,2}(\omega\setminus\Sigma_R;\mathbb{R}^3)$. Since $\omega\setminus\Sigma_R \subset \omega$, it holds $\psi_R = \psi$ in $\omega\setminus\Sigma_R$, so $\psi \in W^{2,2}(\omega\setminus\Sigma_R;\mathbb{R}^3)$, and $\nabla\psi_\varepsilon \to \nabla\psi$ pointwise a.e. in $\omega\setminus\Sigma_R$. By the weak lower semicontinuity of the norm, using (5.11), it thus holds

$$\liminf_{\varepsilon\to 0} \mathcal{W}^\varepsilon[\psi_\varepsilon] \geqslant \liminf_{\varepsilon\to 0} \int_{\omega\setminus\Sigma_R} |D^2\psi_\varepsilon|^2 \,\mathrm{d}x = \int_{\omega\setminus\Sigma_R} |D^2\psi|^2 \,\mathrm{d}x\,.$$

Since $R > 0$ was chosen arbitrarily, by the pointwise convergence of $\nabla\psi_\varepsilon$, together with the estimate (5.10), ¸we have $\nabla\psi^\top\nabla\psi = I_2$ almost everywhere in $\omega\setminus\Sigma$, and thus also almost everywhere in ω. With this, we finally get the lim inf-inequality

$$\liminf_{\varepsilon\to 0} \mathcal{W}^\varepsilon[\psi_\varepsilon] \geqslant \sup_{R>0} \int_{\omega\setminus\Sigma_R} |D^2\psi|^2 \,\mathrm{d}x = \int_{\omega\setminus\Sigma} |D^2\psi|^2 \,\mathrm{d}x = \mathcal{W}^\Sigma[\psi]\,.$$

lim sup-**inequality** *(ii)*. Let now $\psi \in W^{1,\infty}(\omega;\mathbb{R}^3) \cap W^{2,2}(\omega\setminus\Sigma;\mathbb{R}^3)$. We now focus on the construction of the recovery sequence $(\psi_\varepsilon)_{\varepsilon>0}$. Without loss of generality, we can assume that $\mathcal{W}^\Sigma[\psi] < \infty$, hence

$$\nabla\psi^\top\nabla\psi = I_2 \text{ almost everywhere,} \tag{5.12}$$

so ψ is a Lipschitz function with Lipschitz constant 1, as the following calculation shows. For almost every $x, y \in \omega$, by the fundamental theorem of calculus, we get

$$\begin{aligned}
|\psi(x) - \psi(y)| &= \left|\int_0^1 \nabla\psi(x + t(y-x))(y-x)\,\mathrm{d}t\right| \\
&\leqslant \int_0^1 |\nabla\psi(x + t(y-x))(y-x)|\,\mathrm{d}t \\
&= \int_0^1 \sqrt{(y-x)^\top\nabla\psi(x + t(y-x))^\top\nabla\psi(x + t(y-x))(y-x)}\,\mathrm{d}t \\
&= \int_0^1 \sqrt{(y-x)^\top(y-x)}\,\mathrm{d}t = |y-x|\,.
\end{aligned} \tag{5.13}$$

Here, we used the triangle inequality, and the isometry constraint (5.12). We can extend ψ to all of $\mathbb{R}^2$, having the same Lipschitz constant 1, cf. [Kir34].

In order to construct ψ_ε, let $\vartheta_{b_\varepsilon}$ be a smooth cutoff-function, such that

$$\vartheta_{b_\varepsilon} = 0 \quad \text{on } \mathbb{R}^2 \backslash \Sigma_{b_\varepsilon}\,, \qquad \vartheta_{b_\varepsilon} = 1 \quad \text{on } \Sigma_{\frac{b_\varepsilon}{2}}\,, \qquad |\nabla \vartheta_{b_\varepsilon}| \leqslant \frac{4}{b_\varepsilon}\,. \tag{5.14}$$

Let $\rho : \mathbb{R}^2 \to \mathbb{R}$ be the standard mollifier

$$\rho(x) := \begin{cases} c \exp\left(\frac{-1}{1-|x|^2}\right) & , \text{ if } x \in B_1(0) \\ 0 & , \text{ else} \end{cases}\,, \qquad \text{with } c = \left(\int_{B_1(0)} \exp\left(\frac{-1}{1-|x|^2}\right) \mathrm{d}x\right)^{-1}\,,$$

with $B_1(0)$ being the unit disk $B_1(0) := \{x \in \mathbb{R}^2 : |x| < 1\}$. In Figure 5.2, a cross section of the standard mollifier through the origin is displayed. We write

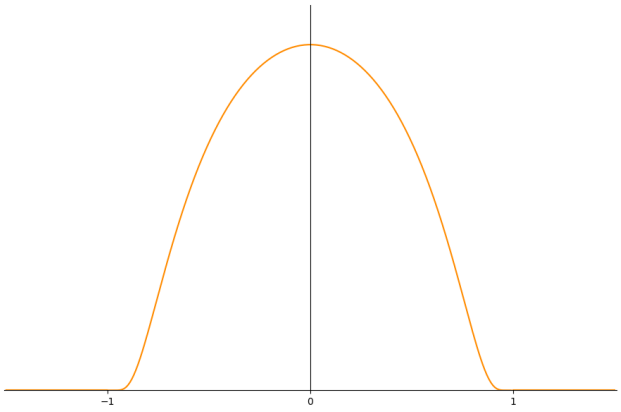

Figure 5.2: Cross section of the standard mollifier.

$$\rho_{b_\varepsilon}(x) := \frac{1}{b_\varepsilon^2} \rho(\frac{x}{b_\varepsilon}) \tag{5.15}$$

for a scaled version of the mollifier. Note that

$$\int_{\mathbb{R}^2} \rho_{b_\varepsilon}(x)\,\mathrm{d}x = \int_{\mathbb{R}^2} \rho(x)\,\mathrm{d}x = 1\,.$$

By the Lipschitz continuity of ψ, cf. (5.13), we have the pointwise estimate

$$\begin{aligned} |(\rho_{b_\varepsilon} * \psi)(x) - \psi(x)| &= \left| \int_{B_{b_\varepsilon}(0)} (\psi(x-y) - \psi(x)) \rho_{b_\varepsilon}(y)\,\mathrm{d}y \right| \\ &\leqslant \sup_{z \in B_{b_\varepsilon}(x)} |\psi(z) - \psi(x)| \leqslant b_\varepsilon\,. \end{aligned} \tag{5.16}$$

We define the recovery sequence ψ_ε as

$$\psi_\varepsilon := \psi + ((\rho_{b_\varepsilon} * \psi) - \psi)\,\vartheta_{b_\varepsilon}\,, \tag{5.17}$$

i.e.,

$$\psi_\varepsilon \in W^{2,2}(\omega; \mathbb{R}^3) \text{ and } \psi_\varepsilon = \psi \quad \text{in } \omega \backslash \Sigma_{b_\varepsilon}\,. \tag{5.18}$$

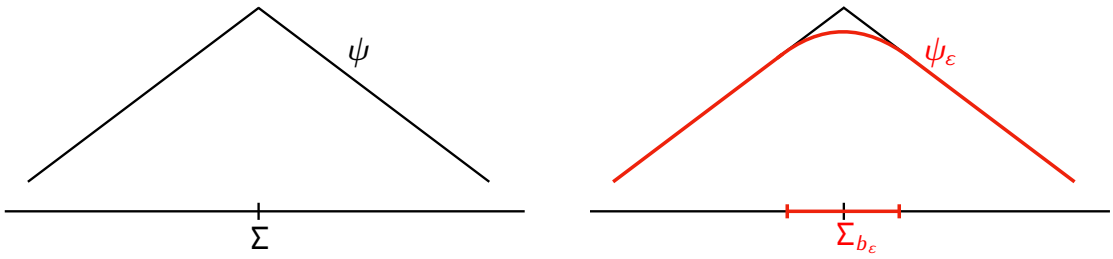

Figure 5.3: Left: Cross section of an isometry ψ with a sharp fold. Right: Constructed recovery sequence ψ_ε, cf. (5.17), with a smooth transition in Σ_{b_ε}.

In Figure 5.3, a cross-section of a fold and the corresponding recovery sequence is shown.

Differentiating (5.17) yields

$$\nabla\psi_\varepsilon = \nabla\psi + ((\rho_{b_\varepsilon} * \nabla\psi) - \nabla\psi)\,\vartheta_{b_\varepsilon} + ((\rho_{b_\varepsilon} * \psi) - \psi) \otimes \nabla\vartheta_{b_\varepsilon}\,. \tag{5.19}$$

With the gradient (5.19), we can estimate, again using the isometry constraint (5.12),

$$\begin{aligned}
&\left|\nabla\psi_\varepsilon^\top\nabla\psi_\varepsilon - I_2\right| \\
\leqslant&|\vartheta_{b_\varepsilon}|^2|(\rho_{b_\varepsilon} * \nabla\psi) - \nabla\psi|^2 + |\nabla\vartheta_{b_\varepsilon}|^2|(\rho_{b_\varepsilon} * \psi) - \psi|^2 \\
&+ 2|\nabla\psi||\vartheta_{b_\varepsilon}||(\rho_{b_\varepsilon} * \nabla\psi) - \nabla\psi| + 2|\nabla\psi||(\rho_{b_\varepsilon} * \psi) - \psi||\nabla\vartheta_{b_\varepsilon}| \\
&+ 2|\vartheta_{b_\varepsilon}||(\rho_{b_\varepsilon} * \nabla\psi) - \nabla\psi||\nabla\vartheta_{b_\varepsilon}||(\rho_{b_\varepsilon} * \psi) - \psi| \\
\leqslant&C < \infty\,.
\end{aligned} \tag{5.20}$$

Here we used $|(\rho_{b_\varepsilon} * \nabla\psi)| \leqslant (\rho_{b_\varepsilon} * |\nabla\psi|) \leqslant \sup_{x\in\omega}|\nabla\psi| = \sqrt{2}$, the properties of the cutoff-function $\vartheta_{b_\varepsilon}$, i.e. $|\vartheta_{b_\varepsilon}| \leqslant 1$ and $|\nabla\vartheta_{b_\varepsilon}| \leqslant \frac{4}{b_\varepsilon}$, cf. (5.14), and the estimate (5.16). It follows that, with the pointwise estimate (5.20), the *membrane part* of the energy can be bounded by

$$\begin{aligned}
\limsup_{\varepsilon\to0}\frac{\alpha}{\varepsilon}\int_\omega \left|\nabla\psi_\varepsilon^\top\nabla\psi_\varepsilon - I_2\right|^2 \mathrm{d}x &= \limsup_{\varepsilon\to0}\frac{\alpha}{\varepsilon}\int_{\omega\cap\Sigma_{b_\varepsilon}} \left|\nabla\psi_\varepsilon^\top\nabla\psi_\varepsilon - I_2\right|^2 \mathrm{d}x \\
&\leqslant C\alpha\limsup_{\varepsilon\to0}\frac{|\Sigma_{b_\varepsilon}|}{\varepsilon} = C\alpha\lim_{\varepsilon\to0}\frac{|\Sigma_{b_\varepsilon}|}{2b_\varepsilon}\frac{2b_\varepsilon}{\varepsilon} = 0\,.
\end{aligned}$$

Here, in the first equality, we used (5.18). The regularity assumption $\lim_{\varepsilon\to0}\frac{|\Sigma_{b_\varepsilon}|}{2b_\varepsilon} = \mathcal{H}^1(\Sigma) \leqslant C < \infty$ was used in the last equality, together with the assumption $\lim_{\varepsilon\to0}\frac{b_\varepsilon}{\varepsilon} = 0$.

Using (5.4), the *bending part* of $\mathcal{W}^\varepsilon[\psi_\varepsilon]$ can be estimated as

$$\int_\omega (v_\varepsilon^2 + \eta_\varepsilon)|D^2\psi_\varepsilon|^2\,\mathrm{d}x \leqslant \int_{\omega\setminus\Sigma_{b_\varepsilon}} (v_\varepsilon^2 + \eta_\varepsilon)|D^2\psi|^2\,\mathrm{d}x + (c+1)\int_{\omega\cap\Sigma_{b_\varepsilon}} \eta_\varepsilon|D^2\psi_\varepsilon|^2\,\mathrm{d}x\,. \tag{5.21}$$

The first term on the right-hand side converges to $\int_{\omega\setminus\Sigma}|D^2\psi|^2\,\mathrm{d}x$, by monotone convergence. It remains to show that the second term on the right-hand side vanishes in the limit. To this end, note that, by the definition of the mollifier, cf. (5.15),

$$|D^2\psi_\varepsilon(x)| = |(\nabla\rho_{b_\varepsilon} * \nabla\psi)(x)| \leqslant Cb_\varepsilon^{-1} \qquad \text{for } x \in \Sigma_{\frac{b_\varepsilon}{2}}\,.$$

Hence, integrating over $\Sigma_{\frac{b_\varepsilon}{2}}$ yields

$$\int_{\omega\cap\Sigma_{\frac{b_\varepsilon}{2}}} \eta_\varepsilon |D^2\psi_\varepsilon|^2 \,\mathrm{d}x \leqslant \frac{\eta_\varepsilon}{b_\varepsilon^2} |\Sigma_{\frac{b_\varepsilon}{2}}| \,. \tag{5.22}$$

In $\Sigma_{b_\varepsilon}\backslash\Sigma_{\frac{b_\varepsilon}{2}}$, we have

$$\begin{aligned} D^2\psi_\varepsilon = D^2\psi + \vartheta_{b_\varepsilon}\left((\rho_{b_\varepsilon} * D^2\psi) - D^2\psi\right) \\ + 2\left((\rho_{b_\varepsilon} * \nabla\psi) - \nabla\psi\right) \otimes \nabla\vartheta_{b_\varepsilon} + \left((\rho_{b_\varepsilon} * \psi) - \psi\right) \otimes D^2\vartheta_{b_\varepsilon} \,. \end{aligned}$$

Here, the first two terms are bounded in $L^2(\omega\backslash\Sigma)$. For the third term it holds

$$|\left((\rho_{b_\varepsilon} * \nabla\psi) - \nabla\psi\right) \otimes \nabla\vartheta_{b_\varepsilon}| \leqslant C b_\varepsilon^{-1} \,.$$

For the last term we have $|D^2\vartheta_{b_\varepsilon}| \leqslant C b_\varepsilon^{-2}$, and $|(\rho_{b_\varepsilon} * \psi) - \psi| \leqslant b_\varepsilon$, cf. (5.16), hence it is of order b_ε^{-1}. This implies

$$\int_{\omega\cap\Sigma_{b_\varepsilon}\backslash\Sigma_{\frac{b_\varepsilon}{2}}} \eta_\varepsilon |D^2\psi_\varepsilon|^2 \,\mathrm{d}x \leqslant C\eta_\varepsilon \left\|D^2\psi\right\|^2_{L^2(\omega\backslash\Sigma)} + C\frac{\eta_\varepsilon}{b_\varepsilon^2} |\Sigma_{b_\varepsilon}\backslash\Sigma_{\frac{b_\varepsilon}{2}}| \,. \tag{5.23}$$

Collecting (5.22) and (5.23), we conclude

$$\begin{aligned} 0 \leqslant \int_{\omega\cap\Sigma_{b_\varepsilon}} \eta_\varepsilon |D^2\psi_\varepsilon|^2 \,\mathrm{d}x &= \int_{\omega\cap\Sigma_{\frac{b_\varepsilon}{2}}} \eta_\varepsilon |D^2\psi_\varepsilon|^2 \,\mathrm{d}x + \int_{\omega\cap\Sigma_{b_\varepsilon}\backslash\Sigma_{\frac{b_\varepsilon}{2}}} \eta_\varepsilon |D^2\psi_\varepsilon|^2 \,\mathrm{d}x \\ &\leqslant \frac{\eta_\varepsilon}{b_\varepsilon^2} |\Sigma_{\frac{b_\varepsilon}{2}}| + C\eta_\varepsilon \left\|D^2\psi\right\|^2_{L^2(\omega\backslash\Sigma)} + C\frac{\eta_\varepsilon}{b_\varepsilon^2} |\Sigma_{b_\varepsilon}\backslash\Sigma_{\frac{b_\varepsilon}{2}}| \,. \end{aligned}$$

Now, by Assumption 5.2, $\frac{\eta_\varepsilon}{b_\varepsilon} \to 0$ as $\varepsilon \to 0$, hence the first and third term vanish in the limit. The second term is of order η_ε. All in all, we obtain that the second term on the right-hand side of (5.21) vanishes in the limit. With this, we obtain the lim sup-inequality.

□

Remark 5.5. *The terminology phase field approximation might be misleading here, since the function v_ε is given a priori, and does not result from the minimization of a variational phase field energy. In Section 5.3, however, an Ambrosio-Tortorelli type energy [AT92] is used to determine a phase field representation of the fold, because there the determination of the fold is part of this free discontinuity problem.*

Remark 5.6. *Note that the regularity of Σ required here is much lower than the regularity assumptions needed to derive* (5.1) *from three-dimensional nonlinear elasticity, as has been done in [BBH22], where only a single Lipschitz fold curve dividing ω into two distinct Lipschitz domains ω_1, ω_2 is allowed.*

The quantity

$$\lim_{\delta\to 0} \frac{|\Sigma_\delta|}{2\delta}$$

is also called the one-dimensional Minkowski content of Σ, cf. [Fed96]. An example of a set $\Sigma \subset \omega$ not satisfying the assumption

$$\lim_{\delta\to 0} \frac{|\Sigma_\delta|}{2\delta} = \mathcal{H}^1(\Sigma)$$

is $\Sigma = \mathbb{Q} \cap \omega$. In [AFP00], an example is given, showing that there also exist compact sets Σ for which this equality does not hold.

5.2 Numerical Experiments for Plates with Prescribed Folds

In this section, several examples of plate deformations with prescribed folds under different forces and boundary conditions are presented. To discretize the energy (5.2), we once more make use of the discrete Kirchhoff triangle (DKT) introduced in Section 2.4. We confine ourselves to rectangular domains ω and work on regular triangulations with grid size H. In the following, $\varepsilon > 0$ is always chosen to be proportional to the grid size, and we typically choose $\varepsilon = 2H$. For a given fold Σ, we take a piecewise affine interpolation $v_{\varepsilon,H}$ of the phase field function v_ε defined in (5.6). The discrete version of the energy (5.2) then reads

$$\mathcal{W}_H^\varepsilon[\psi_H] := \int_\omega (v_{\varepsilon,H}^2 + \eta_\varepsilon)|\nabla\theta_H[\psi_H]|^2 \,\mathrm{d}x + \frac{c}{\varepsilon}\int_\omega \left|\nabla\psi_H^\top\nabla\psi_H - I_2\right|^2 \,\mathrm{d}x\,. \tag{5.24}$$

To evaluate the integral, a Gauss quadrature of degree 6 with 12 quadrature points is used. For the minimization, a Newton scheme with Armijo step size control from the IPOPT library [WB06] is used, with a stopping criterion $\texttt{tol} < 10^{-8}$. The problem is first solved on a coarse regular grid with $H = 2^{-4}$, and then successively halved, up to $H = 2^{-10}$. Hence, the parameter $\varepsilon > 0$ is also halved for every refinement of the mesh. Additionally we set $\eta_\varepsilon = \varepsilon^2$, which fulfills the growth condition described in Section 5.1.

The experiments that are presented in this section always incorporate (clamped) boundary conditions and/or forces $f \in L^2(\omega;\mathbb{R}^3)$. Hence, the following minimization problem is considered

$$\min_{\psi\in\mathcal{A}^{\mathrm{BC}}} \left(\mathcal{W}^\varepsilon[\psi] - \int_\omega f\cdot\psi\,\mathrm{d}x\right),$$
$$\text{with } \mathcal{A}^{\mathrm{BC}} = \{\psi \in W^{2,2}(\omega;\mathbb{R}^3) \,:\, \psi = \phi\,,\ \nabla\psi = \nabla\phi \text{ on } \Gamma_D \subset \partial\omega\}\,,$$

with some given function $\phi \in W^{2,2}(\omega;\mathbb{R}^3)$, and $\Gamma_D \subset \partial\omega$, $\mathcal{H}^1(\Gamma_D) > 0$.

Single arc fold. In the first experiment, we consider a single fold curve in the domain $\omega = (0,1)^2$. The fold curve is given by

$$\Sigma = \left\{(x_1,x_2)\in\omega \,:\, \sqrt{(x_1-\tfrac{1}{2})^2 + x_2^2} = \tfrac{3}{5}\right\}.$$

The fold and the corresponding phase field, with $\varepsilon = 2H = 2^{-7}$ are displayed in Figure 5.1. To compute a deformation of a thin plate with this given fold, we considered the force

$$f(x) = \begin{cases} (0,0,1)^\top & , \quad \text{if } x_2 \geqslant \frac{3}{4} \\ (0,0,0)^\top & , \quad \text{else,} \end{cases}$$

and boundary conditions

$$\psi(x) = (0.1875, x_2, 0)^\top \text{ on } \{0\}\times[0,0.25]\,, \quad \psi(x) = (0.8125, x_2, 0)^\top \text{ on } \{1\}\times[0,0.25]\,,$$
$$\partial_1\psi(x) = (0,0,1)^\top \text{ on } \{0\}\times[0,0.25]\,, \quad \partial_1\psi(x) = (0,0,-1)^\top \text{ on } \{1\}\times[0,0.25]\,.$$

The parameter $\alpha > 0$ in front of the penalty term $\frac{\alpha}{\varepsilon}\int_\omega \left|\nabla\psi^\top\nabla\psi - I_2\right|^2 \mathrm{d}x$ is chosen to be $\alpha = 1000$. While the large constant $\frac{1000}{\varepsilon}$ could lead to numerical instabilities, we did not encounter such in our numerical experiments. In [BGM24], the approximation of bending

Figure 5.4: Left: Computed deformation of a thin plate with a single arc as fold curve. Right: Picture of a sheet of paper folded along the arc curve Σ.

and stretching deformations of thin structures with folding was studied. In their numerical experiments, they chose a factor 10^5 in front of the membrane term, in comparison to the bending term, which is similar to the scaling used here.

The deformation, together with a picture of a sheet of paper with this arc fold, is displayed in Figure 5.4.

Spiral fold. In this experiment, we consider a set of curves Σ that meet in the middle of the square domain $\omega = (-\frac{1}{2}, \frac{1}{2})^2$. The fold curves in $[-\frac{1}{2}, 0]$ are given as

$$\hat{\Sigma} = \left\{ (x_1, x_2) \in [-\tfrac{1}{2}, 0]^2 \,:\, \sqrt{(x_1 + \tfrac{1}{2})^2 + x_2^2} = \tfrac{1}{2} \right\} \cup \left\{ (x_1, x_2) \in [-\tfrac{1}{2}, 0]^2 \,:\, \sqrt{(x_1 + \tfrac{1}{4})^2 + (x_2 - \tfrac{1}{4})^2} = \tfrac{1}{2\sqrt{2}} \right\}.$$

Let $Q_{\frac{\pi}{2}} = \begin{pmatrix} 0 & -1 \\ 1 & 0 \end{pmatrix}$. The set of fold curves we consider is

$$\Sigma = \hat{\Sigma} \cup Q_{\frac{\pi}{2}} \hat{\Sigma} \cup Q_{\frac{\pi}{2}} Q_{\frac{\pi}{2}} \hat{\Sigma} \cup Q_{\frac{\pi}{2}} Q_{\frac{\pi}{2}} Q_{\frac{\pi}{2}} \hat{\Sigma}.$$

Again we consider $\alpha = 1000$, and apply compressed boundary conditions:

$$\begin{aligned}
\psi(x) &= (x_1 + \tfrac{1}{8}, x_2 + \tfrac{1}{8}, 0)^\top,\ \partial_1 \psi(x) = (1, 0, 0)^\top \text{ on } \{-\tfrac{1}{2}\} \times [-\tfrac{1}{2}, -\tfrac{3}{8}] \\
\psi(x) &= (x_1 - \tfrac{1}{8}, x_2 + \tfrac{1}{8}, 0)^\top,\ \partial_2 \psi(x) = (0, 1, 0)^\top \text{ on } [\tfrac{3}{8}, \tfrac{1}{2}] \times \{-\tfrac{1}{2}\} \\
\psi(x) &= (x_1 - \tfrac{1}{8}, x_2 - \tfrac{1}{8}, 0)^\top,\ \partial_1 \psi(x) = (1, 0, 0)^\top \text{ on } \{\tfrac{1}{2}\} \times [\tfrac{3}{8}, \tfrac{1}{2}] \\
\psi(x) &= (x_1 + \tfrac{1}{8}, x_2 - \tfrac{1}{8}, 0)^\top,\ \partial_2 \psi(x) = (0, 1, 0)^\top \text{ on } [-\tfrac{1}{2}, -\tfrac{3}{8}] \times \{\tfrac{1}{2}\}.
\end{aligned}$$

The phase field describing the spiral fold curves, the resulting deformation, and the corresponding physical experiment with folded paper are shown in Figure 5.5.

Periodic fold pattern. In this numerical experiment, we consider deformations of a thin plate with a periodic folding tessellation pattern. The periodic folding pattern is defined on $\omega = (0, 1) \times (0, 2)$ with the following folding curves

$$\begin{aligned}
\hat{\Sigma} &= [0, 1]^2 \cap \left(\left\{ \sqrt{x_1^2 + x_2^2} = \tfrac{1}{2} \right\} \cup \left\{ \sqrt{(x_1 - 1)^2 + x_2^2} = \tfrac{1}{2} \right\} \cup \left\{ x_1 = \tfrac{1}{2} \right\} \right) \\
\Sigma &= \hat{\Sigma} \cup \left(\hat{\Sigma} + \begin{pmatrix} 0 \\ 1 \end{pmatrix} \right).
\end{aligned}$$

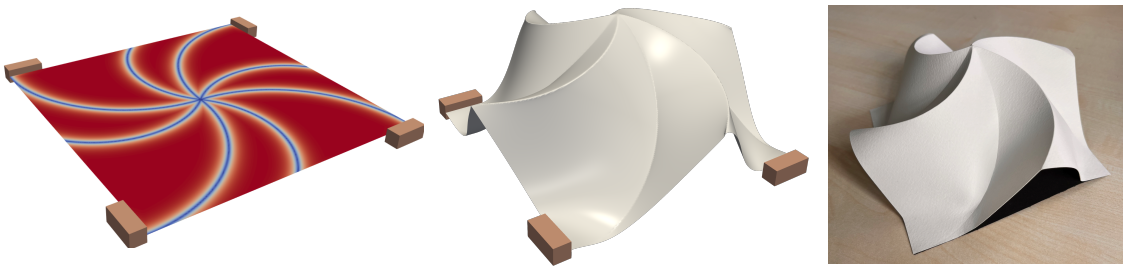

Figure 5.5: Left: Phase field representation of the described spiral fold curves Σ. Middle: Deformation under compressed boundary conditions and vertical force. Right: Picture of a sheet of paper folded along the spiral curves.

A phase field representation of the fold curves Σ is displayed in Figure 5.6 on the left. The following periodic boundary conditions for the deformation ψ of the fundamental cell ω are imposed:

$$\begin{aligned} \partial_1 \psi &= (1,0,0)^\top \quad \text{on } \{0\} \times [0,2] \cup \{1\} \times [0,2]\,, \\ \partial_2 \psi &= (0,1,0)^\top \quad \text{on } [0,1] \times \{0\} \cup [0,1] \times \{2\}\,. \end{aligned}$$

Strictly speaking, these boundary conditions do not suffice as periodic boundary conditions. However, because of the (almost) isometric deformation, the boundary conditions fit nicely together when multiple of these fold patterns are fit together, see Figure 5.6 in the middle.

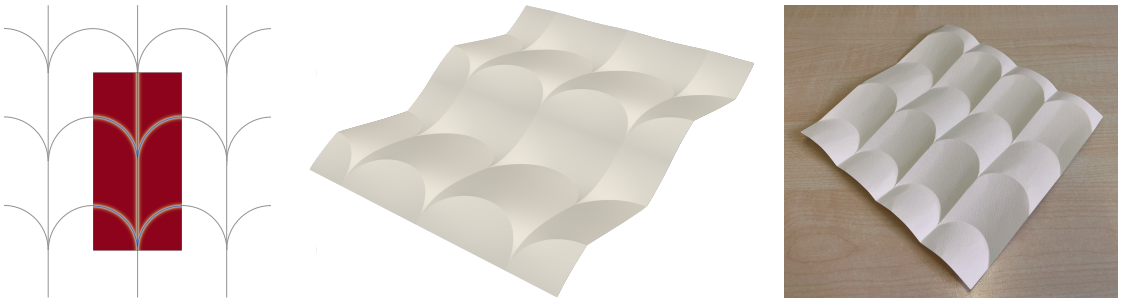

Figure 5.6: Left: Phase field representation of the described periodic fold curves Σ. Middle: Deformation under boundary conditions of 3×2 fold patterns. Right: Picture of a sheet of paper folded along the tessellation pattern curves.

Additionally, to get a nontrivial deformation, we apply the compression boundary conditions

$$\begin{aligned} &\psi_2 = 0 \quad \text{on } [0,1] \times \{0\}\,, \qquad \psi_2 = \tfrac{3}{2} \quad \text{on } [0,1] \times \{2\}\,, \\ &\psi = (0,0,0)^\top \quad \text{on } \{0\} \times \{0\} \end{aligned}$$

In the middle of Figure 5.6, the computed deformation of a thin plate with this periodic fold pattern is shown, with three repetitions of the periodic folding pattern in the x_1-direction and two repetitions of the periodic folding pattern in the x_2-direction. On the right of Figure 5.6, the picture of a deformed sheet of paper with the described fold tessellation pattern is shown. This fold pattern is inspired by [Luk21, Etude A2].

5.3 Optimization of Folds

We now turn our attention to the optimization of folding curves. In the previous section, we saw how the deformation of a thin plate with given fold curves, under given forces and boundary conditions, can be computed. Now, we instead want to optimize the shape and position of the fold curves, such that the deformation of the thin plate is optimal in an abstract way, which will be later made more concrete. For example, a possible optimization task is to design fold patterns such that the thin plate deforms in a desirable way when a specific force is applied. When designing mechanical micro devices for medical applications, such optimization tasks are of interest, cf. [MPL+24].

Now, the fold curves and thus their phase field representation are no longer a priori given, but are determined by a PDE constraint optimization problem. The PDE constraint is exactly given by the elastic deformation of the thin plate. To this end, the phase field function is denoted as $v \in W^{1,2}(\omega)$ and is a quantity that is to be computed, in addition to the deformation $\psi \in \mathcal{A}_{\mathrm{BC}}$. For a force $f \in L^2(\omega; \mathbb{R}^3)$, let

$$E^\varepsilon[\psi, v] := \frac{1}{2} \int_\omega (v^2 + \eta_\varepsilon) |D^2 \psi|^2 \, \mathrm{d}x + \frac{\alpha}{\varepsilon} \int_\omega \left| \nabla \psi^\top \nabla \psi - I_2 \right|^2 \, \mathrm{d}x - \int_\omega f \cdot \psi \, \mathrm{d}x \,, \tag{5.25}$$

now depending on ψ and v. For fixed phase field function v, let

$$\psi[v] \in \operatorname*{arg\,min}_{\psi \in \mathcal{A}_{\mathrm{BC}}} \left(E^\varepsilon[\psi, v] \right) \tag{5.26}$$

be an elastic deformation of the thin plate, under the boundary conditions $\mathcal{A}_{\mathrm{BC}}$ and force f, with fold curves given by v. We assume that the given optimization task for v can be formulated as a minimization of a positive functional

$$\min_{v \in W^{1,2}(\omega)} \left(\hat{\mathcal{C}}[v, \psi[v]] \right) \qquad \text{subject to } \psi[v] \in \operatorname*{arg\,min}_{\psi \in \mathcal{A}_{\mathrm{BC}}} \left(E^\varepsilon[\psi, v] \right) \tag{5.27}$$

that may depend on the phase field v and a corresponding elastic deformation $\psi[v]$. Since we want v to be a phase field approximation of one-dimensional fold curves, the functional $\hat{\mathcal{C}}[\cdot, \cdot]$ has to contain a regularizer for v. To this end, we recall the Ambrosio-Tortorelli functional

$$\mathcal{AT}^\varepsilon[v] := \int_\Omega \varepsilon |\nabla v|^2 + \frac{(1 - v)^2}{4\varepsilon} \, \mathrm{d}x \,,$$

introduced in Section 2.6. We assume $\hat{\mathcal{C}}[\cdot, \cdot]$ to be of the form

$$\hat{\mathcal{C}}[v, \psi[v]] := \mathcal{C}[v, \psi[v]] + \beta \mathcal{AT}^\varepsilon[v] \,.$$

Here, $\mathcal{C}[\cdot, \cdot]$ is a positive cost functional associated with the desired optimization task and $\beta > 0$ is a positive constant. For small, but fixed $\varepsilon > 0$, this functional penalizes deviations of v away from $v \equiv 1$, only allowing to drop to zero on a set of small measure (an approximation of the one-dimensional fold curve set), while ensuring $W^{1,2}$–regularity. The Ambrosio-Tortorelli functional as part of the cost functional $\hat{\mathcal{C}}[\cdot, \cdot]$ at the same time serves as a measure of the length of the optimal fold curves approximated by v. Hence, minimizing $\hat{\mathcal{C}}[\cdot, \cdot]$ is a trade-off between minimizing the true cost $\mathcal{C}[\cdot, \cdot]$ and not spending too much fold curve length.

Optimization with the Lagrangian. In general, there is no unique minimizer $\psi[v]$ of (5.26), since $E^\varepsilon[\cdot, v]$ is non-convex, but minimizers $\psi[v]$ can be characterized by being solutions to the Euler-Lagrange equation

$$\partial_\psi E^\varepsilon[\psi[v], v](\vartheta) = 0 \qquad \text{for all } \vartheta \in W^{2,2}(\omega; \mathbb{R}^3) \text{ with } \vartheta = 0\,,\ \nabla\vartheta = 0 \text{ on } \Gamma_D\,. \tag{5.28}$$

Of course, solving the Euler-Lagrange equation is only a necessary condition for being a minimizer of the energy. Only if $G[\cdot, v]$ were convex, it would be sufficient. On the other hand, it is easy to see that $G[\cdot, v]$ has a minimizer, by applying the direct method, since it is convex in the highest order term.

With this, the constraint optimization problem (5.27) can be formulated as finding a critical point of the Lagrangian

$$\mathcal{L}^\varepsilon[v, \psi, p] = \mathcal{C}[v, \psi] + \beta\mathcal{AT}^\varepsilon[v] + \partial_\psi E^\varepsilon[\psi, v](p)\,. \tag{5.29}$$

Here, as before, $v \in W^{1,2}(\omega)$ is the phase field approximating the fold curves, $\psi \in \mathcal{A}_{\mathrm{BC}}$ is the associated elastic deformation, and $p \in W^{2,2}(\omega; \mathbb{R}^3)$, with $p = 0$ and $\nabla p = 0$ on Γ_D, is the corresponding Lagrange multiplier, ensuring the PDE constraint (5.28).

For readers not familiar with constraint optimization, we briefly discuss here the reason for writing (5.27) in the Lagrangian formulation (5.29). For a critical point $(\hat{v}, \hat{\psi}, \hat{p})$ of $\mathcal{L}^\varepsilon[\cdot,\cdot,\cdot]$ it holds

$$\partial_v \mathcal{L}^\varepsilon[\hat{v}, \hat{\psi}, \hat{p}](w) = 0\,, \quad \partial_\psi \mathcal{L}^\varepsilon[\hat{v}, \hat{\psi}, \hat{p}](\vartheta) = 0\,, \quad \partial_p \mathcal{L}^\varepsilon[\hat{v}, \hat{\psi}, \hat{p}](q) = 0\,, \quad \text{for all } (w, \vartheta, q)\,.$$

Here, the third equation is equivalent to (5.28), and hence ensures that $\hat{\psi}$ solves the Euler-Lagrange equation associated with the elastic energy. The second equation is the so-called adjoint equation, a linear equation that determines the Lagrange multiplier $\hat{p}$. The first equation is the optimality condition of the actual optimization variable $\hat{v}$.

Cost functional. So far, we have only introduced the abstract, positive cost functional $\mathcal{C}[v, \psi[v]]$, in which the optimization task is encoded, without providing details about possible choices of applications. We will make up for that here. In classical elastic shape optimization with phase fields, where the task is to distribute a certain amount of hard material in the computational domain, cf. [HRS20, PRW12], a natural choice for the cost functional is to take the *compliance energy* $\mathcal{C}[v, \psi] = \int_\omega \psi \cdot f \,\mathrm{d}x$. The physical interpretation of this optimization task is the following: Distribute the hard material so that the elastic object resists the force f acting on it most strongly. Since in our application, where we want to distribute fold curves optimally, and hence weaken the material instead of strengthening it, compliance shape optimization does not seem to be the right application of interest in our case. However, a possible compliance shape optimization task could be to design a folding pattern, such that the already deformed configuration is resistant to a second force $\tilde{f}$, different from the force f that deformed the thin plate at first. A concrete example of this is a paper box for French fries, where the design of the bottom part of the box involves curved fold curves, cf. [BST25].

Another widespread application in elastic shape optimization is the minimization of a so-called *tracking-type* cost functional, cf. [DDH15]. In this case, $\mathcal{C}[v, \psi[v]]$ is given by $\mathcal{C}[v, \psi] = \int_\omega |\psi - \phi|^2 \,\mathrm{d}x$, where $\phi\colon \omega \to \mathbb{R}^3$ is a prescribed desired shape that is to be matched by the elastic deformation ψ. This is a classical optimization task in Origami design, where the primary interest is to figure out the right folds to turn the thin plate (here, the sheet of paper) into a swan or a frog, for example.

A third possible choice for an optimization task is inspired by engineering applications: In Figure 5.4, the deformation of a thin plate with a curved arc fold is displayed. This deformation is caused by a vertical force, to flip up the upper part of the square plate, and by pushing the boundary together from left and right on the bottom part of the plate. Once the plate is deformed in this way, a variation of the degree of compression of the boundary conditions leads to a variation of the folding angle, and hence creates a mechanical hinge device. This phenomenon is also present in nature, for example, in the snapping mechanism of fly trap plants [SWM+20]. An obvious question is how the geometry of the fold influences the mechanical transmission of force, which in turn brings the optimization of force transmission through optimal design of the fold curve into focus.

Optimal design for microscopic fold patterns as displayed in Figure 5.6 to achieve certain macroscopic, effective elastic responses is another interesting field where our method could be applied. This requires the derivation of a homogenized model. With this at hand, a two-scale optimization procedure similar to [DPRS19] could be applied.

The optimization problems listed above are interesting approaches for future projects that require a deeper understanding of the modeling of such cost functionals. Here, we will limit ourselves to a simpler example of a cost function to illustrate the practical application of the optimization framework presented here. The motivation for this choice is as follows: Given fixed boundary conditions and forces, choose an area $\hat{\omega} \subset \omega$ inside the plate. Now optimize the fold curves such that this set is lifted as high as possible (in the third coordinate direction). A simple cost functional modeling this optimization task is

$$\mathcal{C}[v, \psi] = -\int_{\hat{\omega}} \psi_3 \, \mathrm{d}x \,. \tag{5.30}$$

In the experiments shown in this thesis, the choice of the set $\hat{\omega}$ depends on the experiment and will be specified.

Optimization algorithm. We have seen that the phase field fold optimization discussed in this section can mathematically be formulated as finding a critical point of the Lagrangian (5.29), i.e., a root of $\nabla_{(v,\psi,p)}\mathcal{L}^\varepsilon$. Strictly speaking, this is not a gradient, but a variation in the infinite dimensional space $W^{1,2}(\omega) \times W^{2,2}(\omega;\mathbb{R}^3) \times W^{2,2}(\omega;\mathbb{R}^3)$, but in our FE discretization we will approximate this with a finite dimensional gradient. To ease notation, we will sketch the optimization algorithm here using the continuous notation, and after that, we will introduce the FE discretization. Since the Lagrangian formulation (5.29) turns the optimization into a saddle point problem, standard gradient descent methods, which are used for unconstrained minimization problems, cannot be applied here. A common, and usually fast algorithm to find the root of a function is Newton's method, which would involve second derivatives of the Lagrangian, and hence third derivatives of $E^\varepsilon[\cdot,\cdot]$, which are computationally out of reach. One possibility would be to approximate the Hessian of the Lagrangian by using a quasi-Newton method like BFGS, or to directly formulate the constraint optimization problem as an iterative method like sequential quadratic program (SQP) with equality constraints, cf. [NW06]. Here, we will follow a nested optimization method also used in [HRS20] for shape optimization on shells with phase fields: Given a phase field v_k at the k-th iteration step, first compute a minimizer ψ_k of $E^\varepsilon[v_k,\cdot]$ via Newton's method. With this, solve the linear adjoint problem $\partial_\psi^2 E^\varepsilon[v_k,\psi_k](p_k) = -\partial_\psi \mathcal{C}[v_k,\psi_k]$ for p_k. Having computed ψ_k and p_k, the phase field for the next iteration is obtained by gradient descent: $v_{k+1} = v_k - \tau_k(\partial_v \mathcal{C}[v_k,\psi_k] + \beta\partial_v \mathcal{A}\mathcal{T}^\varepsilon[v_k] + \partial_v\partial_\psi E^\varepsilon[v_k,\psi_k](p_k))$, with variable step size τ_k. The procedure is summarized in Algorithm 5.1.

Algorithm 5.1 Nested phase field fold optimization

Input: Initial phase field v_0
Output: Optimal phase field $\hat{v}$

1: $k = 0$
2: **while** not converged **do**
3: Compute minimizer ψ_k of $E^\varepsilon[v_k, \cdot]$ via Newton's method
4: Solve the linear adjoint problem $\partial_\psi^2 E^\varepsilon[v_k, \psi_k](p_k) = -\partial_\psi \mathcal{C}[v_k, \psi_k]$ for p_k
5: Compute the next phase field by gradient descent with step size control τ_k:

$$v_{k+1} = v_k - \tau_k(\partial_v \mathcal{C}[v_k, \psi_k] + \beta \partial_v \mathcal{AT}^\varepsilon[v_k] + \partial_v \partial_\psi E^\varepsilon[v_k, \psi_k](p_k))$$

6: $k = k + 1$
7: **end while**

We implemented this optimization algorithm using the IPOPT library, cf. [WB06], both for the inner Newton's method for computing ψ_k, similar to [RSS22, RSS24], and for the outer gradient descent algorithm for computing v_{k+1}, with Armijo step size control.

Finite element discretization. We use a similar discretization as in (5.24), where we additionally discretize the Lagrange multiplier p_H with the DKT finite element, cf. Section 2.4. The phase field v_H is again discretized by piecewise affine finite elements, but now treated as a variable instead of a fixed input vector. For the inner Newton's method, we typically choose a tolerance of 10^{-8}, and for the outer gradient descent, a tolerance of 10^{-6} as a stopping criterion. As before, we start with a coarse mesh, compute an optimal solution there, and then interpolate the phase field, deformation, and Lagrange multiplier onto a refined mesh. Here, instead of uniform refinement, we employ an adaptive refinement strategy, which involves refining an element if the norm of the gradient of the phase field is larger than 1, i.e. $|\nabla v_H| > 1$, or if the average phase field value is smaller than $\frac{1}{4}$. The first condition implies mesh refinement in areas where the phase transition is steep, while the second condition implies mesh refinement where the approximate fold curve is ($v = 0$). In this fold optimization setting, we choose $\varepsilon = 5H$ instead of $\varepsilon = 2H$, where H denotes the smallest triangle diameter in the mesh. We found that this choice significantly improved the convergence of our optimization algorithm, which we attribute to improved regularity at larger ε. As before, we set $\eta_\varepsilon = \varepsilon^2$.

Cross fold optimization. In this first experiment, we consider a physical setting similar to the spiral fold displayed in Figure 5.5. We investigate optimal fold curves on a square plate, given by $\omega = (0, 1)^2$, where we push the four corners into the middle, exactly as the compressed, clamped boundary conditions for the spiral fold experiment. As described before, we consider the simple optimization task of optimizing the fold curves, such that a small area in the middle of the plate, $\hat{\omega} = (0.45, 0.55)^2$, is lifted as high as possible in the third coordinate direction, i.e., in the direction perpendicular to the plate. For this, we consider the cost functional given by (5.30). The described setup is displayed in Figure 5.7 The phase field for the optimization algorithm is initialized by the constant 1 function, i.e. $v_0 \equiv 1$, and we start the optimization on a regular grid with uniform grid size $H = 2^{-4}$. The constant in front of the Ambrosio-Tortorelli functional, which controls the length penalization of the fold curves, is chosen to be $\beta = 0.001$. The constant α in front of the membrane term in (5.25) is set to $\alpha = 1$.

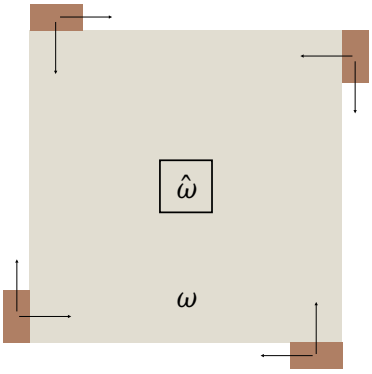

Figure 5.7: Setup for the cross fold optimization, with clamped boundary conditions (brown boxes), and the area $\hat{\omega}$ that is to be lifted in normal direction.

The optimal phase fields computed on different resolutions, together with the underlying mesh, are displayed in Figure 5.8. There, we see that the phase field directly constructs a fold where the clamped boundary conditions are imposed, and thus switches them off. Another surprising observation is the crossing of the phase field in the middle of the plate, building angles of 90°, instead of a crossing of three fold curves that meet in 120° angles, cf. [ABM03], which are minimizers of the Mumford-Shah functional, the sharp interface limit of the Ambrosio-Tortorelli functional. A possible explanation for this is that in our experiment, ε is still too large, such that the gradient term in the Ambrosio-Tortorelli functional causes the phase field to blur out the middle, whereas the sharp interface optimal fold curves would not meet at all. Also, the nonlinear elastic energy has a big influence, as (almost) isometric deformations are very rigid and may cause nonlocal phenomena. The computed deformation for the optimal phase field on the finest grid is shown in Figure 5.9 on the left.

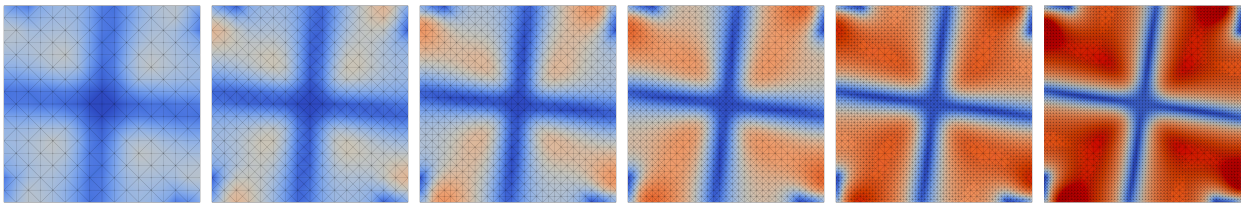

Figure 5.8: Computed optimal phase field solutions for the cross fold optimization, with $\beta = 0.001$, on different stages of refinement. From left to right, the grid resolution is increased adaptively. On the coarsest grid, the phase field function is initialized with constant one for the optimization. On the refined grids, the optimal solution on the previous, coarser grid serves as the initialization for the phase field function, interpolated onto the refined grid.

To investigate the influence of the regularizing length penalization term $\mathcal{AT}^{\varepsilon}[\cdot]$, we ran the same experiment, but now halved the factor in front of the Ambrosio-Tortorelli energy, i.e., $\beta = 0.0005$. In theory, this allows for more freedom for the optimizer with regard to the length of the folds. In Figure 5.10, the computed optimal phase field functions are shown on increasing mesh resolutions. Indeed, the length of the approximate, diffuse fold curves increases, in comparison to Figure 5.8, and a different fold structure appears, breaking the symmetry with two new folds building a diagonal fold in one direction.

The corresponding deformation computed on the finest grid is shown in Figure 5.9 on the

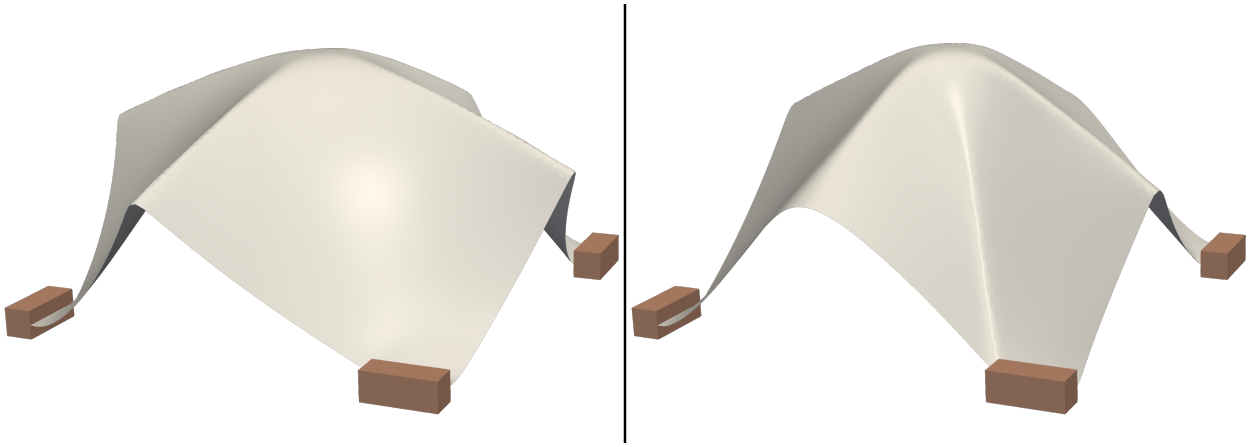

Figure 5.9: Computed deformations with optimal phase field for the cross fold optimization on the finest mesh. Left: Deformation corresponding to the phase field displayed in Figure 5.8 on the right. Right: Deformation corresponding to the phase field displayed in Figure 5.10 on the right.

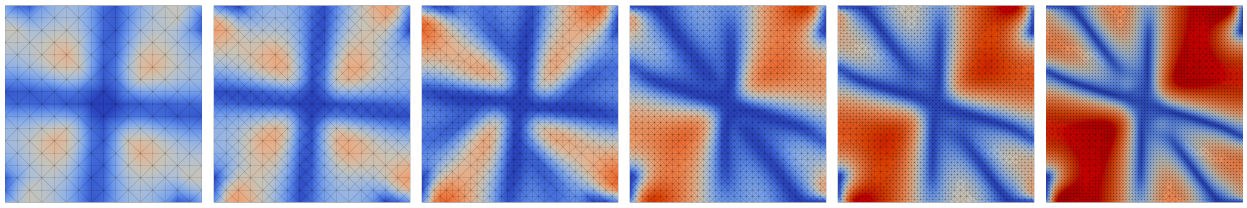

Figure 5.10: Computed optimal phase field solutions for the cross fold optimization, with $\beta = 0.0005$, on different stages of refinement. From left to right, the grid resolution is increased adaptively. On the coarsest grid, the phase field function is initialized with constant one for the optimization. On the refined grids, the optimal solution on the previous, coarser grid serves as the initialization for the phase field function, interpolated onto the refined grid.

right. A direct comparison, see Figure 5.11, shows that the increased length of the fold curves is indeed beneficial for minimizing the cost functional, leading to a higher lift of the middle part of the plate $\hat{\omega}$.

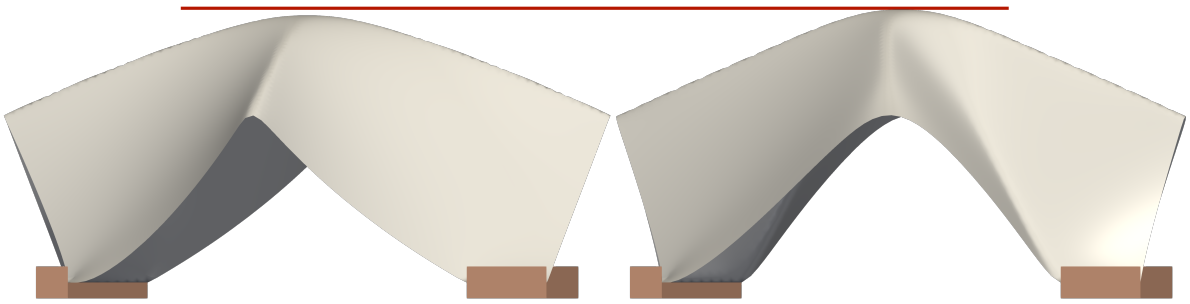

Figure 5.11: Comparison of the deformations corresponding to the optimal phase field fold curves with different length penalization (Left: $\beta = 0.001$, right: $\beta = 0.0005$). We see that increased length of the approximate fold curves leads to a higher lifting of the middle part of the plate $\hat{\omega}$.

Arc fold optimization. In the previous optimization experiment, we saw that our phase field method for optimizing fold curves on elastic plates leads to interesting, almost straight fold patterns that cross in the middle of the plate. Next, we want to design an optimization problem that leads to a curved fold geometry. Inspired by the arc fold experiment shown in

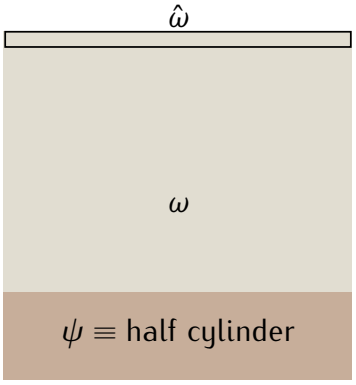

Figure 5.12: Setup for the arc fold optimization, where the lower quarter of the plate is deformed into a half cylinder (brown box), and the area $\hat{\omega}$ that is to be lifted in the vertical direction.

Figure 5.4, we take into account the square plate $\omega = (0,1)^2$, where we now enforce that the lower quarter of the plate $[0,1] \times [0,0.25]$ is deformed into a half cylinder, explicitly

$$\psi(x_1, x_2) \equiv (-\tfrac{1}{\pi}\cos(\pi x_1), x_2, \tfrac{1}{\pi}\sin(\pi x_1)) \qquad \text{for } (x_1, x_2) \in [0,1] \times [0,0.25]\,.$$

Additionally, the vertical force $f(x_1, x_2) = (0, 0, 60)^\top$ is applied on $\hat{\omega} = (0,1) \times (0.96, 1)$, the area that also appears in the cost functional (5.30). The physical setting is displayed in Figure 5.12.

The constant in front of the Ambrosio-Tortorelli functional, which controls the length penalization of the fold curves, is chosen to be $\beta = 0.00\bar{6}$. The constant α in front of the

membrane term in (5.25) is set to $\alpha = 1$. Here, we directly started the optimization on a finer grid, with $H = 2^{-6}$.

We found that initializing the optimization algorithm with a constant phase field $v_0 \equiv 1$ did not lead to satisfying results. A reason for this could be that the strong contribution of the membrane term that leads to almost isometric deformations does not allow for large deformations in the vertical direction when the plate is deformed into a half cylinder, in the case of constant hard material (i.e., when there is no fold region). Instead, we initialized the phase field with a prescribed curved fold. This initialization and the corresponding elastic deformation are displayed in Figure 5.13. The computed optimal phase field and the corresponding elastic deformation after one refinement step are shown in Figure 5.14.

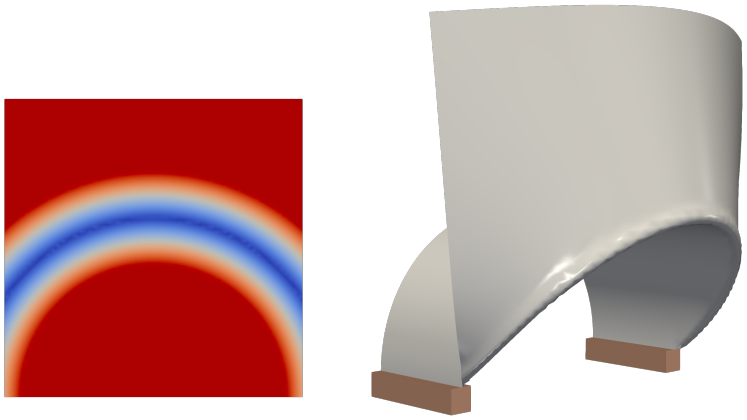

Figure 5.13: Left: Initialization of the phase field for the arc fold optimization. Right: Corresponding elastic deformation, with a sharp fold along the initial fold.

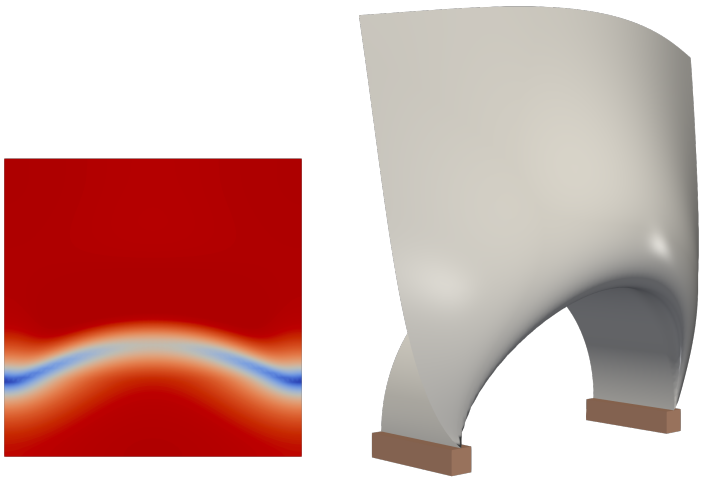

Figure 5.14: Left: Optimal phase field for the arc fold optimization. Right: Corresponding elastic deformation, with a less sharp fold, in comparison to the initial fold deformation, caused by higher values of the phase field function.

An interesting observation here is that the phase field does not drop to zero (blue color) in the middle of the fold, but stays in the region ≈ 0.5 (white color), leading to a less sharp fold deformation, which can be seen in Figure 5.14 on the right. A higher factor α in front of the

membrane term would probably lead to a sharper optimal fold curve, but would definitely come with more difficulties in the optimization, as we experienced in our numerical experiments. That is why we restrict ourselves to the experiment presented here. At the boundary of the plate, the phase field forms 90° angles, a common phenomenon when minimizing the Ambrosio-Tortorelli functional. The direct comparison in Figure 5.15 clearly displays the better performance of the optimal phase field in minimizing the cost functional $\mathcal{C}[\psi] = -\int_{\hat{\omega}} \psi_3 \, \mathrm{d}x$, compared to the deformation corresponding to the initial phase field.

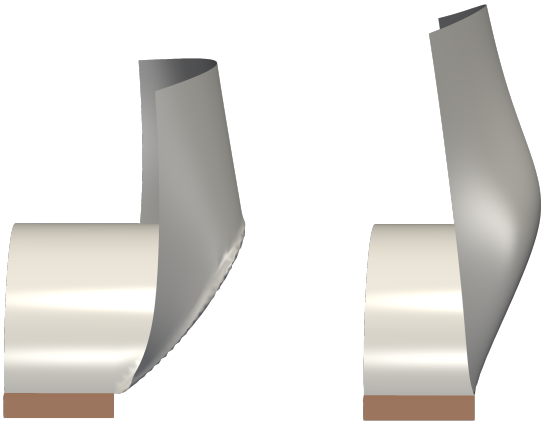

Figure 5.15: Left: Deformation corresponding to the initial phase field for the arc fold optimization. Right: Deformation corresponding to the optimal phase field.

Chapter 6

A Hybrid Minimizing Movement and Neural Network Approximation of Willmore Flow

We present a hybrid method combining a minimizing movement scheme with neural operators for the simulation of phase field-based Willmore flow. The minimizing movement component is based on a standard optimization problem on a regular grid, whereas the functional to be minimized involves a neural approximation of mean curvature flow proposed by Bretin et al. [BDMT22]. Numerical experiments confirm stability for large time step sizes, consistency, and significantly reduced computational cost compared to a traditional finite element method. Moreover, applications demonstrate its effectiveness in surface fairing and reconstructing of damaged shapes. Thus, our approach offers a robust and efficient tool for geometry processing.

Collaboration. This chapter is the result of joint work with Josua Sassen and Martin Rumpf that is currently under review, and available as a preprint [RSS25]. In particular, Josua Sassen implemented the basic learning algorithm and the Newton CG algorithm for the nested Willmore scheme with neural networks. Furthermore, he rendered the images of the three-dimensional examples.

Willmore flow is the L^2-gradient flow of the Willmore energy, which is defined as the surface integral over the squared mean curvature. For closed surfaces of genus zero, the Willmore energy allows to quantify how much a surface deviates from being a perfect sphere, with a round sphere having minimal Willmore energy. Physically, the Willmore energy reflects an approximation of the stored energy in a thin elastic shell with a planar physical reference configuration [Cia00]. It is also used to model the behavior of cell membranes, which have the tendency to minimize their bending. To this end, an extension of the Willmore energy, the Helfrich model, is used to describe elastic cell membranes in biology [CAMK14]. Furthermore, in computer graphics and geometry processing, Willmore flow is used for surface smoothing [CPS13], and surface restoration [CDD+04, LC23]. This motivates the study of Willmore flow, and in particular, the development of numerical schemes.

However, as we will discuss below, Willmore flow is described by a fourth-order PDE, which makes it challenging to devise schemes that allow for large time steps and are computationally efficient. We will show that our proposed hybrid scheme is stable for large time steps and indeed leads to an efficient scheme for Willmore flow in the case of a phase field formulation,

which is, in particular, practical for applications with implicitly described geometries. To compute Willmore flow, we will consider a minimizing movement time discretization. Therein, we combine a discretization of the minimizing movement scheme on a regular grid with a neural network approximation of the mean curvature arising in the Willmore energy.

The work presented in this chapter deals with phase field models approximating hypersurfaces $\mathcal{M}$ in the computational domain $\Omega = (0,1)^d$ and their evolution by Willmore flow. To motivate the hybrid method, we first recall the parametric formulation of Willmore flow. We denote by $x\colon \mathcal{M} \to \Omega$ the identity restricted to the surface $\mathcal{M}$. Then the *Willmore energy* of $\mathcal{M}$ is given by

$$w[x] := \frac{1}{2}\int_{\mathcal{M}} \mathbf{h}^2(x)\,\mathrm{d}\mathcal{H}^{d-1},$$

where $\mathbf{h}$ is the mean curvature, which we take to be the sum of the principal curvatures. The *Willmore flow* for parametrizations is then the L^2-gradient flow of this energy, i.e. the evolution $x\colon [0,T]\times\mathcal{M}\to\Omega$ that fulfills

$$(\partial_t x, \vartheta)_{L^2(\mathcal{M})} = -\partial_x w[x](\vartheta)$$

for all test functions $\vartheta \in C^\infty(\mathcal{M},\mathbb{R}^d)$, where $(\cdot,\cdot)_{L^2(\mathcal{M})}$ denotes the L^2-scalar product on the hypersurface $\mathcal{M}$ and $\partial_x w[x](\vartheta)$ the variation of the Willmore energy in direction ϑ.

However, here, the goal is not to minimize the Willmore *energy* but to efficiently simulate Willmore *flow*, i.e. the L^2-gradient flow of the Willmore energy.

To this end, we will consider a *variational time-discretization* of Willmore flow based on the minimizing movements paradigm [DG93, AGS08]. In case of parametric Willmore flow and time step size $\tau > 0$, given a parametrization $x^k\colon \mathcal{M}\to\Omega$ approximating the evolution at time $k\tau$, the next time step x^{k+1} is given as the minimizer of

$$e[x^k, x] := \|x - x^k\|^2_{L^2(\mathcal{M}^k)} + 2\tau\, w[x]. \tag{6.1}$$

To obtain a fully implicit, variational formulation of Willmore flow that is (experimentally) unconditionally stable and allows for large step sizes, Balzani and Rumpf [BR13] proposed to approximate the Willmore functional $w[x]$ in (6.1) using an approximate mean curvature. To this end, one denotes by $y_{\tilde\tau}[x]\colon \mathcal{M}\to\Omega$ the solution of one discrete time step of mean curvature flow (MCF) with time step size $\tilde\tau$ starting from the initial parametrization x corresponding to the surface $\mathcal{M}$. By definition, the mean curvature $\mathbf{h}$ is the normal velocity of mean curvature flow. Hence, $\frac{1}{2}\int_{\mathcal{M}} \frac{|y_{\tilde\tau}[x]-x|^2}{\tilde\tau^2}\,\mathrm{d}\mathcal{H}^{d-1}$ constitutes a difference quotient approximation of the Willmore energy $w[x]$ and a minimizing movement functional is given as

$$e[x^k, x] := \|x - x^k\|^2_{L^2(\mathcal{M}^k)} + \tau\int_{\mathcal{M}} \frac{|y_{\tilde\tau}[x]-x|^2}{\tilde\tau^2}\,\mathrm{d}\mathcal{H}^{d-1}. \tag{6.2}$$

As a discrete solution for mean curvature motion, one might consider the time step of a semi-discrete backward Euler scheme with time step $\tilde\tau$ as proposed by Dziuk [Dzi91]. Thus, minimizing the energy $e[x^k,x]$ in x amounts to solving a nested time discretization with time-discrete mean curvature motion as the inner and the actual time-discrete Willmore flow as the outer problem, It can also be understood as a PDE-constrained optimization problem, where one optimizes the energy (6.2) subject to the constraint that $y_{\tilde\tau}[x]$ is the solution of the linear discrete semi-implicit backward Euler scheme for mean curvature motion.

In this work, we pick up the approach proposed by Franken et al. [FRW11] and focus on the corresponding scheme for phase fields. Our core idea is to construct a hybrid scheme where the

inner problem is solved using a neural network, whereas the outer problem remains a classical minimizing movement optimization scheme. For the inner problem, we will build on recent work by Bretin et al. [BDMT22] on neural operators for time-discrete mean curvature flow in a phase field formulation. These neural operators are efficient to evaluate, straightforward to differentiate, and convergent under spatial refinement in numerical experiments.

Using them in the variational time-discretization, we obtain a numerical scheme for the phase field approximation of Willmore flow that, similar to the original nested scheme, remains stable for large time steps while being computationally more efficient.

By adopting this hybrid strategy, we take a step towards a fully neural treatment of Willmore flow, where the ultimate goal is to learn the solution operator itself. Indeed, considering a network that approximates a minimizing movement scheme for the phase field approximation of the Willmore energy would be a promising alternative. However, it requires sufficient training data for a suitable large set of initial conditions, which has to be computed in the training phase. Given the usual computing times for Willmore flow, this is surely a major computational challenge. Furthermore, the selection of a suitable class of initial conditions is still open.

The advantage of our approach is that the nested scheme by Franken et al. [FRW11] allows for an approximation of the mean curvature based on a neural operator for the approximation of MCF. This only requires training data for a corresponding phase field approximation of MCF. Such training data is easy and computationally cheap to generate, as discussed by Bretin et al. [BDMT22]. Indeed, they showed that training on hypersphere evolutions is sufficient.

Within this context, the integration of a learned mean curvature flow operator into the nested framework provides a practical and principled intermediate step: it leverages the efficiency of neural operators while retaining the well-established structure of the nested algorithm. We show that this integration indeed leads to a viable hybrid scheme.

Related work. Willmore surfaces, i.e., minimizers of the Willmore energy, and Willmore flow have been the subject of intense theoretical study. Simonett proved in [Sim01] the existence of a unique and locally smooth solution of Willmore flow for sufficiently smooth initial surfaces as well as exponential convergence to a sphere for initial surfaces close to a sphere. Similarly, Dall'Acqua et al. [DMSS23] proved that if the initial datum is a torus of revolution with Willmore energy less than16π then the Willmore flow converges to the Clifford Torus. Kuwert and Schätzle treated long-time existence and regularity of solutions in co-dimension one in [KS01, KS02, KS04], and Rivière [Riv08] extended these results to arbitrary co-dimension. In 2014, Marques and Neves [MN14] were able to prove the famous Willmore conjecture, i.e. that for every smooth immersed torus in $\mathbb{R}^3$ the Willmore energy is lower bounded by $4\pi^2$.

Similarly, the numerical treatment of Willmore flow for surfaces has garnered significant attention. Rusu [Rus05] introduced a semi-implicit finite element scheme for the computation of the parametric Willmore flow of surfaces, which was applied by Clarenz et al. [CDD$^+$04] to surface restoration problems. Droske and Rumpf [DR04] introduced a level set formulation for Willmore flow and a corresponding numerical scheme. Deckelnick and Dziuk provided in [DD06] a priori error estimates for a spatially discretized but time-continuous finite element scheme on two-dimensional graphs. Alternative finite element schemes for parametric Willmore flow were introduced by Barrett et al. [BGN07] and Dziuk [Dzi08]. In contrast, Bobenko and Schröder [BS05] introduced a discrete Willmore energy and flow based on discrete differential geometry. Concerning phase field models, Du et al. introduced and analyzed a discrete semi-implicit scheme for Willmore flow in [DLW04, DW07]. In [BMO15], Bretin et al.

investigated flows for various diffuse approximations of the Willmore energy and its relaxations and introduced corresponding numerical schemes. If the goal is to minimize Willmore energy, one can also consider gradient flows with respect to other metrics. For example, Schumacher [Sch17] analyzed H^2-gradient flows for the Willmore energy with numerical experiments on triangle meshes. Soliman et al. [SCD+21] extended this idea on triangle meshes to incorporate further constraints – most notably on the conformal class of the surface.

Outline. The remainder of the chapter is organized as follows. In Section 6.1, we recapitulate the adaptation of the variational time-discretization to phase fields from [FRW11] and introduce a neural operator approximation of mean curvature flow for phase fields inspired by [BDMT22]. We combine both to obtain the spatially discrete hybrid scheme for Willmore flow in Section 6.2. In Section 6.3, we first experimentally validate the convergence properties of the neural network-based discrete mean curvature flow to then underpin a corresponding validation of our hybrid Willmore flow scheme. Furthermore, we use our hybrid scheme to compute the evolution for different interesting initial curves in 2D and surfaces in 3D. Afterwards, in Section 6.4, we apply the scheme for curve and surface restoration.

6.1 Synthesis of the time-discrete Willmore flow

Our scheme has two essential ingredients: a *phase field based minimizing movement scheme for Willmore flow* as introduced by Franken et al. [FRW11], and a *convolution based approximation of mean curvature*. Below, we will first discuss the relevant parts of the former, then detail the latter and describe how both are combined for the purpose of a robust and efficient approximation of Willmore flow.

Phase field based minimizing movement scheme for Willmore flow. Following Franken et al. [FRW11], we assume that hypersurfaces under consideration are represented by Modica–Mortola-type phase field functions [MM77] with periodic boundary conditions. In what follows, we assume that all functions and interfaces are sufficiently smooth. We consider the interfacial energy

$$\mathcal{P}^\varepsilon[v] := \frac{1}{2}\int_\Omega \varepsilon\|\nabla v\|^2 + \frac{1}{\varepsilon}\Psi(v)\,\mathrm{d}x \tag{6.3}$$

with the double well potential $\Psi(v) = \frac{9}{16}(1-v^2)^2$. Modica and Mortola [MM77] showed that the Γ-limit of $\mathcal{P}^\varepsilon[\cdot]$ in the L^1 topology is half the total variation of a function $u \in BV(\Omega;\{-1,1\})$ in Ω, i.e. the perimeter of the set $\{u=1\}$.

Phase field functions minimizing (6.3) follow an optimal profile in normal direction across the boundary of a set $\omega \subset \Omega$, which is $\tilde{v}_\varepsilon\colon \mathbb{R}\to\mathbb{R};\ s\mapsto \tanh(-\frac{3s}{4\varepsilon})$. Thus, $\tanh\left(-\frac{3}{4\varepsilon}\mathrm{sdist}(y,\omega)\right)$ is the optimal phase field profile of an interface $\mathcal{M} = \partial\omega\cap\Omega$ for fixed ε, where the signed distance function of $\mathcal{M}$ is defined as $\mathrm{sdist}(x,\omega) = \mathrm{dist}(x,\omega) - \mathrm{dist}(x,\omega^c)$ with ω^c being the complement of ω. Now, let u_ε^k denote the phase field representations of the hypersurface $\mathcal{M}^k$ with parametrization x^k, which is the boundary of a subset $\omega^k\subset\Omega$, i.e. $\mathcal{M}^k = \partial\omega^k\cap\Omega$. Similarly, let u_ε be the representation of $\mathcal{M} = \partial\omega\cap\Omega$ with parametrization x, and $v_{\tilde{\tau}}[u_\varepsilon]$ a phase field representation of the image of $\mathcal{M}$ under timestep of mean curvature flow with step size $\tilde{\tau}$ and initial data u_ε. Following Franken et al. [FRW11], we take into account a further

minimizing movement scheme to define the operator $v_{\tilde{\tau}}[\cdot]$ variationally and obtain

$$v_{\tilde{\tau}}[u] := \operatorname*{arg\,min}_{v \in H^1(\Omega)} \left(\varepsilon \|u - v\|^2_{L^2(\Omega)} + 2\tilde{\tau} \mathcal{P}^\varepsilon[v] \right). \tag{6.4}$$

To translate (6.2) to the phase field context, one observes for a shift δ of the optimal profile $\tilde{v}_\varepsilon$ in one dimension

$$\varepsilon \int_{\mathbb{R}} (\tilde{v}_\varepsilon(s) - \tilde{v}_\varepsilon(s-\delta))^2 \, \mathrm{d}s = \delta^2 (1 + \Theta(\delta, \varepsilon)),$$

where $\Theta(\delta, \varepsilon) = C \left(\frac{\delta}{\varepsilon} + \frac{\delta^2}{\varepsilon^2} \right)$. A detailed calculation is given in [FRW11]. Chosing $\delta = \varepsilon^\beta$ with $\beta > 1$ implies $\Theta(\delta, \varepsilon) \leqslant C\delta^{(1-\frac{1}{\beta})}$ and thus

$$\varepsilon \int_\Omega (u_\varepsilon(x + \delta(x) n(x)) - u_\varepsilon(x))^2 \, \mathrm{d}x = \int_{\mathcal{M}} \delta^2(x) \mathcal{H}^{d-1} \left(1 + O(\Theta(\|\delta\|_\infty, \varepsilon))\right),$$

where now δ is some function on $\mathcal{M}$, n is the normal field of $\mathcal{M}$ and δ is assumed to be extended constantly in normal direction to $\mathcal{M}$. Next, assuming that all involved phase field functions u^k, u, and $v_{\tilde{\tau}}[u]$ follow the optimal profile, one observes that

$$\begin{aligned} \varepsilon \|v_{\tilde{\tau}}[u] - u\|^2_{L^2(\Omega)} &= \|y_{\tilde{\tau}}[x] - x\|^2_{L^2(\mathcal{M})} \left(1 + O(\Theta(\|y_{\tilde{\tau}}[x] - x\|_{L^\infty(\mathcal{M})}, \varepsilon))\right), \\ \varepsilon \|u - u^k\|^2_{L^2(\Omega)} &= \|x - x^k\|^2_{L^2(\mathcal{M}^k)} \left(1 + O(\Theta(\|x - x^k\|_{L^\infty(\mathcal{M}^k)}, \varepsilon))\right). \end{aligned}$$

The above estimates were presented in [FRW11] using the double well function $\Psi(v) = (1-v^2)^2$ and thus consistently with an additional factor $\frac{4}{3}$ (and optimal profile $\tilde{v}_\varepsilon(s) = \tanh(-s\varepsilon^{-1})$).

Finally, with these approximations at hand, one can define the energy

$$e^\varepsilon[u^k, u] = \varepsilon \|u - u^k\|^2_{L^2(\Omega)} + \frac{\tau\varepsilon}{\tilde{\tau}^2} \|v_{\tilde{\tau}}[u] - u\|^2_{L^2(\Omega)} \tag{6.5}$$

for two functions u^k and u considered as phase field descriptions of $\mathcal{M}^k$ and $\mathcal{M}$. By our above estimates, this energy is equivalent to the energy $e[\cdot]$ associated with the variational time-discretization in (6.2).

Altogether for sufficiently small phase field parameter ε and sufficiently small time step sizes τ, $\tilde{\tau}$, this leads to the following nested variational time discretization of Willmore flow:

Definition 6.1 (Variational time discretization of Willmore flow [FRW11]). *For $e^\varepsilon[\cdot,\cdot]$ defined in* (6.5) *based on some mapping $v_{\tilde{\tau}} \colon L^2(\Omega) \to L^2(\Omega)$ with τ, $\tilde{\tau} > 0$ and some $u^0 \in L^2(\Omega)$ we iteratively compute*

$$u^{k+1} = \operatorname*{arg\,min}_{u \in L^2(\Omega)} e^\varepsilon[u^k, u] \tag{6.6}$$

as the time discrete phase field solution at time $(k+1)\tau$ for $k \in \mathbb{N}_0$.

Convolution-based approximation of mean curvature. Thus far, we have defined $v_{\tilde{\tau}}[u]$ variationally, and obtained an inner variational problem to be solved for every u in the outer problem (6.6). Instead of solving the Euler-Lagrange equation associated with (6.4) for every function u arising in the outer problem, we pick up the approach by Bretin et al. [BDMT22].

To this end, we define a spatially continuous neural operator $v_{\tilde{\tau}}^{f,\kappa}\colon L^2(\Omega) \to L^2(\Omega)$ that will be trained to approximate $v_{\tilde{\tau}}[\cdot]$. We follow the structure proposed for the discrete context in [BDMT22] and combine a nonlinear activation function and a convolution operator to define the neural operator $v_{\tilde{\tau}}^{f,\kappa}$. This leads to the definition of the still spatially continuous neural operator

$$v_{\tilde{\tau}}^{f,\kappa}[u] \coloneqq f_{\tilde{\tau}} \circ (\kappa_{\tilde{\tau}} * u), \tag{6.7}$$

where one first applies a convolution kernel $\kappa_{\tilde{\tau}} \in L^2(\mathbb{R}^d)$, followed by the concatenation with a nonlinear activation function $f_{\tilde{\tau}} \in C^0(\mathbb{R})$. When applying the kernel $\kappa_{\tilde{\tau}}$ to u, we assume that u is periodically extended to all of $\mathbb{R}^d$. The convolution $\kappa_{\tilde{\tau}} * u$ with $\kappa_{\tilde{\tau}} \in L^2(\mathbb{R}^d)$ is in $C^0(\mathbb{R}^d)$. Thus, $v_{\tilde{\tau}}^{f,\kappa}[u] \in C^0(\mathbb{R}^d)$ as well and can in particular be evaluated point-wise.

When using the neural operator $v_{\tilde{\tau}}^{f,\kappa}$ in the nested scheme (6.5), we obtain a time-discrete but spatially still continuous scheme. It combines a standard optimization problem over functions in $L^2(\Omega)$ with a neural operator acting on functions in $L^2(\Omega)$.

Remark 6.2 (Relation to the Merriman–Bence–Osher scheme and semi-implicit time stepping for Allen-Chan flow)**.** *To motivate the neural network architecture used by Bretin et al. we first observe that the rescaled L^2-gradient flow of $\mathcal{P}^\varepsilon$ with time discretization* (6.4) *is given by the Allen–Cahn equation $\partial_t u - \Delta u + \frac{1}{2\varepsilon^2}\Psi'(u) = 0$. Evaluating the nonlinearity Ψ' implicitly at u^{k+1} and the Laplace operator explicitly at u^k we obtain the time-discrete equation*

$$\tfrac{u^{k+1}-u^k}{\tilde{\tau}} - \Delta u^k + \tfrac{1}{2\varepsilon^2}\Psi'(u^{k+1}) = 0 \tag{6.8}$$

to iteratively compute the sequence $(u^k)_{k\in\mathbb{N}}$ of phase fields given an initial phase field u^0. The function $\phi_{\varepsilon,\tilde{\tau}}(u) = u + \frac{\tilde{\tau}}{2\varepsilon^2}\Psi'(u)$ is monotone for $\frac{\tilde{\tau}}{\varepsilon^2} < \frac{8}{9}$ and thus invertible. Hence, (6.8) *can be rewritten as $u^{k+1} = \phi_{\varepsilon,\tilde{\tau}}^{-1}((\mathrm{Id} + \tilde{\tau}\Delta)u^k)$ and finally using the approximation $(\mathrm{Id} + \tilde{\tau}\Delta)u^k = e^{-\tilde{\tau}\Delta}u^k + O(\tilde{\tau}^2)$ we obtain $u^{k+1} = \phi^{-1}(e^{-\tilde{\tau}\Delta}u^k)$. This indeed reflects the structure* (6.7) *proposed by Bretin et al. [BDMT22] and resembles the Merriman–Bence–Osher (MBO) scheme [MBO92, MBO94] for characteristic functions, where one first solves the linear heat equation with time step $\tilde{\tau}$ for a characteristic function as the initial data and then applies a thresholding function to obtain the time step updated characteristic function. In this sense, the application of the function $\phi_{\varepsilon,\tilde{\tau}}^{-1}$ acts as a soft thresholding. For the convergence to mean curvature motion, we refer to [Eva93] and [BG95]. Recently, Budd and van Gennip [BvG20] studied a semi-implicit time-discretization for the double obstacle Allen–Cahn equation on graphs and proved that the MBO scheme coincides with a particular choice of a semi-implicit scheme for Allen–Cahn flow. The scheme takes the form $u^{k+1} = \rho \circ \left(e^{-\tilde{\tau}\Delta}u^k\right)$, with Δ being the (positive definite) graph Laplacian, ρ a monotone Lipschitz continuous (activation) function, and $e^{-\tilde{\tau}\Delta}$ the linear operator representing one timestep of the heat flow with time step size $\tilde{\tau}$. The authors explicitly refer to the analogy of a convolutional neural network in [BvG20, footnote 6].*

As proposed in [BDMT22], both the kernel $\kappa_{\tilde{\tau}}$ and the scalar function $f_{\tilde{\tau}} \in C^0(\mathbb{R})$ are learned from data. Bretin et al. suggested using (discrete) phase field profiles for the explicitly known evolution of hyperspheres in $\mathbb{R}^d$ as training data. Indeed, the radius of a hypersphere evolving under mean curvature flow with initial radius r_0 at time $\tilde{\tau}$ is given by

$$R(r_0, \tilde{\tau}) = \sqrt{r_0^2 - 2(d-1)\tilde{\tau}}\,. \tag{6.9}$$

For a hypersphere of radius r, we define the corresponding phase field profile by $u_r(x) := \tanh\left(\frac{3(r-|x|)}{4\varepsilon}\right)$. The aim is to learn $f_{\tilde{\tau}}$ and $k_{\tilde{\tau}}$ such that, for a range of radii r, the phase field representation of a hypersphere of radius r is mapped to one of a hypersphere of radius $R(r,\tilde{\tau})$, i.e. $v_{\tilde{\tau}}^{f,\kappa}[u_r] \approx u_{R(r,\tilde{\tau})}$. This way, $v_{\tilde{\tau}}^{f,k}$ approximates the time-discrete solution operator of mean curvature flow on the chosen training data. We formulate an optimization problem by turning the desired relation into a least-squares loss, and thus determine $f_{\tilde{\tau}}$ and $k_{\tilde{\tau}}$ as solutions of

$$\min_{f,\kappa} \int_{r_{\min}}^{r_{\max}} \|v_{\tilde{\tau}}^{f,\kappa}[u_r] - u_{R(r,\tilde{\tau})}\|_{L^2(\mathbb{R}^d)}^2 \,\mathrm{d}r, \tag{6.10}$$

where one optimizes over suitable classes of nonlinear functions f and convolution kernels κ for a suitable choice of $r_{\min}$ and $r_{\max}$.

Remark 6.3. *In their study, Bretin et al. [BDMT22] focused on a discrete formulation on regular grids and directly developed a time and space discrete evolution operator for mean curvature motion. The underlying neural network consists of a single convolution layer and a scalar activation function realized with a multilayer perceptron. Bretin et al. demonstrated empirically that this also leads to a reasonable approximation of mean curvature flow for fairly general initial data and corresponding phase fields. Functions of the form* (6.7) *are efficient to evaluate and differentiate when implemented on discrete grids using neural networks. We will retrieve this discrete formulation in the next section.*

Furthermore, employing the scheme composed of (6.5) and (6.7), we can show the existence of time-discrete Willmore flow, i.e. the existence of minimizers of (6.5) for fixed scalar function$f$ and convolution kernel κ:

Proposition 6.4. *For $\Omega = (0,1)^d$, $u^0 \in L^2(\Omega)$ periodically extended on $\mathbb{R}^d$, and $e^\varepsilon[u^0,\cdot]$ as in* (6.5) *with $v_{\tilde{\tau}}$ of the form $v_{\tilde{\tau}}[u] = f(\kappa * u)$ for fixed $f \in C(\mathbb{R})$ and $\kappa \in L^2(\mathbb{R}^d)$ there exists a minimizer $u \in L^2(\Omega)$ of $e^\varepsilon[u^0,\cdot]$ in the class of periodically extended $L^2(\Omega)$ functions.*

Proof. Let $(u_j)_j \subset L^2(\Omega)$ be a minimizing sequence of $e^\varepsilon[u^0,\cdot]$, with

$$C = e^\varepsilon[u^0,u^0] \geqslant e^\varepsilon[u^0,u_j] \geqslant \varepsilon\|u^0-u_j\|_{L^2(\Omega)}^2 \geqslant \frac{\varepsilon}{2}\|u_j\|_{L^2(\Omega)}^2 - \varepsilon\|u^0\|_{L^2(\Omega)}^2,$$

for a constant C depending on $\|u^0\|_{L^2(\Omega)}$. Here, we used that $\|\kappa * u_0\|_{C^0(\bar{\Omega})}$ is bounded and applied Young's inequality. Hence, $\|u_j\|_{L^2(\Omega)} \leqslant \hat{C}$ for some constant $\hat{C}$, and thus there exists $u \in L^2(\Omega)$, and a subsequence (not relabeled), with $u_j \rightharpoonup u$ weakly in $L^2(\Omega)$. Once more using that $\kappa \in L^2(\mathbb{R}^d)$, we have

$$(\kappa * u_j)(x) = \int_\Omega \kappa(x-y)u_j(y)\,\mathrm{d}y \to \int_\Omega \kappa(x-y)u(y)\,\mathrm{d}y = (\kappa * u)(x)$$

for $j \to \infty$. Furthermore, we observe

$$\sup_{x\in\Omega} \left|(\kappa * u_j)(x)\right| \leqslant \|\kappa\|_{L^2(\mathbb{R}^d)}\|u_j\|_{L^2(\Omega)} \leqslant \hat{C}\|\kappa\|_{L^2(\mathbb{R}^d)}.$$

Since f is uniformly continuous on $[-\hat{C}\|\kappa\|_{L^2(\mathbb{R}^d)}, \hat{C}\|\kappa\|_{L^2(\mathbb{R}^d)}]$, we obtain $f(\kappa * u_j) \to f(\kappa * u)$ pointwise and in $L^2(\Omega)$. Finally, lower semicontinuity of the L^2 norm implies

$$\inf_{\tilde{u}\in L^2(\Omega)} e^\varepsilon[u^0,\tilde{u}] = \liminf_{j\to\infty} e^\varepsilon[u^0,u_j] \geqslant e^\varepsilon[u^0,u].$$

Thus $u \in L^2(\Omega)$ and minimizes $e^\varepsilon[u^0,\cdot]$ in the class of periodically extended $L^2(\Omega)$ functions. □

6.2 Spatial discretization

Minimizing movement scheme for Willmore flow. To discretize the time-discrete Willmore flow in $\mathbb{R}^d$ based on the minimizing movement scheme (6.5), we consider a regular grid on $[0,1]^d$ with gridsize $h = \frac{1}{n}$ for $n \in \mathbb{N}$ and nodes $x_\alpha = (\frac{\alpha_1}{n}, \cdot, \frac{\alpha_d}{n})$ for a multi-index α in the multi index set $\mathcal{I}_n := (\{0, \dots, n\})^d$. On this grid we consider functions represented by nodal vectors $U \in \mathbb{R}^{|\mathcal{I}_n|}$ with function values U_α at nodes x_α. A discrete L^2 norm is defined as

$$\|U\|_{L^2} := \sqrt{(n+1)^{-d} \sum_{\alpha \in \mathcal{I}_n} (U_\alpha)^2},$$

i.e. the square root of the average of the squared entries of U. Thus, the discrete counterpart of the energy (6.5) is given by

$$E^\varepsilon[U^k, U] = \varepsilon \|U - U^k\|_{L^2}^2 + \frac{\tau\varepsilon}{\tilde{\tau}^2} \|V_{\tilde{\tau}}[U] - U\|_{L^2}^2, \tag{6.11}$$

where $V_{\tilde{\tau}}[U]$ denotes a spatially discrete counterpart of (6.7).

Neural approximation of discrete mean curvature flow. Here, we follow the approach by Bretin et al. [BDMT22] and consider discrete kernels and nonlinear activation functions, which are defined themselves as networks. For a discrete kernel $K \in \mathbb{R}^{\mathbb{Z}^d}$, one defines the nodal vector resulting from the discrete convolution with this kernel as

$$(K * U)_\alpha := \sum_{\beta \in \mathbb{Z}^d} K_\beta U_{\alpha+\beta}.$$

Here, we assume periodicity of the discrete function to which we apply the discrete convolution, i.e. $U_{\alpha+\beta n} = U_\alpha$ for $\beta \in \mathbb{Z}^d$. Now, one considers discrete kernels with a fixed width n_K and a n_K^d stencil, i.e. $K_\alpha = 0$ for $\max_{i=1,\dots,d} |\alpha_i| > \frac{n_K - 1}{2}$. To ensure consistency with the continuous mean curvature motion, the necessary size n_K of the kernel depends on the time step size $\tilde{\tau}$ and the grid size h. At the same time, smaller kernels are more efficient to train, which creates a trade-off between accuracy and speed. This trade-off will be explored in our numerical experiments below. The point-wise function f is discretized using a fully-connected neural network $F^\theta \colon \mathbb{R} \to \mathbb{R}$ with L layers and layer sizes $N_1, \dots, N_L$. The lth layer is described in terms of a weight matrix $W^l \in \mathbb{R}^{N_l \times N_{l-1}}$ with $N_0 = 1$ and a bias vector $b^l \in \mathbb{R}^{N_l}$. These degrees are gathered in a parameter vector $\theta = (W^1, \dots, W^L, b^1, \dots, b^L)$. Then, one defines $F^\theta(s) = s^L$ with $s^l := \rho\left(W^l s^{l-1} + b^l\right)$ and $s^0 = s$ and the choice $\rho(s) = \exp(-s^2)$ as the nonlinear activation function. In practice, we used six layers with sizes 32, 16, 8, 4, 2, 1. For given parameters θ and K, we obtain the discrete operator

$$V_{\tilde{\tau}}^{\theta,K}[U] := F^\theta(K * U). \tag{6.12}$$

Now, one approximates the optimization problem (6.10) via our discretization and a sampling of training data. To this end, one considers m radii $r_1, \dots, r_m$ sampled uniformly from an interval $[r_{\min}, r_{\max}]$ and minimizes the loss functional

$$\mathcal{L}[\theta, K] = \frac{1}{m} \sum_{i=1}^{m} \|V_{\tilde{\tau}}^{\theta,K}[U_{r_i}] - U_{R(r_i,\tilde{\tau})}\|_{L^2}^2, \tag{6.13}$$

over the total set of parameters (θ, K), where U_r are nodal evaluations of the hypersphere phase fields u_r. We approximately solve problem (6.13) using the Adam optimizer [KB15], with $m = 100$, $r_{\min} = 0.05$, $r_{\max} = 0.4$, and usually employ mini-batching, i.e. approximating the sum in (6.13) using only ten randomly drawn radii, to speed up the minimization as was proposed by Bretin et al. [BDMT22]. The overall method is described in Algorithm 6.1. The resulting neural phase field operator $V_{\tilde{\tau}}^{\theta,K}[\cdot]$ approximates the PDE solution $v_{\tilde{\tau}}$ defined in (6.4) and is inexpensive to evaluate.

Algorithm 6.1 Learning the fully discrete mean curvature operator (offline phase) [BDMT22]

Input: Time step size $\tilde{\tau}$ of mean curvature flow, interface parameter ε, kernel size n_K, gridsize $h = \frac{1}{n}$, number of samples m, minimal radius $r_{\min}$, maximal radius $r_{\max}$

Output: Discrete convolution kernel K and parameter vector θ

1: Create the training data by uniformly sampling m radii $r_1, \dots, r_m$ from the interval $[r_{\min}, r_{\max}]$ and computing the corresponding pairs of discrete phase fields $(U_{r_i}, U_{R(r_i,\tilde{\tau})})$
2: Initialize kernel K and parameter vector θ as zero or using interpolation of coarser resolution
3: **while** not converged **do**
4: Randomly sample $\frac{m}{B}$ mini-batches $\{i_1, \dots, i_B\}$ of size B from $\{1, \dots, m\}$ by drawing without replacement
5: **for all** mini-batches $\{i_1, \dots, i_B\}$ **do**
6: Compute the loss for the mini-batch

$$\mathcal{L}[\theta, K] = \frac{1}{B} \sum_{k=1}^{B} \| V_{\tilde{\tau}}^{\theta,K}[U_{r_{i_B}}] - U_{R(r_{i_B},\tilde{\tau})} \|_{L^2}^2$$

7: Compute the gradient of the previous loss using back-propagation
8: Update the parameters θ and K using the Adam optimizer
9: **end for**
10: **end while**

Hybrid scheme for Willmore flow We employ Newton's method with Armijo line search to minimize $E^\varepsilon[U^k, U]$ over U. Thus, to determine the descent direction P, we approximately solve the linear system $D^2E^\varepsilon[U^k, \cdot]P = DE^\varepsilon[U^k, \cdot]$ using the conjugated gradient method (see [NW06, Chapter 7]). This also prevents us from having to assemble the Hessian. Instead, we only compute the corresponding matrix-vector product. Furthermore, we manually implemented the derivatives of $E^\varepsilon[U^k, \cdot]$ to improve performance. The overall method is described in Algorithm 6.2. We developed our hybrid method in Python using the PyTorch library [PGM+19] and the nonlinear optimization algorithms used in the pytorch-minimize [Fei21] package, which is based on the optimization module of SciPy [VGO+20].

Here, D_2 and D_2^2 indicate the Jacobian and the Hessian with respect to the second argument, respectively.

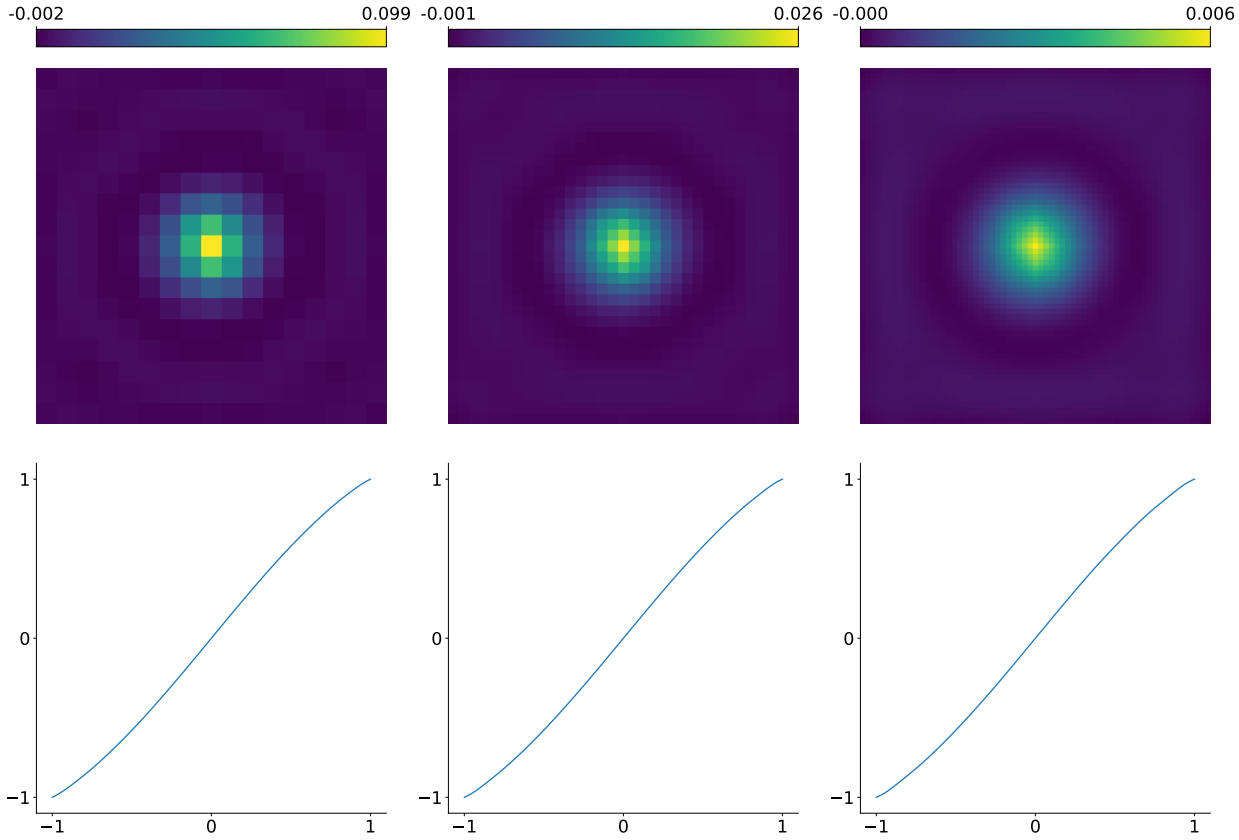

Figure 6.1: Learned networks for $\varepsilon = 2^{-6}$ and $\tilde{\tau} = 2^{-14}$ are displayed via a color coding of the learned kernels K and the graphs of learned activation function F^θ on the interval $[-1, 1]$ for increasing $n = 128, 256, 512$, with stencil widths $n_K = 17, 33, 65$, respectively.

Algorithm 6.2 Hybrid scheme for Willmore flow (online phase)

Input: Discrete phase field U^k at time $k\tau$ of Willmore flow, discrete convolution kernel K, parameter vector θ, time step size τ of Willmore flow, time step size $\tilde{\tau}$ of inner mean curvature flow, interface parameter ε

Output: Discrete phase field U^{k+1} at time $(k+1)\tau$ of Willmore flow

1: Initialize $U^{k+1} = U^k$
2: **while** not converged **do**
3: Evaluate $V_{\tilde{\tau}}^{\theta,K}[U^{k+1}] = F^\theta(K * U^{k+1})$ ▷ (6.12)
4: Compute $E^\varepsilon[U^k, U^{k+1}] = \varepsilon\|U^{k+1} - U^k\|_{L^2}^2 + \frac{\tau\varepsilon}{\tilde{\tau}^2}\|V_{\tilde{\tau}}[U^{k+1}] - U^{k+1}\|_{L^2}^2$ ▷ (6.11)
5: Compute $D_2E^\varepsilon[U^k, U^{k+1}]$ and $D_2^2E^\varepsilon[U^k, U^{k+1}]$ using chain rule
6: Solve $D_2^2E^\varepsilon[U^k, U^{k+1}]P = D_2E^\varepsilon[U^k, U^{k+1}]$ using the CG method
7: Determine step size t via Armijo line search
8: Set $U^{k+1} = U^{k+1} + tP$
9: **end while**

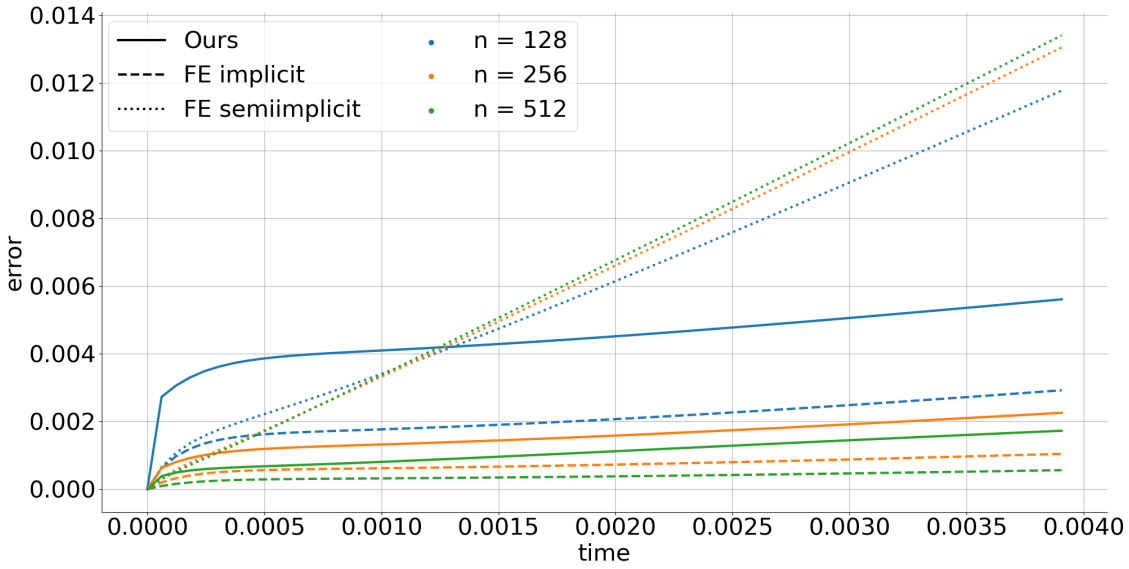

Figure 6.2: Convergence plot for mean curvature flow with fixed $\varepsilon = 2^{-6}$ and $\tilde{\tau} = 2^{-14}$ while increasing n, with $n_K = \frac{n}{8} + 1$. We plot the average L^2-error to the analytic solution along time for 30 circles with radii $r_i = 0.05\pi + \frac{0.15\pi i}{30}$, $i = 0, \dots, 29$. The line styles correspond to the different methods and the colors to the varying resolution. For comparison: for the averaged L^2 distance between the solution at time 0.004 and at the initial time zero, one obtains $\frac{1}{30}\sum_{i=1}^{30} \|U_{R(r_i,0.004)} - U_{R(r_i,0)}\|_{L^2} \approx 0.133$.

6.3 Numerical experiments

As usual in nonlinear optimization, the chosen initialization when solving (6.13) impacts the result. For example, Bretin et al. [BDMT22] successfully trained their network on a resolution of $n = 256$ with stencil width $n_K = 17$, $\varepsilon = 2h$, and $\tilde{\tau} = \varepsilon^2$. They initialized the kernel as zero and the parameters θ randomly sampled from a normal distribution. However, when refining h while keeping ε fixed, and thus consistently increasing n_K, we observed a degradation of the approximation quality of $V_{\tilde{\tau}}^{\theta,K}[\cdot]$. We mitigated this by first training the network on a coarse resolution as proposed by Bretin et al. and then progressively passing to finer resolutions. In each step, we initialize the kernel using a bilinear interpolation of the coarser one. For the nonlinearity F^θ, we kept the previous parameters as initialization. The networks resulting from this training process are displayed in Figure 6.1. Using color coding, we show the discrete convolution kernels K. We observe an improved radial symmetry under the spatial refinement and an overall similarity to heat kernels, as it was also observed by Bretin et al. This is consistent with the expected smoothing behavior of mean curvature flow. The learned scalar function F^θ is plotted on the interval $[-1, 1]$, and it is rather stable across different refinement levels.

With this setup, we first investigate the convergence of the neural network-based MCF scheme (6.12) and (6.13) in two dimensions under spatial refinement, i.e. we keep the scale parameter ε and the time step size $\tilde{\tau}$ fixed and increase the spatial resolution and the width of the kernel n_K. We compare the neural network scheme by Bretin et al. [BDMT22] with a fully implicit (cf. (6.4)) and semi-implicit finite element scheme. In the latter, one computes

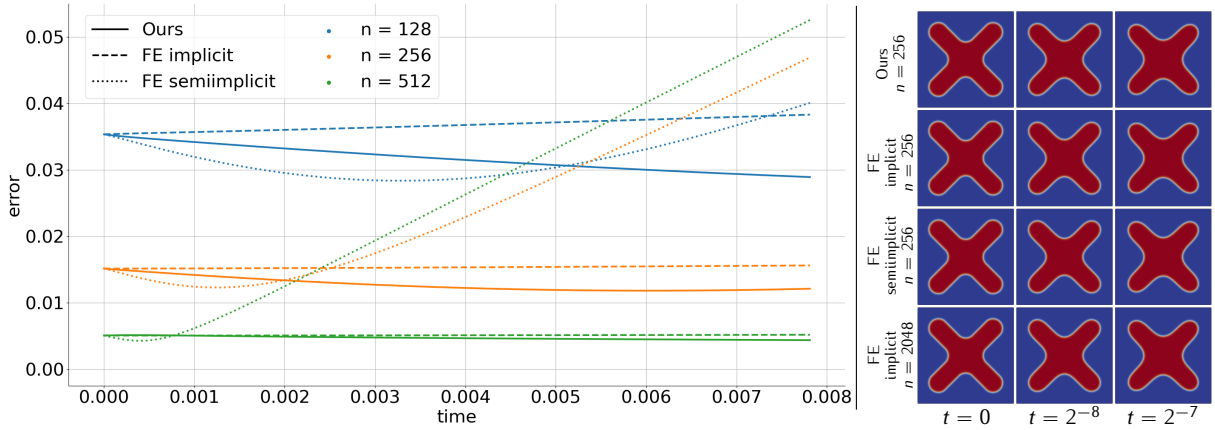

Figure 6.3: Left: Convergence plot for mean curvature flow with fixed $\varepsilon = 2^{-6}$ and $\tilde{\tau} = 2^{-14}$ while increasing n, with $n_K = \frac{n}{8} + 1$ on a cross shape. We plot the L^2-error to an implicit finite element solution with $n = 2048$ and
$tilde\tau = 2^{-16}$. The line styles correspond to the different methods and the colors to the varying resolution. Right: computed mean curvature flow evolution of the cross shape for the different schemes at time steps 0 ($t = 0$), 64 ($t = 2^{-8}$), and 128 ($t = 2^{-7}$).

the solution v at the next timestep as the solution of

$$\frac{v - u}{\tilde{\tau}} = \Delta v - \frac{1}{2\varepsilon^2}\Psi'(u)$$

for given u at the current timestep. Here, we consider a multi-linear finite element approach on the regular quad mesh. We perform the validation of convergence for the evolution of circles on the computational domain $\Omega = (-1, 1)^2$. In Figure 6.2, we plot the average L^2-error over 30 radii ranging from 0.05π to 0.2π when comparing to the exact solutions corresponding to circles with radii given by (6.9). The error is displayed along 64 timesteps of size $\tilde{\tau} = 2^{-14}$ for the different schemes and varying resolution.

One observes that the neural network-based MCF scheme performs noticeably better than the semi-implicit finite element scheme. This confirms the observations made by Bretin et al. [BDMT22] for a single resolution. The fully implicit FE scheme outperforms the network-based scheme, which is not that surprising due to its semi-implicit nature. Besides the error caused by the semi-implicit approach, further error sources are related to the neural operator itself, such as limitations of the network architecture or training data set.

In Figure 6.2, one observes an increase of the error in time for increasing spatial resolution, which appears to be caused by a dominant time discretization error for a fixed time step size $\tilde{\tau}$, which increases with the increasing spatial resolution. Indeed, for $n = 1024$ we observed a further small increase of the error, but the error appeared to saturate (e.g., at about ≈ 0.01353 for $t \approx 0.0039$).

To validate the convergence of the neural network-based MCF scheme on other shapes than circles, where it was trained on, we also investigated the convergence for increasing n on a nonconvex cross shape on the domain $\Omega = (-1, 1)^2$. Since an analytic solution of mean curvature flow for this shape is not at hand, we compared the solutions of the different schemes to a solution of the nested finite element scheme [FRW11] with $n = 2048$, $\tilde{\tau} = 2^{-16}$. In Figure 6.3 on the left, the evolution of the error in time is depicted for the different schemes

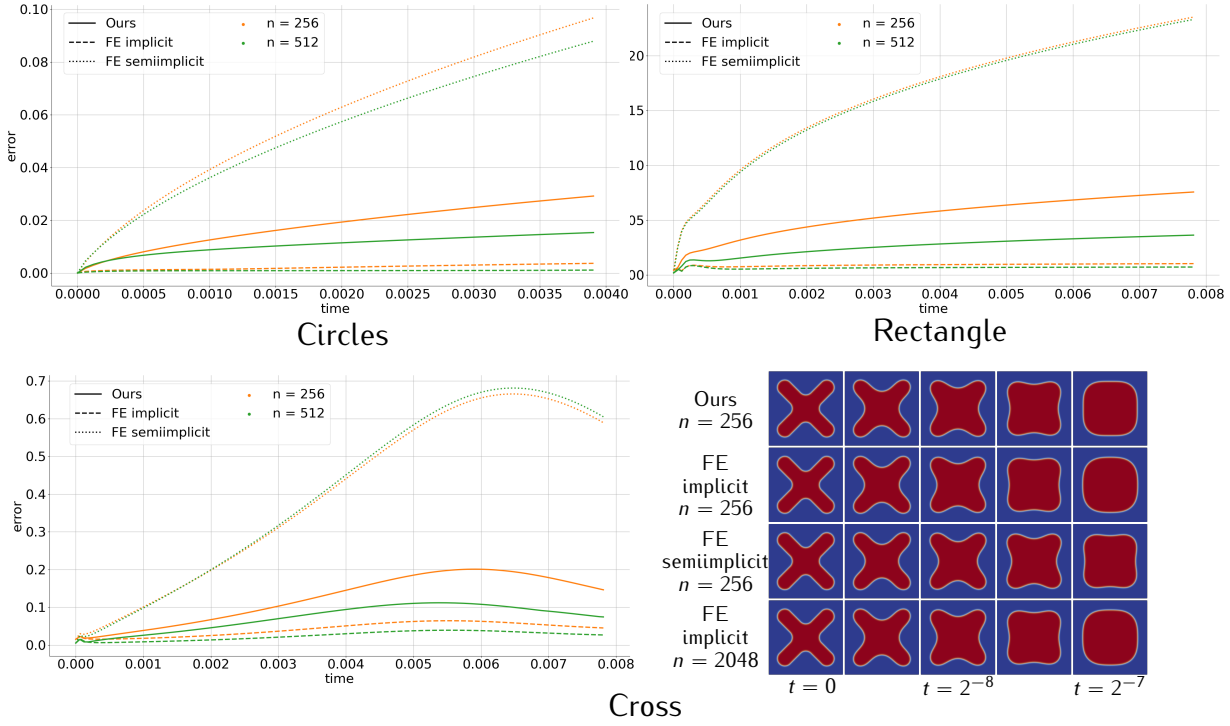

Figure 6.4: Convergence tests for Willmore flow with fixed $\varepsilon = 2^{-6}$ and $\tilde{\tau} = \tau = 2^{-14}$ while increasing n, with $n_K = \frac{n}{8} + 1$. As in Figure 6.2, the line styles correspond to the different methods for approximating the mean curvature evolution and the colors to the varying resolution. In the top left, we plot the average L^2-error to the analytic solution for 30 circles with radii $r_i = 0.05\pi + \frac{0.15\pi i}{30}$, $i = 0, \dots, 29$ over time. For comparison: for the averaged L^2 distance between the solution at time 0.004 and at the initial time zero, one obtains $\frac{1}{30}\sum_{i=1}^{30} \|U_{R_W(r_i,0.004)} - U_{R_W(r_i,0)}\|_{L^2} \approx 0.414$. In the top right, we plot the L^2-error of the evolution of a rectangle with sidelengths 0.4 and 0.2 compared to an implicit finite element solution with $n = 2048$. In the bottom left, we plot the L^2-error of the evolution of a non-convex cross shape compared to an implicit finite element solution with $n = 2048$. In the bottom right, the computed evolution of the cross shape for the different schemes is displayed, for times $t = 0$, $t = 2^{-9}$, $t = 2^{-8}$, $t = 3 \cdot 2^{-9}$, and $t = 2^{-7}$.

and resolutions. Here, ε and $\tilde{\tau}$ are chosen as before. Again, we see that the neural network-based scheme outperforms the semi-implicit finite element scheme, and in this example, even the implicit finite element scheme. That the observed error does not start at zero is due to the interpolation error between the computational resolutions ($n = 128, 256, 512$) and the reference resolution ($n = 2048$). The evolution of the cross shape is displayed on the right in Figure 6.3. We observe that in the time interval considered here, mean curvature flow varies only moderately, whereas the variation is significant for Willmore flow on the identical time interval, see Figure 6.4.

In summary, the network-based MCF scheme positions itself between the semi-implicit and the fully implicit finite element scheme in terms of accuracy.

2d cross shape	$n = 256$	$n = 512$
Ours	122 sec	1020 sec
FE implicit	4970 sec	28622 sec
FE semiimplicit	4307 sec	22045 sec

Table 6.1: Computing time for 128 time steps (until time $t = 0.0078125$) of Willmore flow of the different schemes at different resolutions.

In two dimensions, the evolution of a circle with initial radius r under Willmore flow is given at time τ by a circle with radius

$$R_W(r, \tau) = \sqrt[4]{r^4 + 2\tau}\,.$$

In Figure 6.4 in the top left, the error of our hybrid scheme based on (6.5), with the neural operator (6.12), is displayed, averaging over the same set of initial radii as in Figure 6.2. Again, the different line styles (solid, dashed, dotted) correspond to the different methods for solving the inner MCF problem (hybrid, finite element implicit and semi-implicit). As shown in [FRW11], for $\varepsilon = 2h$ ($h = \frac{1}{n}$), the nested Willmore scheme suffers from numerical instabilities. Hence, we only consider the error evolution for $n = 256$, 512 and for fixed $\varepsilon = 2^{-6}$.

To test our scheme not only on circles, on which the networks were trained, we applied the hybrid scheme to initial data given as the phase field approximation of a rectangle sized 0.4×0.2. Since there is no known analytic solution for Willmore flow in this case, we compare the results to a solution of the nested finite element scheme by Franken et al. [FRW11] on a much finer resolution ($n = 2048$). The corresponding error evolution is displayed on the top right. In addition, we tested our scheme for the cross-shaped initial condition, whose MCF evolution is already examined in Figure 6.3. Again, we compared to the solution of the nested scheme with $n = 2048$, cf. Figure 6.4 on the bottom left.

In all three experiments, we observe that our hybrid approach performs noticeably better than the nested scheme from [FRW11] using a semi-implicit finite element approach for the inner MCF problem, while the fully implicit nested finite element scheme remains the most accurate. This mirrors the observations for MCF in the circle experiment.

Regarding computing time, our hybrid scheme clearly outperforms both finite element schemes. Table 6.1 displays the time required to compute the 128 time steps for the evolution of the cross shape, with an online computing time of our hybrid scheme more than 20 times faster. Here, the computing time of the offline training of the neural operator has not been

taken into account. However, once the model is trained, our experiments indicate that the reduction in computing time appears to be independent of different choices of the initial data.

In Figure 6.4 on the bottom right, we show the evolution of the cross shape under Willmore flow. Compared to the corresponding evolution under MCF, we observe a significantly faster shape variation in the case of Willmore flow, evolving it into an already convex shape at time $t = 2^{-7}$. It is clearly visible that the finite element scheme relying on a semi-implicit time discretization of the inner MCF problem leads to a poorer approximation of Willmore flow, while the results of our scheme are qualitatively indistinguishable from those computed with $n = 2048$ already for $n = 256$. In particular, for applications where one is primarily interested in the qualitative effects of Willmore flow, one can effectively achieve satisfying results already on coarser resolutions, as it will be exploited in the next section.

Our method also captures interesting phenomena of phase field Willmore flow in settings where singularities appear: In Figure 6.5 the Willmore flow evolution of two disjoint circles is shown, forming a singularity where they touch and converging to a growing eight, similar to the numerical experiments in [BMO15].

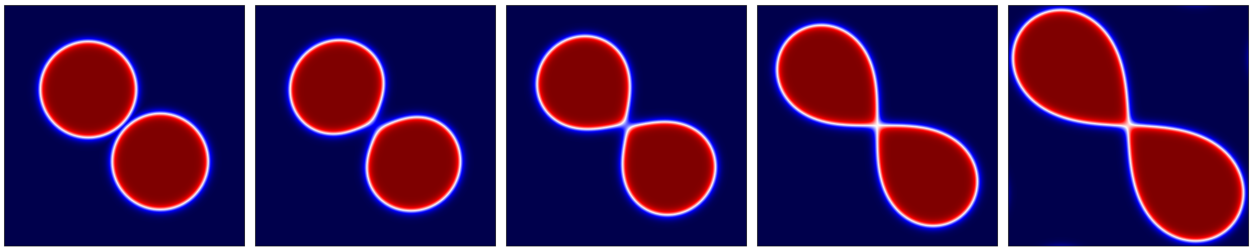

Figure 6.5: Willmore evolution of two circles with radius 0.2. The computing parameters are $n = 512$, $\varepsilon = 2^{-6}$, $\tilde{\tau} = \tau = 2^{-14}$. Shown are time steps 0, 1, 5, 20, and 50.

Remarks on the implementation and the data processing pipeline. We end this section with details on the implementation and data processing pipeline to facilitate reproducibility. As for our hybrid scheme (see Section 6.2), we have implemented the finite element-based approaches in Python using standard libraries. We implemented the nested scheme using Newton's method as described in [FRW11] with direct linear solver PARDISO [SGFS01]. All experiments using the finite element-based approaches were run on a workstation with two 32-core AMD EPYC 7601 processors with 1TB RAM. All experiments using our hybrid approach were run on a workstation with an NVIDIA A100 GPU with 40GB of memory and two 24-core AMD EPYC 7402 processors with 256GB RAM using double-precision floating-point arithmetic on the GPU. The training of the neural MCF operator benefits from additional memory as it allows for caching more of the training data. However, the training is possible with less memory at the moderate expense of speed. Running our scheme, once the MCF operator is trained, requires only a small fraction of the available GPU and CPU memory. For the largest 3D experiment (cf. Figure 6.7) 6.6 GB GPU cache is used for $n = 128$.

The phase fields for the armadillo and the rocker-arm were generated as follows: First, using the tool `mesh_to_voxels` from [Kle21] signed distances were generated on a n^3 grid given a triangular mesh. Then, the optimal phase field profile, as described in Section 6.1, was concatenated with the signed distances to obtain the initial phase field approximation. To generate the images in Figure 6.10 and in Figure 6.7, the zero-level set of the phase field

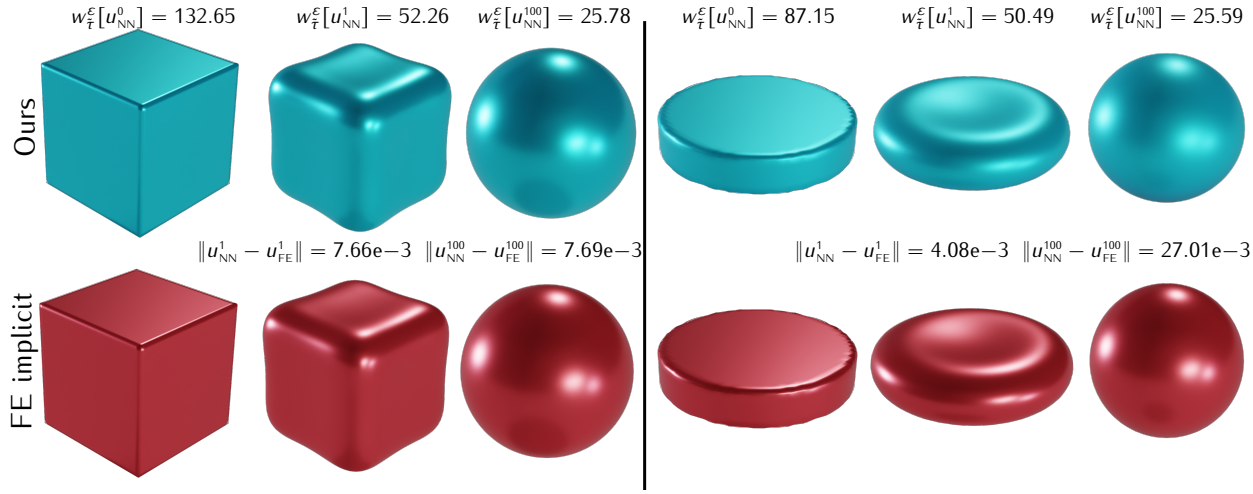

Figure 6.6: Evolution by Willmore flow for a cube surface and a thick disk surface with spatial resolution $n = 64$, interface parameter $\varepsilon = 2^{-5}$, inner stepsize $\tilde{\tau} = 2^{-12}$, and Willmore flow stepsize $\tau = 2^{-18}$. Top row: Our hybrid scheme with kernel size $n_K = 17$. Bottom row: nested implicit finite element scheme from [FRW11]. Results are shown at time 0, 1, and time 100, which reproduce concave surface patches as common effects for Willmore. The approximate phase field Willmore energy (6.14), and the L^2-error between the results of the two schemes are also displayed. For comparison: The exact Willmore energy of a sphere is $8\pi \approx 25.13$.

was extracted using the `Contour` function from Paraview [AGL05]. Finally, all results in 3D were rendered in Blender [Ble18].

6.4 Applications in image and geometry processing

Now that we have introduced and studied our proposed scheme, we will briefly discuss its use for two closely related applications: surface fairing and surface restoration.

In the first of these applications, *surface fairing*, the goal is to create a visually smooth and seamless surface starting from an input surface that is usually noisy or otherwise corrupted. The problem has been studied in the computer graphics and vision communities and curvature flows have established themselves as a classical tool [DMSB99]. Willmore flow is particularly interesting as a basic model for this application [BS05, GA20, SCD+21] since it avoids singularities that could arise with mean curvature flow [CPS13] and preserves C^1 boundary conditions. Certainly, other flows decreasing the Willmore energy, e.g. an H^2-flow [Sch17], would also be suitable. In Figure 6.6, we consider the Willmore flow of surfaces in $\mathbb{R}^3$ for different initial surfaces and compare to the scheme from [FRW11]. Additionally, we see that the approximate Willmore energy of the final shapes

$$w_\tilde{\tau}^\varepsilon[u] := \tfrac{\varepsilon}{2\tilde{\tau}^2}\|v_\tilde{\tau}[u] - u\|^2\,, \tag{6.14}$$

with $v_\tilde{\tau}[u]$ given by (6.4), discretized by finite elements, is close to $8\pi \approx 25.13$, the exact Willmore energy of a round sphere. As the evolution under Willmore flow in 3D is quite fast, we choose a small outer step size τ to prevent the shape losing too many details too quickly. It is in fact usually smaller than the inner MCF step size $\tilde{\tau}$. To show stability for large step sizes, we consider the evolution of the armadillo, often referenced in computer graphics, in

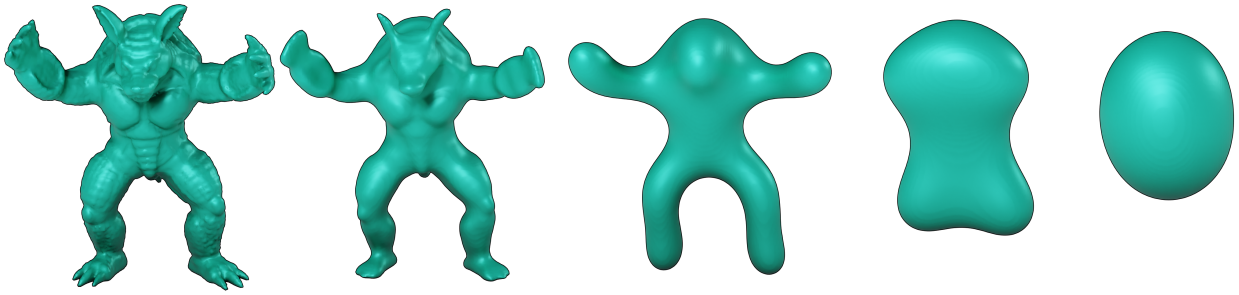

Figure 6.7: Evolution of the armadillo shape under Willmore flow for $n = 128$ and $n_K = 17$, $\varepsilon = 2^{-6}$, and $\tilde{\tau} = 2^{-14}$. The initial outer step size is $\tau = 2^{-22}$. After every time step, the outer step size is doubled. Results are shown at time steps $0, 1, 8, 11$, and 16, respectively.

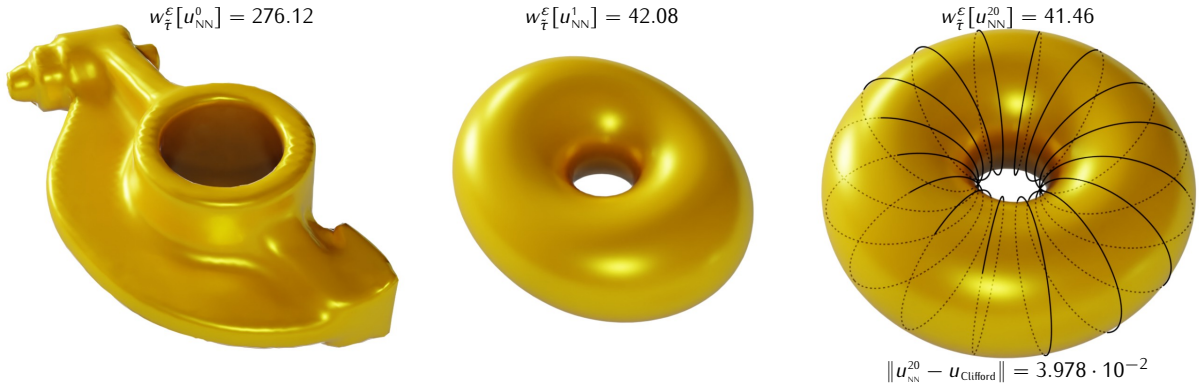

Figure 6.8: Evolution of a rocker arm shape under Willmore flow. The spatial resolution is $n = 64$, the kernel size is $n_K = 17$, the interface parameter $\varepsilon = 2^{-5}$, the inner MCF step size $\tilde{\tau} = 2^{-12}$, and the Willmore flow step size $\tau = 2^{-12}$. We show the discrete timesteps $0, 1$, and 20 leading to an approximation of the Clifford torus. For the last time step, we additionally draw minor circumcircles of the best-approximating Clifford torus.

Figure 6.7, were we start with the very small outer step size $\tau = 2^{-22}$, but double it after every time step, leading to a almost sphere-like shape in 16 time steps.

In Figure 6.8, the Willmore flow of a rocker-arm is displayed, showing the evolution towards a Clifford torus. In [MN14], it was shown that such a torus is a minimizer of the Willmore energy among immersed tori in $\mathbb{R}^3$ with Willmore energy $4\pi^2 \approx 39.48$. Our final shape, after 20 time steps, has an approximate Willmore energy $w_{\tilde{\tau}}^{\varepsilon}[u_{\mathrm{NN}}^{20}] \approx 41.46$, close to $4\pi^2$. To visually compare the final shape to a Clifford torus, we fitted a phase field u_{Clifford} representing a Clifford torus to the phase field of the final shape u_{NN}^{20}. A phase field representation of the Clifford torus is obtained by concatenating the optimal Modica–Mortola profile and a signed distance function of the torus. The free parameters for this fitting are the center coordinates and a SO(3) rotation, and the outer radius. Indeed, the final shape is close to a Clifford torus, with $\|u_{\mathrm{NN}}^{20} - u_{\mathrm{Clifford}}\|_{L^2} \approx 3.978 \cdot 10^{-2}$. The phase field representing a Clifford torus has an approximate Willmore energy $w_{\tilde{\tau}}^{\varepsilon}[u_{\mathrm{Clifford}}] \approx 41.11$.

Concerning computational cost, we show the results comparing our hybrid scheme to the original finite element-based nested Willmore approach by Franken et al. [FRW11] in Table 6.2.

The second application we consider, *surface inpainting*, is a fundamental topic in geometry

Method	Armadillo ($n = 64$)
Ours	807 sec
FE implicit [FRW11]	14589 sec

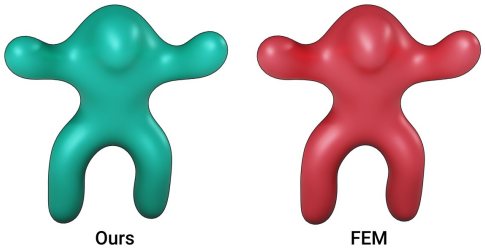

Table 6.2: Performance comparison of our hybrid method to the nested finite element scheme by Franken et al. [FRW11] on the example from Figure 6.7: The results after one step of Willmore flow starting from the shape on the far-left of Figure 6.7 (right), computing time (left). The parameters are $n = 64$, $\varepsilon = 2^{-5}$, $\tau = 2^{-18}$, and $\tilde{\tau} = 2^{-12}$.

and image processing, where one aims to restore corrupted or destroyed parts of an image or a surface. We investigate in this section the use of our hybrid approach to tackle this problem. In a first step, one replaces the corrupted or missing part by an ansatz geometry, whose primary purpose is to prescribe the desired topology. Following the edge restoration approach by Nitzberg et al. [NMS93], one considers the energy (6.5) on the full domain Ω, but only takes into account degrees of freedom in a part $D \subset \Omega$, where the image or surface is corrupted. Then, Willmore flow under this constraint leads to smooth reconstructions of the corrupted area while preserving C^1 boundary conditions on $\partial D \cap \Omega$. We illustrated two examples in two dimensions in Figure 6.9, where the reconstruction region D is outlined in green. In Figure 6.10, we carried out similar experiments in three dimensions. A particularity of Willmore flow in two dimensions is that the reconstruction of the circle in Figure 6.9 takes the enormous number of 2000 timesteps of size $2h$. This is due to the competition of the convex and concave parts in the reconstruction area: positive curvature on the sides pushes the surface outwards, while the middle part with negative curvature tends to move inwards. Only because the curvature of the outer part dominates slightly, the surface moves slowly outwards. In contrast, the reconstruction of the ball in Figure 6.10 does not have the same slow behavior as the circle, because the three-dimensional Willmore energy is scale-invariant.

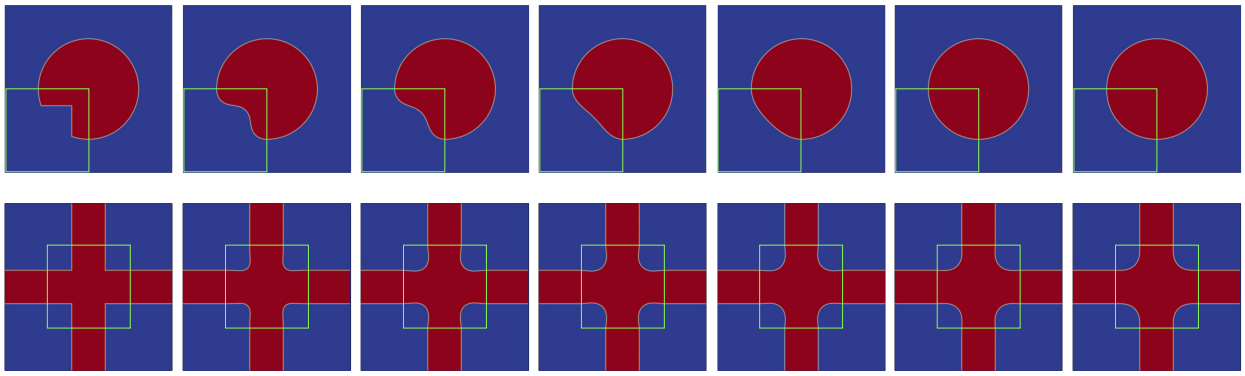

Figure 6.9: Application of our hybrid scheme to image restoration in two dimensions. In both examples, the spatial resolution is $n = 1024$, the kernel size is $n_K = 17$, and the interface parameter $\varepsilon = 2^{-8}$ and the reconstruction region D is outlined in green. In the top row, a disk with a cut-out corner is considered as the initial image and we use $\tilde{\tau} = 2^{-14}$, $\tau = 2^{-7}$. The restoration evolution is shown at times $0, 1, 100, 500, 1000, 1500$, and 2000. In the bottom row, a cross shape is given as the initial image, where the central part is smoothed under discrete Willmore flow with stepsizes $\tilde{\tau} = 2^{-14}$ and $\tau = 2^{-14}$. We show the flow at times $0, 1, 5, 10, 20, 35$, and 50.

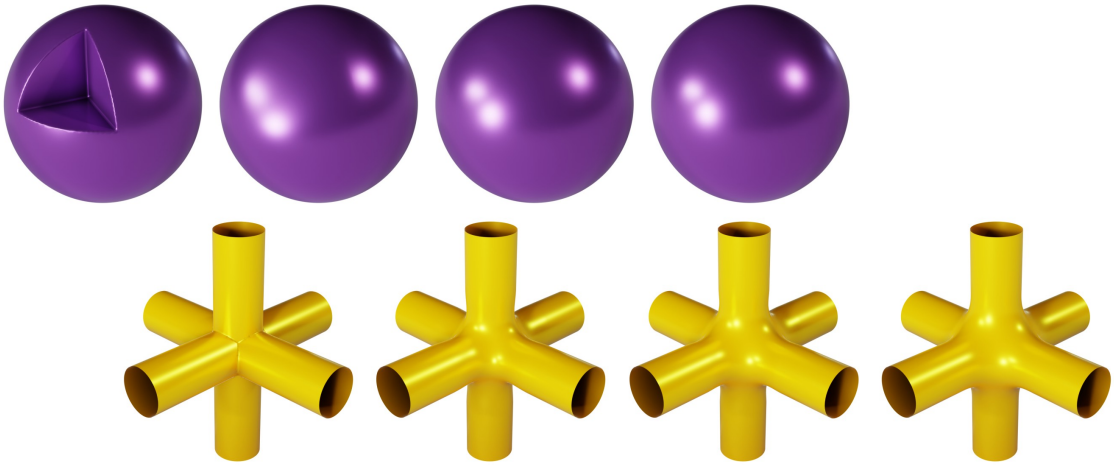

Figure 6.10: Application of our hybrid scheme to surface restoration in three dimensions. In both examples, the spatial resolution was $n = 128$, the kernel size was $n_K = 17$, the interface parameter was $\varepsilon = 2^{-6}$, and the timestep sizes were $\tilde{\tau} = 2^{-14}$ and $\tau = 2^{-21}$. In the top row, the flow at timesteps $0, 1, 3$, and 5 recovering a sphere with an initially cut-out corner is shown. In the bottom row, the flow at timesteps $0, 1, 4$, and 8 leads to a smooth blending of six tubes.

Chapter 7

Conclusion and Outlook

Conclusion. This thesis has explored numerical methods for various nonlinear bending problems. We employed different discretization techniques, ranging from finite element methods based on the DKT element to neural network-based approaches. Alongside extensive numerical experiments to validate the proposed methods, particular emphasis was placed on the numerical analysis of the finite element discretizations, establishing the convergence of discrete solutions to their continuous counterparts.

In Chapter 3, we developed a finite element approximation of a nonlinear bending model for curved surfaces parametrized by a single chart, which was derived by Friesecke et al. [FJMM03]. By reformulating the elastic energy using the nonlinear isometry constraint, we obtained a quadratic dependence on the highest-order terms. We introduced a discretization of this energy based on the DKT element and proved convergence of discrete minimizers to continuous minimizers. Our results extend the work of Bartels [Bar13], which deals with the bending deformations of flat plates. Numerical experiments confirmed both the qualitative and quantitative accuracy of our approach.

In Chapter 4, we introduced a two-scale discretization, based on the heterogeneous multiscale method [EMZ05], of a homogenized plate model derived by Hornung et al. [HNV14]. The microscopic and macroscopic problems were discretized using standard tri-affine finite elements and the DKT element, respectively. Under certain regularity assumptions, we established convergence of discrete solutions to continuous solutions, as the microscopic and the macroscopic grid sizes simultaneously tend to zero. Numerical experiments quantitatively demonstrated this convergence and showed strong agreement with physical experiments on microstructured paper sheets.

In Chapter 5, we proposed a phase field model for the nonlinear bending of a thin plate with a given fold. We provided a Γ-convergence result for the sharp interface limit recovering the model of Bartels et al. [BBH22]. Complementary numerical and physical experiments on folded sheets of paper exhibited qualitatively consistent results. Furthermore, we developed an abstract framework for the optimization of folds described by phase fields, based on the Ambrosio-Tortorelli functional [AT92]. We illustrated its applicability through a representative cost functional.

In Chapter 6, we presented a new hybrid scheme for Willmore flow in a phase field formulation, which combines a minimizing movement ansatz for the flow proposed by Franken et al. [FRW11] with a neural operator approach to compute an approximation of the mean curvature following Bretin et al. [BDMT22]. For a fixed timestep size and scale parameter of the phase field ansatz, the hybrid scheme shows error reduction for increasing spatial

resolution and stencil size of the network kernel. The new scheme comes with significantly reduced computing times. The resulting discrete Willmore flow properly reflects the qualitative behavior of the continuous flow and is, for instance, applicable to the restoration of 2D images and 3D surfaces.

Outlook. The numerical method described in Chapter 3 computes bending deformations of thin shells defined by a single-chart surface parametrization. For more complex geometries, multiple charts are required, motivating the development of an extended numerical framework accommodating multi-chart parametrizations. While we believe that, in principle, our method can be extended to handle several charts, special attention must be given to the consistency of the degrees of freedom along common chart interfaces, for two neighboring charts. A further direction for future research could be the design of optimal shell geometry, for example optimizing structures against gravitational forces. This involves identifying suitable spaces of charts and developing regularization strategies to produce meaningful and manufacturable designs.

The model derived in Chapter 4 relies on a given microstructure, which may vary inside the plate, but is fixed a priori. Recently, Böhnlein et al. [BNS25] extended the approximation result from Chapter 4 to the case of prestrained plates, with a lower regularity assumption on the material coefficients of the microstructure. Extending our two-scale finite element approximation to algorithmic microstructure optimization would enable tailoring of the effective macroscopic elastic behavior. A two-scale optimization framework, possibly based on phase-field descriptions of microstructures as in [DPRS19], would be a natural next step. Furthermore, integrating the methods of Chapter 3 and Chapter 4 could allow for the simulation of bending deformations in microstructured, curved shells—though this would require new analytical results to justify the homogenized, dimension-reduced models.

The phase field fold model from Chapter 5 could also be transferred to the case of curved shells. While this appears feasible numerically, it poses new analytical challenges. Another direction could be to combine Chapter 4 and Chapter 5, to derive a numerical method for microstructured thin plates with folds. Furthermore, we presented a new method for the optimization of folds on nonlinear elastic plates, using phase fields. This method allows for general positive cost functionals and is hence a flexible tool in various applications. We presented two numerical experiments that show the applicability of the method for a simple cost functional. Future work will aim to address more complex optimization objectives and to establish a Γ-convergence result for the sharp-interface limit in this setting.

The results of Chapter 6 encourage the use of neural networks when simulating geometric flows. A future challenge would be to directly learn a solution operator for Willmore flow. In [GH08], Grzhibovskis and Heintz described a convolution thresholding scheme for Willmore flow. Hence, designing a neural network to directly learn Willmore flow does not seem to be out of reach. However, creating proper training data is more subtle. The striking observation in [BDMT22] is that the evolution of spheres under mean curvature flow is sufficient for the approximation of mean curvature flow for a wide range of initial data. For Willmore flow, surely a significantly richer set of training data is required. It is unclear what training data to choose that is adequate to capture Willmore flow.

Bibliography

[AB05] Grégoire Allaire and Robert Brizzi. A multiscale finite element method for numerical homogenization. *Multiscale Modeling and Simulation*, 4(3):790–812, 2005.

[Abd05] Assyr Abdulle. On a priori error analysis of fully discrete heterogeneous multiscale fem. *Multiscale Modeling & Simulation*, 4(2):447–459, 2005.

[Abd06] Assyr Abdulle. Analysis of a heterogeneous multiscale fem for problems in elasticity. *Mathematical Models and Methods in Applied Sciences*, 16(04):615–635, 2006.

[ABM03] Giovanni Alberti, Guy Bouchitté, and Gianni Dal Maso. The calibration method for the Mumford-Shah functional and free-discontinuity problems. *Calc. Var. Partial Differential Equations*, 16 (3):299–333, 2003.

[AFP00] L. Ambrosio, N. Fusco, and D. Pallara. *Functions of bounded variation and free discontinuity problems*. Oxford Mathematical Monographs, 2000.

[AGDP19] Grégoire Allaire, Perle Geoffroy-Donders, and Olivier Pantz. Topology optimization of modulated and oriented periodic microstructures by the homogenization method. *Computers & Mathematics with Applications*, 78(7):2197–2229, October 2019.

[AGL05] James Ahrens, Berk Geveci, and Charles Law. ParaView: An end-user tool for large data visualization. In *Visualization Handbook*. Elsevier, 2005. ISBN 978-0123875822.

[AGS08] Luigi Ambrosio, Nicola Gigli, and Giuseppe Savaré. *Gradient flows: in metric spaces and in the space of probability measures*. Springer Science & Business Media, 2008.

[AT92] Luigi Ambrosio and Vincenzo M. Tortorelli. On the approximation of free discontinuity problems. *Bollettino dell'Unione Matematica Italiana, Sezione B*, 6(7):105–123, 1992.

[Bar13] Sören Bartels. Approximation of large bending isometries with discrete Kirchhoff triangles. *SIAM Journal on Numerical Analysis*, 51(1):516–525, 2013.

[Bar15] Sören Bartels. *Numerical methods for nonlinear partial differential equations*, volume 47 of *Springer Series in Computational Mathematics*. Springer, Cham, 2015.

[Bar17] Sören Bartels. Numerical solution of a Föppl–von Kármán model. *SIAM Journal on Numerical Analysis*, 55(3):1505–1524, 2017.

[BBH80] Jean-Louis Batoz, Klaus-Jürgen Bathe, and Lee-Wing Ho. A study of three-node triangular plate bending elements. *International Journal for Numerical Methods in Engineering*, 15:1771 – 1812, 12 1980.

[BBH22] Sören Bartels, Andrea Bonito, and Peter Hornung. Modeling and simulation of thin sheet folding. *Interfaces and Free Boundaries*, 24(4):459–485, 2022.

[BBHN25] Sören Bartels, Andrea Bonito, Peter Hornung, and Michael Neunteufel. Babuska's paradox in a nonlinear bending model, 2025. arXiv pre-print.

[BBN17] Sören Bartels, Andrea Bonito, and Ricardo H Nochetto. Bilayer plates: Model reduction, Γ-convergent finite element approximation, and discrete gradient flow. *Communications on Pure and Applied Mathematics*, 70(3):547–589, 2017.

[BBN+25] Klaus Böhnlein, Lucas Bouck, Stefan Neukamm, David Padilla-Garza, and Kai Richter. Commutativity and non-commutativity of limits in the nonlinear bending theory for prestrained microheterogeneous plates, 2025. arXiv pre-print.

[BBT23] Sören Bartels, Andrea Bonito, and Philipp Tscherner. Error estimates for a linear folding model. *IMA Journal of Numerical Analysis*, 44(1):1–23, 2023.

[BCC+21] Johanna Burtscheidt, Matthias Claus, Sergio Conti, Martin Rumpf, Josua Sassen, and Rüdiger Schultz. A pessimistic bilevel stochastic problem for elastic shape optimization. *Mathematical Programming*, Nov 2021.

[BDGP23] Eberhard Bänsch, Klaus Deckelnick, Harald Garcke, and Paola Pozzi. *Interfaces: Modeling, Analysis, Numerics*. Oberwolfach Seminars. Birkhäuser, Cham, 2023.

[BDMT22] Elie Bretin, Roland Denis, Simon Masnou, and Garry Terii. Learning phase field mean curvature flows with neural networks. *Journal of Computational Physics*, 470:111579, 2022.

[BG95] Guy Barles and Christine Georgelin. A simple proof of convergence for an approximation scheme for computing motions by mean curvature. *SIAM Journal on Numerical Analysis*, 32(2):484–500, 1995.

[BGM23] Andrea Bonito, Diane Guignard, and Angelique Morvant. Numerical approximations of thin structure deformations. *Comptes Rendus. Mécanique*, 351(S1):181–217, 2023.

[BGM24] Andrea Bonito, Diane Guignard, and Angelique Morvant. Finite element methods for the stretching and bending of thin structures with folding. *Numer. Math.*, 156(6):2031–2068, October 2024.

[BGN07] John W. Barrett, Harald Garcke, and Robert Nürnberg. A parametric finite element method for fourth order geometric evolution equations. *Journal of Computational Physics*, 222(1):441–467, 2007.

[BGNY22] Andrea Bonito, Diane Guignard, Ricardo H. Nochetto, and Shuo Yang. Ldg approximation of large deformations of prestrained plates. *Journal of Computational Physics*, 448:110719, 2022.

[BGNY23] Andrea Bonito, Diane Guignard, Ricardo Nochetto, and Shuo Yang. Numerical analysis of the LDG method for large deformations of prestrained plates. *IMA Journal of Numerical Analysis*, 43:627 – 662, 2023.

[Ble18] Blender Online Community. Blender - a 3d modelling and rendering package, 2018.

[BLS16] Kaushik Bhattacharya, Marta Lewicka, and Mathias Schäffner. Plates with incompatible prestrain. *Archive for Rational Mechanics and Analysis*, 221(1):143–181, 2016.

[BMO15] Elie Bretin, Simon Masnou, and Édouard Oudet. Phase-field approximations of the Willmore functional and flow. *Numerische Mathematik*, 131(1):115–171, 2015.

[BNN21] Andrea Bonito, Ricardo H. Nochetto, and Dimitrios Ntogkas. DG approach to large bending plate deformations with isometry constraint. *Mathematical Models and Methods in Applied Sciences*, 31:133 – 175, 2021.

[BNPGS23] Klaus Böhnlein, Stefan Neukamm, David Padilla-Garza, and Oliver Sander. A homogenized bending theory for prestrained plates. *Journal of Nonlinear Science*, 33(22), 2023.

[BNRS25] Klaus Böhnlein, Stefan Neukamm, Markus Rüggeberg, and Oliver Sander. Dimension-reduced mathematical modeling of self-shaping wooden composite bilayers. *Wood Material Science & Engineering*, 20(3):539–549, 2025.

[BNS25] Klaus Böhnlein, Stefan Neukamm, and Oliver Sander. Finite element discretizations of bending plates with prestrained microstructure, 2025. arXiv pre-print.

[BR13] Nadine Balzani and Martin Rumpf. A nested variational time discretization for parametric Willmore flow. *Interfaces and Free Boundaries*, 14(4):431–454, 2013.

[Bra02] Andrea Braides. *Gamma-Convergence for Beginners*. Oxford University Press, 07 2002.

[Bra13] Dietrich Braess. *Finite Elements*. Springer, 5 edition, 2013.

[BS05] Alexander I. Bobenko and Peter Schröder. Discrete Willmore flow. In *Proceedings of the Third Eurographics Symposium on Geometry Processing*, SGP '05, pages 101–es, Goslar, DEU, 2005. Eurographics Association.

[BST25] Sören Bartels, Bernd Schmidt, and Philipp Tscherner. Numerical simulation of a fine-tunable Föppl-von Kármán model for foldable and bilayer plates, 2025. arXiv pre-print.

[BvG20] Jeremy Budd and Yves van Gennip. Graph Merriman–Bence–Osher as a Semi Discrete Implicit Euler Scheme for Graph Allen–Cahn Flow. *SIAM Journal on Mathematical Analysis*, 52(5):4101–4139, 2020.

[CAMK14] Felix Campelo, Clement Arnarez, Siewert J. Marrink, and Michael M. Kozlov. Helfrich model of membrane bending: From gibbs theory of liquid interfaces to membranes as thick anisotropic elastic layers. *Advances in Colloid and Interface Science*, 208:25–33, 2014. Special issue in honour of Wolfgang Helfrich.

[CD08] Sergio Conti and Georg Dolzmann. Γ-convergence for incompressible elastic plates. *Calc. Var.*, 34:531–551, 2008.

[CDD+04] Ulrich Clarenz, Udo Diewald, Gerhard Dziuk, Martin Rumpf, and Radu B. Rusu. A finite element method for surface restoration with smooth boundary conditions. *Computer Aided Geometric Design*, 21(5):427–445, 2004.

[Cia78] Philippe G. Ciarlet. *The finite element method for elliptic problems*. North-Holland Publishing Co., Amsterdam-New York-Oxford, 1978. Studies in Mathematics and its Applications, Vol. 4.

[Cia88] Philippe G. Ciarlet. *Mathematical Elasticity: Three-Dimensional Elasticity*. Elsevier, 1988.

[Cia00] Philippe G. Ciarlet. *Mathematical Elasticity: Theory of Shells*. Society for Industrial and Applied Mathematics, Philadelphia, PA, 2000.

[CM08] Sergio Conti and Francesco Maggi. Confining thin elastic sheets and folding paper. *Arch. Rat. Mech. Anal.*, 187:1–48, 2008.

[CPS13] Keenan Crane, Ulrich Pinkall, and Peter Schröder. Robust fairing via conformal curvature flow. *ACM Transaction on Graphics*, 32(4), July 2013.

[CZ18] Sebastien JP Callens and Amir A Zadpoor. From flat sheets to curved geometries: Origami and kirigami approaches. *Materials Today*, 21(3):241–264, 2018.

[dBDS21] Miguel de Benito Delgado and Bernd Schmidt. A hierarchy of multilayered plate models. *ESAIM: Control, Optimisation and Calculus of Variations*, 27:S16, 2021.

[DD06] Klaus Deckelnick and Gerhard Dziuk. Error analysis of a finite element method for the Willmore flow of graphs. *Interfaces and Free Boundaries*, 8(1):21–46, 2006.

[DDH15] Marc Dambrine, Charles Dapogny, and Helmut Harbrecht. Shape optimization for quadratic functionals and states with random right-hand sides. *SIAM Journal on Control and Optimization*, 53(5):3081–3103, 2015.

[DFP+22] Xiangxin Dang, Fan Feng, Paul Plucinsky, Richard D James, Huiling Duan, and Jianxiang Wang. Inverse design of deployable origami structures that approximate a general surface. *International Journal of Solids and Structures*, 234:111224, 2022.

[DG93] Ennio De Giorgi. New problems on minimizing movements. *Boundary Value Problems for PDE and Applications*, page 81–98, 1993.

[DGF75] Ennio De Giorgi and Tullio Franzoni. Su un tipo di convergenza variazionale. *Atti Accad. Naz. Lincei Rend. Cl. Sci. Fis. Mat. Nat. (8)*, 58(6):842–850, 1975.

[DLW04] Qiang Du, Chun Liu, and Xiaoqiang Wang. A phase field approach in the numerical study of the elastic bending energy for vesicle membranes. *Journal of Computational Physics*, 198(2):450–468, 2004.

[DM93] Gianni Dal Maso. *An introduction to Γ-convergence*, volume 8 of *Progress in Nonlinear Differential Equations and their Applications, 8*. Birkhäuser Boston, Inc., Boston, MA, Boston, 1993.

[DMSB99] Mathieu Desbrun, Mark Meyer, Peter Schröder, and Alan H. Barr. Implicit fairing of irregular meshes using diffusion and curvature flow. In *Proceedings of the 26th Annual Conference on Computer Graphics and Interactive Techniques*, SIGGRAPH '99, page 317–324, USA, 1999. ACM Press/Addison-Wesley Publishing Co.

[DMSS23] Anna Dall'Acqua, Marius Müller, Reiner Schätzle, and Adrian Spener. The Willmore flow of tori of revolution. *Analysis and PDEs*, 2023. to appear.

[DPRS19] Patrick Dondl, Patrina S. P. Poh, Martin Rumpf, and Stefan Simon. Simultaneous elastic shape optimization for a domain splitting in bone tissue engineering. *Proceedings of the Royal Society A: Mathematical, Physical and Engineering Sciences*, 475(2227):20180718, jul 2019.

[DR04] Marc Droske and Martin Rumpf. A level set formulation for Willmore flow. *Interfaces and Free Boundaries*, 6(3):361–378, 2004.

[DW07] Qiang Du and Xiaoqiang Wang. Convergence of numerical approximations to a phase field bending elasticity model of membrane deformations. *International Journal of Numerical Analysis and Modeling*, 4(3–4):441–459, 2007.

[Dzi91] Gerhard Dziuk. An algorithm for evolutionary surfaces. *Numerische Mathematik*, 58(6):603–611, 1991.

[Dzi08] Gerhard Dziuk. Computational parametric Willmore flow. *Numerische Mathematik*, 111(1):55–80, 2008.

[EE03] Weinan E and Björn Engquist. The heterogeneous multiscale methods. *Commun. Math. Sci.*, 1(1):87–132, 2003.

[EEH03] Weinan E, Björn Engquist, and Zhongyi Huang. Heterogeneous multiscale method: A general methodology for multiscale modeling. *Physical Review B*, 67(9):1–4, March 2003.

[EMZ05] Weinan E, Pingbing Ming, and Pingwen Zhang. Analysis of the heterogeneous multiscale method for elliptic homogenization problems. *J. Amer. Math. Soc.*, 18(1):121–156, 2005.

[Eva93] Lawrence C. Evans. Convergence of an algorithm for mean curvature motion. *Indiana University Mathematics Journal*, 42(2):533–557, 1993.

[Fed96] Herbert Federer. *Geometric Measure Theory*. Springer-Verlag, New York, 1996.

[Fei21] Reuben Feinman. Pytorch-minimize: a library for numerical optimization with autograd, 2021.

[FJM02] Gero Friesecke, Richard D. James, and Stefan Müller. A theorem on geometric rigidity and the derivation of nonlinear plate theory from three-dimensional elasticity. *Comm. Pure Appl. Math.*, 55(11):1461–1506, 2002.

[FJMM03] Gero Friesecke, Richard D. James, Maria Giovanna Mora, and Stefan Müller. Derivation of nonlinear bending theory for shells from three-dimensional nonlinear elasticity by Gamma-convergence. *C. R. Math. Acad. Sci. Paris*, 336(8):697–702, 2003.

[FKZ25] Manuel Friedrich, Leonard Kreutz, and Konstantinos Zemas. Derivation of kirchhoff-type plate theories for elastic materials with voids, 2025. arXiv pre-print.

[FRW11] Martina Franken, Martin Rumpf, and Benedikt Wirth. A phase field based PDE constraint optimization approach to time discrete Willmore flow. *International Journal of Numerical Analysis and Modeling*, 2011.

[GA20] Anthony Gruber and Eugenio Aulisa. Computational p-Willmore flow with conformal penalty. *ACM Transaction on Graphics*, 39(5), August 2020.

[Gau27] Carl Friedrich Gauß. Disquisitiones generales circa superficies curvas. *Commentationes Societatis Regiae Scientiarum Gottingensis recentiores*, 6:99–146, 1827.

[GH08] Richards Grzhibovskis and Alexei Heintz. A convolution thresholding scheme for the Willmore flow. *Interfaces and Free Boundaries*, 10(2):139–153, 2008.

[GHDS03] Eitan Grinspun, Anil N. Hirani, Mathieu Desbrun, and Peter Schröder. Discrete shells. In *Proceedings of the 2003 ACM SIGGRAPH/Eurographics Symposium on Computer Animation*, SCA '03, page 62–67, Goslar, DEU, 2003. Eurographics Association.

[GO23] Peter Gladbach and Heiner Olbermann. Approximation of the willmore energy by a discrete geometry model. *Advances in Calculus of Variations*, 16(2):403–424, 2023.

[GT83] David Gilbarg and Neil S. Trudinger. *Elliptic partial differential equations of second order*, volume 224 of *Grundlehren der math. Wissensch.* Springer, 1983.

[Gur81] Morton E. Gurtin. *An Introduction to Continuum Mechanics*. Academic Press, 1981.

[Hee16] Behrend Heeren. *Numerical Methods in Shape Spaces and Optimal Branching Patterns*. PhD thesis, University of Bonn, 2016.

[HN59] Philip Hartman and Louis Nirenberg. On spherical image maps whose Jacobians do not change sign. *Amer. J. Math.*, 81:901–920, 1959.

[HNV14] Peter Hornung, Stefan Neukamm, and Igor Velčić. Derivation of a homogenized nonlinear plate theory from 3d elasticity. *Calculus of variations and partial differential equations*, 51(3-4):677–699, 2014.

[Hor11] Peter Hornung. Approximation of flat $W^{2,2}$ isometric immersions by smooth ones. *Arch. Ration. Mech. Anal.*, 199(3):1015–1067, 2011.

[Hor17] Peter Hornung. Stationary points of nonlinear plate theories. *J. Funct. Anal.*, 273(3):946–983, 2017.

[HRS+14] Behrend Heeren, Martin Rumpf, Peter Schröder, Max Wardetzky, and Benedikt Wirth. Exploring the geometry of the space of shells. *Comput. Graph. Forum*, 33(5):247–256, 2014.

[HRS+16] Behrend Heeren, Martin Rumpf, Peter Schröder, Max Wardetzky, and Benedikt Wirth. Splines in the space of shells. *Comput. Graph. Forum*, 35(5):111–120, 2016.

[HRS20] Peter Hornung, Martin Rumpf, and Stefan Simon. On material optimisation for nonlinearly elastic plates and shells. *ESAIM Control Optim. Calc. Var.*, 26:82, 2020.

[HRWW12] Behrend Heeren, Martin Rumpf, Max Wardetzky, and Benedikt Wirth. Time-discrete geodesics in the space of shells. *Comput. Graph. Forum*, 31(5):1755–1764, 2012.

[HZRS18] Behrend Heeren, Chao Zhang, Martin Rumpf, and William Smith. Principal geodesic analysis in the space of discrete shells. *Comput. Graph. Forum*, 37(5):173–184, 2018.

[JMR+19] Caigui Jiang, Klara Mundilova, Florian Rist, Johannes Wallner, and Helmut Pottmann. Curve-pleated structures. *ACM Transactions on Graphics (TOG)*, 38(6):1–13, 2019.

[KB15] Diederik P. Kingma and Jimmy Ba. Adam: A Method for Stochastic Optimization. In *International Conference on Learning Representations*, 2015.

[KFC+08] Martin Kilian, Simon Flöry, Zhonggui Chen, Niloy J Mitra, Alla Sheffer, and Helmut Pottmann. Curved folding. *ACM transactions on graphics (TOG)*, 27(3):1–9, 2008.

[Kir50] Gustav R. Kirchhoff. 4. Über das Gleichgewicht und die Bewegung einer elastischen Scheibe. *Journal fur die Reine und Angewandte Mathematik*, 1850(40):51 – 88, 1850.

[Kir34] Mojżesz D. Kirszbraun. Über die Zusammenziehende und Lipschitzsche Transformationen. *Fundamenta Mathematicae*, 22(1):77–108, 1934.

[Kle21] Marian Kleineberg. Mesh-to-sdf: Calculate signed distance fields for arbitrary meshes, 2021.

[KS01] Ernst Kuwert and Reiner Schätzle. The Willmore flow with small initial energy. *Journal of Differential Geometry*, 57(3):409–441, 2001.

[KS02] Ernst Kuwert and Reiner Schätzle. Gradient flow for the Willmore functional. *Communications in Analysis and Geometry*, 10(5):1228–1245 (electronic), 2002.

[KS04] Ernst Kuwert and Reiner Schätzle. Removability of point singularities of Willmore surfaces. *Annals of Mathematics*, pages 315–357, 2004.

[Kui55] Nicolaas H. Kuiper. On C^1-isometric imbeddings. I, II. *Nederl. Akad. Wetensch. Proc. Ser. A.* **58** = *Indag. Math.*, 17:545–556, 683–689, 1955.

[LC23] Seunggyu Lee and Yongho Choi. Curvature-based interface restoration algorithm using phase-field equations. *Plos one*, 18(12):e0295527, 2023.

[LDR95] Hervé Le Dret and Annie Raoult. The nonlinear membrane model as variational limit of nonlinear three-dimensional elasticity. *J. Math. Pures Appl. (9)*, 74(6):549–578, 1995.

[LDR96] Hervé Le Dret and Annie Raoult. The membrane shell model in nonlinear elasticity: a variational asymptotic derivation. *J. Nonlinear Sci.*, 6(1):59–84, 1996.

[LJ24] Huan Liu and Richard D. James. Design of origami structures with curved tiles between the creases. *Journal of the Mechanics and Physics of Solids*, 185:105559, 2024.

[LL20] Marta Lewicka and Danka Lučić. Dimension reduction for thin films with transversally varying prestrain: Oscillatory and nonoscillatory cases. *Communications on Pure and Applied Mathematics*, 73(9):1880–1932, 2020.

[Lov88] Augustus Edward Hough Love. Xvi. the small free vibrations and deformation of a thin elastic shell. *Philosophical Transactions of the Royal Society of London.(A.)*, 179:491–546, 1888.

[LP17] Ke Liu and Glaucio H Paulino. Nonlinear mechanics of non-rigid origami: an efficient computational approach. *Proc. Roy. Soc. A*, 473(20170348), 2017.

[Luk21] Ekaterina Lukasheva. *Curved Origami*. New Origami Publishing, 2021.

[MBO92] Barry Merriman, James K. Bence, and Stanley J. Osher. Diffusion generated motion by mean curvature. CAM Report 92-18, University of California Los Angeles, 1992.

[MBO94] Barry Merriman, James K. Bence, and Stanley J. Osher. Motion of multiple junctions: A level set approach. *Journal of Computational Physics*, 112:334–363, 1994.

[MM77] Luciano Modica and Stefano Mortola. Un esempio di Γ-convergenza. *Boll. Un. Mat. Ital. B (5)*, 14(1):285–299, 1977.

[MN14] Fernando C Marques and André Neves. Min-max theory and the Willmore conjecture. *Annals of Mathematics*, pages 683–782, 2014.

[MNP02] Gianni Dal Maso, Matteo Negri, and Danilo Percivale. Linearized elasticity as gamma-limit of finite elasticity. *Set-Valued Anal. 10 (2002), p.165-183*, 10(SISSA;69/2001/M), 2002.

[MP05] Stefan Müller and Mohammad Reza Pakzad. Regularity properties of isometric immersions. *Mathematische Zeitschrift*, 251:313–331, 2005.

[MPG79] Luiz Carlos Martins and Paolo Podio-Guidugli. A variational approach to the polar decomposition theorem. *Atti della Accademia Nazionale dei Lincei. Classe di Scienze Fisiche, Matematiche e Naturali. Rendiconti*, 66(6):487–493, 6 1979.

[MPL+24] Diego Misseroni, Phanisri P. Pratapa, Ke Liu, Biruta Kresling, Yan Chen, Chiara Daraio, and Glaucio H. Paulino. Origami engineering. *Nature Reviews Methods Primers*, 4(40), 2024.

[MRS21] Janos Meny, Martin Rumpf, and Josua Sassen. A phase-field approach to variational hierarchical surface segmentation. *Computer Aided Geometric Design*, 89:102025, 2021.

[MS89] David Mumford and Jayant Shah. Optimal approximations by piecewise smooth functions and associated variational problems. *Comm. Pure Appl. Math.*, 42(5):577–685, 1989.

[Nas54] John Nash. C^1 isometric imbeddings. *Annals of Mathematics*, 60(3):383–396, 1954.

[Neu12] Stefan Neukamm. Rigorous derivation of a homogenized bending-torsion theory for inextensible rods from three-dimensional elasticity. *Archive for Rational Mechanics and Analysis*, 206, 11 2012.

[NMS93] Mark Nitzberg, David Mumford, and Takahiro Shiota. *Filtering, Segmentation and Depth (Lecture Notes in Computer Science Vol. 662)*. Springer-Verlag Berlin Heidelberg, 1993.

[NO15] Stefan Neukamm and Heiner Olbermann. Homogenization of the nonlinear bending theory for plates. *Calculus of Variations and Partial Differential Equations*, 53(3-4):719–753, 2015.

[NV13] Stefan Neukamm and Igor Velčić. Derivation of a homogenized von-Kármán plate theory from 3d nonlinear elasticity. *Mathematical Models and Methods in Applied Sciences*, 23(14):2701–2748, 2013.

[NW06] Jorge Nocedal and Stephen J. Wright. *Numerical optimization*. Springer series in operations research and financial engineering. Springer, New York, NY, 2 edition, 2006.

[Ogd97] R. W. Ogden. *Non-Linear Elastic Deformations*. Dover Publications, Mineola, New York, 1997.

[OR09] Nadine Olischläger and Martin Rumpf. Two Step Time Discretization of Willmore Flow. In Edwin R. Hancock, Ralph R. Martin, and Malcolm A. Sabin, editors, *Mathematics of Surfaces XIII*, volume 5654, pages 278–292. Springer Berlin Heidelberg, Berlin, Heidelberg, 2009.

[Pak04] Mohammad Reza Pakzad. On the Sobolev space of isometric immersions. *J. Differential Geom.*, 66(1):47–69, 2004.

[PGM+19] Adam Paszke, Sam Gross, Francisco Massa, Adam Lerer, James Bradbury, Gregory Chanan, Trevor Killeen, Zeming Lin, Natalia Gimelshein, Luca Antiga, Alban Desmaison, Andreas Kopf, Edward Yang, Zachary DeVito, Martin Raison, Alykhan Tejani, Sasank Chilamkurthy, Benoit Steiner, Lu Fang, Junjie Bai, and Soumith Chintala. Pytorch: An imperative style, high-performance deep learning library. In H. Wallach, H. Larochelle, A. Beygelzimer, F. dAlché-Buc, E. Fox, and R. Garnett, editors, *Advances in Neural Information Processing Systems*, volume 32. Curran Associates, Inc., 2019.

[PRW12] Patrick Penzler, Martin Rumpf, and Benedikt Wirth. A phase-field model for compliance shape optimization in nonlinear elasticity. *ESAIM Contr. Opt. Calc. Var.*, 18:229–258, 2012.

[Rin18] Filip Rindler. *Calculus of Variations*. Universitext. Springer Cham, 2018.

[Riv08] Tristan Rivière. Analysis aspects of Willmore surfaces. *Inventiones Mathematicae*, 174(1):1–45, 2008.

[RSS22] Martin Rumpf, Stefan Simon, and Christoph Smoch. Finite element approximation of large-scale isometric deformations of parametrized surfaces. *SIAM Journal on Numerical Analysis*, 60(5):2945–2962, 2022.

[RSS24] Martin Rumpf, Stefan Simon, and Christoph Smoch. Two-scale finite element approximation of a homogenized plate model. *SIAM Journal on Numerical Analysis*, 62(5):2121–2142, 2024.

[RSS25] Martin Rumpf, Josua Sassen, and Christoph Smoch. A hybrid minimizing movement and neural network approach to Willmore flow, 2025. arXiv pre-print.

[Rus05] Raluca E. Rusu. An algorithm for the elastic flow of surfaces. *Interfaces and Free Boundaries*, 7(3):229–239, 2005.

[San17] Filippo Santambrogio. {Euclidean, metric, and Wasserstein} gradient flows: An overview. *Bull. Math. Sci.*, 7:87–154, 2017.

[SCD+21] Yousuf Soliman, Albert Chern, Olga Diamanti, Felix Knöppel, Ulrich Pinkall, and Peter Schröder. Constrained Willmore surfaces. *ACM Transaction on Graphics*, 40(4), 2021.

[Sch07] Bernd Schmidt. Plate theory for stressed heterogeneous multilayers of finite bending energy. *Journal de Mathématiques Pures et Appliquées*, 88(1):107–122, 2007.

[Sch17] Henrik Schumacher. On H^2-gradient flows for the Willmore energy, 2017. arXiv pre-print.

[SGFS01] Olaf Schenk, Klaus Gärtner, Wolfgang Fichtner, and Andreas Stricker. PARDISO: a high-performance serial and parallel sparse linear solver in semiconductor device simulation. *Future Generation Computer Systems*, 18(1):69–78, 2001. I. High Performance Numerical Methods and Applications. II. Performance Data Mining: Automated Diagnosis, Adaption, and Optimization.

[Sim01] Gieri Simonett. The Willmore Flow near spheres. *Diff. and Integral Eq.*, 14(8):1005–1014, 2001.

[Smo21] Christoph Smoch. Numerical analysis for the approximation of elastic deformations between parametric surfaces. Master's thesis, Rheinische Friedrich-Wilhelms-Universität Bonn, 2021.

[SSRC24] Josua Sassen, Henrik Schumacher, Martin Rumpf, and Keenan Crane. Repulsive shells. *ACM Trans. Graph.*, 43(4), 2024. best paper award SIGGRAPH 2024.

[SWM+20] Renate Sachse, Anna Westermeier, Max Mylo, Joey Nadasdi, Manfred Bischoff, Thomas Speck, and Simon Poppinga. Snapping mechanics of the venus flytrap (dionaea muscipula). *Proceedings of the National Academy of Sciences*, 117(27):16035–16042, 2020.

[TBWP16] Chengcheng Tang, Pengbo Bo, Johannes Wallner, and Helmut Pottmann. Interactive design of developable surfaces. *ACM Transactions on Graphics (TOG)*, 35(2):1–12, 2016.

[Vel15] Igor Velčić. On the derivation of homogenized bending plate model. *Calculus of variations and partial differential equations*, 53:561–586, 2015.

[VGO+20] Pauli Virtanen, Ralf Gommers, Travis E. Oliphant, Matt Haberland, Tyler Reddy, David Cournapeau, Evgeni Burovski, Pearu Peterson, Warren Weckesser, Jonathan Bright, Stéfan J. van der Walt, Matthew Brett, Joshua Wilson, K. Jarrod Millman, Nikolay Mayorov, Andrew R. J. Nelson, Eric Jones, Robert Kern, Eric Larson, C J Carey, İlhan Polat, Yu Feng, Eric W. Moore, Jake VanderPlas, Denis Laxalde, Josef Perktold, Robert Cimrman, Ian Henriksen, E. A. Quintero, Charles R. Harris, Anne M. Archibald, Antônio H. Ribeiro, Fabian Pedregosa, Paul van Mulbregt, and SciPy 1.0 Contributors. SciPy 1.0: Fundamental Algorithms for Scientific Computing in Python. *Nature Methods*, 17:261–272, 2020.

[WB06] Andreas Wächter and Lorenz T. Biegler. On the Implementation of a Primal-Dual Interior Point Filter Line Search Algorithm for Large-Scale Nonlinear Programming. *Mathematical Programming*, 106(1):25–57, 2006.

[WBH+07] Max Wardetzky, Miklós Bergou, David Harmon, Denis Zorin, and Eitan Grinspun. Discrete quadratic curvature energies. *Computer Aided Geometric Design*, 24(8):499–518, 2007. Discrete Differential Geometry.

[YN07] Takashi Yokoyama and Kenji Nakai. Evaluation of in-plane orthotropic elastic constants of paper and paperboard. In *Proceeding of 2007 SEM Annual Conference & Exposition on Experimental and Applied Mechanics*, 2007.